Report
R-23-01
November 2024

Baseline Forsmark – A discrete fracture network (DFN) model applying grown fractures and hydromechanical (HM) coupling

Lee Hartley
Simon Libby
Tomas Bym
James Carty
Mark Cottrell
Kyle Mosley

SVENSK KÄRNBRÄNSLEHANTERING AB

SWEDISH NUCLEAR FUEL
AND WASTE MANAGEMENT CO

Box 3091, SE-169 03 Solna
Phone +46 8 459 84 00
skb.se

SVENSK KÄRNBRÄNSLEHANTERING

ISSN 1402-3091
SKB R-23-01
ID 2058547

November 2024

Baseline Forsmark – A discrete fracture network (DFN) model applying grown fractures and hydromechanical (HM) coupling

Lee Hartley, Simon Libby, Tomas Bym, James Carty, Mark Cottrell, Kyle Mosley

WSP Sverige AB

Abstract

In preparation for the start of construction of the repository accesses and associated underground characterisation initiatives, an update of the surface-based Forsmark site models, SDM-Site Forsmark and SDM-PSU, is taking place. The updated model is named Baseline Forsmark and describes the site conditions prior to start of constructions. The main objective of the update is to account for additional information acquired since SDM-Site and SDM-PSU, including some new boreholes near the access area of the planned spent nuclear fuel repository (SFK) and investigations associated with the extension of SKB's repository for short-lived radioactive waste (SFR). The updated model is intended to serve development needs for both the spent nuclear fuel (SFK) and SFR facilities.

A second objective of the work reported here is to apply, as far as possible, the latest novel DFN modelling methodology presented in (Selroos et al. 2022). This differs in several ways from the DFN modelling methodology applied in SDM-Site, SDM-PSU, SR-Site, and SR-PSU. For the sake of clarity, the two methodologies are named DFN-M2022 (this work) and DFN-M2008 (former projects), respectively. Two models will be tested in Baseline Forsmark to gain insights differences between the DFN-M2008 and DFN-M2022 methodologies and what consequences their applications have for regional scale groundwater flow and solute transport modelling. The model tested in Baseline Forsmark are preliminary named DFN-BF1 (based on DFN-M2022) and DFN-BF2 (based on DFN-M2008). In conclusion, this report describes the development of the DFN-BF1 model having been defined for the underground construction and characterisation phase.

A more holistic approach has been taken in the current modelling relative to SDM-Site. The DFN-BF1 model makes a seamless integration of deterministic, stochasticstochastic, and semi-stochastic structural modelling across scales from metres to several kilometres. Geometric, geomechanical and hydraulic properties of fractures and physical dependencies between them are all incorporated in the same model to ensure consistency of conceptual descriptions. For example, strong links are made between the fracture geometric description with understanding of deformation and hydrothermal alteration histories, and hydromechanics are used as a basis for predicting trends in fracture hydraulics and their responses to changes in loadings. This opens new possibilities to identify inter-dependencies between these parameters and how uncertainties can be constrained. It is expected that recognising such inter-disciplinary dependencies will compound the benefits of any advances made in reducing individual uncertainties across models for hydraulic and mechanical properties and the stress field, especially as new opportunities for bedrock characterisation are realised during underground construction of SFK and SFR facilities. Hence, a central focus for the bedrock description is an update of the DFN model to provide an integrated hydro-structural-mechanical conceptual and numerical model as a foundation for hydrogeological and hydrogeochemical property and process models.

Some highlights of the new novel DFN modelling methodology, DFN-M2022, include:

- Describing fracturing as occurring through a sequence of main deformation phases and mimicking these phases through use of a grown-DFN (G-DFN);
- Representing deformation zones (deterministic and stochastic) as tabular domains of fracture networks representing their damage zones;
- Representing additional stochastic and semi-stochastic deformation zones outside, and smaller ones inside, the volume of focused characterisation;
- Representing structural variability on a continuous range of scales by introducing small stochastic deformation zones (smaller than any modelled deterministically) to describe variability in background fracturing within each of the regional fracture domains, again as a G-DFN;
- Identifying differences in fracture characteristics, including spatial variability, intensity openness and stress field, between inside the Forsmark tectonic lens and outside, by analysing both KFM and KFR fracture data;
- Integrating a 3D rock mass mechanical model and stress field to describe the drivers for spatial controls and variability in flow; and
- Utilising detailed hydro-structural-mechanical DFN models to simulate each specific PFL test and interference test to demonstrate the improved matching of structural-hydraulic conditions around individual boreholes and hydraulic connections between them.

Sammanfattning

Under förberedelserna för byggstarten av slutförvaren i Forsmark pågår en uppdatering av de platsbeskrivande modellerna från SDM-Site Forsmark och SDM-PSU, vilka mestadels bygger på data som samlats genom undersökningar från markytan. De uppdaterade modellerna benämns Baseline Forsmark och beskriver platsförhållandena före byggstart. Huvudsyftet med uppdateringarna är att ta hänsyn till nytillkommen information som erhållits sedan SDM-Site och SDM-PSU. För sprickmodellen omfattar detta några nya borrhål i närheten av tillträdesområdet för det planerade förvaret för använt kärnbränsle (SFK) och undersökningar utförda inför utbyggnaden av SKB:s slutförvar för kortlivat låg- och medelaktivt radioaktivt avfall (SFR). Den uppdaterade sprickmodellen är avsedd att omfatta både SFK och SFR.

Ett andra syfte med det arbete som rapporteras här är att tillämpa, så långt som möjligt, den senaste DFN-modelleringsmetodiken som presenteras i Selroos et al. (2022). Denna skiljer sig på flera sätt från den DFN-modelleringsmetodik som tillämpades i SDM-Site, SDM-PSU, SR-Site och SR-PSU. För tydlighetens skull namnges de två metodikerna DFN-M2022 (detta arbete) och DFN-M2008 (tidigare projekt). Två modeller, vilka bygger på DFN-M2022- och DFN-M2008-metodiken, kommer att testas i Baseline Forsmark för att få insikt om skillnader mellan metodikerna och vilka konsekvenser appliceringen av dem har för grundvattenflödes- och ämnestransportsmodellering på regional skala. Modellerna som testas i Baseline Forsmark är preliminärt namngivna DFN-BF1 (baserat på DFN-M2022) och DFN-BF2 (baserat på DFN-M2008). Sammanfattningsvis beskriver denna rapport utvecklingen av DFN-BF1-modellen inför den bygg- och platsbeskrivningsfasen.

Ett större helhetsgrepp har tagits i den nuvarande modelleringen jämfört med SDM-Site. DFN-BF1-modellen utgör en sömlös integration för modellering, från meter- till kilometerskala, av stokastiska, semistokastiska och deterministiska strukturer. Sprickornas geometriska, geomekaniska och hydrauliska beroenden och egenskaper är införlivade i samma modell för att säkerställa konsistens i de konceptuella beskrivningarna. Till exempel görs starka kopplingar mellan geometrisk sprickbeskrivning och förståelse av den historiska utvecklingen av deformation och hydrotermal alterationshistoria. Även hydromekaniska kopplingar används som grund för att förutsäga spatiala trender i sprickors flödesegenskaper liksom deras flödesrespons till följd av förändringar i spänningsfältet. Detta öppnar för nya möjligheter att identifiera beroenden mellan parametrar och därmed hur osäkerheter kan minskas. Det förväntas att användandet av sådana tvärvetenskapliga beroenden kommer att minska den totala osäkerheten när osäkerheterna i kopplingarna mellan spänningsfältet och de hydrauliska och de mekaniska egenskaperna minskar, särskilt när nya data blir tillgänglig från underjordsdelarna av SFK och SFR. Således är ett centralt fokus för berggrundsbeskrivningen en uppdatering av DFN-modellen för att tillhandahålla en integrerad hydrostruktur-mekanisk konceptuell och numerisk modell, vilken ligger till grund för hydrogeologiska och hydrogeokemiska egenskaps- och processmodeller.

Några höjdpunkter av den nya DFN-modelleringsmetodiken, DFN-M2022, inkluderar:

- Beskrivning av sprickbildning genom en sekvens av huvudsakliga deformationsfaser och efterliknande av dessa faser genom användning av växande sprickor (G-DFN);
- Representation av deterministiska och stokastiska deformationszoner som volymer fyllda av stokastiska sprickor för att efterlikna den spröda deformationen;
- Representation av små stokastiska och semi-stokastiska deformationszoner inom fokusområdet, samt större utanför fokusområdet;
- Representation av den strukturella variabiliteten, för alla skalor, genom att införa små stokastiska deformationszoner (mindre än de deterministiskt modellerade) för att återskapa den mätta variabiliteten i bakgrundsprickighet inom varje regional sprickdomän, återigen som en G-DFN;
- Identifiering av skillnader i sprickegenskaper, avseende rumslig variabilitet, intensitet, öppenhet och spänningsfält, mellan den tektoniska linsen och runtomliggande berg, genom att analysera sprickdata från både KFM- och KFR-hål;
- Integration av den geometriska 3D modellen och spänningsfältet för att beskriva drivkrafterna för rumsliga kontroll och variabilitet i flöde; och
- Använda detaljerade hydromekaniskt kopplade DFN-modeller för att simulera varje enskilt PFL-test, samt interferenstester, för att demonstrera den förbättrade matchningen av hydrostrukturella förhållanden runt specifika borrhål och de hydrauliska kopplingarna mellan dem.

Contents

1 Introduction

1.1 Context and purpose of model

In preparation for the start of construction of the repository accesses and associated underground characterisation initiatives, an update of the surface-based Forsmark site models, SDM-Site Forsmark (SKB 2008) and SDM-PSU (SKB 2013), is taking place. The main objective of the update is to account for additional information acquired since SDM-Site, including some new boreholes near the access area and investigation associated with the extension of SKB's repository for short-lived radioactive waste (SFR). The updated model is named Baseline Forsmark (SKB *in prep.*) and describes the site conditions prior to start of constructions. Baseline Forsmark is intended to serve as a reference of the development needs for both the spent nuclear fuel (SFK) and SFR facilities. A second objective of Baseline Forsmark is to apply, as far as possible, the latest recent modelling methodologies (Hermanson and Petersson 2022; Selroos et al. 2022), some of which have been defined for the underground construction and bedrock characterisation phase.

The novel DFN modelling methodology presented in (Selroos et al. 2022) differs in several ways from the DFN modelling methodology applied in SDM-Site (SKB 2008), SDM-PSU (SKB 2013), SR-Site (SKB 2011), and SR-PSU (SKB 2015). One essential component of the novel methodology is to provide both a geometric description of brittle fracturing in the bedrock, but also a foundation for modelling the properties, processes, and evolution of bedrock geomechanics, hydrogeology and hydrogeochemistry and the couplings between them. For the sake of clarity, the two methodologies are named DFN-M2022 (this work) and DFN-M2008 (former projects), respectively. Two models will be tested in Baseline Forsmark to gain insights differences between the DFN-M2008 and DFN-M2022 methodologies and what consequences their applications have for regional scale groundwater flow and solute transport modelling. The model tested in Baseline Forsmark are preliminarily named DFN-BF1 (based on DFN-M2022) and DFN-BF2 (based on DFN-M2008). In conclusion, the DFN-M2022 methodology is conceived as an alternative to the DFN-M2008 methodology, and this report describes the development of DFN-BF1 using DFN-M2022.

A working assumption in the DFN modelling methodology for SDM-Site and SDM-PSU, i.e., DFN-M2008, was that a tectonic continuum exists where the number of features of different sizes follows a power-law relationship across scales of metres to kilometres. All structures up to length, L, of 1 000 m (or equivalent radius of a disc $r \approx 564$ m) being modelled in a DFN as stochastically generated planes, while larger structures, deformation zones (DZ), were modelled deterministically based on a geologist's structural interpretation of lineaments, borehole intercepts and geophysics. Although it was recognised that zones are made up of swarms of fractures, their geometric representation was simplified to sub-planar surfaces and the transmissivity of fractures within them lumped across them and extrapolated across them, see Figure 1-1. Hence, there was a fixed border between deterministic and stochastic modelling and limited assessment of the effects of DZ architecture. However, near the planned spent fuel repository (SFK), i.e., on a facility scale (~2 km) the deterministically modelled DZs were tessellated (~100 m) and modelled as hydraulically heterogeneous, see e.g. Figure 6-2 of (Follin 2008). About thirty of these DZ had trace lengths less than 1 000 m.

In the DFN-BF1 modelling work reported here a more holistic approach to DFN modelling is envisaged through strategies that are defined in the DFN-M2022 methodology. For example, integrating deterministic and stochastic structural modelling methods across the scales from metres to several kilometres; making strong links between the fracture description with understanding of deformation and hydrothermal alteration histories, and using hydromechanics as a basis for predicting trends in fracture hydraulics and their responses to changes in loadings.

Many aspects of the new novel DFN data handling, conceptualisation and modelling methods described here were trialled in a preliminary update of the novel DFN modelling approach for the upper part of the bedrock (Hartley et al. 2021), with further proof of concept type work taking place in the DFN methodology project (Libby et al. 2019; Selroos et al. 2022), DFN Studio (Libby et al. 2019; Libby et al. 2024) and other SKB sponsored research (Selroos et al. 2015; Bym and Hermanson 2018).

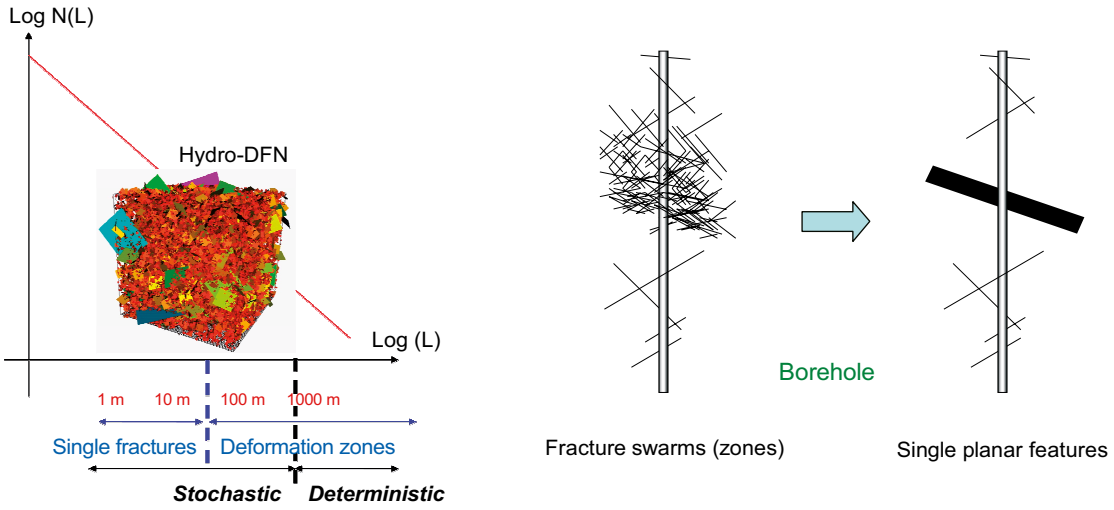

Figure 1-1. *Cartoons showing the approach used for the treatment of single fractures and deformation zones (certain, as well as possible) in the DFN modelling for SDM-Site and SDM-PSU. Left: A tectonic continuum was envisaged in the hydrogeological modelling where the number of features of different sizes follows a power-law relationship. All features up to L = 1 000 m (r ≈ 564 m) were regarded as uncertain and treated stochastically using discrete fractures. Right: The fracture data gathered between the upper and lower bounds of a deformation zone interval were lumped together to form a single planar structure. In the same fashion, all hydraulic data in the interval are also lumped together, to form a single transmissivity value. Reproduced from (Follin 2008).*

It is therefore timely to construct a Baseline DFN model, DFN-BF1, applying the complete alternative DFN modelling methodology across the scale of the Forsmark catchment (see Figure 1-2) and utilising the latest data. The final model should serve the need for reliable predictions of baseline (pre-construction) structural and hydrogeological conditions, and hence some validation of the model is required. At this stage, however, only some new structural mapping data is available from drone mapping of some rock exposures in the bay to the north of Forsmark for use in prediction-outcome exercises. Once construction begins it is the intention to perform further prediction-outcome exercises to gauge the reliability of the model.

Applying the latest novel modelling methodology, DFN-M2022, in Baseline Forsmark is a means to evaluate whether the methodology will align with the conceptual framework envisaged for the construction phase. Once underground investigations begin, reliability of the developed model can be assessed through a series of prediction-outcome exercises against data of a nature and quantity different that available from the surface. That will allow characterisation of fracture geometries, properties and network architecture on scales not seen previously in the subsurface. Cycles of underground investigation, prediction-outcome, model review and potential updating are therefore envisaged during the construction phase. By establishing suitable baseline models, such updates are anticipated to involve refinements of assumptions, parameters and conditioning to location specific geological properties rather than fundamental changes in the modelling concepts, as defined in the methodologies.

To assess the implications of using different DFN modelling methodologies, the alternative DFN methodology (DFN-M2022) will be used in parallel with the DFN methodology used in SDM-Site and SDM-PSU (DFN-M2008) in Baseline Forsmark. Hence, Baseline Formark does not disqualify or promote a particular DFN modelling methodology as both DFN modelling methodologies can provide quantitative prescriptions, or recipes, for constructing DFN model realisations on all scales of interest. These scales range from deposition hole scale to the regional scale, using SKB's SDM model scale conventions shown in Figure 1-3, which coincides with the scale of the Forsmark catchment. This descriptive model will be supported by multiple DFN model realisations on both the facility scale (for SFK and SFR facilities) and the Forsmark catchment, combining both stochastic and current deterministically modelled structures.

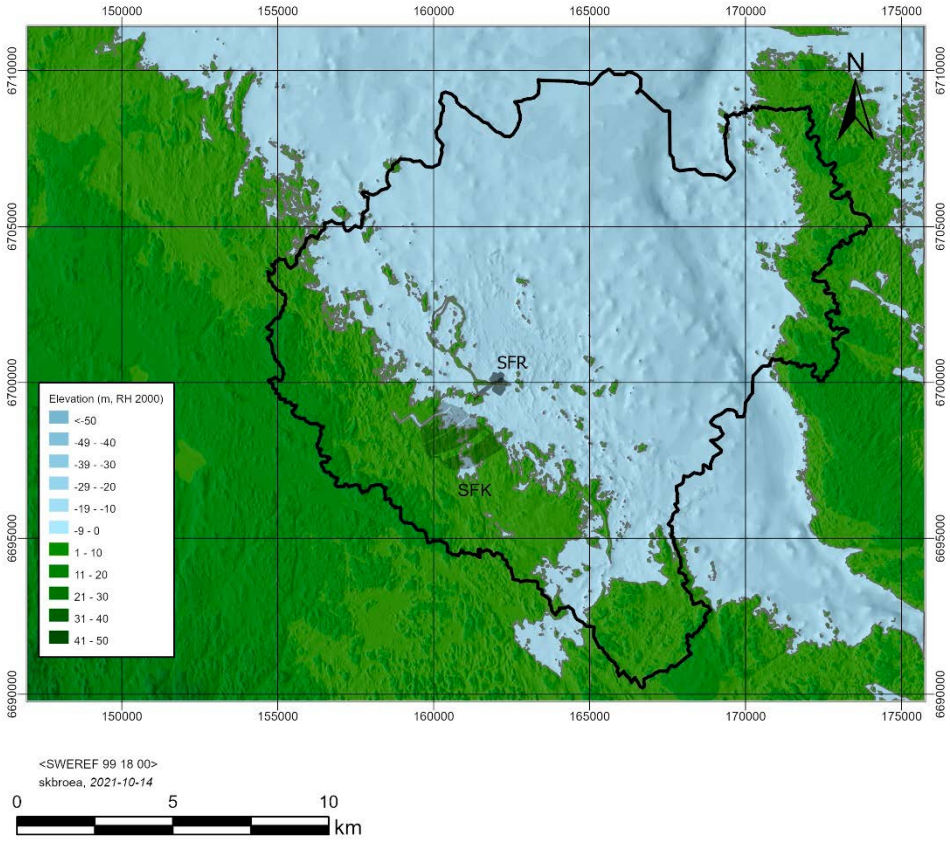

Figure 1-2. *Topographic map of the Forsmark area. The Forsmark catchment (also named the Baseline Forsmark area) shown in black corresponds to the boundary for catchment scale modelling for the Baseline Forsmark SDM. Derivation of the black line is described in (Earon R. 2022).*

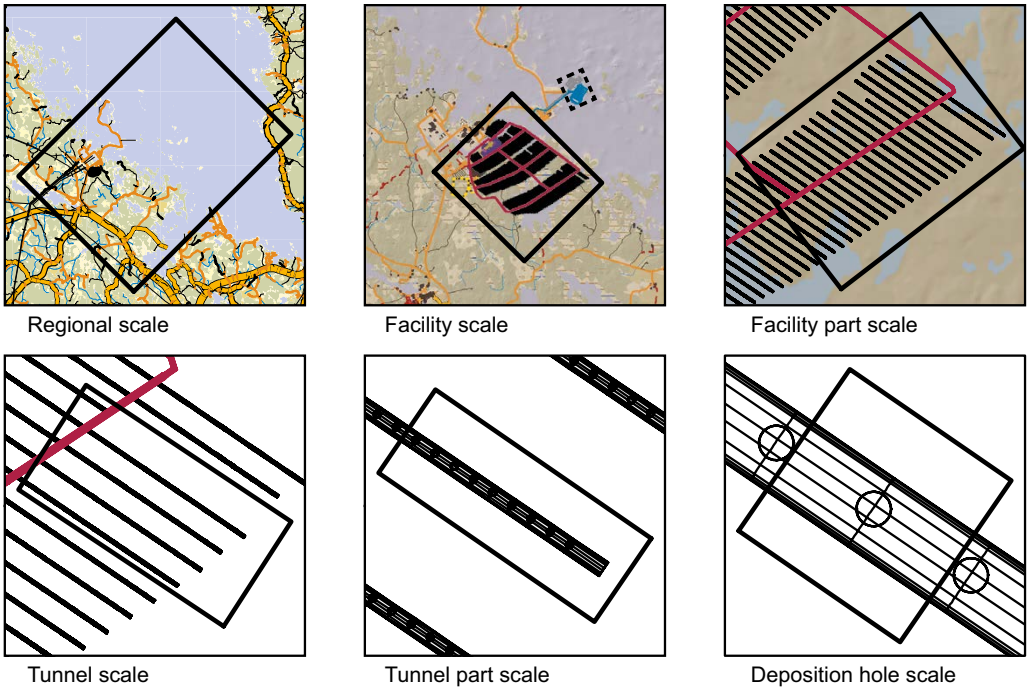

Figure 1-3. *Illustration of the model scales that can be employed during the construction and operation of the final repository and during development of the SDM. After (SKB 2018).*

Finally, DFN modelling is considered to provide the most natural and direct representation of the fractures that determine much of the bedrock mechanical, hydrogeological, and solute transport conditions and hence is the primary integrated numerical model of the bedrock. Interactions between fracture systems and porewater in the matrix can also be considered in fracture and channel systems, e.g. (Neretnieks 1979; Neretnieks 2006; Svensson et al. 2018; Baxter et al. 2021). Recognising that other modelling applications, such as Environmental Impact Assessment and Hydrogeochemical Evolution, use equivalent continuous porous medium (ECPM) representations, realisations will be upscaled to equivalent grid-based properties (Odén et al. in prep.[1]). This represents a change in strategy from SDM-Site, from providing a recipe for DFN models before, to now delivering DFN models and their equivalent continuum properties on grids as required by downstream applications.

1.2 Model scales

The data on which the DFN-BF1 model is based spans borehole radius scale (centimetre) through outcrop scale (tens of metres) to regional scale (tens of kilometres). Views of some of the site data at different scales are shown in Figure 1-4. The clipped edges of the lineaments (red) indicate the maximum extent of the lineaments considered in the deterministic structural geological modelling within the Baseline Forsmark catchment area (i.e. black line shown in Figure 1-2). The outer black box indicates the boundaries of the geological model for rock types and the inner black box corresponds to the facility scale of detailed modelling of fracture domains around the spent nuclear fuel (SFK) repository. To show the areas of focus, a layout for this facility beneath the coastline, and the main SFR tunnel to the north–east are shown in grey in the lower left insert, with associated core drilled investigation boreholes in black.

Definitions of various types of geological domain (ZFM, RFM and FFM) are defined in Section 2.3.

[1] Odén M, Follin S, Werner K, Lindborg E. Methodology for integrated hydrological-hydrogeological modelling of the Forsmark site. SKB R-20-15 (in prep.), Svensk Kärnbränslehantering AB.

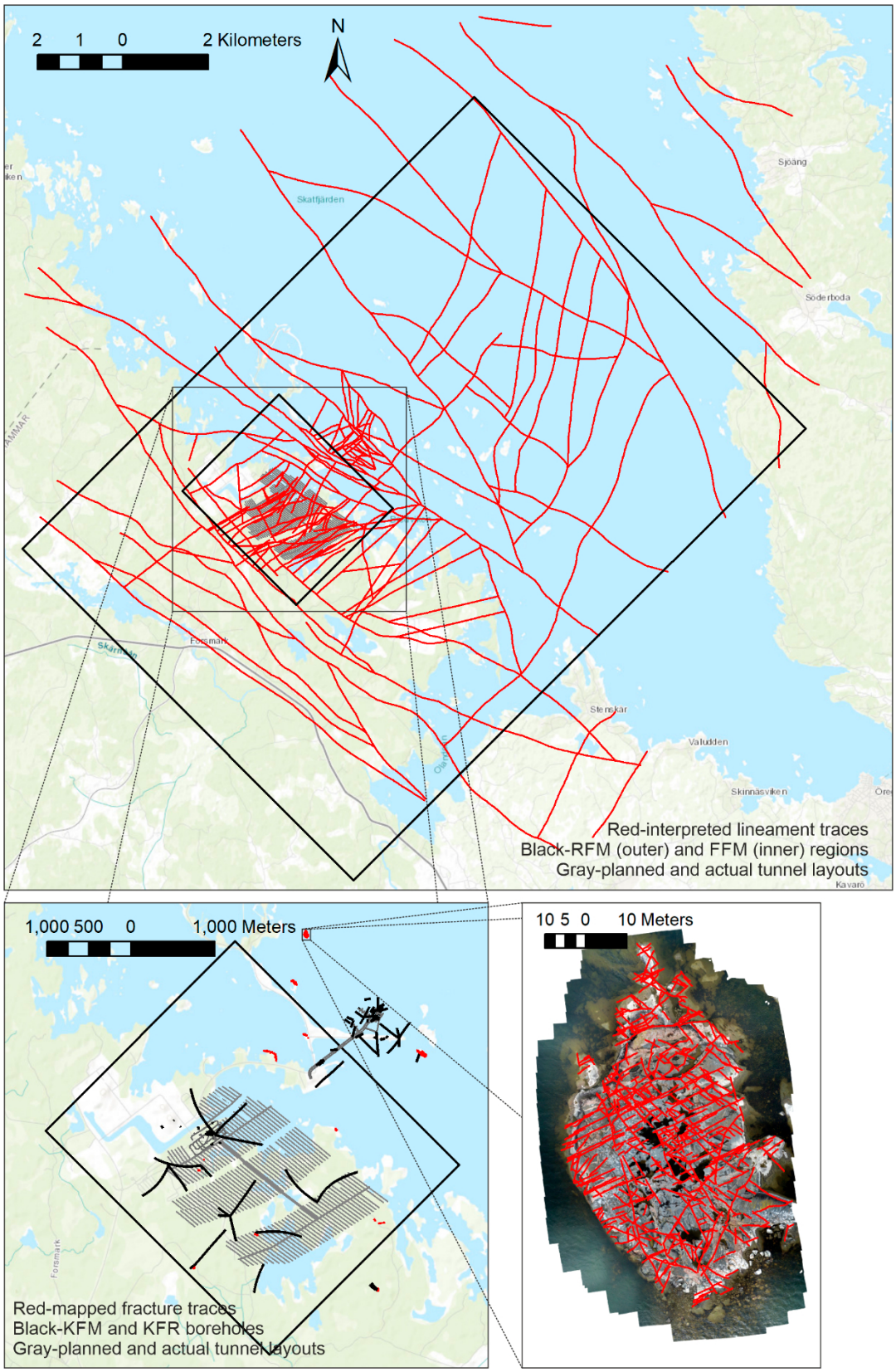

Figure 1-4. *Nested views of site data at different scales. Top) Regional scales used in the deterministic structural geological modelling. Bottom) Left: Facility-scale used for detailed geological modelling. Background Map courtesy of ESRI.*

1.3 Background on methodologies and new data

The latest SDM methodology documents guide the development of the DFN-BF1 model:

- Deterministic geological structural model – (Hermanson and Petersson 2022);
- DFN modelling – (Selroos et al. 2022);
- Rock mechanics modelling – (Hakami et al. 2022); and
- Hydrological and hydrogeological modelling – (Odén et al. in prep.[2]).

These provide updates for some basic modelling strategies outlined prior to SDM-Site and SDM-PSU:

- DFN modelling – (Munier 2004);
- Hydrogeology – (Rhén et al. 2003);
- Transport – (Berglund and Selroos 2004); and
- SDM integration (Andersson 2003).

Noteworthy changes in the DFN modelling methodology (Selroos et al. 2022) used in the DFN-BF1 model relative to SDM-Site and SDM-PSU (DFN 2008) are as follows (with pointers to relevant sections of that report where they are described). A flowchart for the combined DFN-M2022 methodology being illustrated in Figure 1-5, with the details of each step explained in Chapter 5.

- Using genetic growth algorithms to create the DFN rather than pure statistical methods (see Sections 6.3.5, 6.6.6 and 7.1 of (Selroos et al. 2022));
- Working with just three orientation sets related to main phases of deformation (see Section 2.2) and using bootstrapping method to describe variability in orientation around Forsmark tectonic lens structure (see Section 4.2);
- Deterministic (ZFM), semi-stochastic (PDZ) and stochastic (DZ) deformation zones modelled as fracture swarms (see Section 5.2 of (Selroos et al. 2022));
- Division of scales of structure in terms of large DZ (modelled deterministically where possible) on 250 m to 20 km scale, small DZ modelled on a 50 m to 250 m scale, and individual fractures on a dm to 150 m scale (see Section 4.1);
- Representation of variability in fracture intensity according to localised fracturing around discrete large DZ across the model domain and a background fabric of fracturing varying according to tectonic/lithological units known as fracture domains (FFM; see Sections 5.3 and 5.4 of (Selroos et al. 2022));
- Representation of sheet joints in the near-surface bedrock across the catchment area (see Section 5.4 of (Selroos et al. 2022));
- Representing the geometry of all fractures, but distributing openings (and sealed parts) across the network and surface area of each fracture (see Section 8.3 of (Selroos et al. 2022)); and
- Inclusion of hydromechanics in description of fracture hydraulics (see Sections 7.3, 8.4 and 8.8 of (Selroos et al. 2022)).

Several new boreholes have been drilled in the access areas KFM13–27, between 60 and 100 m deep, apart from KFM24, which is about 540 m deep. Hydrological characterisation of the new boreholes in the access area is described in (Follin 2019; Komulainen et al. 2019).

In addition, data from the investigations (e.g. structural and hydraulic data from HFR and KFR boreholes) for the extension of SFR facility is here combined with that available from the investigations for the SFK facility (e.g. boreholes HFM and KFM). Summaries of data and their interpretations from SFR are provided in (Öhman et al. 2012; Öhman et al. 2013; SKB 2013). Summaries of data available for DFN modelling and interpretations made for SDM-Site are provided in (Follin et al. 2007a; Follin et al. 2007b; Fox et al. 2007).

Preliminary structural interpretations of rock exposures on islands in the bay to the north of Forsmark using photogrammetry data taken with drones is (in prep.) has also been utilised.

[2] Odén M, Follin S, Werner K, Lindborg E. Methodology for integrated hydrological-hydrogeological modelling of the Forsmark site. SKB R-20-15 (in prep.), Svensk Kärnbränslehantering AB.

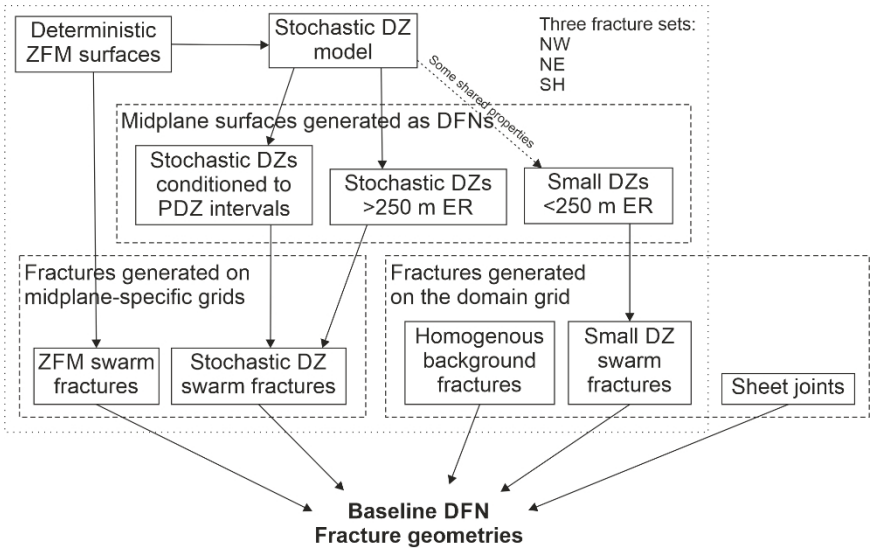

Figure 1-5. *Hybrid Flow Chart-Venn Diagram summarising how the individual geometrical DFN components described in this document are related. ER stands for equivalent radius, DZ for deformation zone, PDZ for borehole intercept with deformation zone type properties, ZFM for deterministically modelled DZ.*

1.4 Report structure

The report is structured to reflect the same themes used in the DFN modelling methodology report (Selroos et al. 2022):

- Chapter 2 provides an overview of the geological conditions at Forsmark, including visualisations of the latest models for rock domain, fracture domains and deformation zones that represent the upstream 3D deterministic models as inputs to the stochastic DFN modelling.
- Chapter 3 describes the input data to the study and some of the tools and methods used to store and analyse the data.
- Chapter 4 describes the development of the conceptual model for fracturing on different scales and the approach to describing variability.
- Chapter 5 presents the inference of other geometrical properties of fracture locations, intensity, size, and terminations with a summary of the recipe for generating realisations of the fracture geometries and illustrations of the resulting DFNDFN-BF1 model.
- Chapter 6 describes the mechanical properties assigned to fractures, including hydromechanical principles and their implementation on the fracture geometries.
- Chapter 7 presents the calibration of the integrated DFN geometries with the hydromechanical model against the flow logging and hydraulic interference tests.
- Chapter 8 considers validation of fracture geometries using the DFN-BF1 model against recent outcomes from mapping of rock exposures using drones.
- Chapter 9 presents the methods and results of upscaling the DFN-BF1 model to equivalent continuous porous medium models as used by downstream hydrogeological models.
- Chapter 10 concludes the study.

2 Geological context

2.1 Regional geological setting

Forsmark is situated approximately 120 km north of Stockholm in the south–eastern part of Sweden (Figure 2-1a). A gentle relief and a landscape situated below the highest shoreline, i.e., the highest level in Sweden reached by the sea during or after the latest Quaternary glaciation, characterise the region around Forsmark (Lidmar-Bergström 1994; Lundqvist 1994). The bedrock surface beneath the unconsolidated, Quaternary glacial and post-glacial deposits, which is exposed only locally on the ground surface at Forsmark, corresponds to the morphological structure referred to as the sub-Cambrian peneplain (Lidmar-Bergström 1994). This ancient denudation surface formed more than 540 million years ago. It corresponds geologically to a sub-Cambrian unconformity and marks a long period of uplift and erosion with loss of the geological record between the formation of the crystalline bedrock and the deposition of the unconsolidated Quaternary cover.

The bedrock at Forsmark is situated inside the Svecokarelian orogen in the south–western part of the Fennoscandian Shield (Figure 2-1a) which forms one of the ancient continental crustal fragments on Earth. This is bordered by an Archaean continental nucleus to the north–east, by the Sveconorwegian orogen to the south–west and by Neoproterozoic and Phanerozoic sedimentary cover rocks of the East European Platform to the south–east. In the west and north–west, it is overthrust by rocks that belong to the Caledonian orogen. The thickness of the continental crust in the region that includes Forsmark is around 50 km.

Intrusive rocks, felsic volcanic rocks and subordinate sedimentary rocks, the majority of which were affected by pervasive or more localized ductile strain and metamorphism at mid crustal levels, dominate the Svecokarelian orogen in south–eastern Sweden (Koistinen et al. 2001). Both the crystallisation of the igneous rocks and the ductile deformation along with metamorphism occurred between 1.9 and 1.8 Ga. Forsmark lies shortly beyond the north–eastern periphery of one of Sweden's important provinces for the exploitation of mineral deposits inside this orogen (Figure 2-1b), the so-called Bergslagen province (Stephens 2009). The abundant Fe oxide and Zn-Pb-Ag ± (Cu-Au) sulphide deposits along the arc-like structure to the west of Stockholm (Figure 2-1b) are hosted by felsic volcanic rocks dated at 1.91 to 1.89 Ga.

The Svecokarelian orogen in south–eastern Sweden has been divided into six regional tectonic domains (tectonic domains 1 to 6 in Figure 2-1b). These domains have been separated on the basis of differences in either the timing of tectonic activity, i.e., the timing of ductile deformation, metamorphism and igneous activity, or in the character and intensity of the ductile strain (Hermansson et al. 2007; Hermansson et al. 2008a; Söderbäck 2008). Forsmark is situated in tectonic domain 2.

Tectonic domain 2 contains broad belts of rocks that have been affected by strong ductile deformation under amphibolite-facies metamorphic conditions. These ductile high-strain belts, which strike approximately WNW−ESE to NW−SE and are subvertical, anastomose around tectonic lenses in which the bedrock is commonly folded and, in general, affected by lower ductile strain (Figure 2-1c). They also contain retrograde deformation zones along which deformation occurred in both the ductile and brittle regimes. The overall structural character of the bedrock in tectonic domain 2, in general, and in the Forsmark area, in particular, is strongly anisotropic. The volume at Forsmark targeted as a site for the disposal of highly radioactive spent nuclear fuel is situated in one of these tectonic lenses, the so-called Forsmark tectonic lens.

A conceptual tectonic model for the Svecokarelian orogen in south–eastern Sweden has been proposed (Hermansson et al. 2008b; Söderbäck 2008). This model envisages approximately northward-directed oblique subduction beneath an active continental margin to the north–east and a progressive migration of the subduction hinge away from or towards the overriding plate, related to long periods of transtensional tectonics and short periods of transpressional tectonics, respectively.

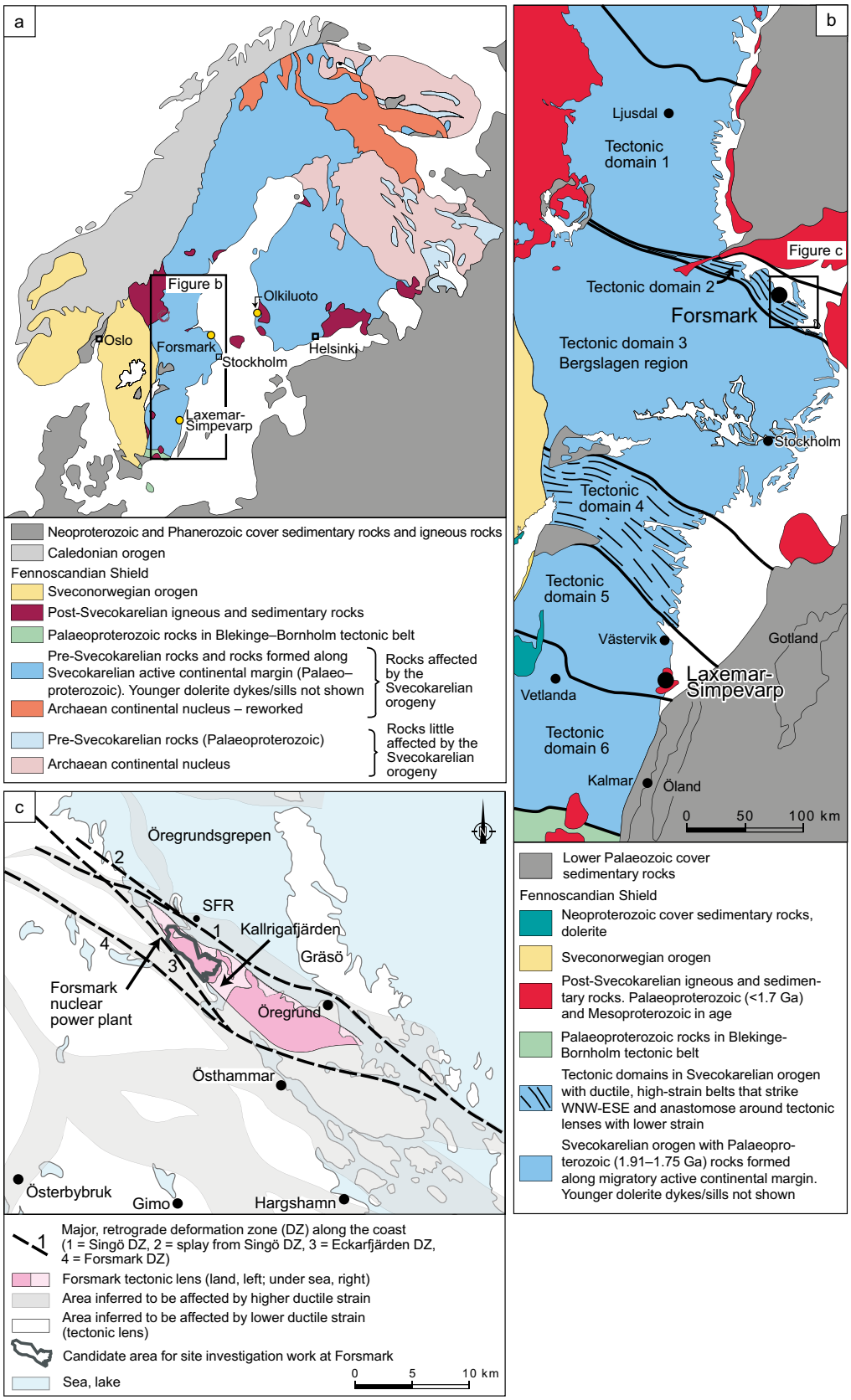

Figure 2-1. *National and regional geological setting of the Forsmark site. (a) Major tectonic units in Fennoscandia at the current level of erosion. The locations of Forsmark and Laxemar-Simpevarp as well as the proposed repository site at Olkiluoto in Finland are also shown on the map. (b) Svecokarelian tectonic domains and post-Svecokarelian rock units in the south–western part of the Fennoscandian Shield, south–eastern Sweden. (c) Inferred high-strain belts and tectonic lenses, including the Forsmark tectonic lens, in the area close to Forsmark, all situated along a coastal deformation belt in the northern part of Uppland, Sweden. Image and caption from (Stephens 2010).*

2.1.1 Lithological summary

Four major groups of rocks (Groups A to D), distinguished by their relative age, are present in the Forsmark model area (Stephens et al. 2008b; Stephens 2010). Their spatial distribution, composition and grain size are summarised in Figure 2-2.

The rocks are dominated by meta-intrusive rocks that formed between 1.89 and 1.86 Ga (Group B) and between 1.86 and 1.85 Ga (Groups C and D). The Group B meta-intrusive rocks consist of granitoids as well as subordinate ultrabasic, basic and intermediate rocks, metamorphosed under amphibolite-facies conditions. The rocks in the subordinate Groups C and D consist solely of granitoids that show a lower degree of metamorphism. The two suites have been distinguished primarily by their relationships to the penetrative ductile deformation in the area. Both suites intruded into supracrustal rocks dominated by the acid metavolcanic rocks of Group A. The bedrock volume that hosts the proposed repository is dominated by metamorphosed, biotite-bearing granite (to granodiorite) that belongs to the older Group B suite. Partly due to the lithological homogeneity of the Forsmark tectonic lens (Figure 2-2), there is limited lithological control on fracture distribution within the host rock of the repository. Outside the lens, the lithology is more heterogeneous (Figure 2-2).

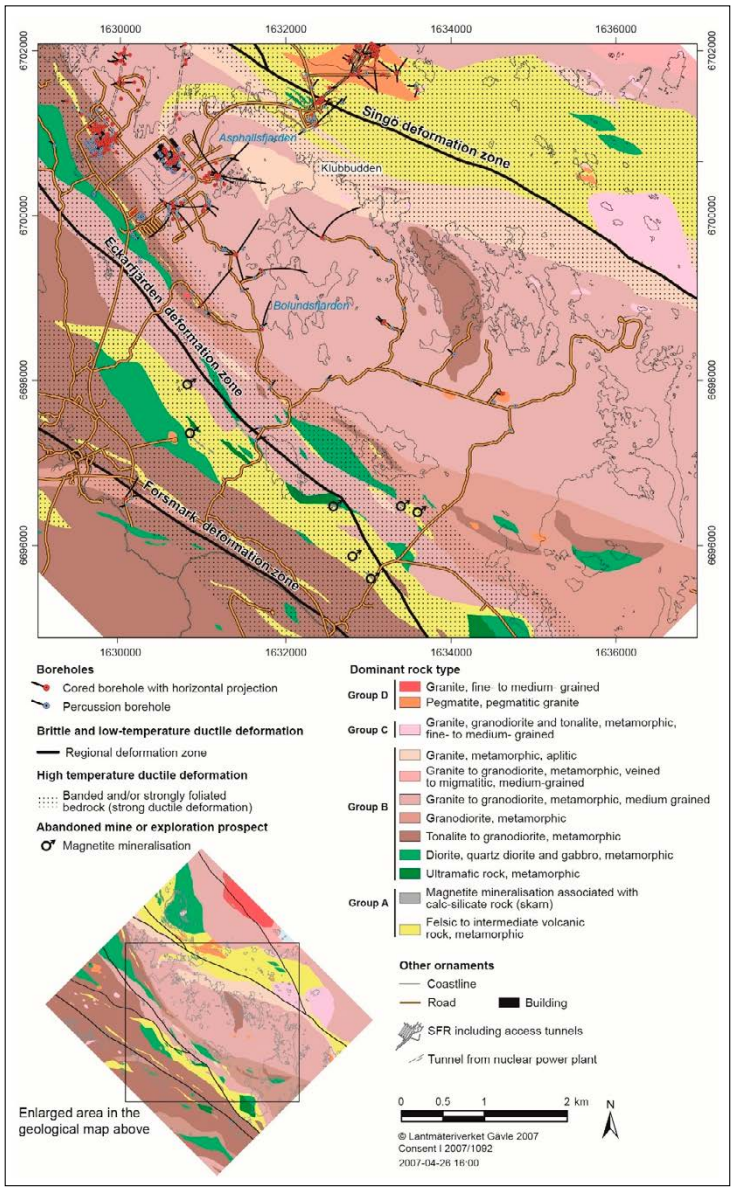

Figure 2-2. *Bedrock geological map of the investigation area at Forsmark modified from Sidborn et al. (2010) by including all cored- and percussion holes up to and including HFM46 registered in Sicada in February, 2018.*

2.2 Deformation history

Various radiometric dating methods have been used to constrain the cooling ages of the Forsmark rocks (Page et al. 2004; Hermansson et al. 2007; Page et al. 2007; Hermansson et al. 2008a; Hermansson et al. 2008b; Söderlund 2008; Söderlund et al. 2009). In combination with the fracture minerology, this dating has permitted the deformation to be divided into six episodes, the first being purely ductile.

The rocks in the Forsmark area display evidence of a protracted ductile deformational history, with the development of a penetrative fabric under amphibolite-facies conditions followed by folding on different scales between 1.87 and 1.86 Ga (Figure 2-3) (Stephens 2010). The rocks inside the Forsmark tectonic lens display a predominantly linear grain-shape fabric and folds that plunge moderately to the south–east. In contrast, the rocks in the ductile high-strain belts that surround the Forsmark tectonic lens (Figure 2-2) show a generally more intense planar and linear grain-shape fabric.

Uplift to the 500 °C geotherm occurred between 1.85 and 1.8 Ga, which is inferred to have contributed to the focusing of strain along more spatially constrained zones. Regionally significant structures with a trace length greater than 10 km at the current ground surface, including the Forsmark (WNW), Eckarfjärden (NW) and Singö (WNW) deformation zones, formed during this time (Figure 2-2 and Figure 2-4A).

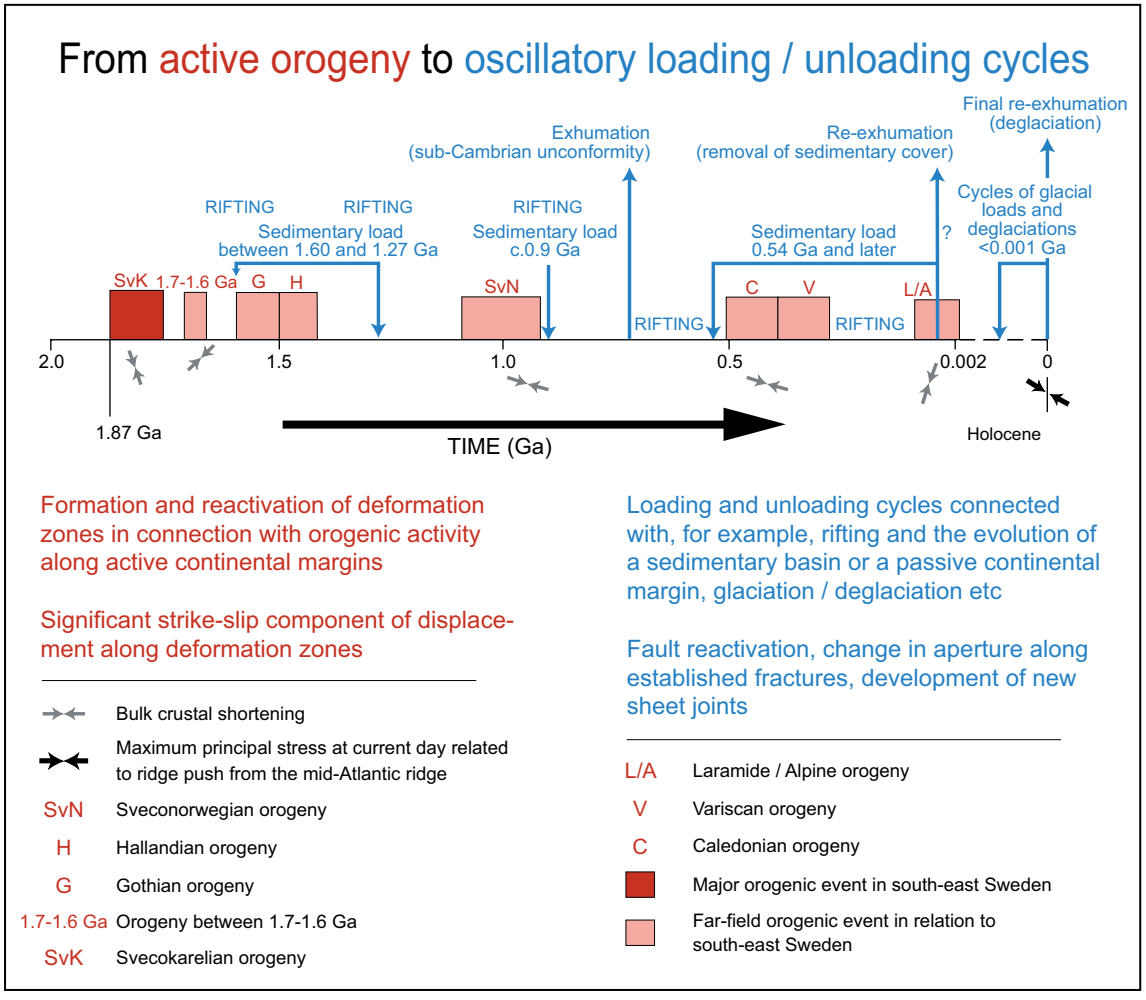

Figure 2-3. *Tectonic activity (red) and oscillatory loading and unloading cycles (blue) from 1.9 Ga to the Holocene in the Fennoscandian Shield in the south–eastern part of Sweden (Stephens 2010).*

Cooling to the 300 °C geotherm occurred between 1.8 and 1.7 Ga, possibly initiating brittle deformation during the latest part of the Svecokarelian orogeny (Söderlund et al. 2009; Stephens 2010). Two more significant local structure sets inside the Forsmark tectonic lens formed during this time (Figure 2-4B). They strike ENE−WSW or NNE−SSE and are steeply or gently dipping fracture zones. Between 1.7 and 1.6 Ga the structures continued to develop (Figure 2-4C), possibly in response to the Gothian orogeny (Stephens et al. 2007). Cooling beneath the c. 225−200 °C geotherm occurred between 1.6 and 1.5 Ga (Stephens 2010).

Brittle deformation continued as a far-field response to Sveconorwegian tectonic activity between 1 100 and 900 Ma (Figure 2-4D). There is evidence for several relatively minor brittle deformation events after the establishment of the sub-Cambrian peneplain, probably during the Phanerozoic (Stephens et al., 2007). Some reactivation of fractures is occurring under the current stress regime (Figure 2-4E) (Stephens et al. 2007).

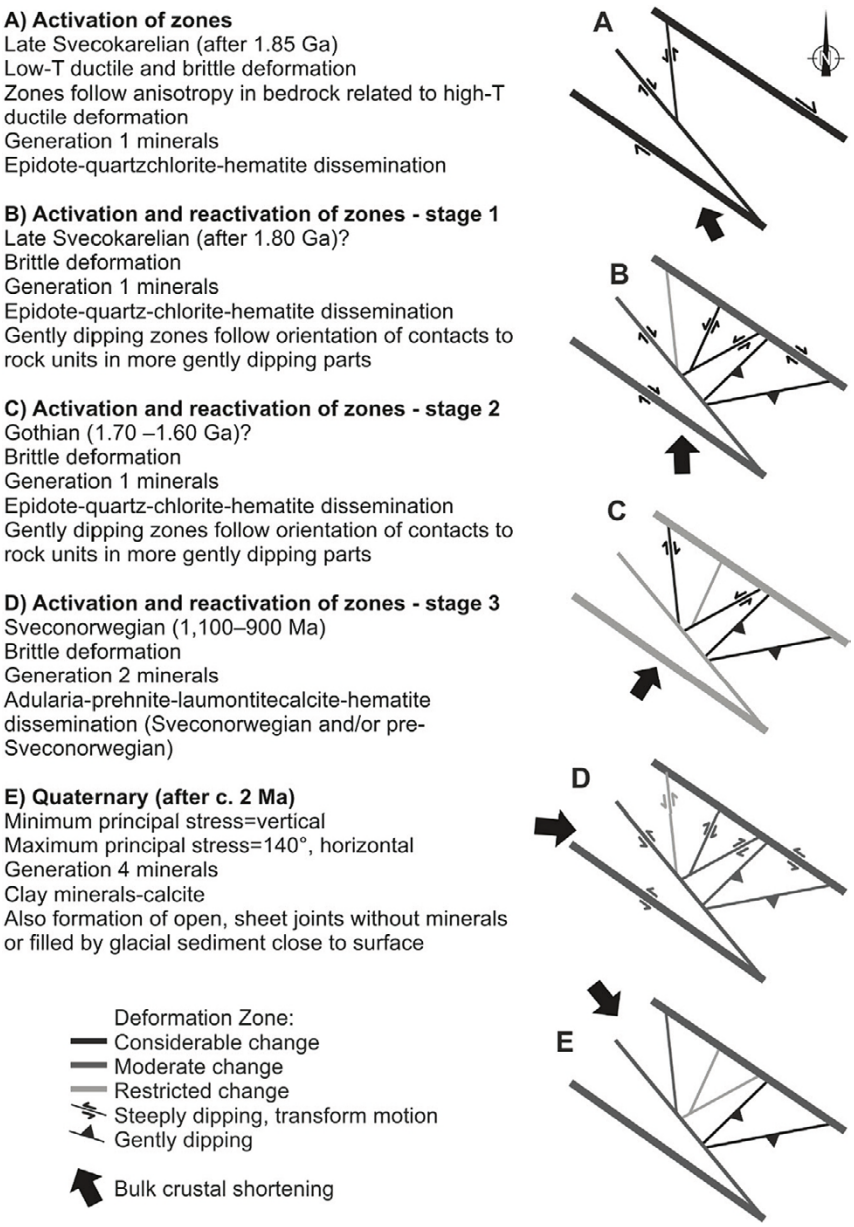

Figure 2-4. *A series of cartoons showing the conceptual model for the brittle deformation episodes (A–E) of activation and reactivation of regional scale deformation zones around Forsmark in response to far-field tectonic activity, and associated fracture fill minerology. The WNW and NW striking deformation zones correspond to the Forsmark, Singö, and Eckarfjärden deformation zones (as shown in Figure 2-2). Adapted from (Stephens et al. 2007).*

A summary of palaeostress field reconstruction using site-by-site and merged data sets from outcrops and oriented drill cores is provided by Saintot et al. (2011) as follows:

Transpressive deformation with a regional NNW–SSE maximum stress axis, associated with clockwise stress deviation inside a tectonic lens, resulted in dextral slip along regionally significant, steep WNW–ESE and NW–SE deformation zones. The semibrittle and most of the brittle structures, including specifically the epidote-bearing fractures, were established during this oldest regime around 1.8 Ga (latest Svecokarelian). A younger palaeostress field with a NE–SW maximum stress axis, which was also transpressive in character, is inferred to have been active at 1.7–1.6 Ga. The best defined palaeostress field is transpressive in character with a WNW–ESE maximum stress axis that resulted in sinistral reactivation along the WNW–ESE and NW–SE zones. The main set of laumontite-stepped faults developed at this stage at 1.1–0.9 Ga (Sveconorwegian). It is impossible to exclude fully the influence of reactivation during even younger Phanerozoic tectonic events. A similar deformation history has been interpreted at Olkiluoto (Mattila and Viola 2014) across the Gulf of Bothnia.

This conceptualisation of the deformation history at the site provides context for interpretation of fracture orientations, size distribution and terminations, and can potentially be used in genetic fracture generation methods (Davy et al. 2013; Libby et al. 2019).

2.2.1 Mineralisation chronology

The walls of natural fractures are rarely clean unaltered surfaces defining open apertures, more often mineralisation occurs on the surfaces due to fluid-rock interactions. On the long timescales of shield rocks, filling materials within fractures may undergo several phases of mineralisation, deformation and re-equilibration, or paragenesis. Identification of fracture minerals and textural characterisation both visually (mm scale) and instrumentally (mm scale e.g. microscopy, X-ray diffraction) can be used to infer the order of formation of associated minerals in geological history and the hydrothermal conditions under which they have formed or re-equilibrated.

Fracture mineralogy, i.e., description of fracture filling materials and coatings are available from core description as input to interpretations of deformation history (Section 2.2), descriptions of fracture openings (Section 7.1), fracture mechanical stiffness and hydromechanics (Chapter 6). The preservation and mapping of fracture fillings recorded in the Boremap data is noted to very good (Sandström et al. 2008b) with a few exceptions:

a) Prehnite is easily mistaken for epidote and can therefore be both underestimated and overestimated in the Boremap data.

b) Hematite-stained adularia was mapped as hematite in the earliest boreholes. Hematite is therefore overestimated in the Boremap data.

c) Different clay minerals are not distinguished during the drill core mapping. It is also probable that clay minerals are partly lost during drilling operations and therefore the frequency of clay minerals in the core mapping can be regarded as an absolute minimum.

Four generations of fracture minerals have been identified, as described below after (Sandström et al. 2008b; Stephens 2010), as detailed in Table 2-1.

The first generation of fracture minerals (generation 1) consists of epidote, quartz and chlorite. The key mineral epidote occurs along cataclastic faults that formed during ductile to brittle conditions (Figure 2-4) and along fractures with solely brittle deformation, all of which are either steeply dipping with an approximately NW−SE strike or are gently dipping. Epidote is also present along fractures in the other steeply dipping sets that strike approximately NE−SW (with ENE−WSW and NNE−SSW sub-sets) and NNW−SSE. Radiometric dating in the Forsmark region infers precipitation of generation 1 minerals between 1.8 and 1.1 Ga, in particular during the late Svecokarelian orogenic stage at 1.8−1.7 Ga. South of Forsmark, alternative radiometric data has yielded ages in the time interval 1.6 to 1.5 Ga (Wickman et al. 1983).

Table 2-1. Summary of the paragenesis of mineralogy at Forsmark, summarised from (Sandström et al. 2008b).

Generation	Dominant Minerals	Formation Temp. (°C)	Comments
1	Epidote, chlorite, quartz	> 200	Dominated by fractures sealed with hydrothermally precipitated epidote, quartz and Fe-rich chlorite. This generation formed between 1.8 and 1.1 Ga and is possibly related to late Svecokarelian and/or Gothian tectonothermal events.
2	Adularia, prehnite, laumontite, chlorite, calcite, hematite	~150–280	Consists of a sequence of hydrothermal fracture minerals particularly common along steep, ENE–WSW to NNE–SSW and NNW–SSE fractures. Consists of both reactivation of older fractures and formation of new fractures
3	Quartz, calcite, pyrite, corrensite, adularia, analcime, asphaltite	~50–190	Consists of minerals precipitated under low-T conditions during the Palaeozoic. Stable isotopes in calcite and the presence of asphaltite indicate that the formation fluid was influenced by organic material. The orientation of fractures with generation 3 minerals suggests reactivation of fractures filled with older minerals but new fractures were also formed.
4	Clay minerals, chlorite, calcite, ± pyrite, ± FeOOH	< 50	Dominated by chlorite/clay minerals and thin precipitates of calcite in predominantly hydraulically conductive fractures. These minerals are prominent along sub-horizontal and gently dipping fractures but are also present in different sets of steeply dipping fractures. Most of the hydraulically conductive fractures are ancient structures.

The second generation of fracture minerals (generation 2) is a sequence of hydrothermal minerals that consists of an early phase of hematite-stained adularia, albite and calcite, followed by prehnite and calcite, and a late phase of hematite-stained laumontite, calcite and chlorite/corrensite. The generation 2 minerals are associated solely with brittle deformation in the bedrock, commonly along sealed fractures. Radiometric dating indicates that the generation 2 minerals formed either prior to or during the early part of the Sveconorwegian orogeny (Sandström et al. 2008a; Söderbäck 2008; Sandström et al. 2009).

The third generation of fracture minerals (generation 3) is dominated by euhedral quartz, calcite and pyrite with several secondary minerals. The generation 3 minerals are associated solely with brittle deformation in the bedrock and occur along both currently sealed and open fractures, as recorded on the core scale. Generation 3 pyrite and asphaltite are conspicuous along NE−SW steep fractures, along gently dipping or sub-horizontal fractures, particularly at an elevation above approximately −150 m elevation, and along fractures in the other steeply dipping sets (Sandström et al. 2008a). A Palaeozoic age (0.5−0.3 Ga) has been supported by radiometric dating, possibly corresponding to a far-field response to the Caledonian orogeny or due to burial/denudation in response to the development of a Caledonian foreland basin.

The fourth and youngest generation of fracture minerals consists of clay minerals and calcite with subordinate pyrite and goethite. The most common clay minerals are corrensite, illite and saponite. The calcite occurs as thin coatings in open fractures (often together with clay minerals). The generation 4 minerals coat open fractures, either as the outermost mineral layer or as a single layer and occur along brittle structures that are hydraulically conductive at the current time. The generation 4 minerals also formed during the Phanerozoic. However distinguishing generation 4 clay minerals from clay minerals formed during earlier generations has proven challenging (Sandström et al. 2008a; Sandström et al. 2009).

Hematite dissemination (oxidation) and albitisation are by far the most abundant types of rock-wall alteration at the Forsmark site. Volumetrically subordinate, but nevertheless conspicuous alteration that involves quartz dissolution and the development of episyenite is also present. Hematite alteration, evident as red staining can be extensive in areas of increased fracture intensity.

2.3 Geological models

As part of the geological site description, the bedrock has been categorised according to properties of the intact rock and structures. The intact rock being divided according to rock domains (RD), while structures have been used to define volumes associated with deformation zones (DZ). As of SDM-site fracture domains (FD) were defined mainly on the basis of fracture orientations and intensities, but also considering stress magnitudes, rock geochemistry and hydrogeochemistry as additional supports. These divisions of the rock have been applied in boreholes and at the surface, and then represented by deterministic 3D models as input to the SDM-Site stage of DFN modelling.

2.3.1 Deformation zone model

Surface mapping and borehole data in the Forsmark region have been used to identify deformation zones. These are tabular structures in which there is a concentration of brittle, ductile or combined ductile and brittle deformation. A 3D model of these deformation zones has been constructed (Figure 2-5) with the aid of geophysical methods to extrapolate the deformation zones between other data points and beyond when possible. The latest model is named DMS 2020 (Hermanson and Petersson 2022), DMS standing for deterministically modelled structures). The previous model was version 2.3 (Stephens and Simeonov 2015). The deterministically modelled structures within the model include the kilometre scale composite ductile and brittle, WNW−ESE or NW−SE deformation zones (Singö and Eckarfjärden) that surround the Forsmark tectonic lens (outlined in Figure 2-4), and three other sets of zones interpreted inside the lens resulting from the focused deep drilling in that area.

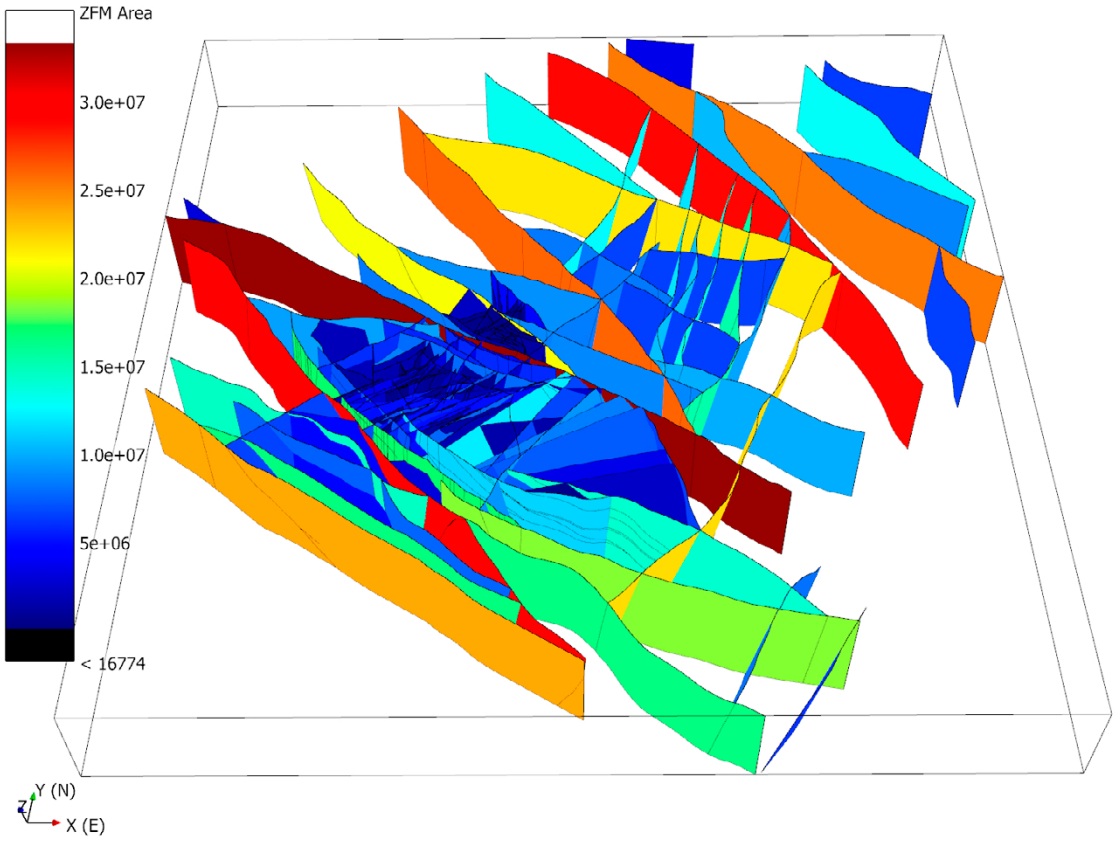

Figure 2-5. *View of the 3D model that shows the deterministically modelled deformation zones in DMS 2020. Here, the ZFM are coloured by area, with brown-red-orange being the largest. Note that the concentration of vertical and steeply dipping relatively small (blue) zones in the facility scale region is primarily an artefact of the focused investigation in that area (see discussion in Section 5.2).*

The two most common sets of facility-scale deformation zones inside the Forsmark tectonic lens strike ENE−WSW to NNE−SSE and are steeply or gently dipping, respectively (Hermanson and Petersson 2022). Subvertical, NNW−SSE oriented zones represent the third, less frequently occurring, set in the Forsmark tectonic lens.

2.3.2 Lithological model

For 3D modelling purposes, the Forsmark regional scale bedrock has been divided into different rock domains, differentiated by a combination of the rock composition, grain size, degree of bedrock homogeneity, and degree and style of ductile deformation (Stephens et al. 2007; Stephens 2010), see Figure 2-6.

The SFR is situated within a broad deformation belt northeast of the Forsmark lens, being an older heterogeneous package of mainly felsic-to-intermediate metavolcanic rocks intercalated with biotite-bearing metagranodiorite (to granite). A substantial volume of the rock mass immediate to the facility is made up of a younger igneous suite of pegmatitic granite and pegmatite that display a conspicuous ductile stretching lineation.

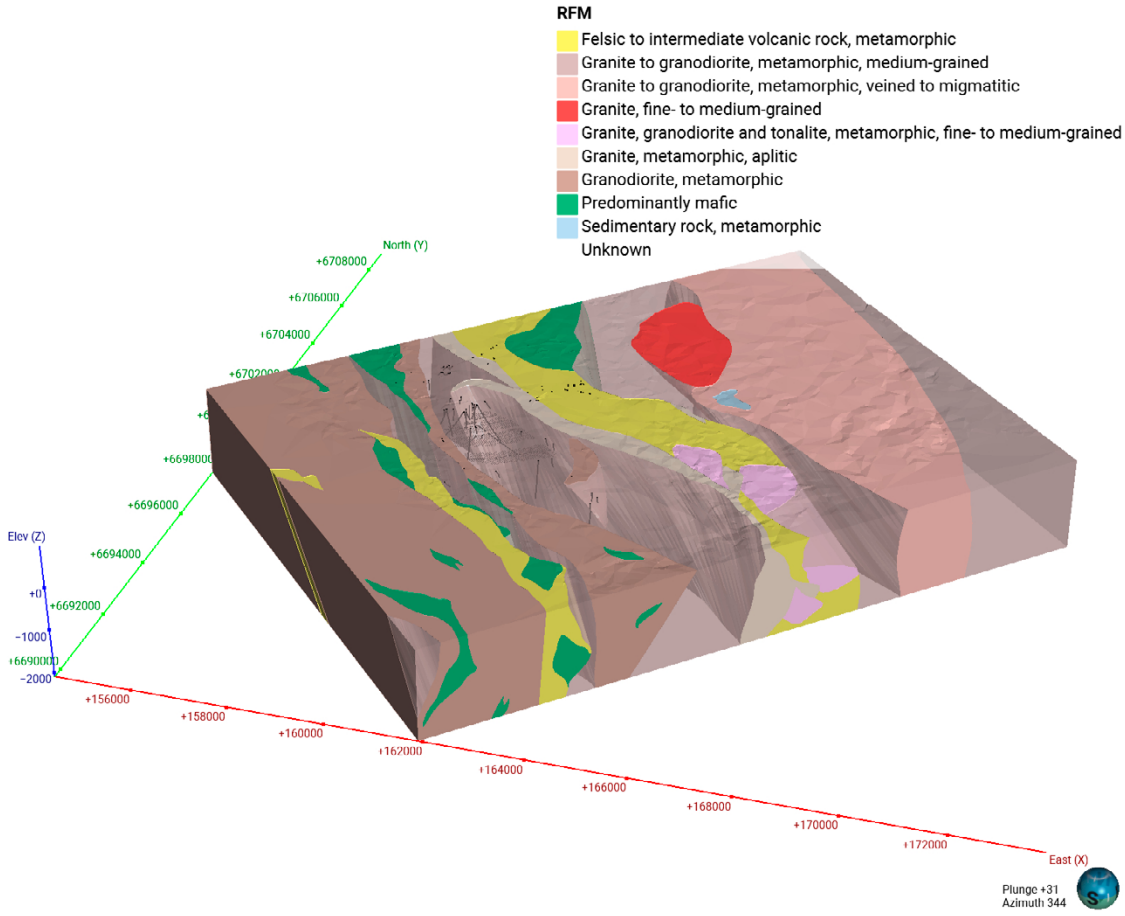

Figure 2-6. *Regional-scale 3D model of Baseline Forsmark rock domains (Hermanson and Petersson 2022). The boreholes are shown in black. Granite to granodiorite, metamorphic, medium-grained is shown semi-transparent so the boreholes (black lines) inside the Forsmark lens can be seen. The concentrations of boreholes indicate the most characterised volumes.*

2.3.3 Fracture domain model

A vital aspect of DFN modelling is the decomposition of the model volume into Fracture Domains, FD, see (Hermanson and Petersson 2022) for details. Fracture domains provide a framework for describing overall spatial heterogeneity in rock fracturing. The goal behind identifying fracture domains is to find rock volumes with fracture characteristics such that the statistical variability between volumes is larger than the intrinsic fracture variability within volumes (Munier et al. 2003; Darcel et al. 2012; Darcel et al. 2013), in line with geologic best practice. That is, if one considers the variability in fracture intensity, at what scales does averaging that variability result in patterns that can be correlated to changes in geology on the same scale. An example if given later in Figure 4-2 where on vertical scales of ~50 m variability in fracture intensity relates to the presence or absence of individual brittle structures (small-large DZ) and on scales of ~500 m relates to different dominant lithologies or major brittle/ductile structures. As such, fracture domains should form the basic divisions over which spatial heterogeneity in rock fracturing is characterised but may not, necessarily, correspond to the limits of other geologically significant volumes such as those defined in the Rock Domain (RD) model although this is generally the case. The resulting output of such domain analysis is a number of rock volumes where the fracture system within each is characterised by a distinct set of statistical laws (see Chapters 4 and 5 for details).

Based on mainly borehole data, six fracture domains (FFM) have been identified inside and immediately outside the proposed repository volume at Forsmark (Olofsson et al. 2007) using a combination of qualitative and quantitative assessment. Most of the site data are focused in FFM01, FFM02, FFM03 and FFM06. Differences in fracture intensity and orientation were important factors in defining the spatial extent of FFM01, FFM02 and FFM03, while FFM06 was differentiated from FFM01 mainly by lithology. These definitions were further supported by distinct hydrogeological and hydrogeochemical characteristics in the different domains. FFM04 and FFM05 had limited data from drilling, being discerned by geophysics to be outside the Forsmark tectonic lens, and with some indications of having different hydrogeological properties. A 3D model of four of these domains (FFM01, FFM02, FFM03 and FFM06) was constructed where sufficient data permitted (Figure 2-7).

In the uppermost c. 100–150 m of bedrock in the region there is a set of sub-horizontal sheet joints that can, locally, be highly transmissive (Stephens et al. 2007; Follin 2008; Hermanson and Petersson 2022). The favoured explanation for the origin of these structures is the release of rock stresses during glacial unloading in the Quaternary (Stephens, 2010). Martel (2011) points out that compression parallel to a convex surface can cause shallow subsurface fractures to open, and therefore sheet joints may form in areas of topographic curvature. This was also confirmed by Moon et al. (2017) in an application to Forsmark. Some of the shallow fractures including these sheet joints have been filled with glacial sediments (Carlsson 1979; Leijon 2005; Lönnqvist and Hökmark 2010; Stephens 2010; Lönnqvist and Hökmark 2013; Hökmark and Lönnqvist 2014; Talbot 2014).

Mechanisms of glacial ripping, beam failure for rock mass disintegration and hydraulic jacking/fracture dilation in the near surface from a survey of terrains across east Sweden, including Forsmark, are discussed in (Krabbendam et al. 2021; Krabbendam et al. 2022a; Krabbendam et al. 2022b).

The lithological and fracture domain models shown in Figure 2-6 and Figure 2-7, respectively, illustrate an important facet of the SDM modelling methodology is that the bedrock is categorised into geological domains that can be modelled as “geobodies” bounded by closed surfaces, as shown in Figure 2-7. The geobody or associated rock domain to which any point within the bedrock belongs to can be realised as a categorical property of the rock and stored on a grid. For example, the rock domain to which each grid cell centre belongs to can be stored as a lithology property on the grid, providing a “geocellular” or “voxel” representation of the lithology model. Numerical variables can also be stored on the geocellular model, for example equivalent permeabilities by upscaling the DFN to an ECPM, or elastic properties through upscaling a DFN to a rock mass.

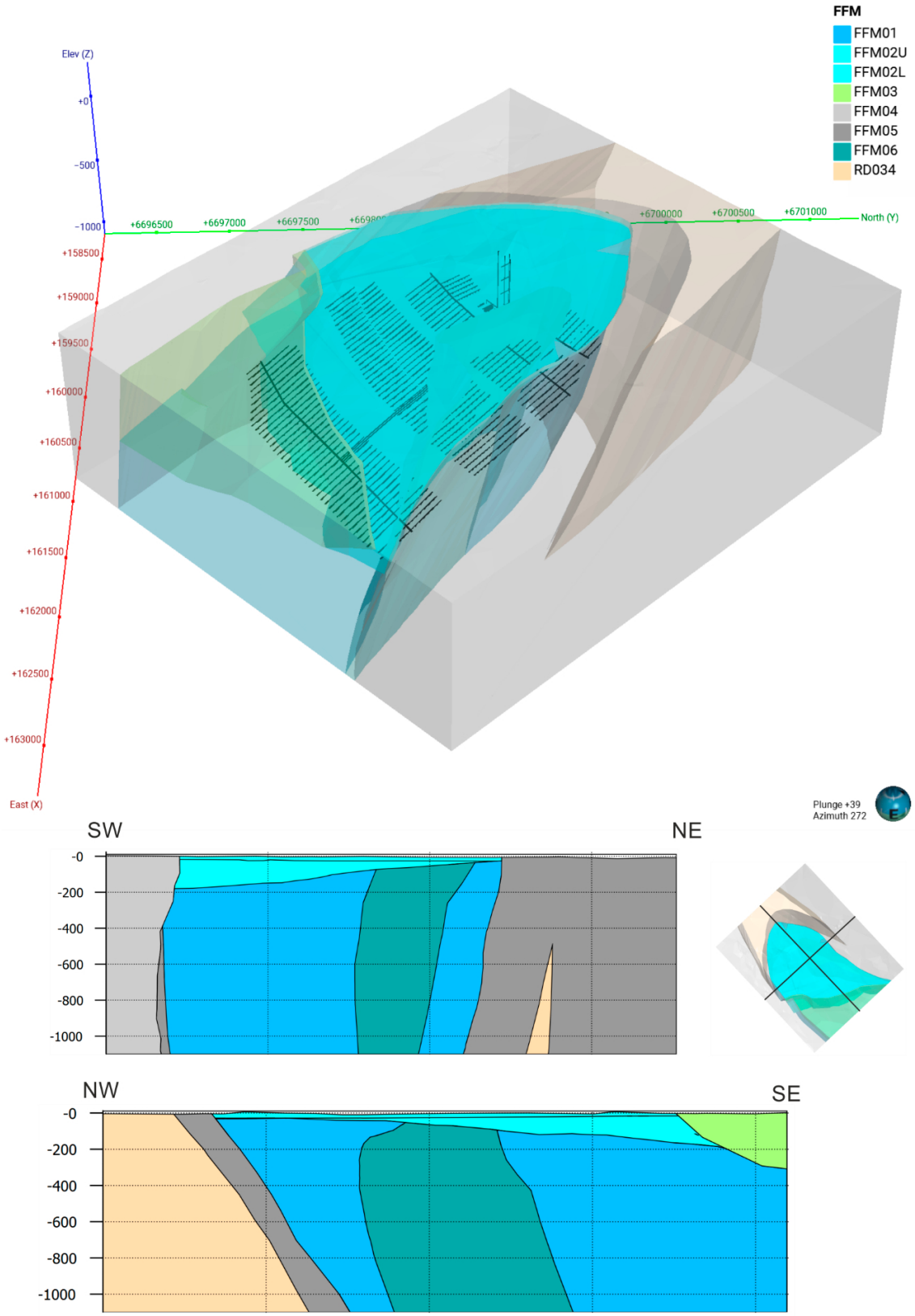

Figure 2-7. *Top) 3D view of the FFM domains with the planned spent fuel tunnel layout shown in black; Bottom) Axial and tangential sections through the Forsmark tectonic lens FFM/RFM.*

2.3.4 Geobody and geocellular modelling

Geological structures (e.g. deformation zones) and volumes (such as lithologies and fracture domains) can be modelled geobodies enclosed by surfaces usually discretised as triangulated surfaces (e.g., Figure 2-8 upper). When doing spatial or numerical analysis of such objects it is often convenient to represent them on a common continuum grid where each geological property is stored as variables for each cell. These can be a categorical, e.g., the predominant lithology in that cell (RFM), within which fracture domain (FFM) it lies, or if it lies within a deformation zone (FFM or null). This is referred to as a geocellular model (Figure 2-8 lower). The accuracy in representing a geobody is determined by the number and density of points used to represent its bounding surfaces, which may vary (unstructured) in regions where the surface has higher curvature or more data points. The accuracy of a geocellular model representation is governed by the cell size, which is usually regular, but can be unstructured if more precision is required in some regions of interest. For a geocellular model to accurately represent a geobody, the cell size needs to be commensurate with the highest curvature of the geobody, which is the case in this study where cells are either 10 or 20 m. The scale of geocellular model mainly effects the resolution of the geological inputs to the creation a fracture model, and not necessarily the range of fracture scales generated, which are defined independently.

Rock mechanics properties, such as elastic moduli or stress tensors, can be stored as geocellular properties. Likewise, upscaled ECPM flow and transport properties can be represented on a geocellular properties.

For example, in SDM-Site a regional scale domain of 15 km × 11 km × 2.1 km was used and the fracture domains as input to DFN modelling were represented on geocells of side 20 m in the facility area, Figure 2-7, increasing to 100 m outside. The DFN was upscaled to ECPM models of flow and transport properties for use in simulating hydraulic interference tests (as here in Section 7.5) and palaeohydrogeology (Follin et al. 2007a). The upscaling method preferred for hydrogeology calculates the permeability tensor for each grid cell that results in an equivalent flow-rate through the part of the fracture network within that cell, see Chapter 9.

If the intact rock is relatively homogeneous, then it may be hypothesised that fracture patterns and spatial variability arises primarily from random processes of fracture nucleation and interaction, and that variability in intact rock properties has only secondary effects (uncorrelated) on fracture distributions, and hence can be neglected. In that case, there is no need to provide spatially varying inputs to the fracture generation process.

If, however, significant correlations between fracturing and other geological properties and structures are apparent, then these drivers for spatial variability must be used as heterogeneous inputs to the fracture generation process. Here, different representations of structures are used as inputs to the fracture generation process, see Figure 1-5. Deterministically modelled deformation zones (ZFMs) are represented as geobodies, but their control on fracture intensity is represented on zone-specific local geocellular meshes to create associated fracture swarms. The cumulative effects of smaller scale (stochastic) deformation zones on fracture intensity are represented on global geocellular grid, while the spatial variability in the background fracturing is driven by the fracture domains as defined on the global geocellular grid.

The geocellular input parameters include those for mean fracture orientations, intensities, fracture propagation and stress. Even with a genetic growth algorithm for creating DFNs (Davy et al. 2013; Libby et al. 2019), an input fracture intensity is used in a (heterogeneous) Poissonian process to nucleate fractures. The minimum scale of heterogeneity associated to deformation zones attempted was 10 m around the facilities and 20 m on the regional scale, which determined the scale of cells used.

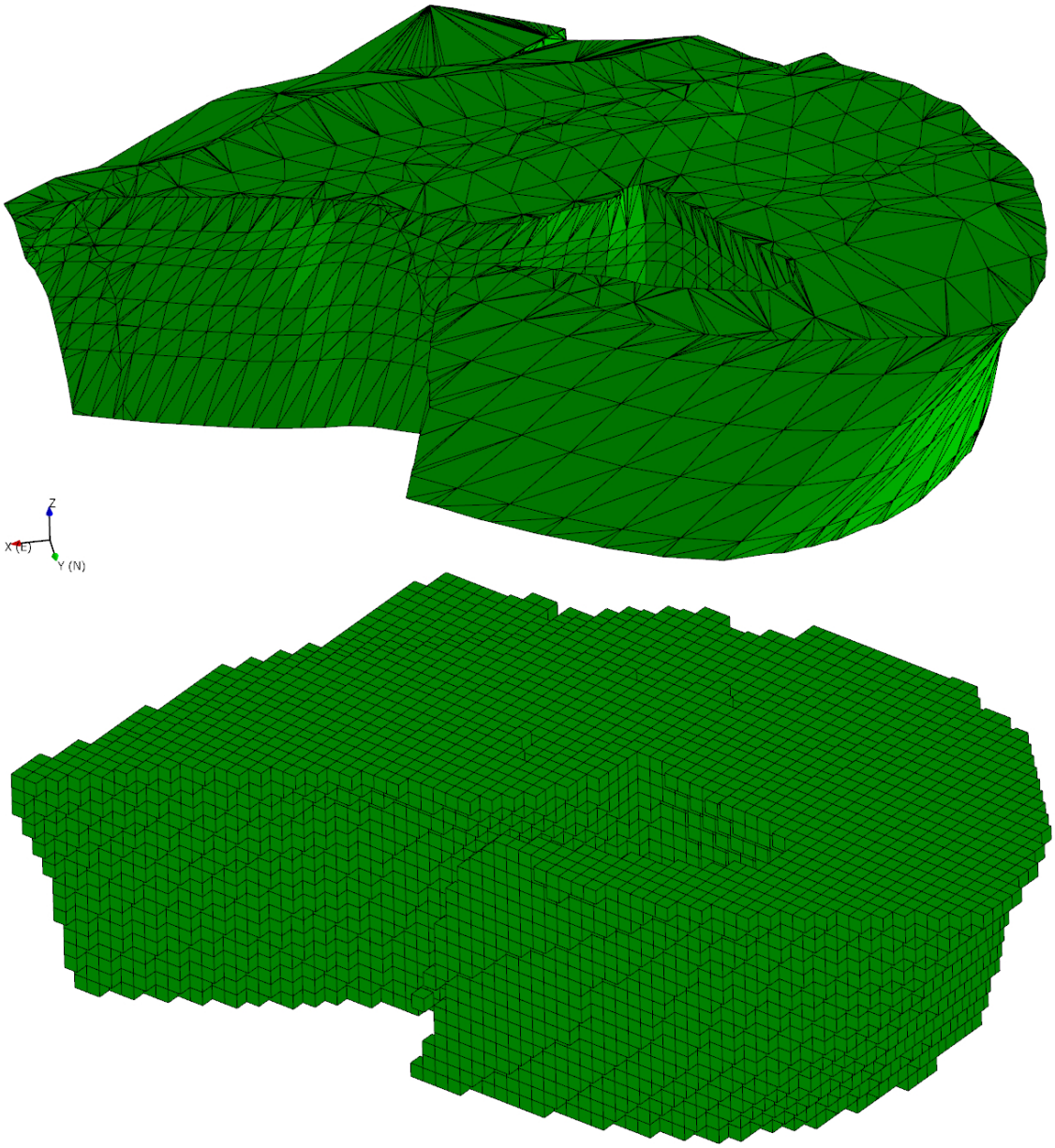

Figure 2-8. *View of the FFM01 enclosed triangulated surface (upper) as provided as in input by SKB, and the same region represented as a geocellular model (lower) at 50 m resolution. A 50 m mesh scale is used here to illustrate the maximum scale considered necessary to represent this geobody. Mesh scales of 10 m or 20 m are used in the DFN modelling to represent other narrower structures, such as small deformation zones.*

3 Input data and data management

Numerous sources of information were provided by SKB for the work described in this document. Their description is categorised by their primary application in Sections 3.1, 3.2 and 3.3 which are Geological, Rock mechanics and Hydrogeological respectively. Most of the data was stored in the database described in Section 3.4. This was integrated with a graphical interface and analysis tool accessed via the web application described in the same section.

3.1 Geological inputs

A summary of the geological related inputs and the main places where they are used in this report is provided in Table 3-1. This amounts to a comprehensive list of all fracture datasets from the site with the exception of some mapping fractures in the SFR that was not of a useful form or detail. Figure 3-1 through Figure 3-5 illustrate aspects of these data. Figure 3-1 provides a visual illustration of the abundance of geological logging data from the different types of boreholes by elevation. For the SFK area, structural logging in HFM (percussion drilled) data dominates to a depth of about 150 m, and KFM (core drilled) data below that. Even in KFM holes, there is a gradual fall off in the abundance of Boremap data below an elevation of about −500 m. This means that uncertainty in mean statistics increases gradually below this depth, as seen later in plots of average intensity in a 10 m widow, Figure 5-22.

For the SFR area, KFR (core drilled) dominates at all depths with a drop off in the abundance of data below about −200 m elevation.

Note that at the time of writing the mapping of the drone data is incomplete and consequently they have not been quality checked. However, they were provided by SKB to permit illustrative comparisons with simulations of the fracturing on these outcrops made using the DFN model based on the geological mapping in the boreholes, see Chapter 8.

Table 3-1. Summary of geological data/models used in the DFN-BF1 model.

Input data / models	Delivery data SKB ref id or provider	Usage
Boremap data, see Figure 3-1	SKB data 21 029 01	Chapter 5
Borehole trajectories, see Figure 3-2	SKB data 21 029 01	Chapters 5–7
Borehole core descriptions, geophysics	SKB data 21 027 029	Chapter 5
Extended single hole interpretations (ESHI)	SKB data 21 029 02	Sections 5.2, 5.3 and 7.4
GIS files – topography, rock surface, lineaments	SKB data 21 027	Section 5.2
Hydrological data	SKB data_21_027	Chapter 7
Deterministic sheet joints	30/08/22 M. Stigsson	Section 5.4
Deterministic DZ geometries (DMS 2020), see Figure 2-5	14/02/22 M. Stigsson	Section 5.2
Rock domain geometries	13/05/22 M. Stigsson, updated 03/11/22 J. Petersson	Section 5.4
Fracture domain geometries	16/05/22 M. Stigsson, updated 03/11/22 J. Petersson	Section 5.4
Field mapped fracture traces (AFM), see Figure 3-3 and Figure 3-4	06/07/22 M. Stigsson	Sections 5.4 and 5.3
Drone mapped fracture traces, see Figure 3-3 and Figure 3-5	13/09/22 M. Stigsson, preliminary data	Chapter 8
Images of fractures on inlet channel for the Forsmark NPP.	Used in (Follin et al. 2007b; Hartley et al. 2021) from (Carlsson 1979)	Section 5.4

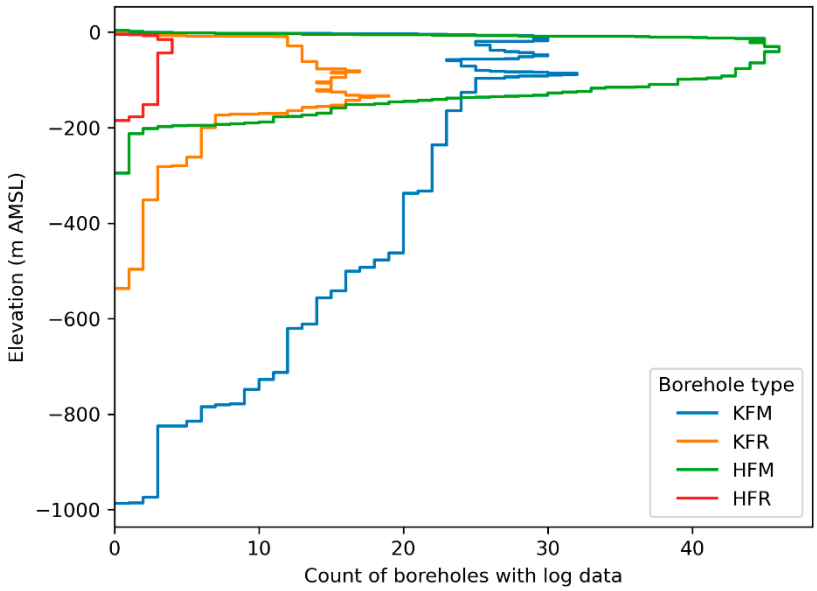

Figure 3-1. *Plot showing the number of boreholes with geological log data at different elevations in the Forsmark site. Some of the KFR holes, such as KFR105, are drilled almost horizontal from the SFR facility, which creates some of the spikes seen in the KFR coverage.*

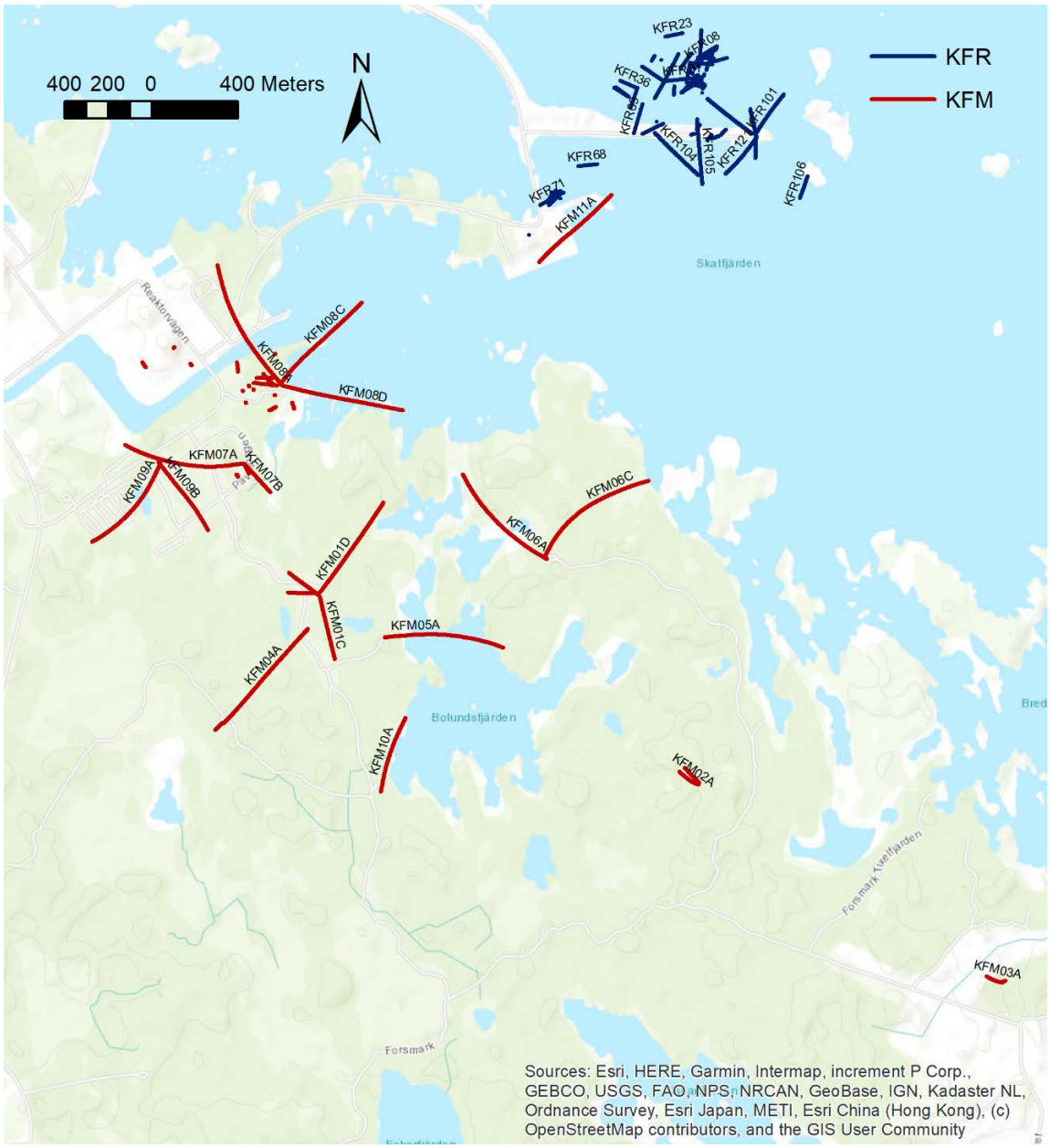

Figure 3-2. *Map showing the trajectories of the KFM and KFR boreholes. KFM12 is not shown here as it lies well outside the main characterisation area near Forsmark village and just outside the southwest corner of this map.*

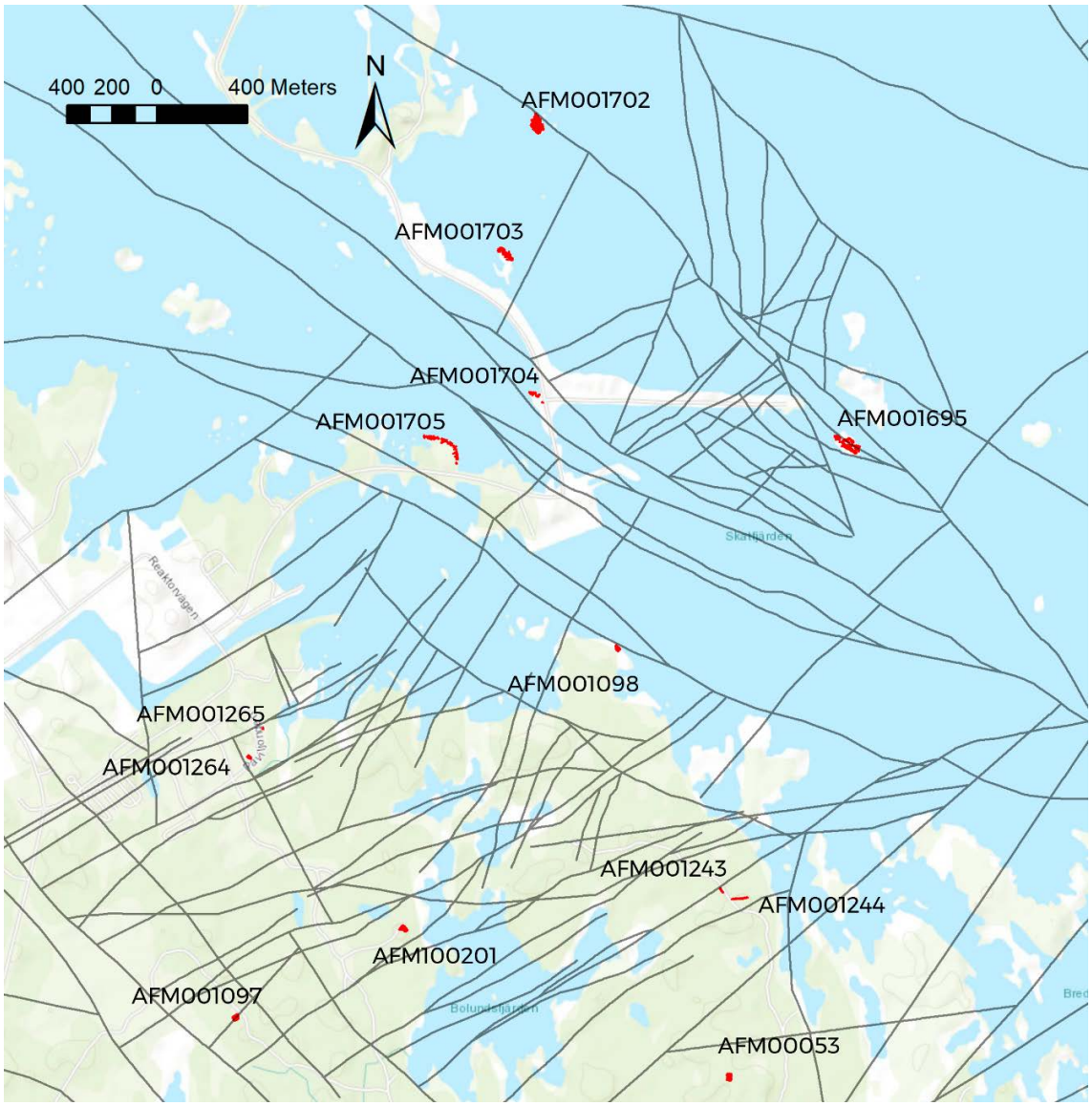

Figure 3-3. *Maps showing the locations of the tracemap data near SFK and SFR. The traces to the SW of AFM001098 (inclusive) are field mapped. The traces to the NE of AFM001098 are mapped from drone data.*

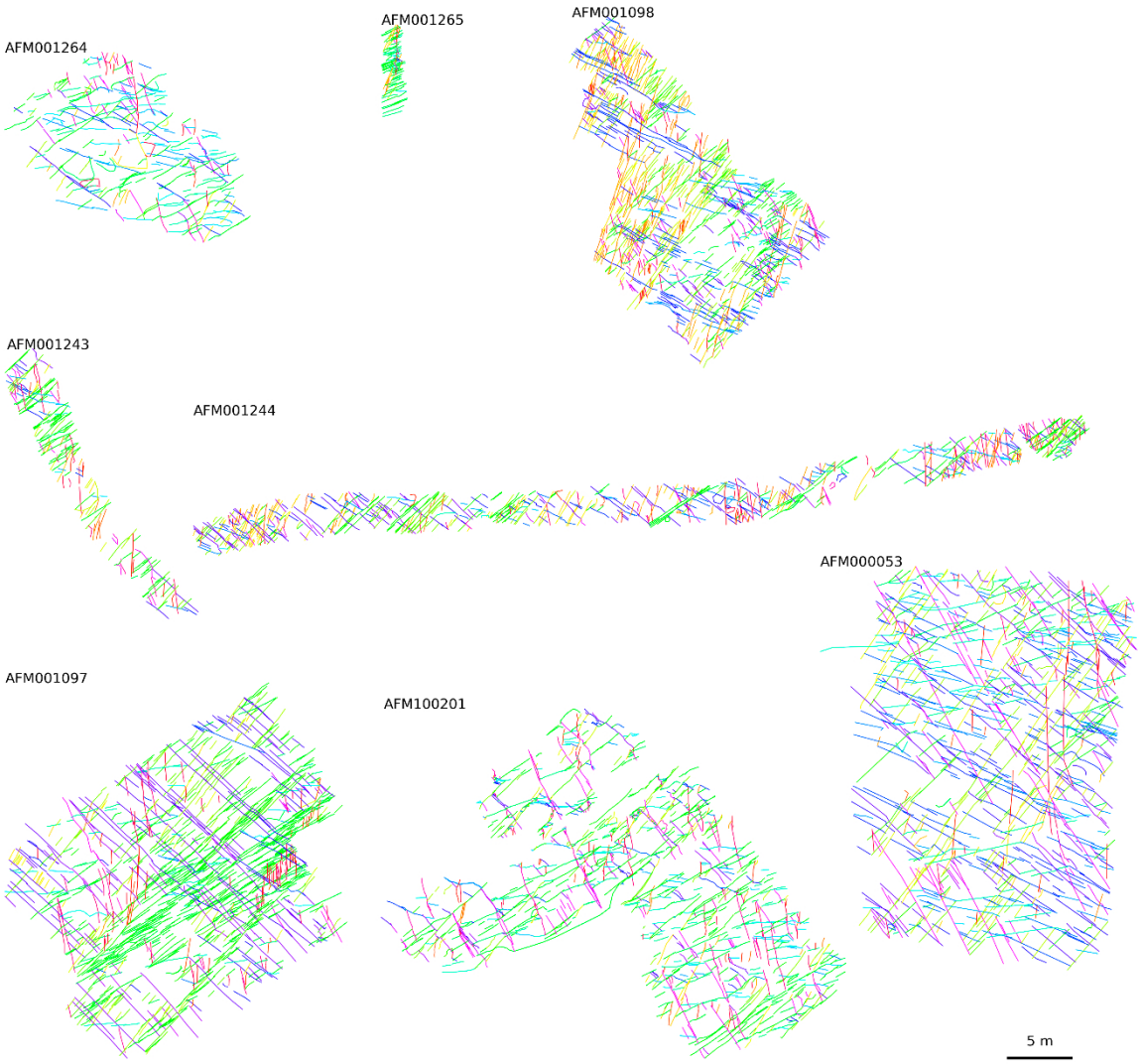

Figure 3-4. *Plan view of surface map fracture traces drawn at the same scale and coloured by orientation.*

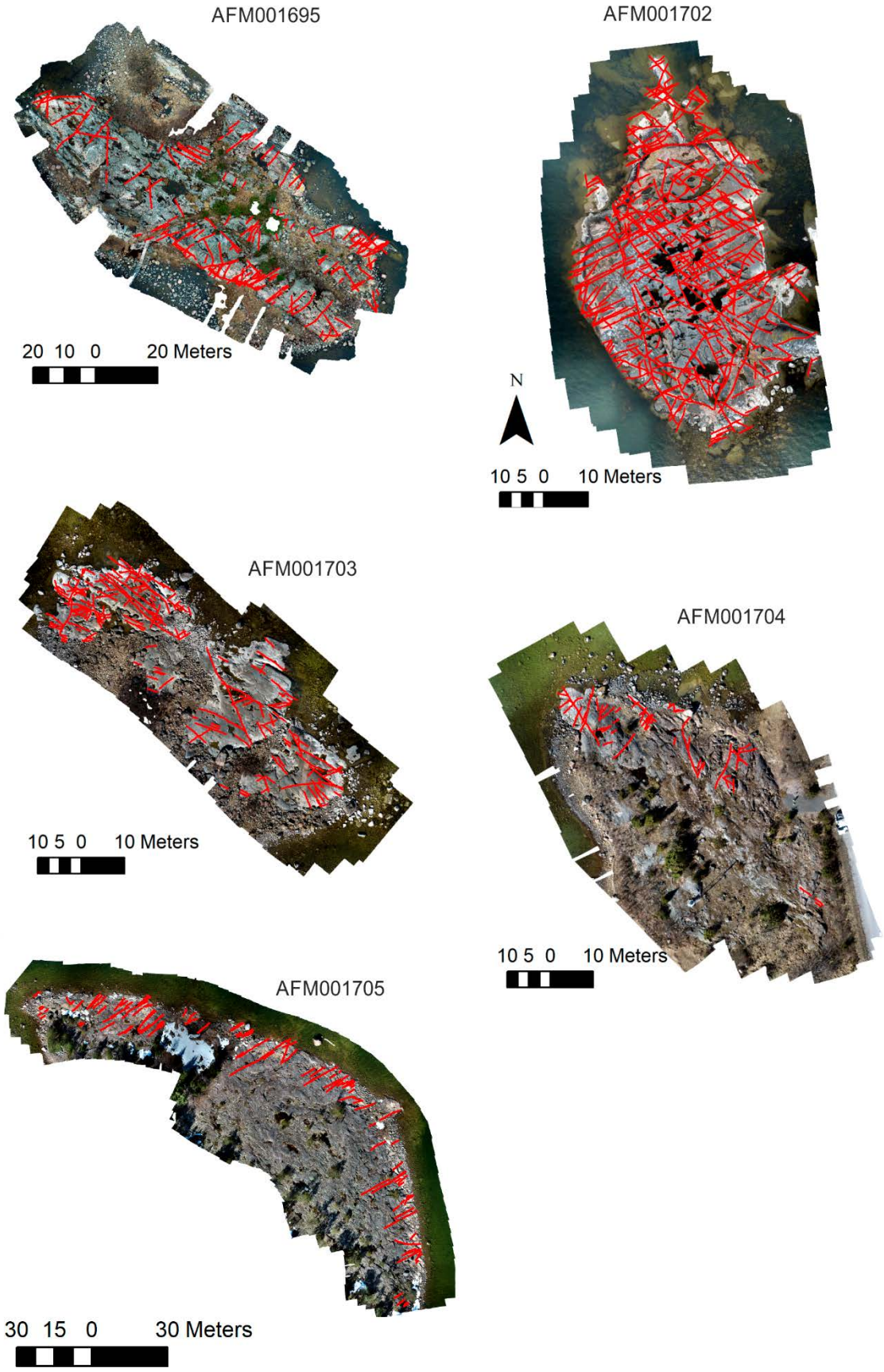

Figure 3-5. *Drone orthophotos and mapped fracture traces. Note that the mapping of these traces is incomplete, and consequently they have not been quality checked.*

3.2 Rock mechanics inputs

A summary of the rock mechanical inputs and the main places where they are used in this report is provided in Table 3-2. The numerically determined (3D) stress field used in this study is the result of modelling by (Hakala et al. 2019) updated and extended in (Valli et al. 2023) using in situ stress data from (Martin 2007) and wider data and models from (Glamheden et al. 2007; Glamheden et al. 2008). Case 2-1 was used as the reference case from that modelling and is visualised in Figure 3-6. Further details are provided in Section 6.1.

Table 3-2. Summary of rock mechanical and hydromechanical data / models used in the Forsmark DFN-BF1 model.

Input data / models	Provenance	Usage
3D stress field, see Figure 3-6. and Section 6.1	06/09/21 D. Mas Ivars with update for extension to depth 11/01/23	Sections 6.1, 7.4 and 7.5
Aperture, size, elastic moduli relationships	16/12/21 A. Sánchez Juncal from (Olson 2003)	Sections 6.2, 7.4 and 7.5
Fracture toughness, rock mass elastic properties	16/12/21 A. Sánchez Juncal from P-21-02 (Glamheden et al. 2007)	Sections 6.2, 7.4 and 7.5
Aperture, stress relationship	16/12/21 A. Sánchez Juncal from (Hökmark et al. 2010; SKB 2010)	Sections 6.2, 7.4 and 7.5

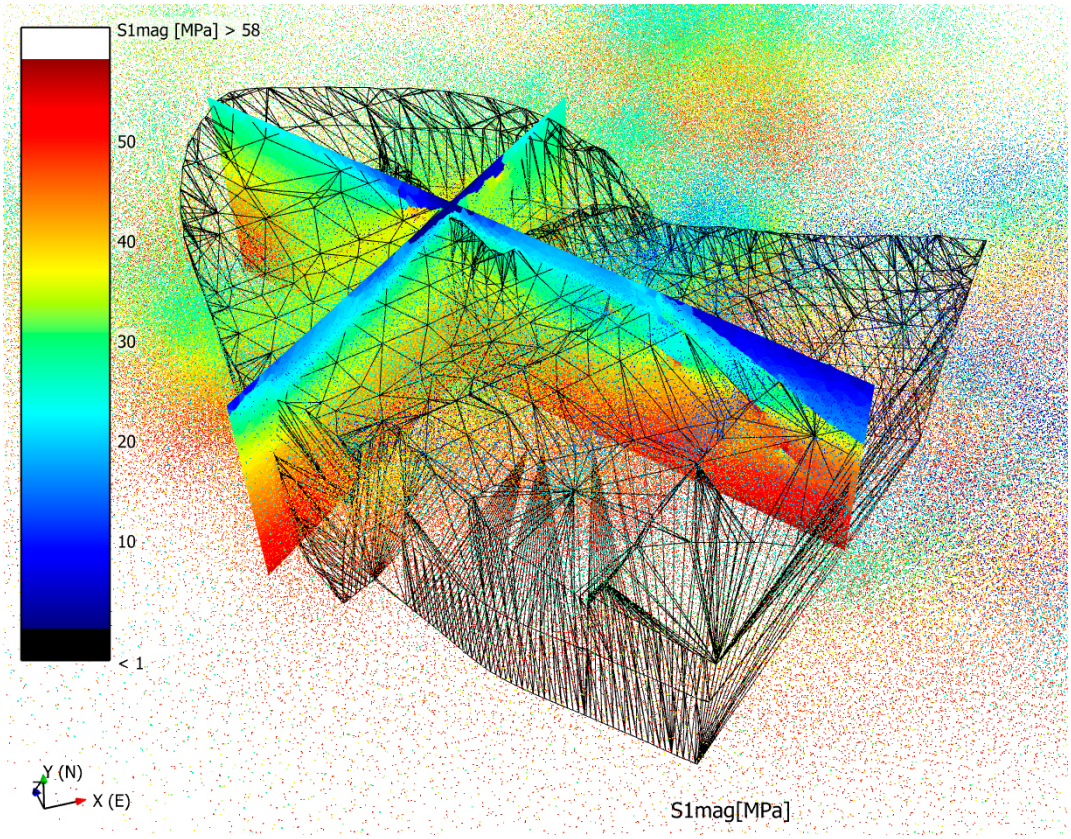

Figure 3-6. *View of the 3D stress field distribution (Valli et al. 2023). The coloured points are the stress data, for illustrative purposes cross sections coloured by the maximum stress of the closest data point are show with a black wireframe of FFM01 highlighting the lens region. This showcases the change in stress inside the lens and in the hanging wall of ZFMA2 that slopes gently towards the ESE. The modelled stresses are shown to an elevation of −1 000 m.*

3.3 Hydrogeological inputs

A summary of the hydraulic data and the main places (see Figure 3-7 and Figure 3-8) where it is used in this report is provided in Table 3-3.

Table 3-3. Summary of hydrogeological data used in the Forsmark DFN-BF1 model.

Input data	Provenance	Usage
Borehole hydraulic testing, see Figure 3-7	01/07/21 M. Stigsson	Sections 7.2, 7.4 and 7.5
PFL best choice fractures	23/09/21 M. Stigsson	Section 7.2
PFL best choice fractures for new KFM holes	09/05/22 M. Stigsson	Section 7.2
HFM14 interference tests, see Figure 3-8	01/06/22 R. Earon from (Gokall-Norman and Ludvigson 2007, 2008)	Section 7.5
KFR27 interference test	31/08/22 J. Öhman from (Harrström et al. 2019)	Section 7.5

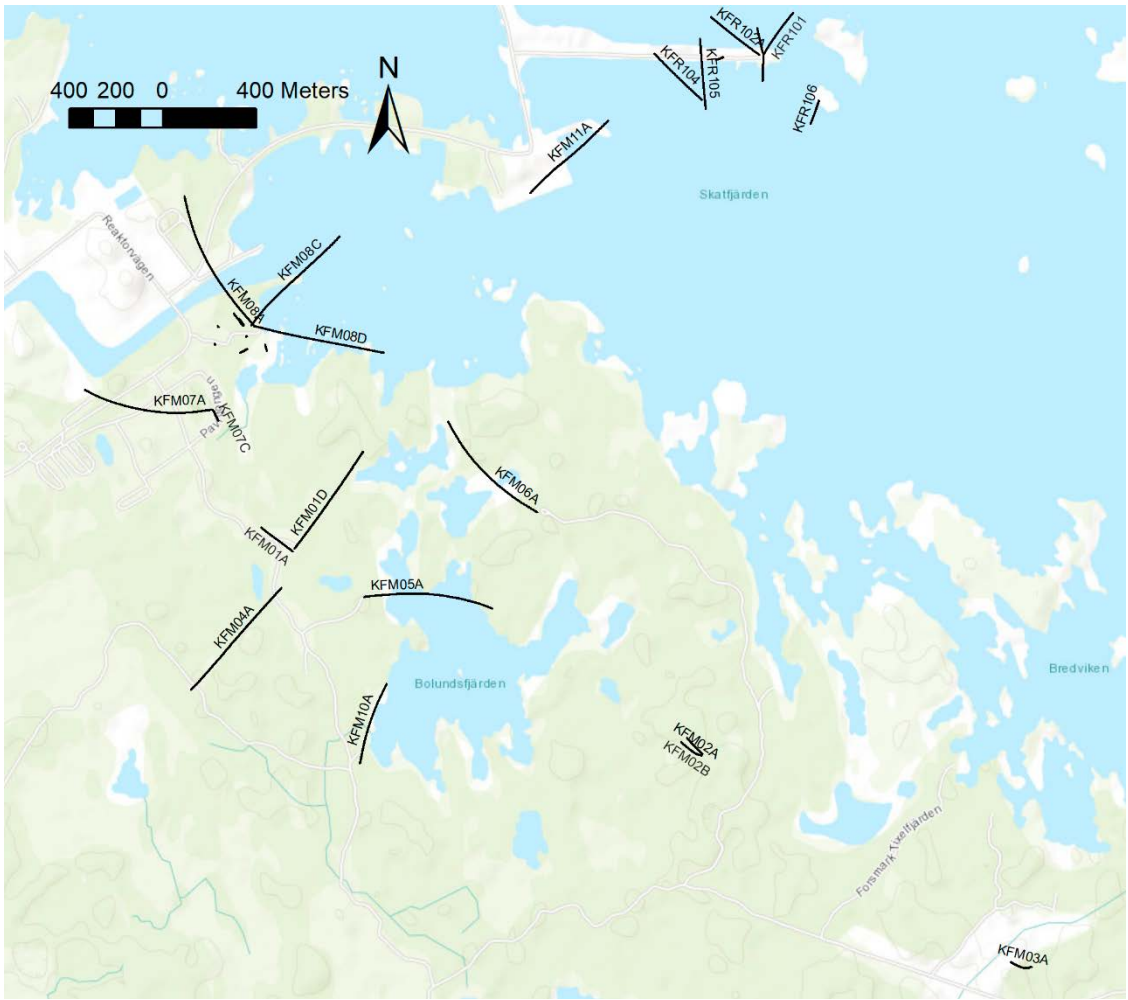

Figure 3-7. *Map showing the location of those boreholes hydraulically logged with the PFL tool. Background map courtesy of ESRI.*

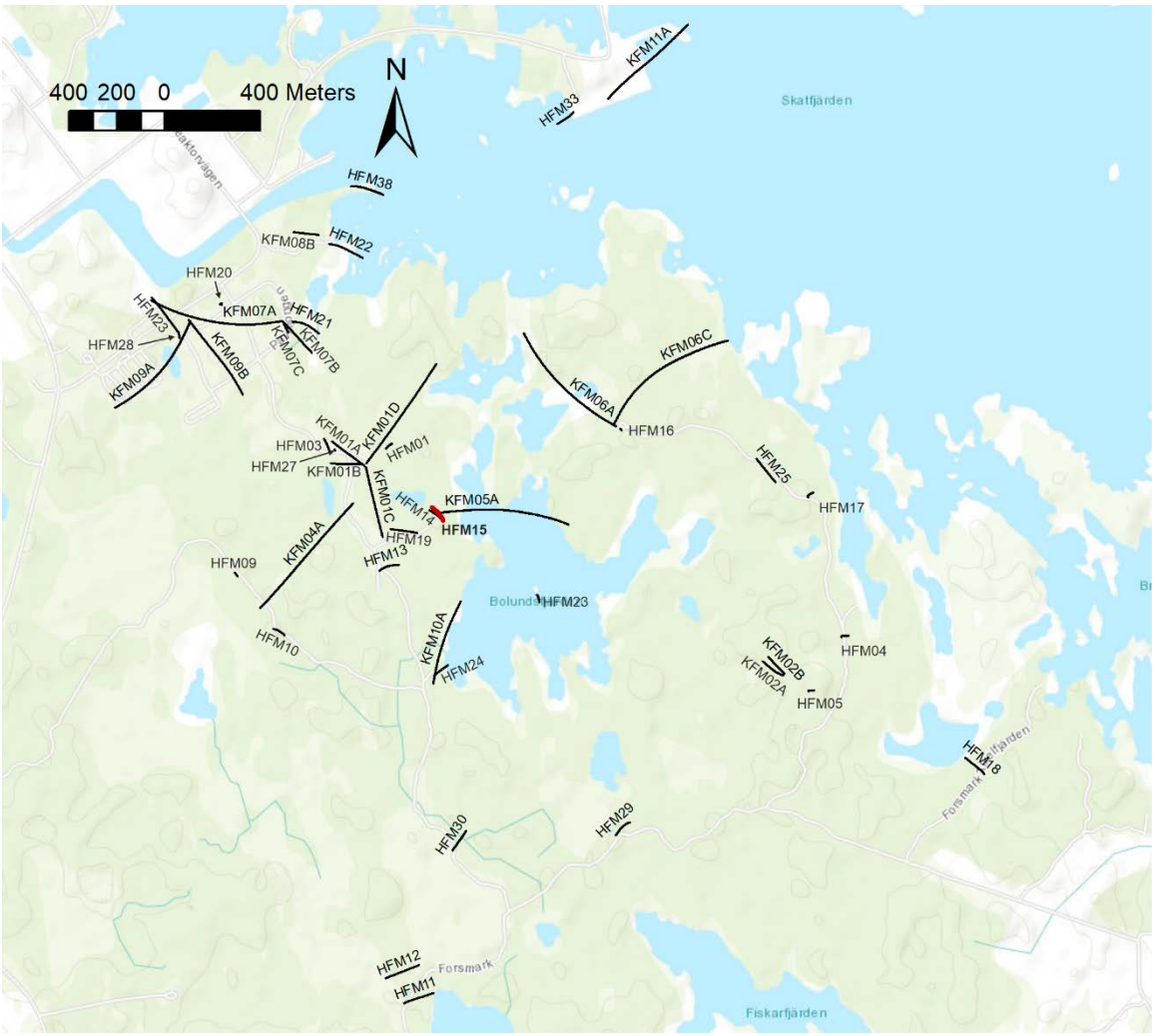

Figure 3-8. *Map showing the location of the boreholes which were monitored during the HFM14 interference tests. The red borehole trajectory is HFM14 as the pumped hole. Background map courtesy of ESRI.*

3.4 Database and data visualisation

A modeller's database was developed to support data management and analysis. It took the form of a bespoke PostgreSQL relational database securely hosted on the Azure cloud which was updated with every data delivery and acted as the single source of trusted information for all analysis and interpretation. A prototype interactive web application, AVI[3], was developed in order to visualise and analyse the data held within the modellers database and support interpretation (Figure 3-9).

The database was constructed using an automated Python build script which loaded both tabular data exports from SICADA and geometric data from geological and structural models (e.g., DZs and FFM 3D models). This allowed the database to be rebuilt in a completely automated manner whenever required.

In addition, the database also contained customised functions and views which were used to produce data analyses and exports. The PostGIS extension to PostgreSQL was employed to produce spatial queries and outputs in addition to conventional statistical queries. Standardised approaches to handling the data were implemented within the database so that they were common across all data interpretation activities. For example, all Terzaghi (Terzaghi 1965) corrections were carried out within the database using the same function and so are consistent across all data analyses. This approach results in traceable, repeatable data analysis and minimises the overhead associated with data updates.

N.B. Terzaghi correction was the main method used in AVI and in this study generally to estimate fracture intensity from fracture counts and orientations, where available, because of its simplicity. Alternative methods were tested for estimating the intensity associated to DZ-related fractures, see Appendix A2, but ultimately rejected as benefits in accuracy did not offset their complexity. A maximum Terzaghi weight of 7 (equivalent to a minimum of 8° to the axes of a borehole) was used, consistent with DFN-M2008.

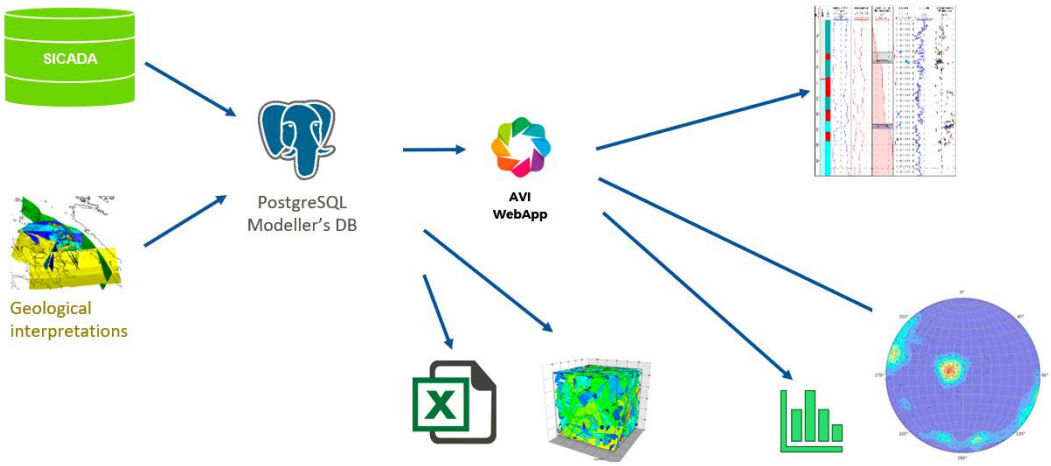

Figure 3-9. *Schematic illustration of the modellers' database. "Cold storage" of site investigation data and interpretations held in SICADA is indicated on the left, that is exported alongside 3D models to the 'hot storage" of the Modeller's database, which can then be accessed interactively through the AVI webApp and used to create graphics.*

[3] AVI stands for Application tool for Visualisation and Interpretation.

Further data analyses and visualisations were carried out on the data using Python scripts which took the database exports as inputs. The prototype AVI web application was developed to extend this approach further. It provided users with access to an interactive website presenting visualisations populated from the database. The end user did not require specialist coding skills or software to access and visualise data in the database. This was all handled through an interactive graphical environment.

The outputs from this database are used by FracMan when undertaking the DFN modelling. To support the efficient implementation of the modelling, a bespoke Python toolkit has been constructed. This toolkit allows tasks that are formed by a series of processes to be run as a single process, such that the sub-processes are automatically run in sequence. FracMan's macro interface means that these Python driven processes can include FracMan processes. By generalising these processes and making them modular they can be efficiently applied to future DFN modelling. This effectively enhances the capabilities of FracMan as some tasks that would otherwise be prohibitively time consuming become readily feasible. An overview of this workflow is illustrated in Figure 3-10.

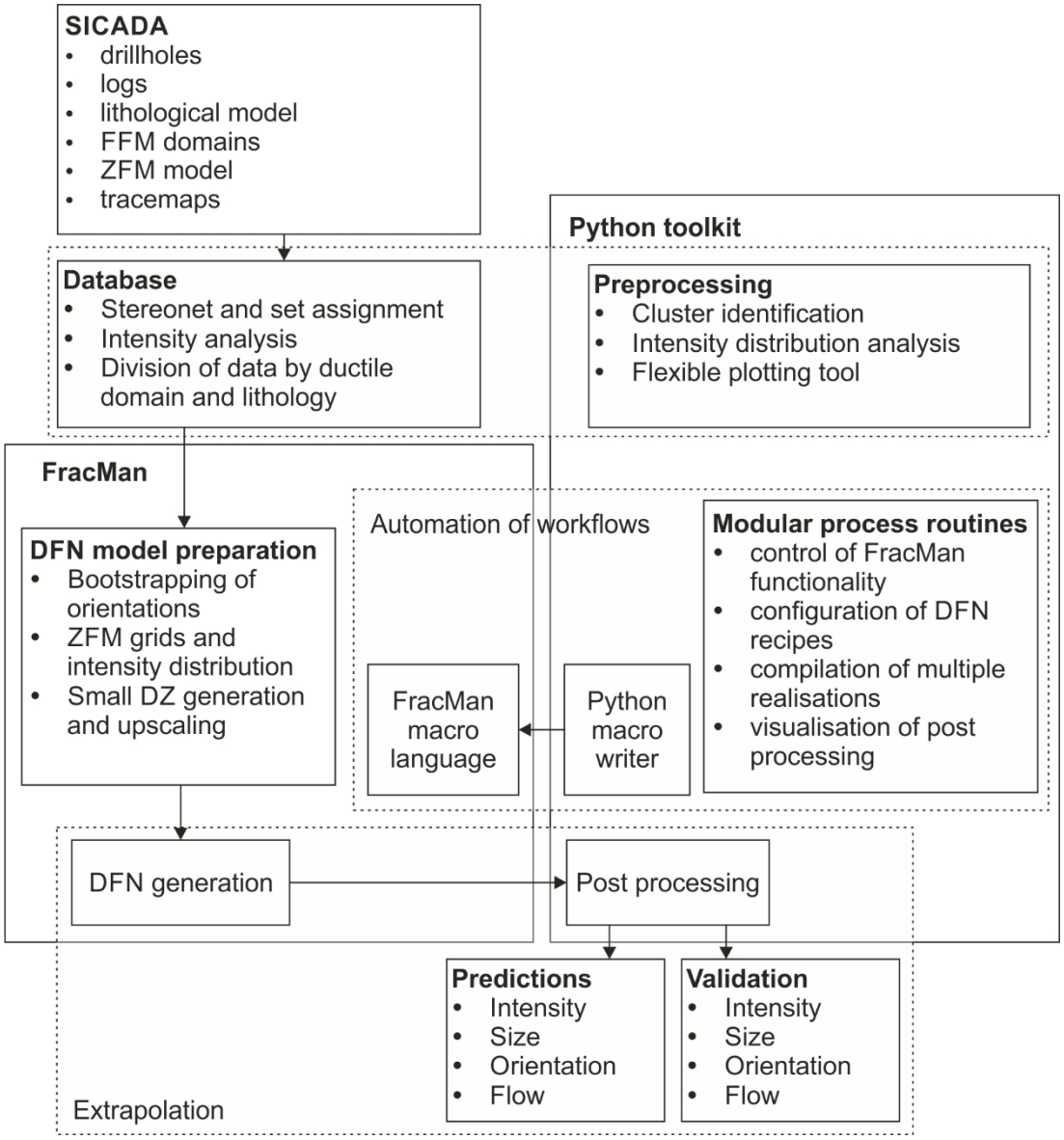

Figure 3-10. *Diagrammatic overview of the DFN model generation process, see Figure 1-5, highlighting the core role of workflows automated with Python.*

4 Describing spatial variability

4.1 Framework for describing spatial variability

In this chapter, we consider spatial variability in the occurrence of fracturing in the bedrock. Fracture occurrence is characterised by linear estimate of fracture intensity (e.g., Terzaghi corrected borehole fracture intensity P_{10} in m^{-1}, as is the general convention used in this report, and was denoted as $P_{10,corr}$ in DFN-M2008). This is the weighted count of fractures per unit borehole length, with the weight (to a maximum of 7) calculated as the reciprocal of the cosine of the angle between the normal to a fracture plane and the borehole axis. The symbol P_{10} for linear fracture intensity uses the standard terminology of Dershowitz and Herda (1992). Fracture intensity can vary on different scales associated to different tectonic settings and rock types, large deterministically modelled deformation zones (ZFM) or smaller, stochastic fracture zones. Describing the absolute fracture intensity (i.e., the intensity of all fractures regardless of whether they are sealed, open or partly sealed/open) and variations in it is the subject of the spatial model.

Large scale variations can be described deterministically through the identification of fracture domains (FFM01-FFM06) defined as volumetric units with different mineralogical and/or structural settings, or as being the damage zones of deterministic deformation zones. The damage zone of each DZ can be considered an individual structural domain with a tabular shape extending several kilometres, possibly spanning more than one fracture domains, but having a width of just a few tens of metres, typically. In terms of single hole interpretations, each borehole is subdivided into a contiguous log of either FFM or DZ-related domains. Some of the single hole interpreted DZ are modelled as deterministic structures, while others do not extend to surrounding holes or the surface to be modelled, implying there exist other DZ than those modelled that also cause variations intensity. Returning to the basic concept of structures existing on all scales sketched in Figure 1-1, it can be assumed that fracture zones exist over a range of scales between several tens to several hundreds of metres with only the larger ones being mapped in sufficiently to be modelled deterministically. These smaller zones will create variability in the distribution of fractures that appear as spikes in P_{10} log when intersected by boreholes, as shown in an example for KFM01D in Figure 4-1, noting that different boreholes would have spikes at different depths. Here, a total intensity log is shown and one for each of three gross sets (see following paragraph and Section 4.2). No compensation is attempted for crush as these are mainly associated to deterministic DZ modelling. Splitting the log by orientation reveals that spikes in intensity typically only belong to one or two orientations, confirming that the variability is directional, assumed tabular (flat and elongated), rather than isotropic. Therefore, by analogy small scale variability in fracture intensity as seen in the boreholes can be modelled as the damage zones around stochastically generated DZ, see Figure 4-7b of (Stephens 2010) as an example of a small DZ on an exposed outcrop.

Several plots in this chapter refer to fracture sets. In SDM-Site (Fox et al. 2007) and other recent DFN modelling (Hartley et al. 2021) six global sets have been identified (SubH, WNW, NS, NE, EW and ENE) to describe individual orientation clusters seen on outcrops based on classifying data as plotted on stereonets into hard sectors. Trying to apply so many sets to statistical analyses across several outcrops and boreholes can introduce uncertainties as to whether variability in the intensity of individual sets between volumes is genuine spatial variability or due to rotations due to folds and local structures moving fracturing between different hard sectors. Nonetheless, it is still necessary to classify fractures by orientation to capture different patterns of deformation seen as described in Section 2.2. Hence, a broad classification of just three classes of orientations is used as a compromise: SubH, NW and NE, described in Section 4.2. The NW set corresponds with Episode A of brittle deformation and subsequent reactivation phases, see Figure 2-4. The NS set corresponds with Episode B of brittle deformation forming sub-vertical structures, and the SubH set corresponds with the sub-horizontal deformation during Episode B and subsequent episode of reactivation. Orientation clusters within these sets are represented by using bootstrapping methods, described in Section 5.1. This reduces the noise in analysing statistical trends between sets and the subjectivity of hard sectoring orientation data.

It should be noted that although the statistical analyses are based on just three orientations, generation of fracture orientations in models is neither unimodal nor stationary for each set. Multiple techniques are used to honour the observed variability in orientations (see Sections 5.1 and 5.2). Firstly, orientation sampling is made using bootstrapping (Efron 1982) to allow the observed multiple modes within each set to be realised. Secondly, mean poles within each set are interpolated on a 3D geocellular grid between the

borehole data to be used in a weighted bootstrap sampling to favour measured orientations consistent with local rotations in fracturing. Thirdly, the generation of fracture swarms around stochastic DZ introduces local clustering in modelled orientations consistent with such characteristics seen in both boreholes and outcrop data. The results of these methods in model simulations of outcrops are exemplified in Section 8.3.

Frequent clusters of fractures with intensity twice or more the average intensity of all fractures within each FFM and low intensity intervening volumes is a general characteristic seen in the Forsmark boreholes. An example is given in Figure 4-1 showing a single deterministic DZ (ZFMENE0061) and three other DZ interpreted in SHI but not modelled in 3D and the variable intensity in the intervening rock, indicative of smaller DZ. We have developed an algorithm to automatically pick out such peaks in intensity to highlight smaller DZ for illustration purposes as seen in this example, and across the full borehole suite to aid our conceptual thinking. It is seen that such peaks occur with an average spacing of about 30 m. In the figure fracture intensity (P_{10}) is calculated in a moving window of 10 m as a balance between smoothing out noise and resolving individual smaller scale DZ (discussed further in the following paragraph), consistent with the typical width of smaller DZ interpreted in the SHI. Using twice the average intensity as a threshold, for this hole, a 20 m windows identifies 16 clusters, 10 m gives 24, and 5 m gives 26 clusters.

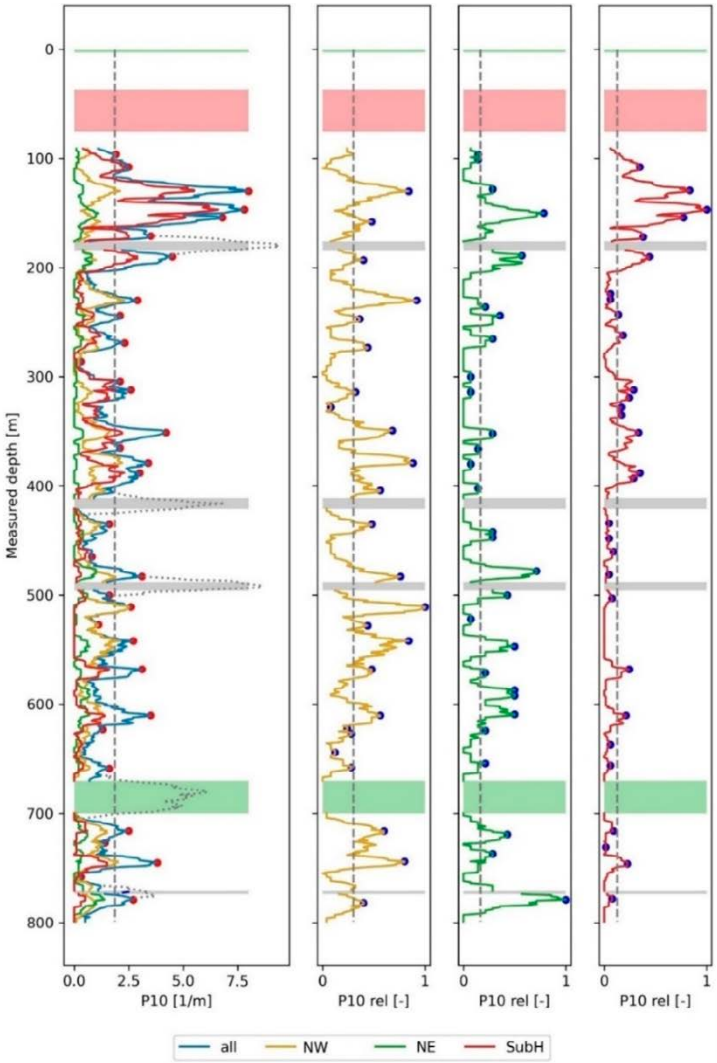

Figure 4-1. *An example of a Terzaghi corrected linear fracture intensity log from KFM01D (for all fractures, i.e. open plus sealed) in a 10 m moving interval. The left plot shows Terzaghi corrected fracture frequency for all fractures with the contributions from individual sets superimposed. These individual components are shown more clearly in the right hand plots. SHI DZ intervals are shown by horizontal bars of the zone width: NW DZ (yellow), NE DZ (green), SH DZ (red), unmodelled DZ (grey). The average intensities are shown as vertical dashed line. Other potential DZ clusters are indicated by red or blue dots at their apex.*

Assuming these to be smaller scale structures and considering them in the DFN spatial model is a significant difference relative to DFN modelling carried out for SDM-Site, where each FFM was modelled assuming a Poisson process, i.e., a statistically random and uncorrelatedfixed spatial model. Recognising these clusters as representing separate statistical subdomains along 1D holes is one step, while conceptualising their 3D shape and size is another. One clue as to their shape is provided by the observation that most clusters are dominated by only one or two sets, with the clusters associated to each set rarely coinciding. This would indicate that these clusters have been created as a coherent plane of deformation, suggesting that they likely correspond to tabular structures rather than spherical or ellipsoidal-shaped structures of enhanced isotropic failure. This concept of small DZ that can be modelled stochastically and create tabular fracture clusters is fundamental to the spatial model developed in the DFN-BF1 model.

The characterisation of these variations in intensity is sensitive to the scale on which these characterisations are made. Figure 4-2 illustrates how the intensity profile in KFM02A is modified when the length of the moving window in which the intensity is calculated changes: a smaller scale results in more and higher peaks and vice versa. For much of the work in this report, 10 m was selected as an optimum scale on which to characterise features because it captures trends that are observable at a range of scales. Examples of small-scale features are the peaks and troughs in intensity between 400 and 450 m depth which are largely absent above 10 m. An example of a large-scale feature is the peak in intensity between 400 and 500 m depth most clearly shown on the 100 m scale, observable at the 10 m scale, but largely obscured at the 1 m scale.

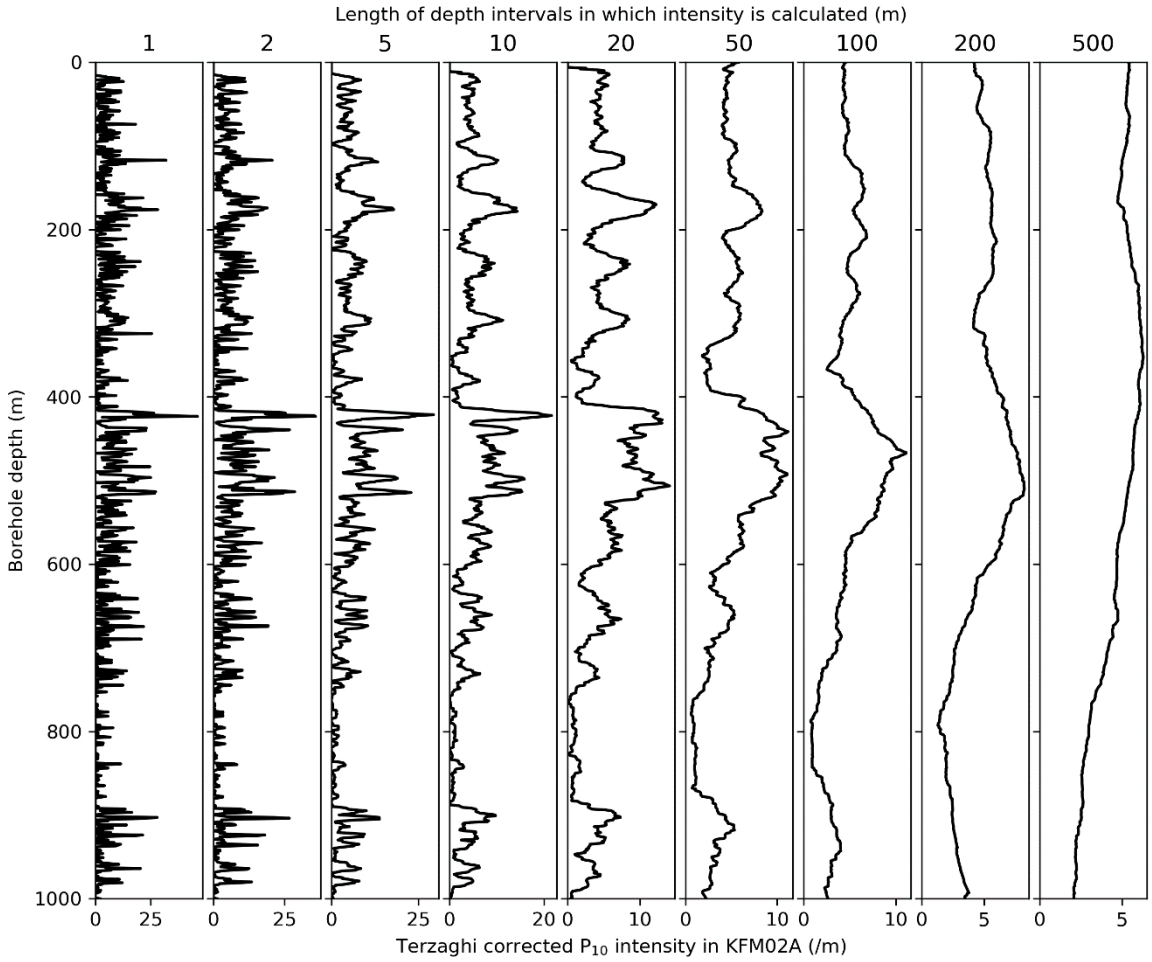

Figure 4-2. *Terzaghi corrected linear fracture intensity (P_{10}) logs of all fractures for KFM02A characterised at different length scales.*

It may be noted that average intensity of all fractures is shown in Figure 4-1 as uniform. This is because there is limited variation in the intensity of all fractures with elevation, as is demonstrated later in Figure 5-22, and as interpreted in the Geological DFN for SDM-Site (Fox et al. 2007). There is some enhanced fracturing as discussed in Section 5.5, but depth dependency is more an issue for hydraulics since the openness of fractures shows a consistent reduction with depth, see Section 7.1, as does transmissivity, see Section 7.2.

The bedrock can be considered as broken into four types of domains:

1. the bulk fracture domains, e.g. FFM01–FFM06 within the Forsmark lens;
2. a near surface domain where fracturing has in places been over-printed with sheet joints, corresponding to FFM02U within the tectonic lens (outlined in Figure 2-7);
3. the deterministically modelled DZ, ZFM; and
4. the stochastically modelled DZ, which include both stochastic ZFM-scale like structures in the far-field and small DZ throughout the bedrock.

The second domain has its roots in SDM-Site where it was recognised that the only statistically significant depth trend in fracturing was a higher intensity of SH fractures at shallow depths. However, most cored holes drilled at that time were cased in the top 100 m, leaving uncertainties in the characterisation of this domain. More recent core drilling of shallow and some deep holes in the access area, KFM13–KFM27, has provided more insights into this domain, albeit within a limited area where the accesses to the SFK repository will be built (Hermanson and Petersson 2022; Hartley et al. 2021). An example log is shown in Figure 4-3 with a zone of mainly SH fractures in the top 30 m with a deeper SH cluster at about 100 m depth. NE fractures are also slightly elevated in the upper bedrock. These general characteristics are typical for many holes. The consistent presence of higher intensity SubH fracturing in the top 30 m led to the subdivision of the FFM02 domain into FFM02U and FFM02L domains (Hartley et al. 2021) with the equivalent of the FFM02U layer interpreted to continue outside the lens as similar characteristics were observed in cored holes outside the lens, see Section 5.4. By representing this layer as a distinct statistical fracture domain, its unique properties can be modelled. The high intensity clusters of SH fractures around 100 m depth in KFM13 or the four clusters between 100–175 m in KFM01D vary in frequency and location between boreholes, and so are modelled as stochastic DZ (domain type 4 above) using an interpreted statistical recipe (see Subsection 5.4.1).

The third domain is modelled as tabular volumes based on the deterministic DZ midplanes provided by the so called DMS 2020 model (Hermanson and Petersson 2022) with thicknesses also provided. These are conceptualised as fracture swarms with their own individual recipe for orientation (relative to the plane of the DZ), spatial model (how intensity varies across the zone) and the size scaling of the individual fractures within them.

Statistical analysis of the deterministic DZ model inside the well-characterised volume inside the lens provides the basis for stochastic extrapolation of the deterministic DZ model outside of that volume in terms of the orientation, intensity-size scaling and terminations. This supplies the basis for the stochastic DZ component of domain type 4 above. Analysis of the intensity of clusters and the fracturing within them provides the basis for conceptualising the other small stochastic DZ component of the fourth domain.

The first domain corresponds with the remaining background of individual fractures outside of deterministic/stochastic DZ and small DZ. For model generation purposes this first domain provides a continuous a background level of fracturing over which structures in domains 2–4 are over printed.

The definition of these domains also implies some demarcation in the sizes of structures conceived in these domains, as follows:

- Deterministically modelled DZ (ZFM) are modelled on scales of 20 km > r > 250 m;
- Small (stochastically modelled) DZ are considered to exist on scales 250 m > r > 50 m;
- Individual fractures, inside DZ, are modelled on scales 150 m > r > r_0; and
- In the background rock outside DZ, individual fractures are modelled on scales 50 m > r > r_0.

The choice of 250 m as the lower limit on deterministic modelling is based on the smallest structures of the DMS 2020 model. Noting that stochastic modelling can be used to augment the deterministic DZ model outside volumes that have been characterised. Below this limit, structures are still expected to be mainly zones rather than single fractures down to a radius of about 50 m. This is a fundamental working assumption supported by examination of the architecture of large structures seen in the extensive ONKALO® tunnel system (Nordbäck and Mattila 2018). These "small DZ" are modelled stochastically in a two-step process to generate their midplanes and then swarms of individual fractures around them. This means they are conceptualised as having some finite thickness and internal structure, see Section 5.3. A working assumption for the location parameter r_0 is the radius of the slim boreholes, 0.038 m, see (Darcel et al. 2006; Fox et al. 2007) for further discussion.

Note: The lower size limit of the deterministic DZ model for SDM-Site was 1 000 m and for SDM PSU 300 m.

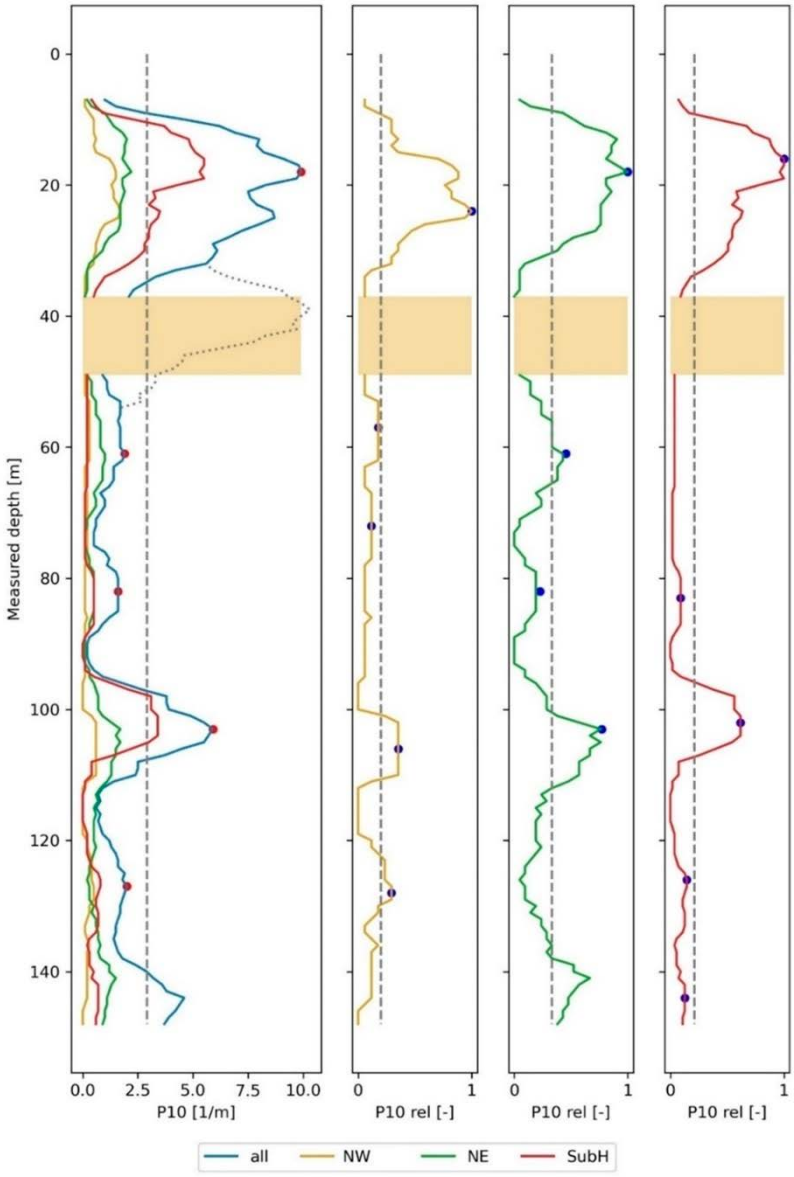

Figure 4-3. *An example linear fracture intensity log from the shallow hole KFM13 using a 10 m moving interval. The left plot shows corrected intensity for all fractures with the contributions from individual sets superimposed. These individual components are shown more clearly in the right hand plots. SHI deformation zone intervals are shown by horizontal bars of the zone width: NW DZ (yellow), NE DZ (green), SH DZ (red), unmodelled DZ (grey). The dotted curve represents on the left plot indicates a DZ related cluster identified by the method described in Subsection 5.3.3. The average intensities are shown as vertical dashed line. Other potential DZ clusters are indicated by red or blue dots at their apex.*

4.2 Basis for orientation models

Before continuing the conceptualisation of the spatial model, the related issue of fracture orientations is expanded here, as it provides a basis for several types of analyses. As seen in Section 2.2 the deformation history of the bedrock has led to activation of distinct orientations of structures, with later reactivation along these same orientations. Grouping fractures into such orientation sets provides a framework for assessing possible differences in statistical properties between orientations. Some examples of splitting fractures by set have already been shown in Figure 4-1 and Figure 4-3. It should be noted that since the DFN-BF1 model aims to model all fractures for multi-disciplinary purposes, then analyses are made on all fractures (open and sealed) with focus on open fractures coming as we move to the hydrogeological description in Chapter 7.

Using just three broad sets (essentially sectors for modelling) reduces noise when analysing differences in statistics between sets. It also mitigates against a common problem in DFN modelling when pooling large datasets across rock volumes of varying deformation. That is, if deformation rotates along a borehole or between multiple boreholes, then the pooled data can give the impression that there are several fracture sets or orientations follow an elliptical distribution. If instead one makes density plots of individual borehole intervals, 30 m say, then typically only 2–4 sets are apparent in any one interval. A model that reflects the number of sets (3, say) seen on such a scale, and models the spatial variations (rotations) of the centres of these sets will be more representative than a model with the larger number of sets seen in pooled data (6, say) throughout the region. Figure 4-4 and Figure 4-5. exemplify this issue by plotting fracture poles by depth. The NE fractures are ENE with WNW dip at shallow depths, rotating to ENE with SE dip, then NE with SE dip, then NS with E dip. The NW fractures mainly exist at shallow depth with diffuse orientations. The SH set remains near horizontal.

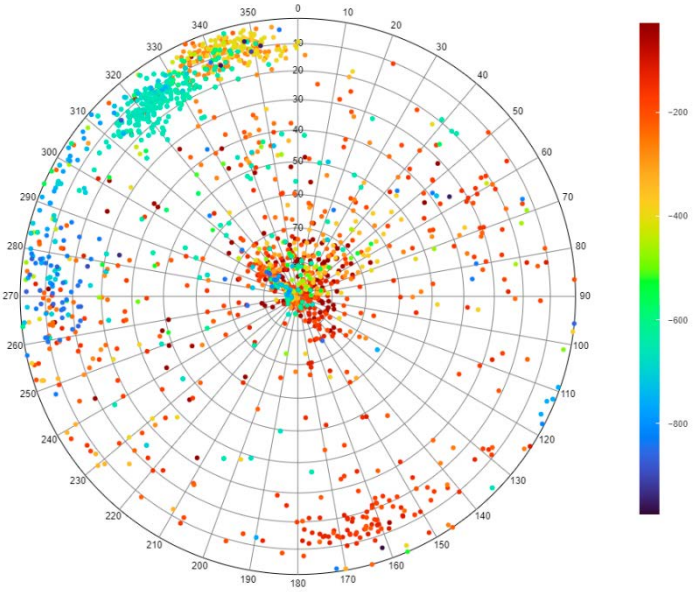

Figure 4-4. *Stereonet of all the fractures logged in KFM01A coloured by elevation (m ASL, see colour bar), showing how clusters of fracture orientations tend to appear at common depths and sometimes rotate.*

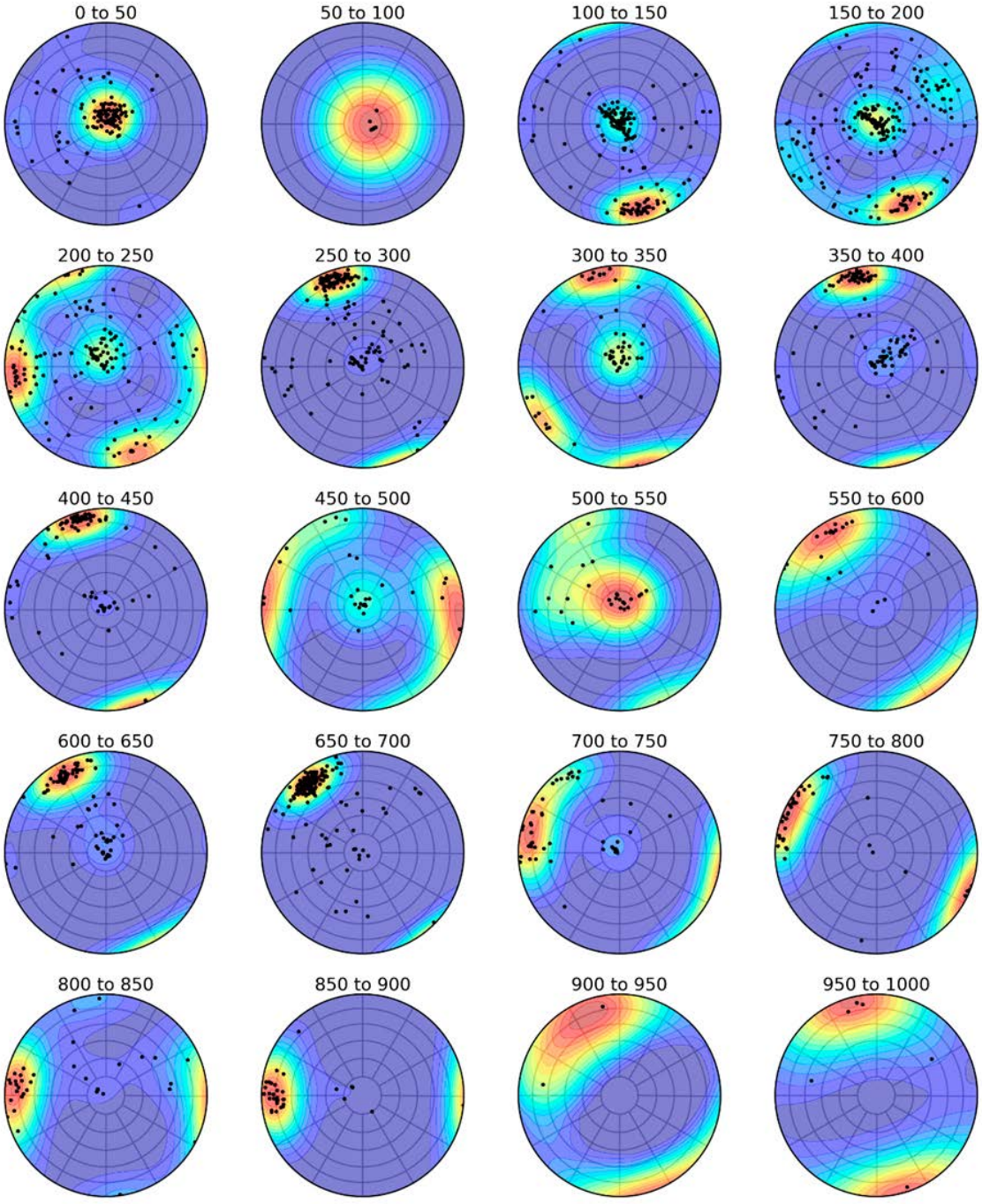

Figure 4-5. *A series of stereonet plots with Terzaghi weighted intensity contours showing 50 m depth intervals down KFM01A, illustrating how the orientation of the observed fractures changes.*

The three fracture sets are applied according to simple rules, as illustrated in Figure 4-6:

- **SH** – fractures with a pole plunge less than 40°;
- **NE** – fractures with a pole plunge greater than 40° and [[trend > 100° and < 190°] or [> 280° or < 10°]]; and
- **NW** – otherwise.

As discussed above and in Section 5.1, this sectoring of the data for analysis does not preclude representation of spatial variation in orientations or multiple clusters of orientations within a set. Modelling techniques are used maintain these possibilities when seen in the data. The main purpose of the sectoring is to provide a simple framework for examining how the general sequence of deformation episodes have affected the fracture network.

The relative fractions of intensities of structures that fall within each of these sets varies according to scale. For deterministic DZ, the ratios of (SH, NE, NW) are approximately (1:5:2), while for small DZ and background fractures they are about (2:4:3). When it comes to openness, the anisotropic in situ stress tensor favours the SH and NW sets, meaning their relative importance becomes more equitable between sets, while in terms of transmissivity, then SH tends to dominate. However, there are trends with depth and scale that are examined in detail in the following chapters.

The observation that the number of apparent sets increases with scale can be quantified by counting the number of orientation clusters as a function of interval length. Figure 4-7 shows an orientation cluster analysis considering the complete KFM and KFR borehole data, excluding DZ intervals identified within the Single Hole Interpretation (SHI) process, see (Hermanson and Petersson 2022), and interval size varying from 20–400 m along the abscissa. The number of possible intervals of that scale are indicated in brackets below the interval size. Only intervals with more than 10 fractures are used, with an average of about 40 fractures in 20 m intervals, increasing proportionately for longer intervals. Both the median and mean number of sets is close to 3 for intervals up to 40 m length, with quartiles between 2 and 4 sets. When pooling data over one to several hundred metres, the mean number of sets gradually increases from 4 to 5 with quartiles between 3 and 5.

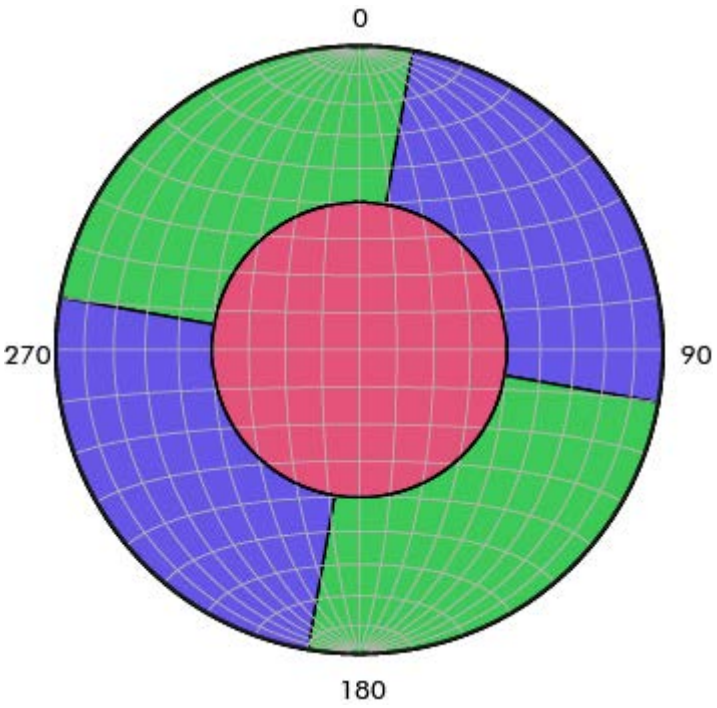

Figure 4-6. *Sketch of the broad orientation sectoring used as the basis for analyses through this study.*

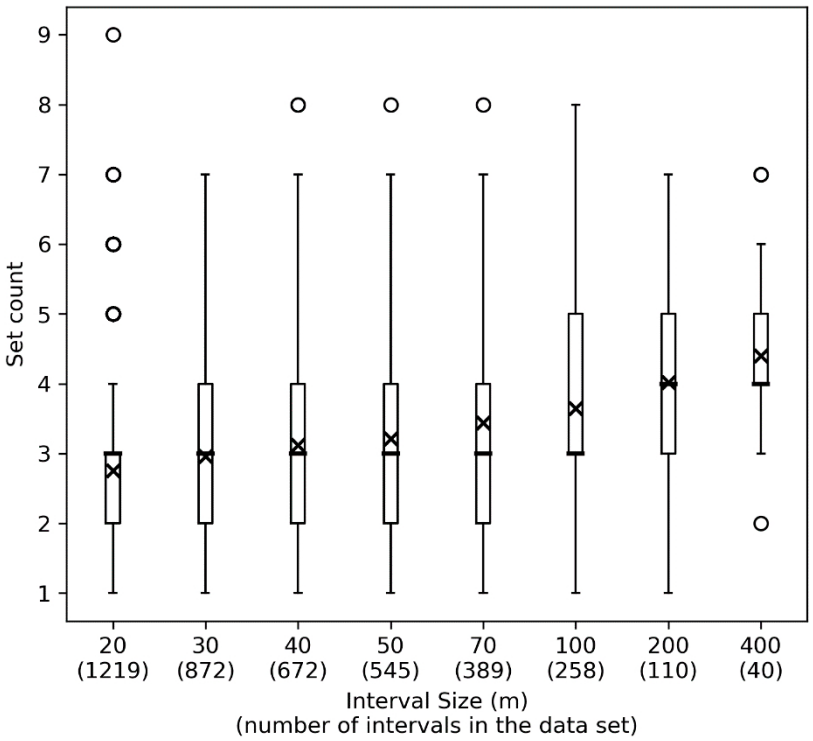

Figure 4-7. *Boxplots showing how the set count varies with the size of the depth interval being considered, for all KFM and KFR borehole data where there were at least 10 fractures identified and not associated with a DZ interval. The bold horizontal lines indicate the median set count and the × symbols indicate the mean set count. The boxes represent first (Q1) and third (Q3) quartiles. The whiskers extend from the box to the farthest data point lying within 1.5x the inter-quartile range (Q3–Q1) from the box. The circles are outliers outside the whiskers.*

On a 20–30 m interval, i.e., spanning the scale of deposition hole and tunnel spacings, then the mean number of sets is below three. Hence, near-field DFN modelling on those scales will be well-represented by just 3 sets in any one location, whereas an orientation model built on statistics of data pooled over several hundred metres would yield 4–5 sets. Modelling 3 sets in any specific location might be expected to give more clustering of fracture orientations compared to DFN models with 5–6 global sets when simulating individual outcrops or tunnel sections on scales of 20–30 m, as suggested by the data. The weighted bootstrapping approach described in Section 5.1 provides an ability to generate a spatially varying number of orientation clusters as driven by orientations statistics from nearby data sources.

Note that this analysis is intended to provide a qualitative illustration of how the set count varies with interval size when analysing the full data set, as it is sensitive to subjective aspects of the workflow used to create the figure. The quantification of fracture set counts was undertaken using the process described in Appendix A1.

The clustering of orientations around typically just 3 sets when viewing individual areas of ~10 m scale is also seen in the mapped fracture traces from outcrops (see Figure 3-4. and Figure 3-5).

Further details on the implementation of the fracture orientation model are given in Section 5.1.

4.3 Conceptual approach to each structural domain type

Returning to the conceptualisation of the different structural domains outlined in Section 4.1, there are several conceptual challenges to address for each type of domain. In many cases conceptual interpretations made for one structural domain type are carried forth to other structural domains for self-consistency. For example, interpretations made for deterministic DZ are generally used to guide model selection and parameters for stochastic DZ. An overview of the conceptual steps and how they cascade down through the hierarchy of structure types is given in Table 4-1.

One cornerstone of the updated DFN methodology (Selroos et al. 2022) is to conceptualise DZ as tabular fracture domains with their own fracture network properties. As seen in boreholes they correspond to interval(s) with more intense fracturing. In 3D, they're represented as swarms of DZ-related fractures centred along and around a midplane. The midplane defining the DZ's location, orientation and size. Representing them as fracture swarms increases the complexity of their description and numerical cost, but avails possibilities to assess variability in connectivity, hydraulic and deformation/strength along and across DZ that links in a natural way to the structural architecture of zones. Although knowledge of the structural architecture of zones is at an early stage of characterisation at Forsmark, it is envisaged that such characterisation will mature during underground investigations and become increasingly important to repository engineering (e.g., support design) and optimisation for safety with regard to critical structures (POSIVA and SKB 2017). The chosen modelling approach was to describe DZ in a 2-step "parent-daughter" method (Chilès 1988; Billaux et al. 1989), by first describing a DFN recipe for generating "parent" midplanes (DZ cores) and then a DFN recipe for "daughter" fractures (DZ-related fracture / damage zones) seeded adjacent to the midplanes. The final model typically removes the parent midplane (unless a continuous core is desired) leaving just a swarm of daughter fractures. Experience from PFL logging of structures between multiple grout holes and multiple shafts at ONKALO® suggest smaller tabular structures are heterogeneous in connectivity/flow, while larger structures are more connected (Libby et al. 2020). Removing the core plane as a working assumption avoids forcing all DZ to be connected, while correlating thickness or intensity of DZ with size results increasing probability of connections across a structure with its size.

This 2-step conceptualisation is reflected in the issues presented in Table 4-1 by first listing the midplane issues and then the DZ-related issues for each of the deformation zone type structures, while background fractures and sheet joints are defined in a single step. Interpretations made for deterministic DZ were also applied to the stochastic DZ modelling. Some were also used for aspects of the small DZ modelling, although some additional analyses/assumptions were made because of the smaller scale of structures concerned.

Table 4-1. Overview of conceptual building blocks for each type of structure and the approach taken to analyse/parameterise each DFN component.

Structure type/Conceptual issue	Assumptions/Approach
Deterministic DZ	
Midplane spatial, size scaling and orientation models	Delivered as DMS 2020 model, Subsection 2.3.1
Deformation history and midplane terminations	See Section 2.2, and inherent within the interpreted geometries of the DMS 2020 model
DZ-related fractures spatial model	From analysis of fracturing within DZ intervals, Section 5.3
DZ-related fractures orientation model	Assumed subparallel
	Model calibration against fracturing within DZ intervals, Table 5-3
DZ-related fractures scaling model	G-DFN: working assumption for the prior size scaling model (before terminations), and an emergent property of fracture growth for the dense regime
DZ-related fracture terminations	Working assumptions for DZ, Table 5-3
Stochastic DZ	
Midplane spatial, size scaling and orientation models	From statistical analysis of the DMS 2020 model
	Calibrated against DZ stats, Subsection 5.2.3
Deformation history and midplane terminations	From statistical analysis of the DMS 2020 model and model calibration, Subsection 5.2.1
Midplane scaling of size to width	From analysis of scaling of deterministic DZ size to width, Subsection 5.2.4
Potential DZ (PDZ) midplanes	Modelled as conditioned semi-stochastic DZ, Subsection 5.2.1
DZ-related fractures spatial model	Same as deterministic DZ model, Table 5-3
DZ-related fractures orientation model	Same as deterministic DZ model, Table 5-3
DZ-related fractures scaling model	Same as deterministic DZ model, Table 5-3
DZ-related fracture terminations	Working assumptions for DZ, Table 5-3
Small DZ	
Midplane spatial models	Global model
	G-DFN
	Stationary intensity per set
	Intensity from analysis of clusters outside of SHI DZ
Midplane size scaling model	Working assumption for the prior model, and an emergent property of fracture growth for the dense regime, Subsection 5.4.1
Midplane orientation models	Bootstrapping within 3 sets, Table 5-4
Deformation history and midplane terminations	Same as deterministic DZ model, Table 5-4
Midplane scaling of size to total intensity (equiv. width)	Analysis of intensity variability on 10 m scale
	Model calibration, Table 5-4
DZ-related fractures spatial model	Associated to midplane, Table 5-4
DZ-related fractures orientation model	Same as deterministic DZ model, Table 5-4
DZ-related fractures scaling model	Same as deterministic DZ model, Table 5-4
DZ-related fracture terminations	Working assumptions for background fractures, Table 5-4
Background individual fractures	
Intensity of background	Total intensity for FFM outside DZ, less total intensity associated to small DZ, Table 5-5
Background fractures spatial model	G-DFN with homogeneous nuclei within each FFM, Table 5-5
Background fractures orientation model	Inverse distance weighted bootstrap from data outside of DZ, Table 5-5
Background fractures scaling model	G-DFN: working assumption for the prior model, and an emergent property of fracture growth for the dense regime, Table 5-5
Background fracture terminations	Working assumptions for background fractures, Table 5-5
Sheet joints	
Sheet joint spatial model	G-DFN, homogeneous in shallow zone, excess intensity above background, Section 5.5
Sheet joint orientation model	Working assumptions based on inlet channel exposures, Section 5.5
Sheet joint scaling model	From R-21-13 (Hartley et al. 2021)
Sheet joint fracture terminations	Working assumptions based on inlet channel exposures

For illustration of the general approach, an example of a small midplane network around one borehole followed by created of DZ-related swarms is shown Figure 4-8 Deterministic mid planes of the DZs are assigned a width for the associated damage zone represented as a grid centred around the midplane. Fracture centres are then grown within these volumes according to a spatial model that may vary across the volume and accounting for any rules on fracture interaction/termination. The conceptualisation for small DZ is essentially the same, but because of the much larger number and smaller volume of such structures a different numerical approach is used, see Subsection 5.4.1.

In line with the DFN methodology (See Section 6.3.5 of (Selroos et al. 2022)), all scales of fractures are generated genetically as a grown DFN (G-DFN) in an attempt to simulate the present-day pattern of the deformation history envisaged in Figure 2-4, and the processes of fracture termination and arrest according to their relative ages and sizes. Including rules for the termination of fractures in the stochastic modelling automates interpretations made within the deterministic modelling of DZ (see Figure 2-5) and mimics terminations seen on outcrops, see Figure 3-4 and Figure 3-5. The G-DFN approach maintains aspects of classical Poissonian DFN methods in stochastic sampling of nucleation points, orientations and target intensity in order to honour basic statistics of fractures characterised in borehole data, but by growing and terminating fractures it also honours fracture interactions and effects on size distributions characterised in outcrop data. The rules for growth and terminations are simplistic, based on general geomechanical principles, such that they can be used to generate networks of millions of fractures on a regional-scale, rather than fully coupled geomechanical simulations of rock fragmentation over geological time. Hence, DFN-BF1 is an attempt to include the processes occurring over the last 2Ga – just in a relatively simple way via the different sets and some rules rather than a very complex physical model.

In the G-DFN approach (Libby et al. 2019), each set is grown in sequence according to the deformation history and each fracture is created through the process of nucleation, growth, termination and arrest. Fractures are nucleated in each cell according to the spatial distribution of fracture intensity specified on the geocellular grid and the prior estimate of fracture size distribution. Because the actual size distribution is an emergent property (due to terminations), the density of nucleation points is adjusted to ensure the target intensity is met. Terminations are determined probabilistically and according to a size hierarchy (only fractures smaller than the ones they impinge on can terminate), and a fracture arrests once either it reaches its target size (sampled from the prior size distribution), or a specified fraction of its circumference has been terminated, 70 % is assumed.

The prior initial size scaling model determines the distribution of sizes before they are affected by terminations. In outcrop data this can be interpreted from area-normalised trace length cumulative frequency plots (La Pointe et al. 2005) over tracelength ranges above the rollover scale for detection but below scales affected either by terminations or the scale of the outcrop. This is used both to estimate the expected number of nucleation points within a cell and the sampling of sizes to which to try to grow each fracture.

As the network develops, the density builds up, and more fractures interact, which if terminations are applied affects the size distribution. The overall size distribution is, therefore, an emergent property, and requires some iteration of size scaling and termination parameters to mimic size and termination statistics. These parameters can be tuned for the different sets and different scales, stochastic DZ against the deterministic DZ model, and individual fractures against outcrops. Hence, the mention of G-DFN and model calibration in Table 4-1. The sequence of fracture generation is NW, NE, then SH for all scales of structure, based on Section 2.2. It is recognised that this is a simplification given the history of reactivation that may give rise to later generations of smaller NW fractures terminating on large NE structures, for example.

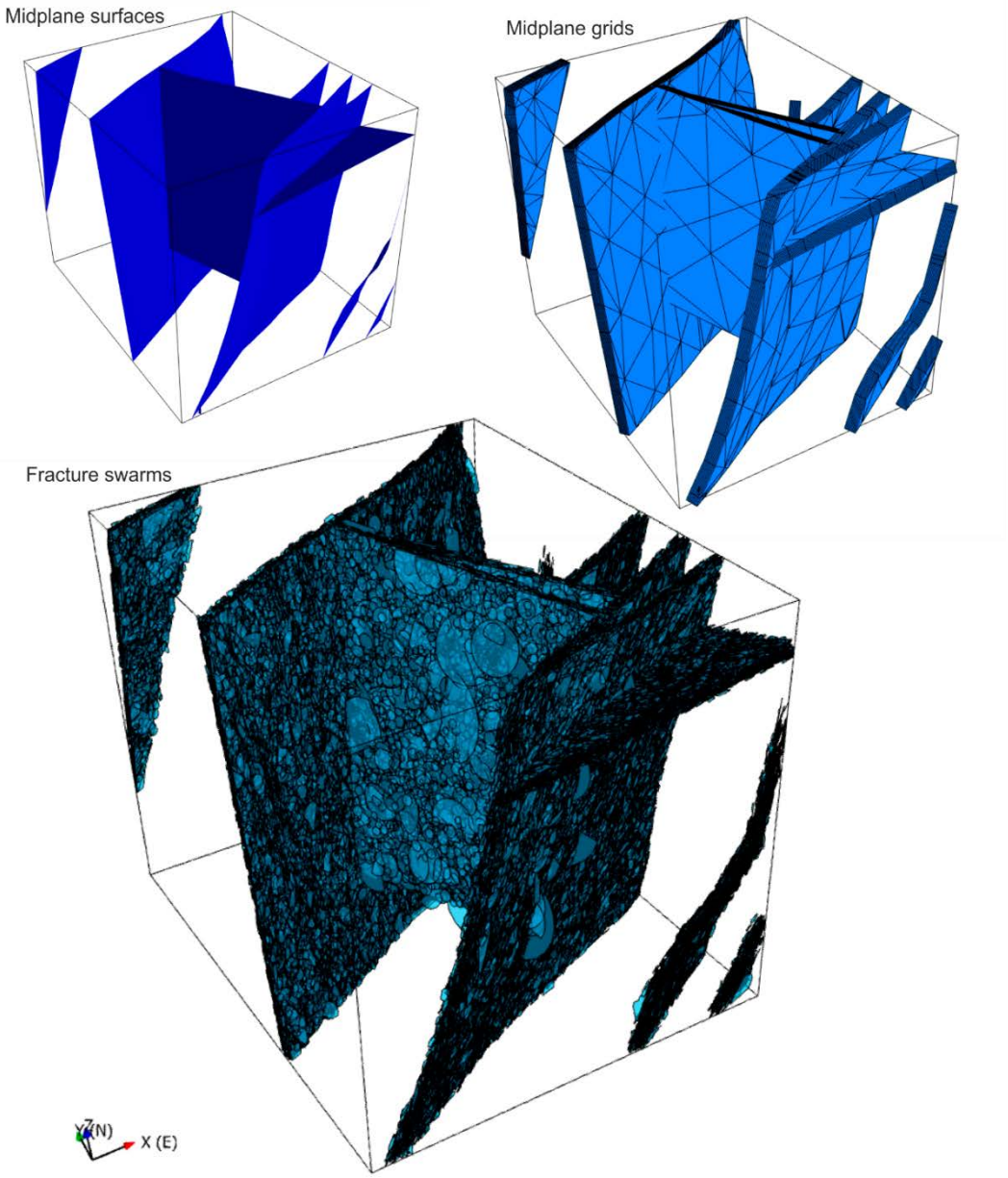

Figure 4-8. *Equivalent views of midplane surfaces, midplane specific grids and associated fracture swarms (for a 500 × 600 × 500 m cuboid around KFM08A) illustrating the geometric relationship between the three.*

4.4 Regional scale fracture domains

Fracture domains FFM01-FFM06 have been previous identified (Olofsson et al. 2007) for DFN modelling around the SFK facility. However, they only describe domains on a facility scale, see Subsection 2.3.3. The DFN-BF1 model needs to describe fracturing on the wider regional scale, at least covering the area of the Forsmark catchment Figure 1-2. The SFR facility lies to the north of the FFM05 domain, is of felsic to intermediate volcanic rock type and is outside the Forsmark lens tectonic unit shown in Figure 2-7. The nature of fracturing between the lens tectonic unit, as seen in KFM holes, and that seen outside, as seen in KFR holes, is distinct as illustrated in Figure 4-9. The KFM holes are characterised by many intervals with relatively low fracture intensity interspersed with several structure-related clusters of intensity of order five times that of the intervening relatively intact sections. The KFR holes have structure-related peak intensities of similar magnitude, but the intervening rock is more fractured. The bedrock is more fragmented and, as will be seen later, more isotropically so. It is, therefore, necessary to assign the tectonic units outside the Forsmark lens as a different regional-scale fracture domain.

There are a few cored boreholes that transect the borders of the lens, passing through either FFM04 to the southwest or FFM05 to the northeast. The KFR holes provide the greatest amount of fracture data outside the lens, to the northeast of FFM05. Given this lack of information for making a more detailed division, a first working assumption was to combine borehole data outside the lens to the northeast with the FFM05 domain, and combine borehole data outside the lens to the southwest with the FFM04 domain. A small volume to the northwest within the lens shown in Figure 2-7 corresponding to rock domain RD034 (granite to granodiorite, metamorphic, medium grained) is kept separate in the first pass analysis. This amounts to assigning the following data to their closest regions:

- The KFR holes were assigned to FFM05; and
- KFM12A was assigned to FFM04.

Intensity statistics as divided between inside/outside DZ (as defined by ESHI), and these extended fracture domains are shown in Figure 4-10. Intensity is also subdivided into the main sets defined in Section 4.2. This confirms that the extended FFM05 domain outside the lens has very different characteristics to the FFM01/02/03/06 domains inside and needs to be modelled differently. The little data available for FFM04 suggest similar statistics to FFM05, and hence, a working assumption is that FFM04/05 be merged into a single “outside lens” or “extended FFM04/05” fracture domain. Fracturing inside DZs within FFM01/02/03/06 is much higher intensity than that in the background rock. The intensity inside DZs in the extended FFM04/05 domain is only marginally higher than the background, and although higher than in DZs within FFM01/02/03/06, the differences are less than the variability between holes, and so no distinction is made here in the statistics of DZ-related fractures inside and outside the lens.

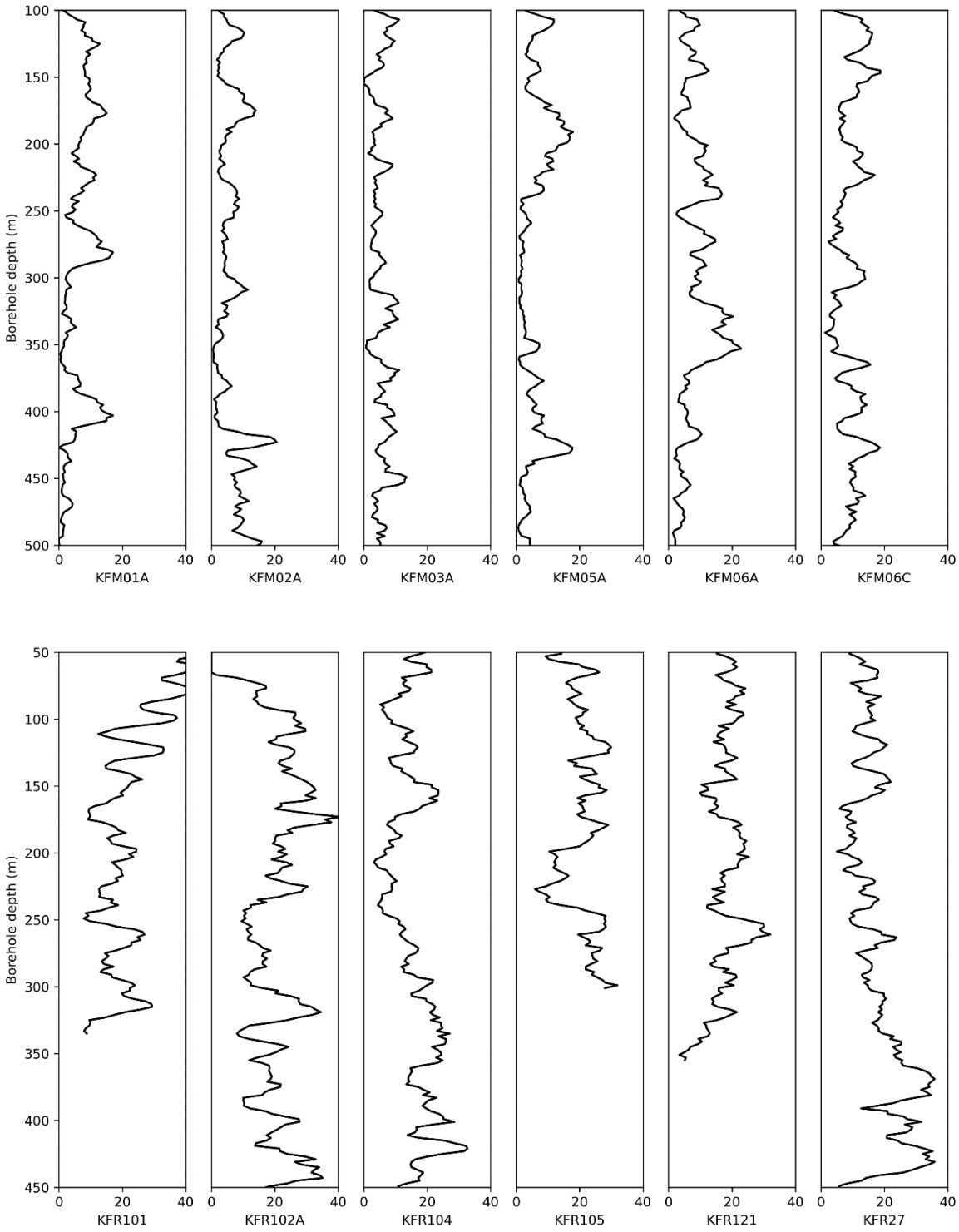

Figure 4-9. *Graphs showing the Terzaghi corrected P_{10} intensity (m^{-1}) of all fractures calculated in 10 m intervals for a selection of KFM and KFR boreholes with lengths of 300 m or more.*

From Figure 4-10 it is apparent that in the tectonic units outside the lens, NW fracturing is predominant consistent with the pattern of deformation in regional tectonic domain 2 shown in Figure 2-1, followed by NE and then SubH fracturing. Inside the lens, NE fracturing parallel to the short axis of the lens fold structure dominates with subsidiary NE and SubH fractures. FFM03 is inside the lens but in the hanging wall of the gently dipping ZFMA2. Structurally, FFM03 appears far more similar to FFM01 than FFM05, i.e. being inside the tectonic lens seems to be more of a control on fracturing in this domain than whether it is in the footwall or hanging wall of ZFMA2. The significance of the distinction between FFM01 and FFM03 comes more in the effects ZFMA2 has on stress and hydraulics, see Chapters 6 and 7, respectively.

In summary, for structural/geometric modelling purposes the distinct domains are:

- DZ-related domains;
- FFM01/03/06 and RD034;
- FFM02U;
- FFM02L; and
- FFM04/05 extended to all volumes outside the Forsmark lens.

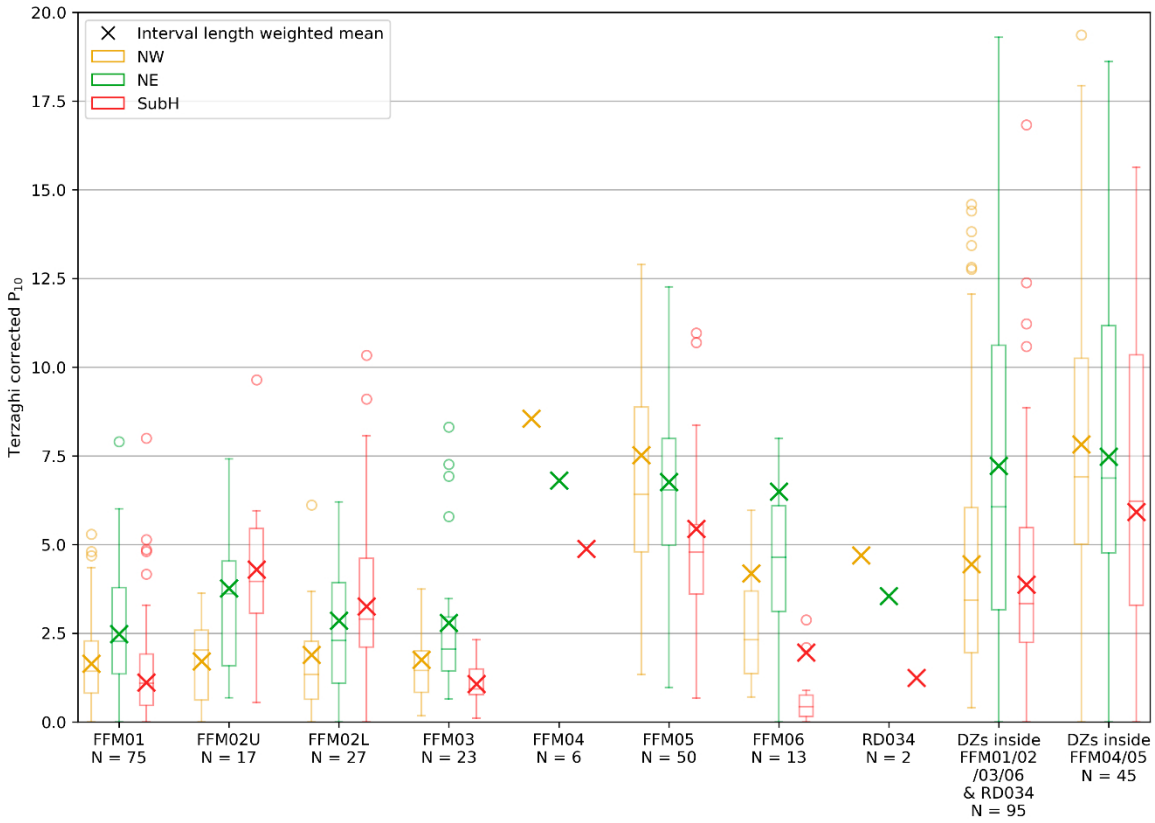

Figure 4-10. *Plot showing the mean Terzaghi corrected P_{10} intensities of fractures in the KFM and KFR boreholes in each FFM region weighted by the length of the intervals from which the intensities are calculated, with bar and whisker plots where the number of sampled intervals (N) is > 10. The bars indicate 25, 50 and 75 percentiles, the whiskers 5 and 95 percentiles, and the crosses the mean. The circles show individual values above the 95-percentile. For the KFM boreholes, the DZs are the ESHI DZ assignments and for the KFR boreholes the DZs are the SHI DZ assignments. The intensities shown for the named FFM regions exclude the DZ intervals.*

5 Fracture geometrical description

A schematic workflow for how each of the different DFN components listed in Table 4-1 is generated and integrated in an overall DFN model is illustrated in Figure 1-5. This chapter describes the configuration of these components.

5.1 Orientation bootstrapping

Rather than try to subdivide the orientation data into several sets and fit distribution models to each, the distribution of orientations is represented using a technique called bootstrapping (Efron 1982; Loh and Stein 2004). This involves stochastically sampling an existing dataset of orientations, such that a sufficiently large output sample will perfectly represent (in the statistical sense) the input dataset including all its subtleties, i.e., what otherwise might have to be included as minor sets. The existing datasets can be borehole logs, as for the background fracture sets described in Section 5.4, or surfaces, as for the DZ midplanes described in Section 5.2.

This behaviour means that bootstrapping can produce multiple clusters of orientations without splitting the data into several orientation-based sets. Still, in order to honour the concept of the rock's deformation history (Section 2.2) and a common termination hierarchy across the tectonic domain (tectonic domain 2 in Figure 2-1b), most of the DFN components are split into the three sets described in Section 4.2. This means that the bootstrapping method is applied to each set individually.

Fractures are generated for each set within each grid cell with the orientation sampled from the dataset of observed fractures in the same set over all boreholes mapped. The sampling is weighted inversely with the 3D distance between the centre of the generated fracture and the cartesian location of each observed fracture (of the same set). An example of this is shown in Figure 5-1, illustrating how the mean strike of the NW set rotates from being NW–SE in the NE of the Forsmark area, to more NNW–SSE in the lens region. A random deviation is superimposed on the bootstrap value using a Fisher distribution to resample (output) data around each sample in original input data.

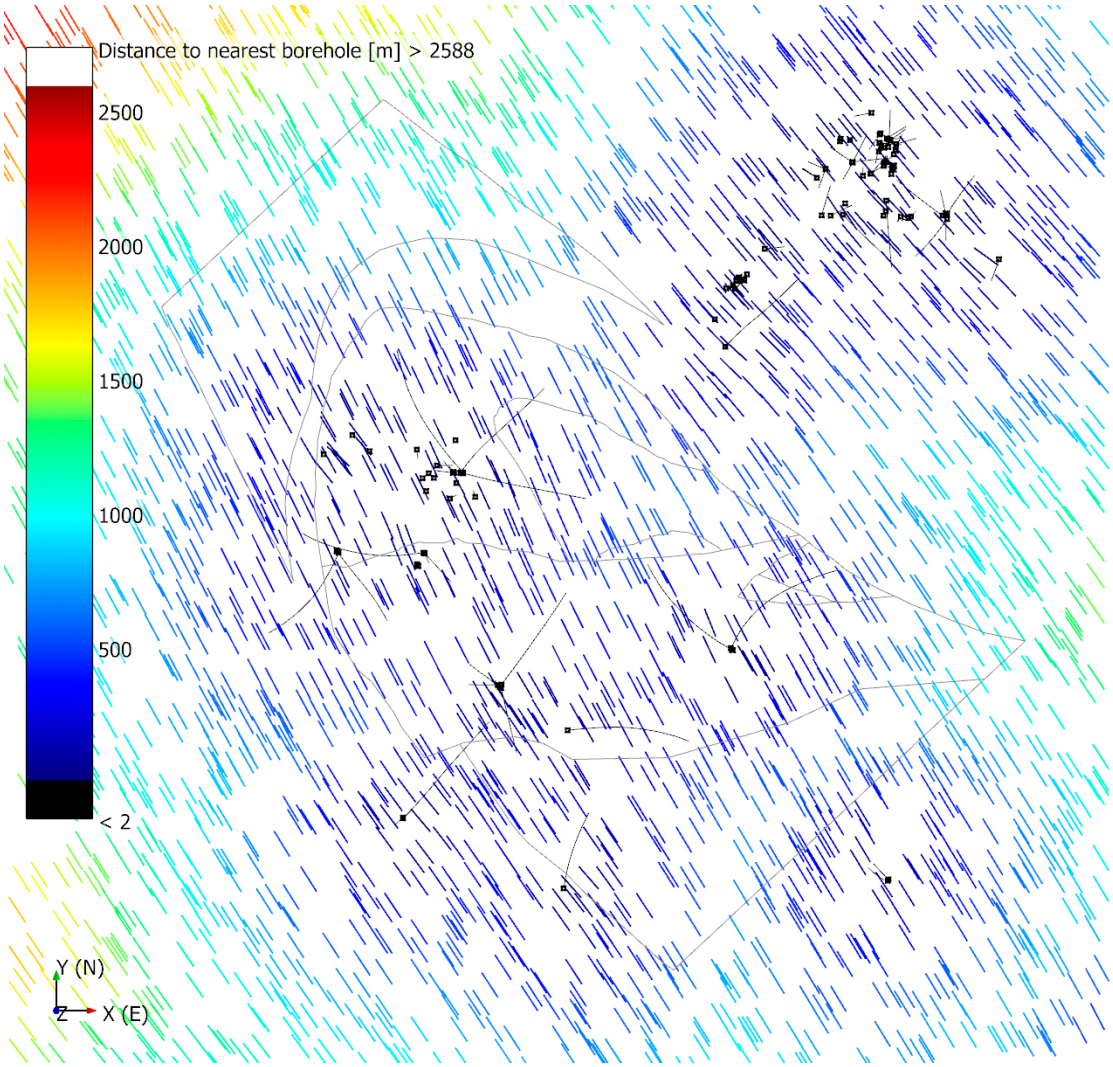

Figure 5-1. *Plan view of the Forsmark area showing mean vectors for fractures logged in KFM and KFR boreholes in the NW set, calculated at elevation −100 m and inverse distance weighted, coloured by their distance to the nearest boreholes. The KFM and KFR boreholes are shown in black, and the intersections of FFM01/02/03/06 and RD034 with a plane at −100 m elevation are shown in grey. The area shown is a square of about 7 km side.*

5.2 Supplementing the DZ model with stochastic modelling

5.2.1 DZ Deformation history and midplane terminations

As indicated in Figure 1-5, the DZ model includes both deterministically and stochastically modelled structures. Stochastic DZ modelling is necessary to both supplement the deterministic model in areas/depths of the regional-scale domain not characterised and to achieve a minimum scale of modelled DZ consistent with the conceptual model, i.e. radius 250 m. In both approaches DZ are ultimately modelled as swarms of fractures surrounding a central plane of the structures termed “midplanes”, even if they are actually sub-planar surfaces for the deterministic DZ. The stochastic midplanes need to both reflect the conceptual model for deformation history in Section 2.2 and how that has manifest in the deterministic DZ model.

It should be noted that the DFN-BF1 model began before finalisation of DMS 2020, and so the spatial analysis of the DZ model used v2.3 (Stephens and Simeonov 2015), with the findings later applied to DMS 2020 when generating the integrated model. However, the differences are very small inside FFM01.

Figure 5-2 illustrates the patterns of terminations interpreted in the DMS 2020 model for the part of the Forsmark lens shown in Figure 2-7 at a mid-depth between the surface and the SFK repository. Many of these larger structures are also seen at the surface as interpreted as linked lineaments (Isaksson and Johansson 2020). From this, NE and SH DZ often terminate on NW DZ, excepting there are some small NW DZ that terminate on NE DZ, which are interpreted as later phase NW reactivation. It is concluded that NW DZ should be grown first, and this will imply also ensure they are generally long structures, as seen in the figure. The termination relationship between NE and SH DZ is uncertain because their strikes are near parallel, reducing the number of intersections between these sets. Based on Section 2.2 it is assumed that SH DZ generally formed last. As will be seen later, results are not highly sensitive to the order between NE and SH sets because of the relatively lower intensities of SH DZ and the acute angle between the sets.

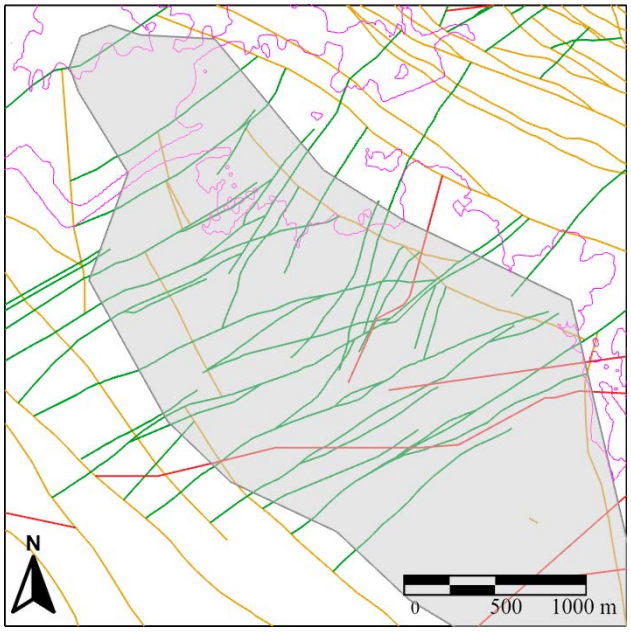

Figure 5-2. *Illustration of interpreted terminations in the DMS 2020 model with deterministic DZ coloured by the associated orientation set, zoomed in on the central area (3.5 km × 3.5 km). This is shown on a slice at an elevation of −250 m. The same colours for sets are used as in the log plots Figure 4-1. Grey area represents SDM-Site investigation area, shoreline is shown in purple.*

5.2.2 Exploration of any evidence for deformation history in the fracture mineral record

A brief exploration was made of whether the mineralogy of fractures within each DZ intersect might offer any further clues as the relative ages of the different DZ sets. Precise interpretations of mineral chronology are difficult because of reactivation with over-printing of earlier mineral assemblages during later reactivation. Also, the minerals which are unique to particular mineral generations in Table 2-1. are relatively sparse – epidote (3 %), prehnite (2 %), laumonite (14 %), hematite (10 %), asphaltite (0.6 %), clay minerals (6 %), iron hydroxide (0.6 %). As an experiment, combinations of other common minerals were combined with these key identifiers in a data query that would make a best guess for most fractures as to which of the four generations in Table 2-1. they belong to:

- Generation 2: (laumonite) or (prehnite) or (hematite);
- Generation 3: (Not G2) and ((analcime) or (asphalt) or (adularia) or (calcite with quartz and/or pyrite));
- Generation 1: (Not G2) and (Not G3) and ((epidote) or (quartz) or (chlorite without clay, calcite or pyrite));
- Generation 4: (Not G2) and (Not G3) and (Not G1) and ((clay) or (chlorite) or (calcite) or (pyrite)).

Having assigned each fracture to a mineral generation the proportions of fractures in each generation within each deterministic DZ as a rough marker as to the degree of mineralisation in each structure during each generation / tectonic phase. The result is shown in Figure 5-3.

This indicates that Generation 1 and 2 minerals are most common in ZFMNW0003, ZFMNW0805 and ZFMNE0870. Generation 4 minerals dominate in the SubH DZ. This provides some confirmation that NW and NE sets were activated during early phases of deformation, while SubH DZ have undergone significant reactivation in the latest phase. Hence, the NW, NE and then SubH order for the genetic growth of the DZ network seems a reasonable working assumption.

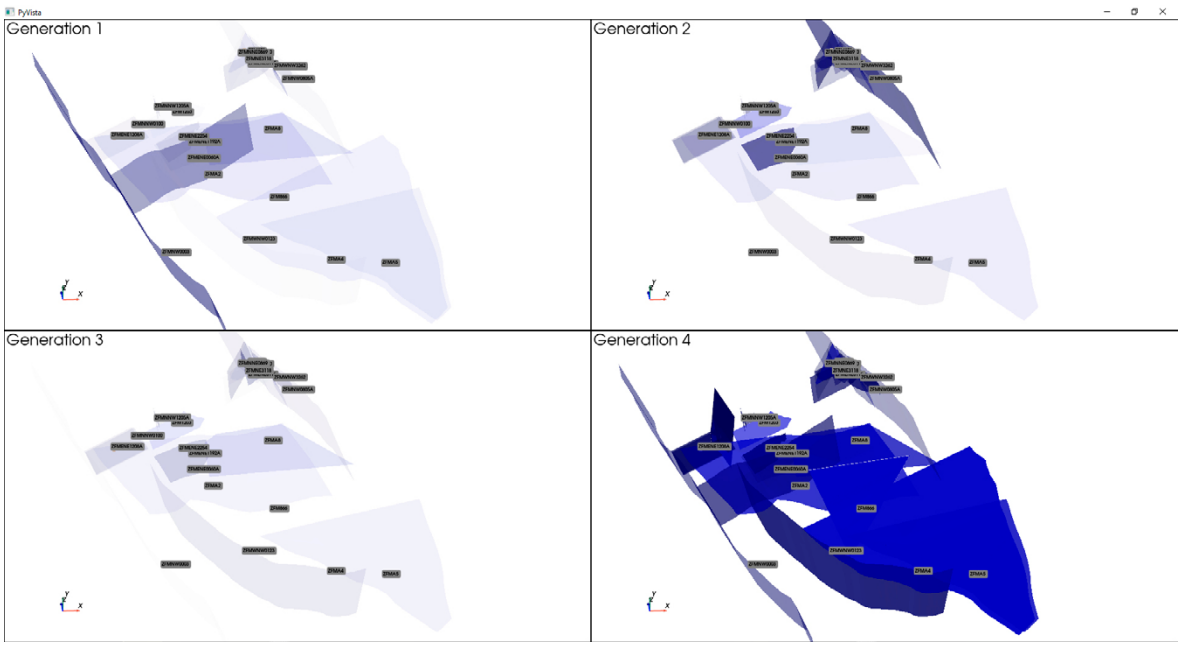

Figure 5-3. *Proportions of each mineral generation within each DZ indicated by the degree of transparency with which it is drawn. The relative ages are: Generation 1 (1.85–1.6 Ga), Generation 2 (1.1–0.9 Ga), Generation 3 (0.5 Ga), Generation 4 (0.002 Ga).*

5.2.3 Stochastic DZ model

The deterministic DZ model only identifies DZ structures to a consistent resolution in the upper part of the central area of the Forsmark lens and SFR area where there has been deep drilling. Outside and beneath this volume, only the largest structures are modelled in the DMS. Hence, the deterministic DZ model does not represent a plausible realisation for all DZ across the whole regional scale due to gaps in and varying degrees of characterisation. Unidentified DZ within the regional scale domain, therefore, need to be realised using stochastic modelling. The goal being creation of one or more plausible realisations of the DZ model at a consistent resolution of structures 20 km > r > 250 m over the whole regional scale domain. A stochastic DZ (i.e. midplane geometries) model description, including the spatial, orientation, scaling and termination properties, is, therefore, needed. The deterministic DZ model (DMS) provides the basis for characterising each of the geometric properties in a statistical sense that can then be used to produce stochastic DZ realisations that mimic key characteristics of the deterministic model, essentially extrapolating its form into uncharacterised volumes. Deterministic DZ model DMS 2020 and the central area of detailed characterisation (3.5 km × 3.5 km**)** are shown in Figure 5-4.

Consistency between the deterministic and stochastic DZ models in terms of intensity and orientation are ensured through the former providing direct input parameters to the latter. Intensity is input as a target for the fracture generation process, and so met by construction. The set of orientations of deterministic DZs is used as the original bootstrap sample, and so is natural matched in the generation process. Consistency in size distribution and terminations are achieved through calibration of these in the stochastic DZ model against the deterministic model, adjusting the parameters used in the G-DFN algorithm, as described in the following subsections.

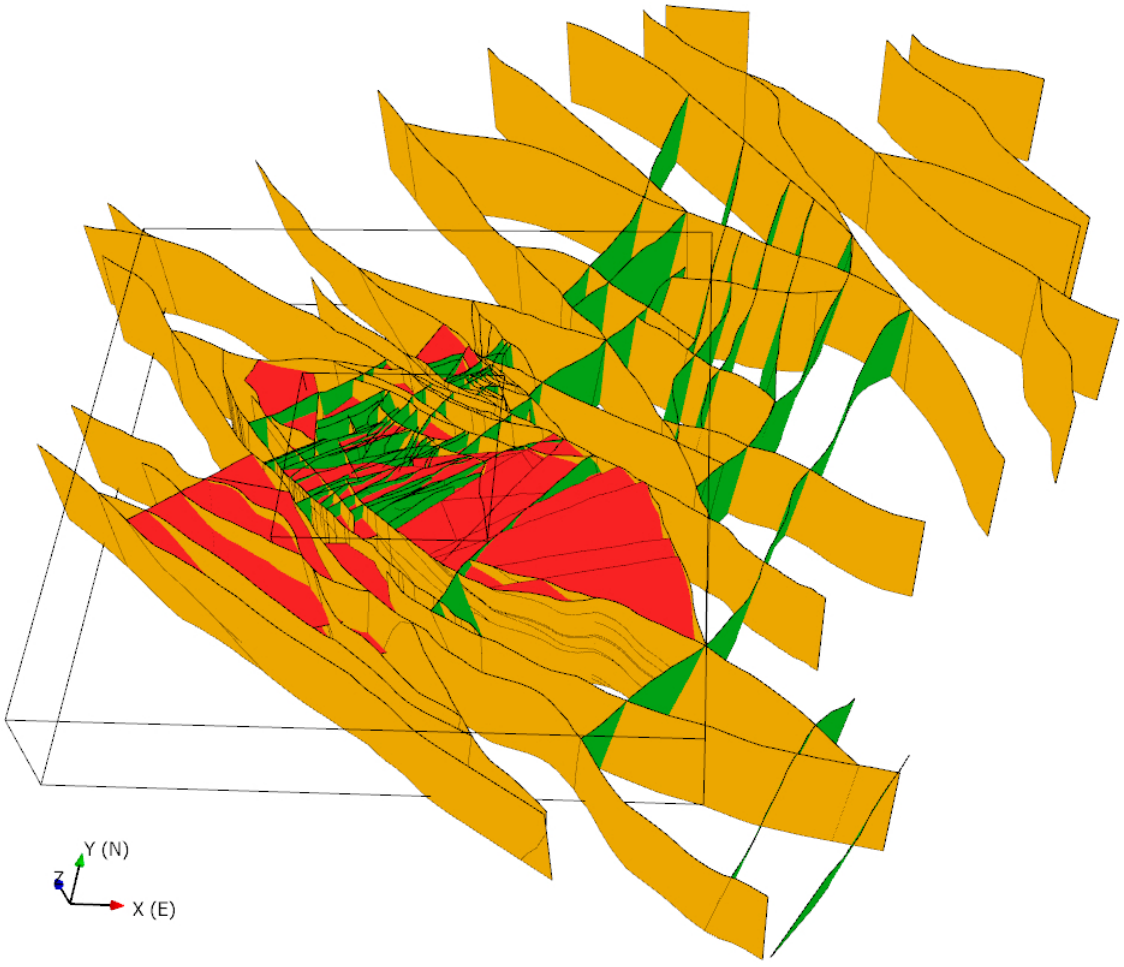

Figure 5-4. *DMS 2020 coloured by set (as in the Figure 4-1. legend) with the inner cube showing the central area (3.5 km × 3.5 km).*

The general approach is to use the highly determined DZ model in the central area of drilling investigations as a "training image" for describing and calibrating a complete DZ spatial, orientation, scaling and termination model, and then use this to grow stochastic DZ around and between the deterministic DZ model. There are in fact three components to the combined deterministic and stochastic DZ model:

- The deterministic DZ model (ZFM) reported as DMS 2020 model;
- A semi-stochastic model of a few (~30) smaller structures where DZ intercepts have been interpreted in the SHI, but there is insufficient information to turn these into DZs in the DMS 2020 model. These are generated here to intersect the known location and orientation, but with their centres and sizes sampled consistently with the stochastic DZ size model. These are conditioned structures within the stochastic DZ model that intersect boreholes at specific locations; and
- Fully stochastic DZ that are conditioned such that none are allowed to intersect the boreholes.

The semi-stochastic DZ are a minor component here, only ~30 structures, but the partial characterisation of smaller DZ has long been an issue recognised in the deterministic modelling, where they have been termed possible deformation zones (PDZ), see (Stephens et al. 2008b; Hermanson and Pettersson 2022), for example. Once underground characterisation begins it is likely further smaller DZ will be encountered and progressively characterised, and hence refinements of the model and conditioning of specific mapped DZ is likely to become an increasingly relevant part of the methodology. The last bullet above recognises the challenge of growing the stochastic DZ up to the deterministic DZ so that they abut and connect in a conceptually consistent way but avoid double counting structures within the well characterised volumes. The techniques used to achieve this are described in Subsection 5.2.5.

Deriving a stochastic DZ model that reproduces key characteristics (intensity, orientations, size distribution and terminations) of the deterministic DZ model using a G-DFN is an iterative process. Analysis of the deterministic DZ model provides initial guesses for the size scaling and termination probabilities for each set. The intensities of the deterministic DZ, quantified as set-wise P_{21} on slices through the deterministic DZ at ground surface and a mid-depth of −250 m, are used as target intensities for the stochastic DZ model. The orientations of the deterministic DZ are used directly for bootstrapping the orientations of the stochastic DZ. The parameters derived on this basis for the stochastic DZ model are presented in Subsection 5.2.4.

An estimated prior size scaling of deterministic DZ (before termination) is then tuned alongside the termination probabilities with the objective to achieve a balance in matching the visual pattern of DZ (Figure 5-5), size scaling (Figure 5-6) and connectivity topology (Figure 5-7). These figures illustrate the metrics and outcome achieved in calibrating the stochastic DZ model parameters to key characteristic of the manually interpreted deterministic DZ model. For the central area (and depth) shown in Figure 5-5 it is reasonable to assume that most DZ have been identified, such that the numbers of stochastic and deterministic DZs of length > 1 000 m are similar, as demonstrated in Figure 5-6. Matching the connectivity topology tends push the probability of terminations higher to have more Y than X nodes, but that pushes the size distribution towards fewer long fractures, and hence one iterates towards optimal termination probabilities that balance a reasonable approximation of both size and connectivity topology.

Below −1 000 m the stochastic model generates far more small DZ than can be interpreted deterministically. In Figure 5-7, connectivity topology counts the numbers of node types of each fracture trace end or intersection – X is a crossing of two fractures, Y is a termination of one fracture against another, V are rare double terminations, I is a free-end. The method is described in Subsection 6.6.6 in (Selroos et al. 2022). Here, the traces are created by taking a slice through the models at −250 m. The ternary plot shows the proportions of each of these three end types as a quantitative characteristic for the pattern of network connectivity.

There are several issues to be taken into account when choosing an acceptable match:

- There are some shorter NW DZ that terminate on NE DZ, likely formed in a reactivation phase. In the model, the size scaling model is shifted towards having more smaller fractures to get a good match on the size comparison (Figure 5-6), but then the numbers of larger NW DZ are slightly under-predicted. This is a consequence of just having one phase of NW DZ generation for simplicity.

- There is a residual uncertainty whether there remain additional DZ of scale 1 000 m or more within the central used for calibration. It is a working assumption that the majority of this scale have been identified and so the intensities used for stochastic DZ modelling are of a representative magnitude.
- The deterministic deformation zone model was constructed to intentionally promote Y node intersections between deformation zones where possible (Hermanson and Petersson 2020), rather leaving a hanging node/edge at some arbitrary location (that would be an I node). The G-DFN algorithm stops growing a stochastic DZ if it either reaches its target size or if it terminates along the prescribed fraction (70 %) fraction of its circumference. (Its target size is sampled from the prior power-law size distribution). Hence, the model simulates the connectivity topology given the specified intensity, initial size distribution and termination probability, allowing calibration of these parameters against the topology of the interpreted deterministic model.

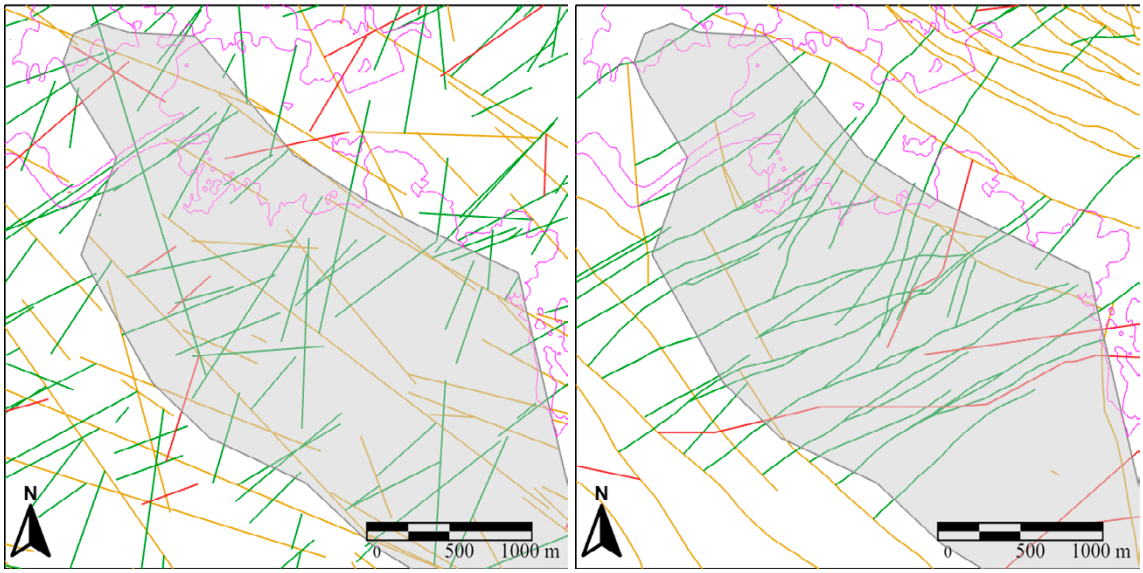

Figure 5-5. *Comparison of a realisation of the unconditioned stochastic DZ model (top) vs. deterministic DZ model (bottom) for central area (3.5 km × 3.5 km) and slice at an elevation of −250 m (NW-yellow, NE-green, SH-red). The grey area represents SDM-Site investigation area, shoreline is shown in purple.*

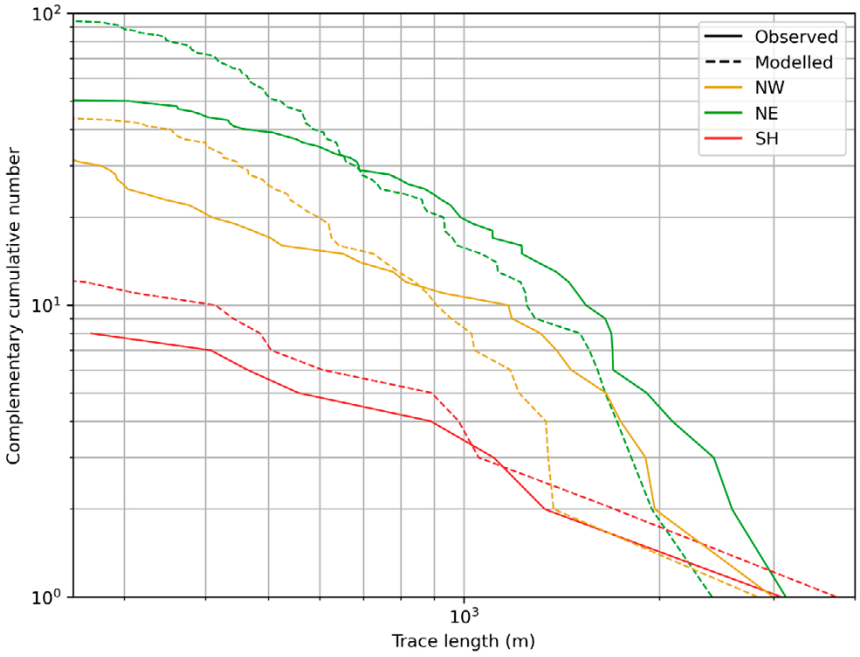

Figure 5-6. *Stochastic (dashed) vs. deterministic (solid) DZ size scaling for central zone.*

The authors consider the agreement across the metrics shown in Figure 5-5 through Figure 5-7 are a good overall balance. Given the uncertainties above, the termination probabilities can only be determined to about ± 10 % of the calibrated value.

An example of a realisation of a pure stochastic model (without integration with the deterministic DZ and semi-stochastic DZ) in a larger 10.5 km × 10.5 km area is shown in Figure 5-8 in 3D for a 2 km thick slab and in Figure 5-9 as a trace map. To prevent the G-DFN midplanes from extending outside the model domain, all midplanes were set to terminate against the bounding box of the fracture generation region, and so the larger stochastic DZ are bevel edged rectangles, while shorter stochastic DZ and more circular in shape unless terminated. The G-DFN algorithm (Libby et al. 2019) requires some numerical parameters to control shape, growth and arrests. Unless otherwise stated, the G-DFN parameters shown in Table 5-1 were applied to all DZ midplane and fracture sets.

The generation timesteps is the number of steps over which fractures are nucleated and grow for each set. Growth timesteps are how many steps it takes for each fracture to reach its target size. Maximum ray arrests determines the fraction of a fracture's circumference needs to terminate before its growth arrests. The number of sides controls the number of rays/sides of a fracture shape, and shadow zone size is an exclusion zone for fracture nucleation around a fracture. Examples of the effects these parameters have on network patterns and connectivity are given and explained in (Libby et al. 2019; Libby et al. 2024).

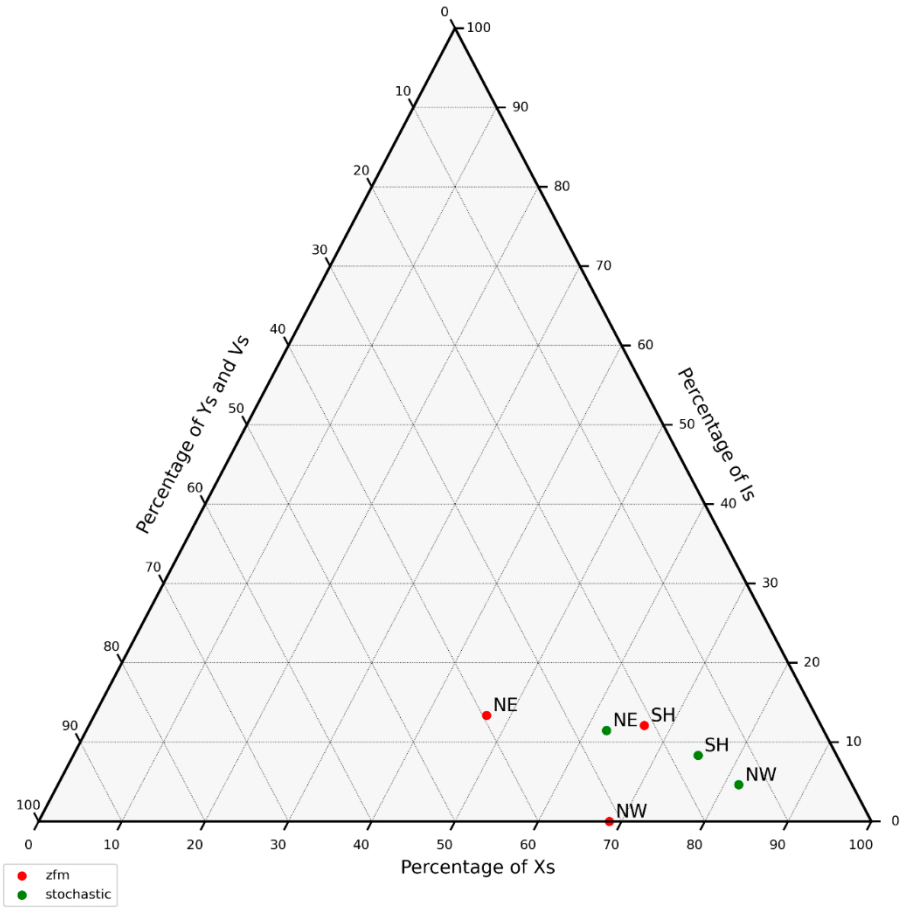

Figure 5-7. *Stochastic (green) vs. deterministic (red) DZ connectivity topology for DZ traces on a slice at −250 m through the central area. See Subsection 5.4.4 for more information on use of termination data. The 3 axes measure the % of each node type (I = free end, X = complete crossing, Y/V = singly or doubly terminated intersect) along traces.*

Table 5-1. G-DFN Parameters common to all generated fracture sets unless otherwise stated.

Generation timesteps	100
Growth timesteps	10
Maximum ray arrests	70 %
Number of sides	20
Shadow zone size	0

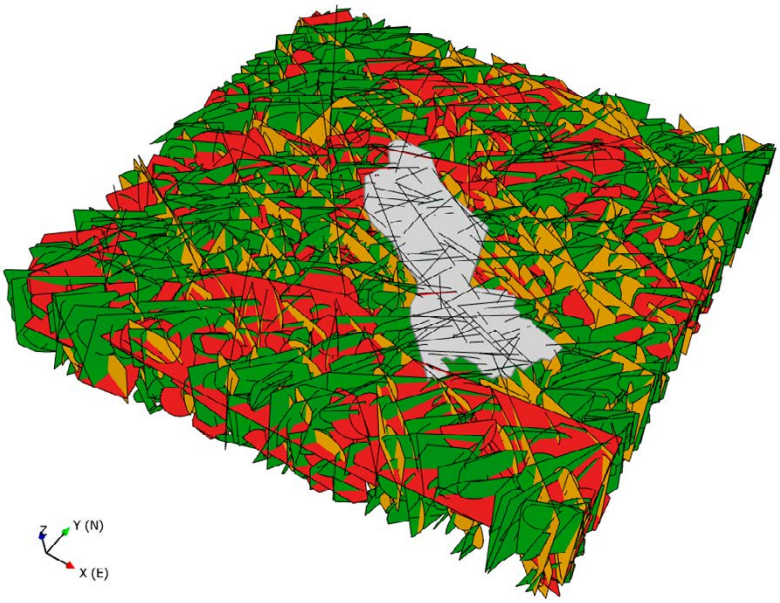

Figure 5-8. *A 3D view of the same realisation of the unconditioned stochastic DZ model (NW-yellow, NE-green, SH-red) shown in the top of Figure 5-9. using the larger volume (10.5 km × 10.5 km × 2 km). Grey area represents SDM-Site investigation area.*

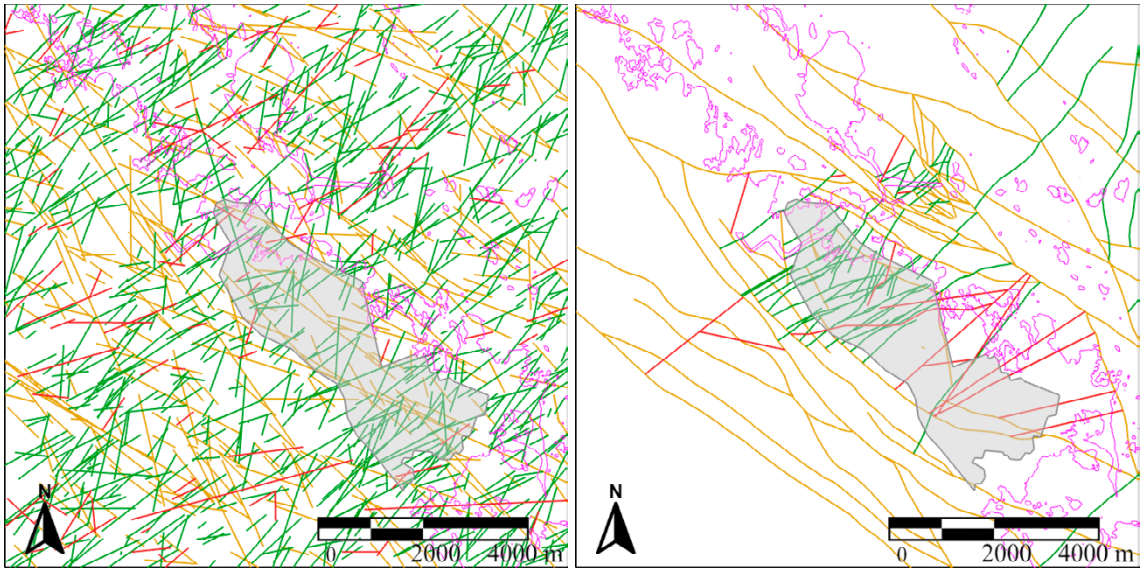

Figure 5-9. *Unconditioned stochastic (left) vs. deterministic (right) DZ models for the larger area (10.5 km × 10.5 km) and slice at an elevation of −250 m (NW-yellow, NE-green, SH-red). Grey area represents SDM-Site investigation area, shoreline is shown in purple.*

5.2.4 Stochastic DZ parameters

The parameters used in the stochastic DZ model are presented in Table 5-2.

Table 5-2. Parameters for the stochastic DZ model created as a G-DFN.

	NW	NE	SH
Target P_{32} ($r_{max} > r > r_0$) [m^2/m^3]	0.00318	0.00586	0.0013965
Input k_r for the prior model	2.01	2.01	2.2
Termination probability on intersect with larger fractures	Self: 0.27	Self: 0.27 NW: 0.53	Self: 0.06 NE: 0.11 NW 0.22
Orientation	Bootstrapped from deterministic structures using random sampling of each triangle in the sample surfaces weighted by the triangle size.		
Fisher κ	100 (to give a small amount of scatter from the bootstrapped value).		
r_{min}	r_0		
r_{max}	20 000 m		
r_0	250 m		
Generation timesteps	300		
Growth timesteps	30		
Number of rays	20		
Maximum ray arrests	90 %		

5.2.5 Conditioning the stochastic DZ model

To integrate the deterministic, stochastic and semi-stochastic DZs it is necessary to grow a conditioned stochastic DZ model around the deterministic DZ model with constraints along the boreholes. The integrated approach is to grow the stochastic DZ set-wise (NW, NE and then SH sets):

- Import the deterministic DZ for the relevant set;
- Grow the stochastic DZ with positive constraints at the semi-stochastic DZ intersects with boreholes from which semi-stochastic are grown, and negative constraints such that unconditioned stochastic DZ cannot intersect a logged borehole (otherwise it would be a deterministic DZ or PDZ); and
- Repeat for each set.

The method used for conditioning networks is described in (Bym and Hartley 2023).

The locations and orientations of semi-stochastic DZ, are shown in Figure 5-10. These are positive constraints (i.e. places where DZ are known to exist) on the stochastic DZ. The rest of the borehole intervals are negative constraints (i.e. places where it is known DZ/PDZ do not exist). These negative constraints together with the probabilistic termination of stochastic DZ on pre-existing deterministic DZ prevent most stochastic DZ that are seeded outside the central area growing into it. When a stochastic DZ grows to meet a deterministic DZ it probabilistically terminates or else continues, either way ensuring connectivity between deterministic and stochastic DZ. Because of the high intensity of deterministic DZ in the central area, most stochastic DZ terminate before growing into that region, and hence avoids double counting of DZ intensity. These processes should provide statistical homogeneity across the model domain and prevent any obvious joins, gaps or double counting. Figure 5-11 and Figure 5-12 provide an illustration of the interfacing between stochastic and deterministic DZ with the semi-stochastic DZ. The map view used here naturally biases the visual impact of the SH set, whereas earlier horizontal trace maps bias the impact of the NW and NE sets. A horizontal slice through the combined network of midplanes is shown in Figure 5-13. This is intended as a viable “complete” network of identified and unidentified structures with $r > 250$ m. This methodology can be extended to the full regional scale area, as required.

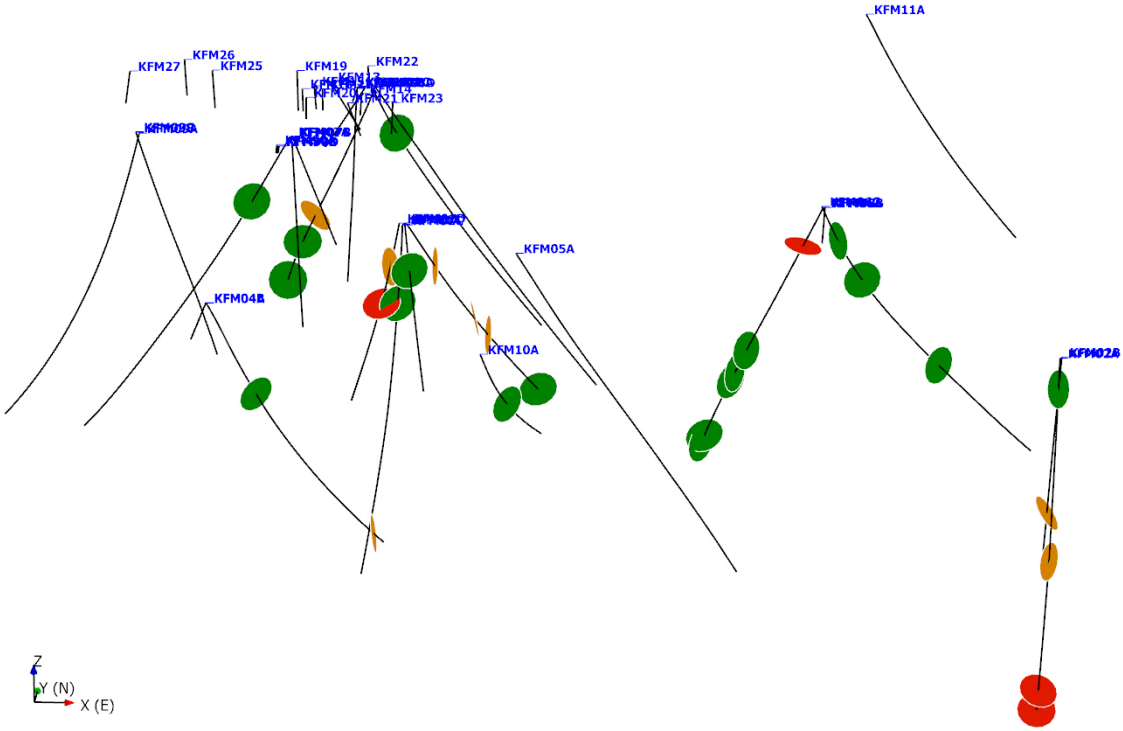

Figure 5-10. *Locations and orientations of SHI of semi-stochastic DZ in boreholes displayed as discs coloured by set.*

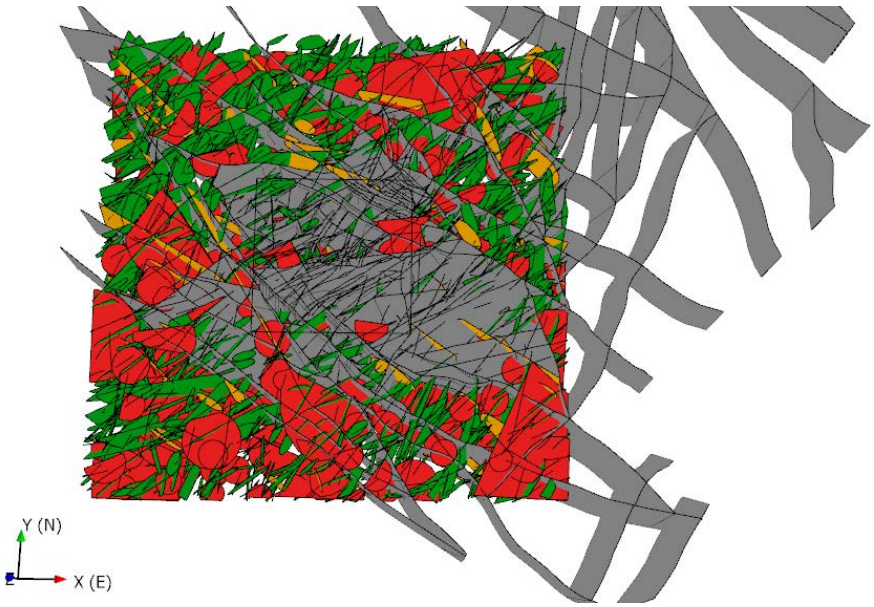

Figure 5-11. *Example of combined conditioned stochastic DZ model (coloured by set) with deterministic DZ coloured grey showing the whole model over a (10.5 km × 10.5 km) area.*

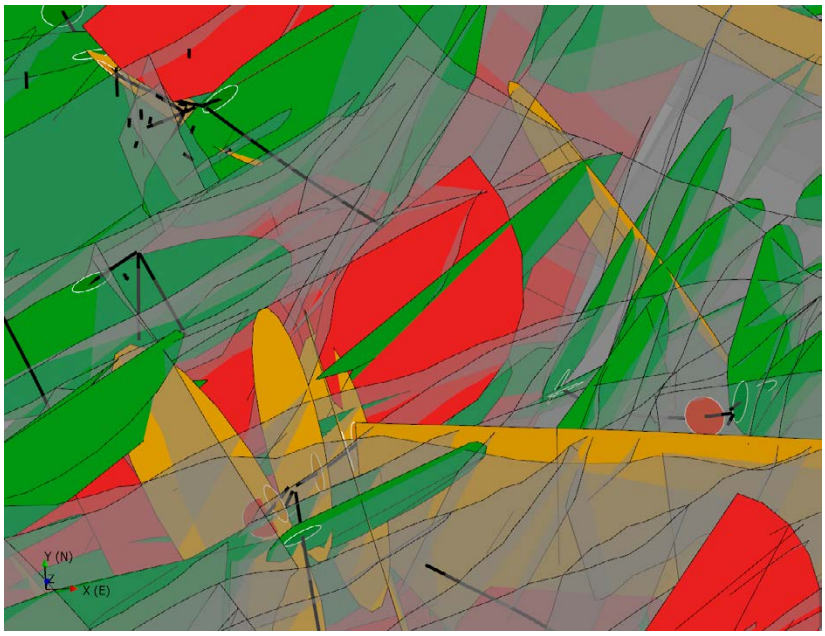

Figure 5-12. *Example of combined conditioned stochastic DZ model (coloured by set) with deterministic DZ coloured grey zooming in on a facility-scale area to show detail of the deterministic/stochastic interface and semi-stochastic DZ through semi-stochastic DZ. Data driving the semi-stochastic DZ generation is shown as discs (coloured by set).*

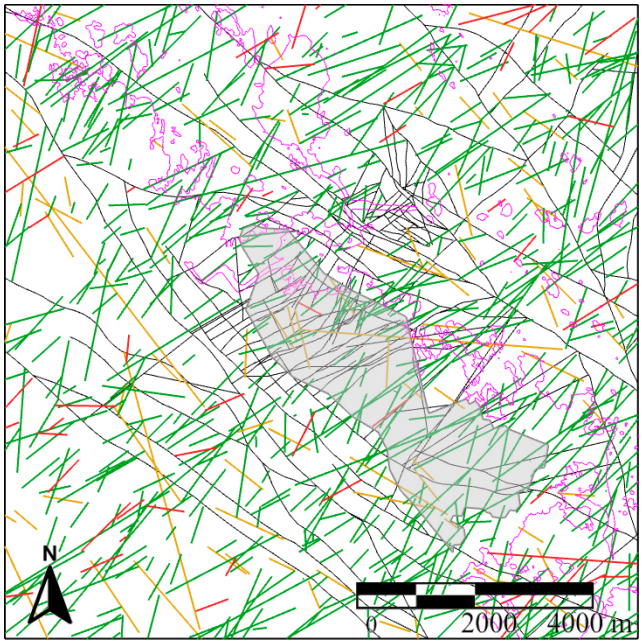

Figure 5-13. *Example of combined conditioned stochastic DZ model (NW-yellow, NE-green, SH-red) with deterministic DZ coloured grey on at a slice at −250 m, showing the continuity and connectivity of the combined midplane network. Grey area represents SDM-Site investigation area, shoreline is shown in purple.*

5.3 DZ-related single fractures

DZ-related fractures are the individual fractures that form the damage zone or splays associated to each DZ. As a working assumption they are modelled in the size range $0.038 < r < 150$ m. In terms of the data, they correspond with the fractures logged within the DZ intervals from the SHI of each borehole/DZ intersect. Statistical analysis of the properties of these fractures provides the basis for parameterising the DZ (both deterministic and stochastic). The properties of the DZ-related fracture characterised include:

- Thickness of the zones;
- Total intensity of the fractures within the zones and how that is distributed across the zone;
- The orientation of fractures within the zone; and
- The prior fracture size scaling model and termination probabilities.

The analysis and conceptualisation of these is described in the following subsections.

5.3.1 Thickness-length correlation

It is possible to interpret a correlation between the modelled thicknesses and trace lengths of the deterministic DZ structures, or alternatively use the SHI intervals directly for the thickness of the structures. The lower plot in Figure 5-14 considers the modelled thicknesses, which accounts for the true thickness of zones rather than apparent thickness due to angle of incidence. It also averages variability in thickness across individual zones. The thickness of damage zones on average has been documented to scale linearly with length (Scholz et al. 1993), however, the coefficient of proportionality of this scaling can be as high as 0.1 or as low as 0.001. This is dependent on the mechanical properties of the host rock and the stress configuration causing different modes of deformation (if there are clear markers of displacement on faults, these can be factored as well, but this is generally not the case at Forsmark). Here, the data appears to fall inside this envelope, with 0.01 offering a good fit to the data overall. There are a few DZ that only appear to have a narrow core zone with coefficient about 0.001, and some small DZ with a coefficient about 0.05. The theoretical basis for the scaling model given by (Scholz et al. 1993) would indicate that the low coefficients occur for faults with relatively large fracture energy and a large reduction from yield strength to residual strength of the fault, while high coefficients correspond to lower fracture energy and smaller changes in fault strength. The upper plot in Figure 5-14 indicates the variability in thickness between different intersects, suggesting that the damage zone does not develop uniformly over the whole area of a DZ, with a 0.01 scaling coefficient providing a reasonable median trend.

An alternative way to interpret a zone thickness scaling model is to fit power-law scaling models separately to the distributions of DZ size and SHI interval thickness, assuming a correlation between thicknesses and length of structures so that these two distributions can be combined. This technique does not require the SHI thicknesses to be linked to DZ length directly, allowing different datasets to be combined. It does, however, assume that the two types of measurements come from the same structures, or range of scales of structures. In essence, it is equivalent to ordering all the data for the widths and all the data for the lengths, fitting trend lines, and assuming the shortest length corresponds to the smallest width, etc.

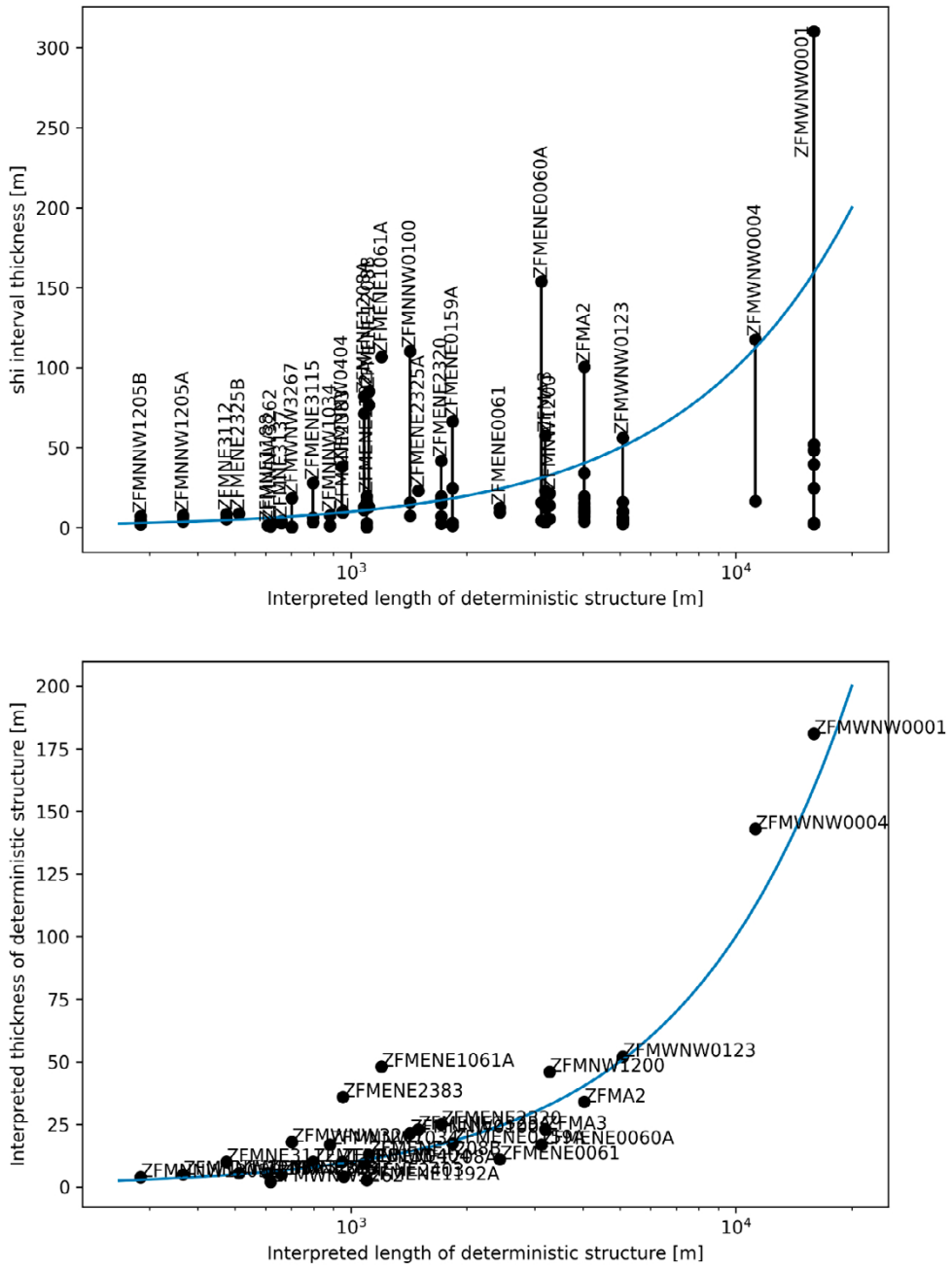

Figure 5-14. *Graphs showing the SHI interval thicknesses (true thickness calculated from the orientation of the DZ surface at each thickness) plotted against the trace length of the deterministic structures, and the interpreted thickness of the deterministic DZs plotted against their horizontal length. The blue lines show length × 0.01.*

This analysis is illustrated in Figure 5-15 to show: A) a histogram of the SHI interval thicknesses with a best fit line, B) a histogram of the DZ lengths with the counts normalised to match with a best fit line, and C) the line plot that results if you equate the best fit line from A) with that from B). The best fit lines are fitted to larger structures based on the assumption that the smaller structures are likely to be progressively under sampled due to their small size. This yields a best fit close to linear scaling with a coefficient of 0.01.

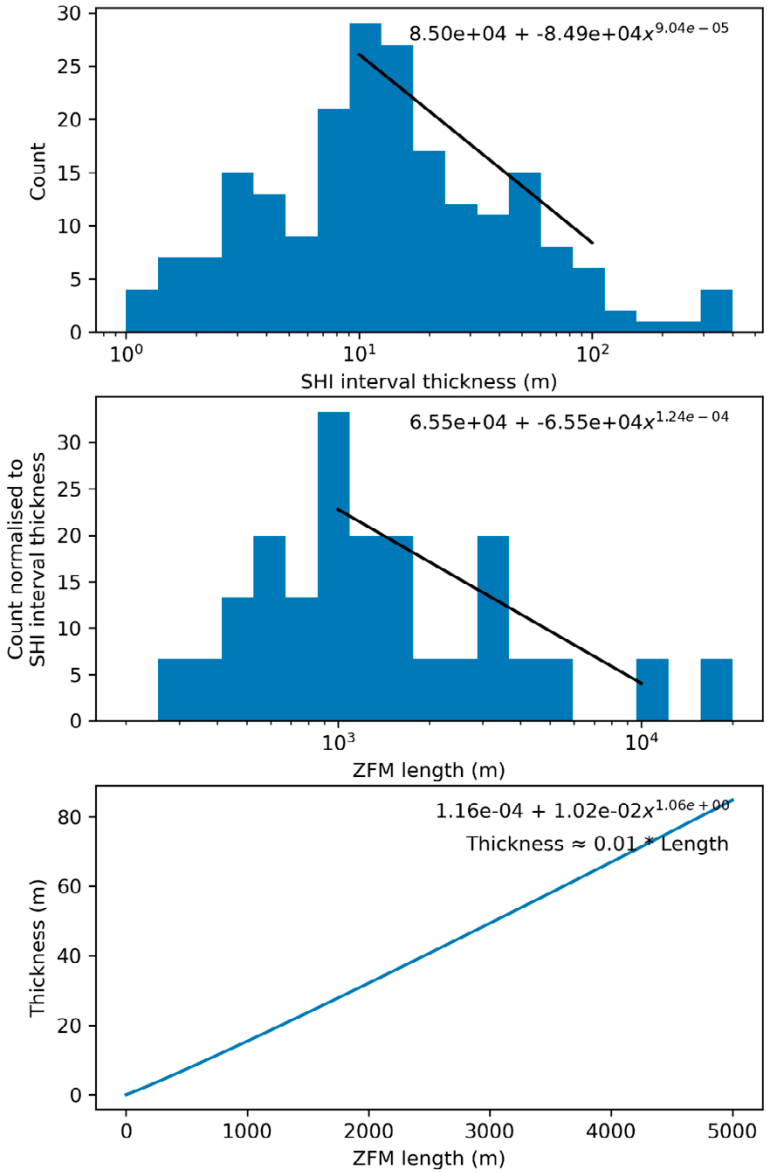

Figure 5-15. *Histograms and line plots describing how a thickness vs. length relationship may be derived from noisy data by assuming a correlation between the two properties.*

The width of DZ is assumed to be symmetric about the midplane with the same width in the hanging wall and footwall because there is considerable noise in the distribution for fracturing across DZ, see Figure 5-16.

5.3.2 Internal fracture intensity distribution of DZ

Having selected a model for the thickness of DZ, the next conceptual question is how DZ-related fractures are distributed spatially across a zone. Observations given in the literature agree on a decay of fracture intensity with distance from fault surfaces, but vary from rapid exponential decay, e.g., (Faulkner et al. 2011), to gentler logarithmic behaviour, e.g., (Vermilye and Scholz 1998). Figure 5-16 shows the distribution of fracture intensity across the DZ SHI intervals and the adjacent sections of boreholes at Forsmark.

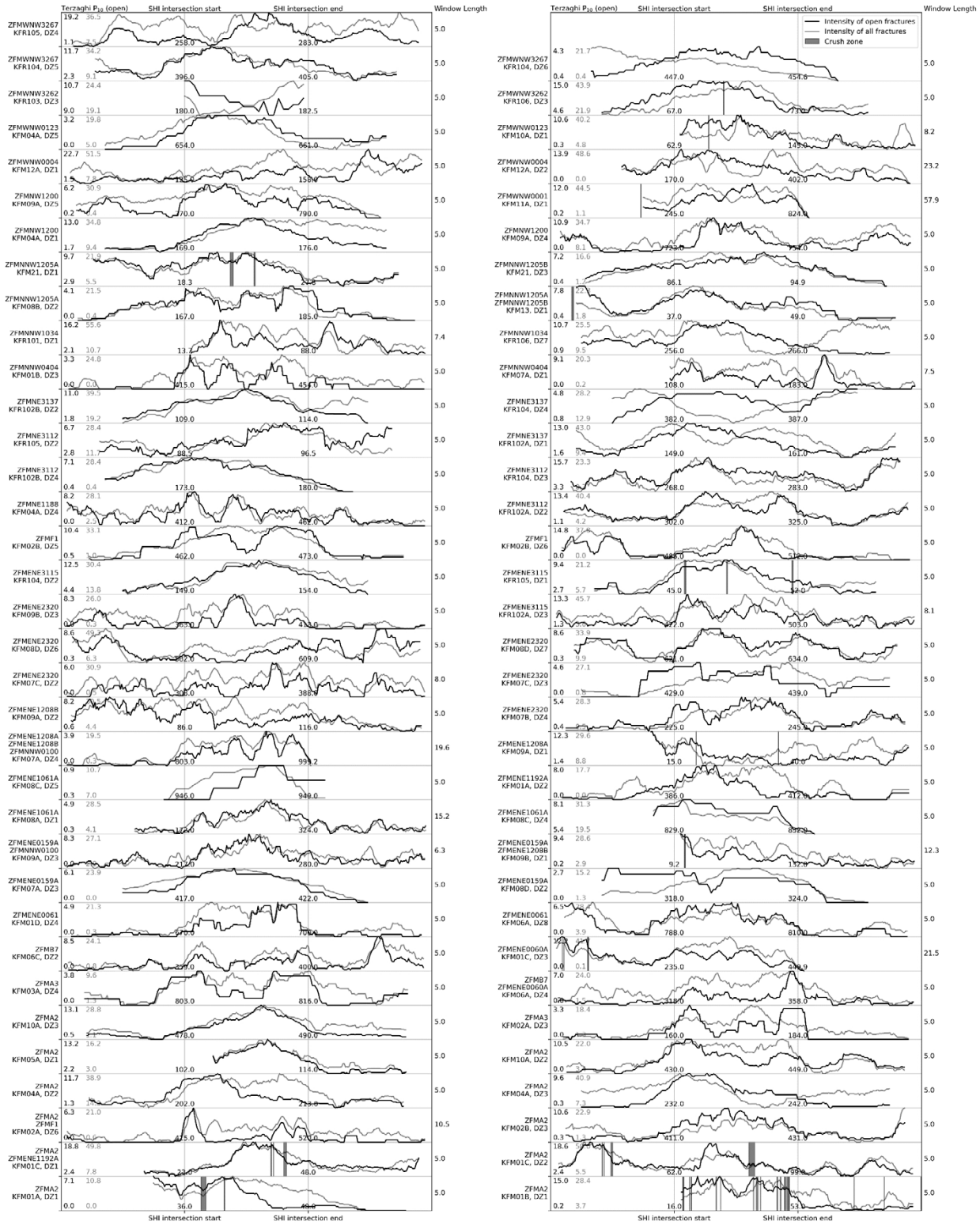

Figure 5-16. *Graphs showing the P_{10} intensity distribution, calculated in subintervals ('windows') of the size given to the right of the graphs, across the SHI intervals for open fractures (black lines) and both open and closed fractures (grey lines). The DZ, borehole and interval each graph is valid for is shown on the left of each graph. The x axis of each graph represents depth down the borehole with length scaled so that the start and end of the SHI interval is aligned with the other graphs, to aid visual comparison of the shape. The start and the end depth of each interval is labelled on the vertical lines adjacent to each graph. The y axis of each graph represents the P_{10} intensity, and is also scaled to the maximum and minimum values shown at the left of each graph to allow comparison of the shapes of distribution of all and open fractures.*

A wide range of variation may be observed in the trends of the intensity profiles:

- Distinct increases in intensity at the limits of the SHI interval (e.g., KFM07, DZ3);
- Higher intensity towards the centre of the SHI interval (e.g., KFM10A, DZ3);
- Symmetrical increases in intensity (e.g., KFR102B, DZ2);
- Asymmetrical increases in intensity (e.g., KFM04A, DZ3);
- Consistent changes in intensity (e.g., KFM09A, DZ3); and
- Irregular changes in intensity (e.g., KFM07C DZ2).

In most cases the shape of the open fracture distribution mimics that of all fractures, i.e. the open fractures are a subset of all fractures. There are several examples where open fractures are distributed in narrower bands within the overall DZ, e.g., KFM01D, DZ4 and KFM02A, DZ6. Open fractures are typically about one third of all fractures, but this varies, primarily with depth as is seen in Section 7.1. For modelling purposes it assumed that open fractures are a subset of all fractures within DZ. The fraction of open fractures varies by depth and whether inside/outside the Forsmark lens. Hence, there is not yet a well-developed conceptual model for which fractures open/closed beyond some statistical associations with depth and structure/orientation. It can be recognised that some zones may have open fracturing more concentrated in thinner bands.

To assess what type of spatial distribution of fractures around a DZ midplane best describes the trends observed at Forsmark, the Beta Distribution (Hazewinkel 2013) is selected as it can mimic a range of possible distributions in intensity across the DZ. Its probability density function has the form:

$$f(x;\alpha,\beta) = \frac{x^{\alpha-1}(1-x)^{\beta-1}}{B(\alpha,\beta)} \qquad \text{Equation 5-1}$$

$$B(\alpha,\beta) = \frac{\Gamma(\alpha)\Gamma(\beta)}{\Gamma(\alpha+\beta)} \qquad \text{Equation 5-2}$$

and Γ is the Gamma function. It can yield a variety of decay shapes. The Beta Distribution is a continuous probability distribution defined on the interval [0, 1]. It has two shape parameters, α and β, for modifying the shape and behaviour of the distribution. $\alpha > \beta$ skews the shape to the right, $\alpha < \beta$ skews to the left, and $\alpha = \beta$ gives a symmetric shape, as in the case of Figure 5-17. Increasing α (= β) makes the shape more modal from uniform (1, 1) to bell curves (5, 5). This makes it suitable for modelling the range of intensity distribution shapes observed in the DZs.

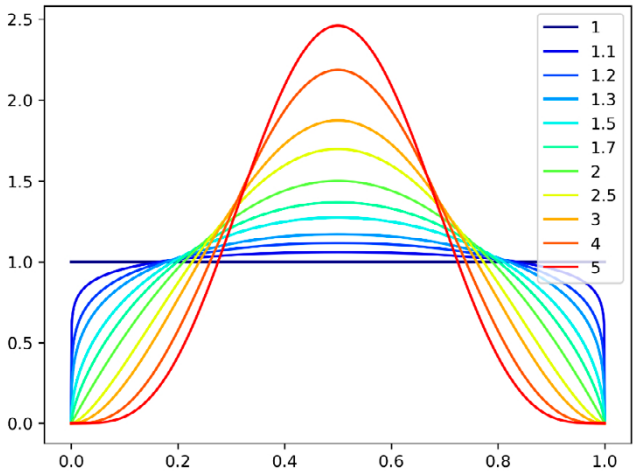

Figure 5-17. *Graph showing how the curve of the Beta distribution varies from a flat line when the alpha and beta parameters are 1 to a bell curve when the alpha and beta parameters are 5.*

Figure 5-18 identifies a best-fit beta distribution for each DZ where α and β are equal and allowed to be in the range 1 to 5. It may be observed that some structures exhibit a convex up-shape, whilst others exhibit a bell curve. Individual fits range from 1 to 5, but values around 2 (a mound) are most frequent. The fitting of these profiles along a depth axis assumes that the borehole path is straight, and the damage zone is planar. Potential asymmetry across the DZ intervals and whether could be associated to different types shear zone has not been investigated at this stage. The modal value for the best fit $\alpha = \beta$ parameters is 2.5 (Figure 5-19). Filtering the subset of the fractures to which a beta distribution is fitted by intensity did not significantly modify the distribution of the best-fit parameters (Figure 5-19). For simplicity, the same $\alpha = \beta = 2.5$ was used in the modelling for all DZ, deterministic or stochastic, large or small.

5.3.3 Internal fracture intensity of deterministic DZ

Having established a spatial model for the distribution of DZ-related constrained to borehole data, the next step is to determine the intensity of fractures in this distribution. This requires the differentiation of fractures associated with the DZ from those associated with background fracturing. From both a conceptual and modelling point of view, the intensity of fracturing within intervals corresponding to DZ represents both the background fracturing and the over-print of the DZ-related fracturing. Hence, to calculate the intensity of the DZ-related fracturing, the intensity of the background component must be estimated and subtracted from the total.

Four methods were considered for deconvolving the DZ-related fractures from background fractures:

1. Calculating the intensity adjacent to the DZ intervals and subtracting it from the intensity in the DZ intervals;
2. Identifying the subset of fractures coplanar with the DZ surface geometries and using the intensity of those as the DZ-related;
3. Using FracMan's set identification tool to isolate fractures that are coplanar with the DZ surface geometries at the point of intersection, whilst taking into account the presence of other clusters of fractures that may be present; and
4. Calculating the total intensity inside DZ regions and outside DZ regions and finding the difference.

The first three methods achieved limited success and are described in Appendix A2.

The last method is conceptually simpler and does not rely on the assumption that the majority of fractures in the DZ-related swarms are coplanar with the DZ structure. Thus, it was deemed a more robust method and was intrinsically compatible with the intensities for the background fractures.

5.3.4 Size distribution of DZ-related fractures

There is limited information available regarding the size distribution of the DZ-related fractures on the surface. There are some rock exposures near ZFMENE0060 as seen on Stop1 of the excursion guide (Stephens 2010) that exemplify intense sub-parallel fracturing on the scale of several metres with both crossing and terminating fractures. Outcrop AFM001098 is close to a NW DZ giving some trace data for DZ with this orientation. There are several trench outcrops (AFM001243, AFM001265 and AFM001244) orthogonal to NE–ENE zones. They are narrow and so don't record the full lengths of most fracture seen. The size-scaling analysis of SDM-Site DFN modelling (Fox et al. 2007), therefore, did consider some DZ affected areas. That study interpreted power-law scaling exponents, k_r, for outcrop scale fractures (10s m at most) of ~2.6 for NE and SubH sets and ~2.4 for NW fractures, see Table 4-40 of (Fox et al. 2007). $k_r = 2.6$ was used here.

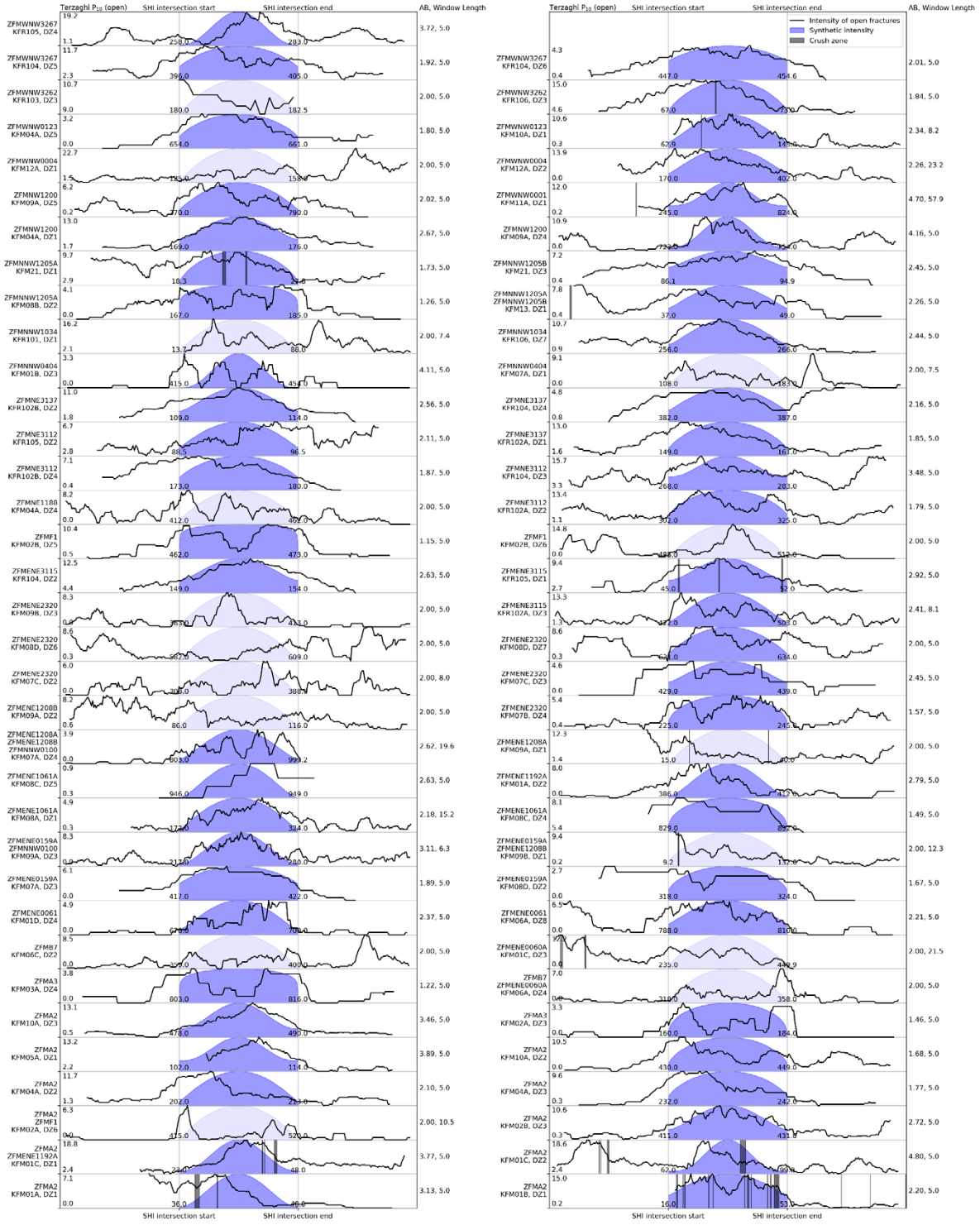

Figure 5-18. *Graphs showing the P_{10} intensity distribution of open fractures, calculated in subintervals ('windows') of the size given to the right of the graphs, across the SHI intervals (black lines), superimposed with best-fit beta distribution profiles (blue). The light blue profiles are intervals with invalid beta distribution fits. The DZ, borehole and interval each graph is valid for is shown on the left of each graph. The x axis of each graph represents depth down the borehole normalised so that the start and end of the SHI interval is aligned with the other graphs, to aid visual comparison of the different scales. The start and the end depth of each interval is labelled on the vertical lines adjacent to each graph. The y axis of each graph represents the P_{10} intensity, normalised to the maximum and minimum values shown at the left of each graph.*

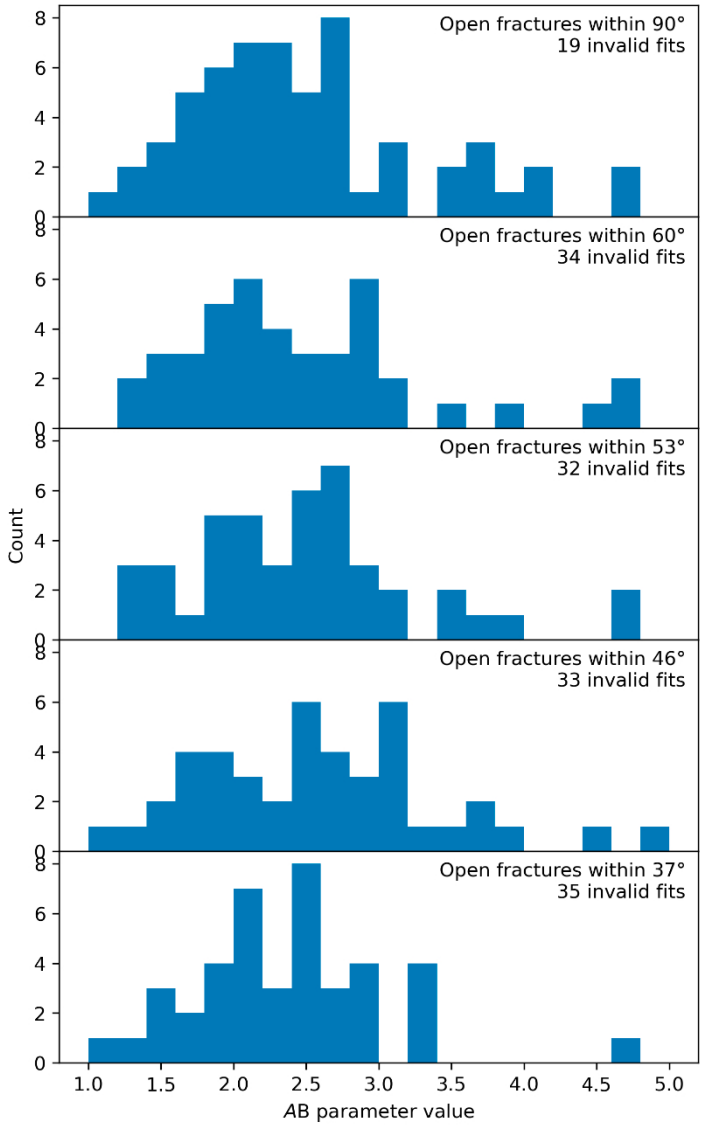

Figure 5-19. *Histograms showing the distribution of α = β values for the best fit Beta Distribution profiles for the subset of open fractures in each DZ SHI interval. To test sensitivities, fractures are filtered on the dihedral angle between the fracture and the modelled DZ structure surface. The count of invalid fits refers to the number intervals for which a reasonable (darker blue in Figure 5-18) beta distribution fit with α = β parameters in the range of 1–5 was not achieved.*

A G-DFN approach was used to generate DZ-related swarms, requiring input guesses for the size scaling model in the prior model and termination probability, see Table 5-3. The actual size scaling then emerges from these parameters. As will be seen in Chapter 7, these parameters have a strong control on the scaling behaviour of hydraulic properties, i.e., on the degree of connectivity between single-hole and multi-hole hydraulic tests. Therefore, the choice of parameters based on geometrical interpretations can be tested through hydraulic calibration. Potentially this can provide additional constrains, accepting that solutions will still be non-unique. A low k_r value, around 2.0, for the prior size model will cause most DZ-related fractures to grow until they intersect and, therefore, connect over long distances. A high k_r value, around 3.0, in the prior model will cause many DZ-related fractures to arrest before they intersect and, therefore, create sparse or tortuous connections within the plane of each zone. In the model, larger zones are assigned thicker damage zones (Subsection 5.3.1),

and so there is a higher probability of generating some large individual fractures within them and them being connected in a large zone than a small (thin) one. Given that the SDM-Site outcrop scale model (OSM) derived k_r exponent ~2.5 when fitting trace data, this was used as an initial guess, and through sensitivity tests on simulating flow, values of 2.5–2.6 were found to be optimal for describing hydraulic characteristics, see Chapter 7.

5.3.5 DZ-related fracture parameters

Both deterministic and stochastic DZs are modelled as fracture swarms once a realisation of the stochastic DZ has been generated across the model domain. The parameters used to generate the swarms that represent the damage zones of each DZ are given in Table 5-3. SDM-site interpretations of orientations seen on outcrops near DZs, found a Fisher concentration, κ, of ~33 for NW fractures on outcrop AFM001098 close to a NW DZ, Table 4-4 of (Fox et al. 2007). Outcrops close to NE structures (AFM001243, AFM001244 and AFM001265) report κ values for NE sets of 34, 25 and 100, respectively, see Tables 4-6, 4-7 and 4-9 of (Fox et al. 2007). Hence, a κ of 35 was considered appropriate for the concentration of orientations within an individual zone about the midplane. An example realisation of DZ swarm fractures is shown in Figure 5-20, demonstrating variable swarm thickness and intensities varying according to the beta distribution.

Table 5-3. Parameters for the DZ swarm fractures (other common parameters are given in Table 5-1).

Target P_{32} ($r_{max} > r > r_0$) [m^2/m^3]	Inside lens: 11.4 Outside lens: It is harder to distinguish between DZ and background fractures. However, during the hydrogeological calibration described in Chapter 7 it was found best the same as inside the lens to achieve hydraulic connectivity of the DZ system.	Based on Figure 5-23.
r_{min}	Dependent on scale of model application	As per Small DZ swarm fractures and background fractures
r_{max}	150 m	Increased from 50 m (as per Small DZ swarm fractures and background fractures) during the hydrogeological calibration described in Chapter 7 to reflect the observed hydraulic connectivity of the DZ system.
r_0	0.038 m	As per Small DZ swarm fractures and background fractures
Intensity distribution	Beta distribution (2.5, 2.5)	Subsection 5.3.2
Thickness [m]	0.01 × sqrt(midplane area)	Subsection 5.3.1
Power-law size scaling k_r (in prior model)	2.6	Typical OSM scaling from (Fox et al. 2007)
Termination probability on intersect with larger fractures	0.5	As per Small DZ swarm fractures and background fractures
Orientation	Mean trend and plunge are set to the orientation of the midplane	
Fisher κ	35 (about the midplane)	Based on outcrops

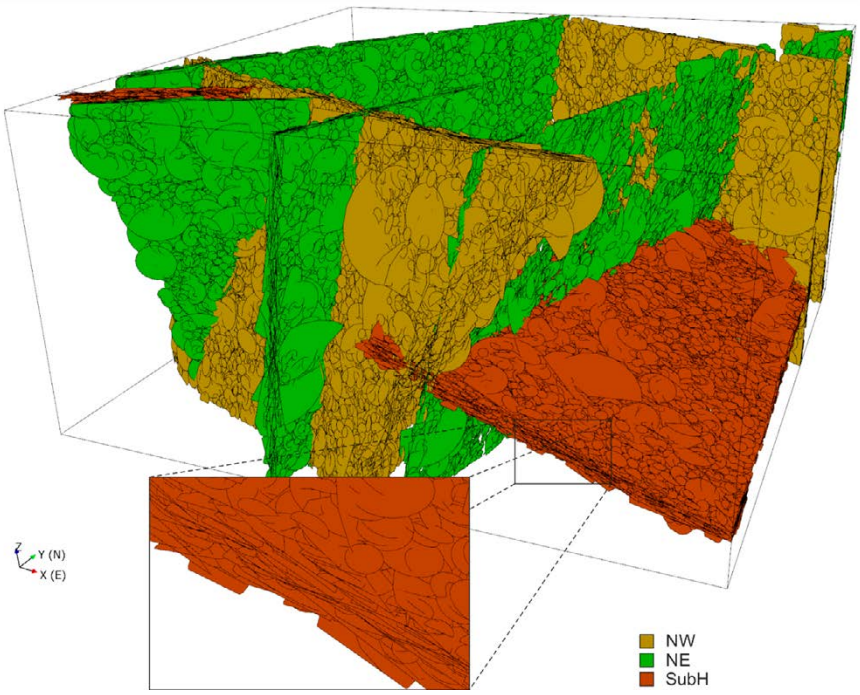

Figure 5-20. *View of DZ-related swarm fractures in a 600 m × 600 m × 300 m volume. Note that the figure shows an early model version, so the fractures shown are not necessarily representative of the final model.*

5.4 Background fractures

The borehole logs reveal a highly heterogeneous distribution of fracture intensities, as shown in Figure 4-9, even when excluding intervals interpreted as DZs in SHI (Figure 4-1 and Figure 4-3). There are typically ten or more peaks in fracture intensity outside of DZ for each deep borehole with intensity of the order of 50–100 % higher than average intensity, and relatively intact rock between.

Systematic variations in fracturing by domain were examined in Section 4.4 with Figure 4-10. showing that inside the lens (FFM01/02/03/06), NE fractures dominate the background, and show the most variability. NW and SubH have similar medians and spread in these domains. Excluding FFM02 from this, i.e., the top domain, shows that SubH background fracturing is in a minority at depth. The FFM02 data reveals that here SubH fracturing equals NE and has large variability in FFM02U, indicating both the presence and variability of sheet joints in the top 30 m. Elsewhere, in FFM04/05, including data from the KFR holes, fracturing is more intense and isotropic. Because of this contrast the regions are split into two categories, 'inside lens' with smaller intensities and 'outside lens' with larger intensities.

To analyse the logged intensity distribution further, data from logged holes was divided into intervals of length ~ 10 m outside of DZ (intervals between DZ are not exact multiples of 10 m, hence the approximations). This permits the statistical variability of intensities and their variations with depth to be investigated, as shown in Figure 5-21 and Figure 5-22, respectively.

Figure 5-21 illustrates the overall distribution of intensity on a 10 m scale taken over all cored KFM holes (mostly in the domains shown in the left-hand figure) and KFR holes (mostly in the domains shown in the right-hand figure). Note the differing scales of the y-axis, this is due to both the different borehole counts in the different regions, and the high count of near-zero intensities inside the lens. This high count of near-zero intensities inside the lens region also increases the visual contrast between the two graphs, but this is somewhat of a distraction: it is the shape of the curves that is key as opposed to their relative magnitudes on the graphs. A key takeaway is that both intra-domain variability in intensity is as important a feature of the data in addition to the variability between inside and outside the Forsmark lens as explored earlier in average intensity statistics shown in Figure 4-10. Inside the lens,

the modal total intensity is less than 5 m^{-1}, whereas outside the lens, the modal total intensity is nearly 20 m^{-1}. As investigated in SDM-Site (Fox et al. 2007), systematic variations in average intensities by depth or between domains are smaller in comparison to the fine-scale variability seen in this graph. Variability is greatest in the NE set with a larger proportion of 10 m intervals with higher intensity.

Notable from Figure 5-21 is that where intensities are high, these intervals must contain multiple sets. This is indicated by the lower counts for individual set on the right-hand side of the graphs in comparison to the combined sets. This suggests that tabular swarms of sub-parallel fractures around DZ need to overprint a background of each orientation.

Figure 5-22 examines both the contrasting variations with intensity inside and outside the lens, and also the variations in intensity at different depths. Much of the apparently random variation in intensity in the −300 m to −800 m elevation interval results from the relatively small number of boreholes that penetrate these depths and so there is limited averaging on the 10 m scale used. The amount of data is indicated in the rightmost column. Similarly, the apparent reduction in intensity inside the lens around −800 m elevation is best explained by the reduction in the number of boreholes that penetrate these elevations. The only statistically significant depth trend is the increased intensity in SubH fracturing in the top −150 m elevation inside the lens, as concluded by (Fox et al. 2007). This represents the FFM02U and FFM02L fracture domains, see Section 5.5.

Bearing all this in mind, a model with a stationary Poissonian distribution, or even stationary within each domain, would be a significant simplification and unable to predict variability that can be expected on the scale of spacings between deposition holes (~10 m) and deposition tunnels (~30 m). Further, the spikes in intensity seen in, e.g. Figure 4-1, tend to be associated to one or two fracture orientations sets rather than isotropic. This coherency of orientation within an individual fracture cluster would point towards them being tabular structures, i.e. small DZs. The working conceptual model is, therefore, that there is a hierarchy of structures as introduced in Figure 1-5 with the background being made up of small DZ and individual fractures. Individual clusters related to these small DZ are typically of thickness a few metres to ten metres. This is consistent with the size ranges, radius 50–250 m, conceived in Figure 1-5 and the interpretation that damage zone thickness is on average of the order of a few percent of length.

However, not all of the background fractures can be associated with small (stochastically modelled) DZ. Those that aren't are termed the homogenous background fractures. The proportion of total background intensity related to small DZ and the homogenous background fractures cannot be measured directly as this would require a knowledge of the extent of structures intersecting a borehole. The boundaries are, therefore, an arbitrary modelling construct. However, assumptions about the size scaling of stochastic DZ and their related fracture intensity can be constrained, through simulation, to mimic the distributions of Figure 5-21. Such a calibration is the main objective in modelling background fractures. The calibration of the proportions of the two background fracture components is described in Subsection 5.4.3. Since these are very different for inside and outside the lens domains, then this calibration has to be performed separately for the two tectonic units.

The total intensity to be distributed between the two background components is converted to P_{32} estimates using the method of Wang (2005). A summary of these values for the main modelled fracture domains is shown in Figure 5-23.

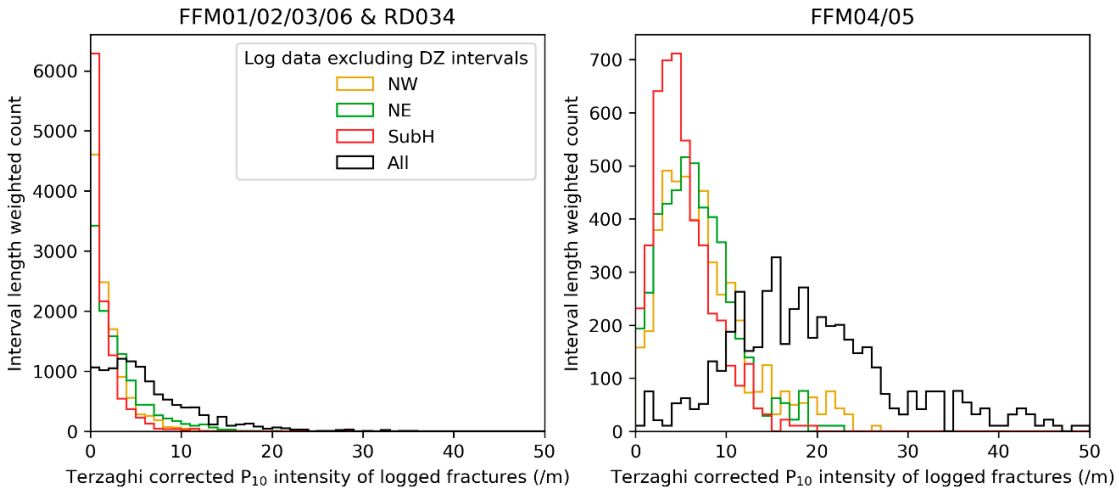

Figure 5-21. *Histogram showing the distribution of Terzaghi corrected intensities observed in ~10 m intervals (and summed as total interval length on the ordinate axis) in the KFM and KFR boreholes, excluding DZ intervals. The count of each intensity is weighted by the length of the associated intervals, reducing the influence of short intervals which often have extreme P_{10} values.*

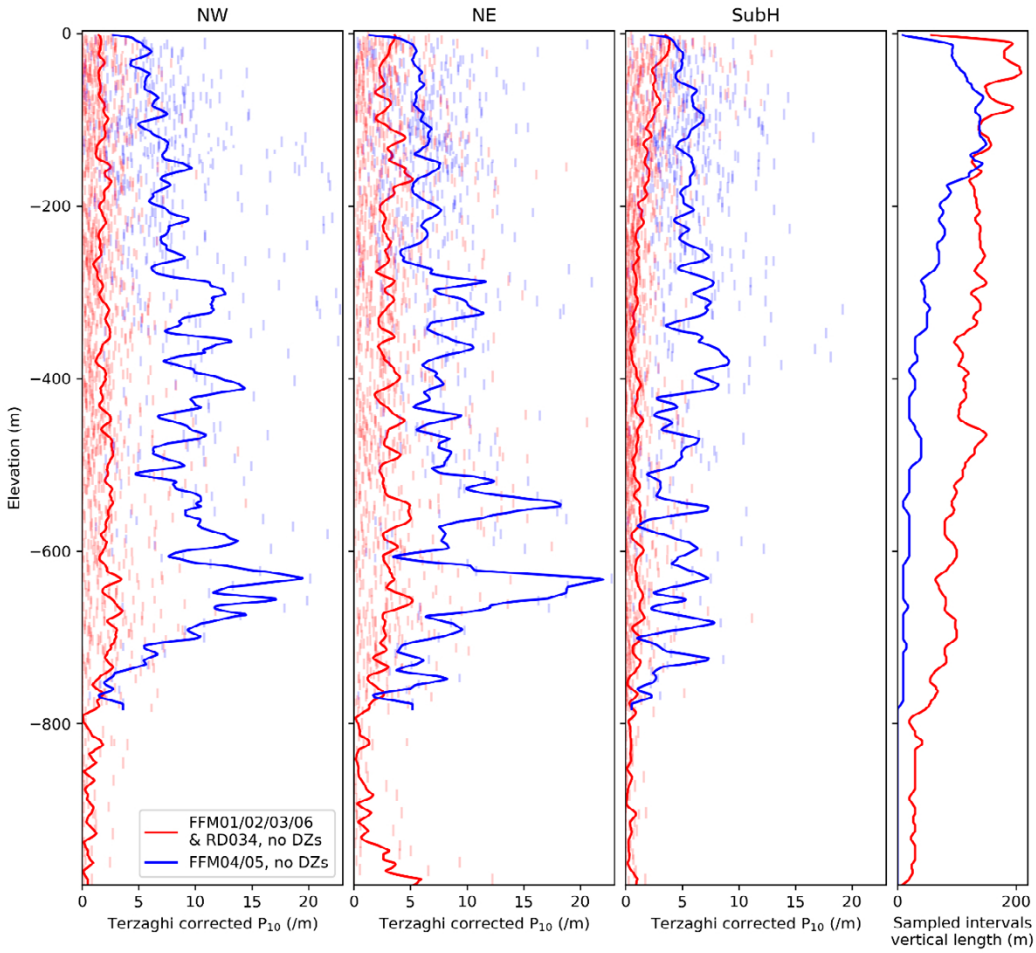

Figure 5-22. *Graphs showing how the intensity of logged fractures in the KFM and KFR boreholes varies with depth inside and outside the lens for each fracture set. The semi-transparent vertical lines indicate the intensities of individual intervals, and the curves on the three intensity graphs show the average intensity measured in a moving 10 m vertical interval. The graph on the right indicates the total vertical length (as opposed to the length of the inclined boreholes) of the intervals sampled in the 10 m windows at each elevation. Note that this excludes the DZ intervals, hence, the variability and it not being monotonically decreasing.*

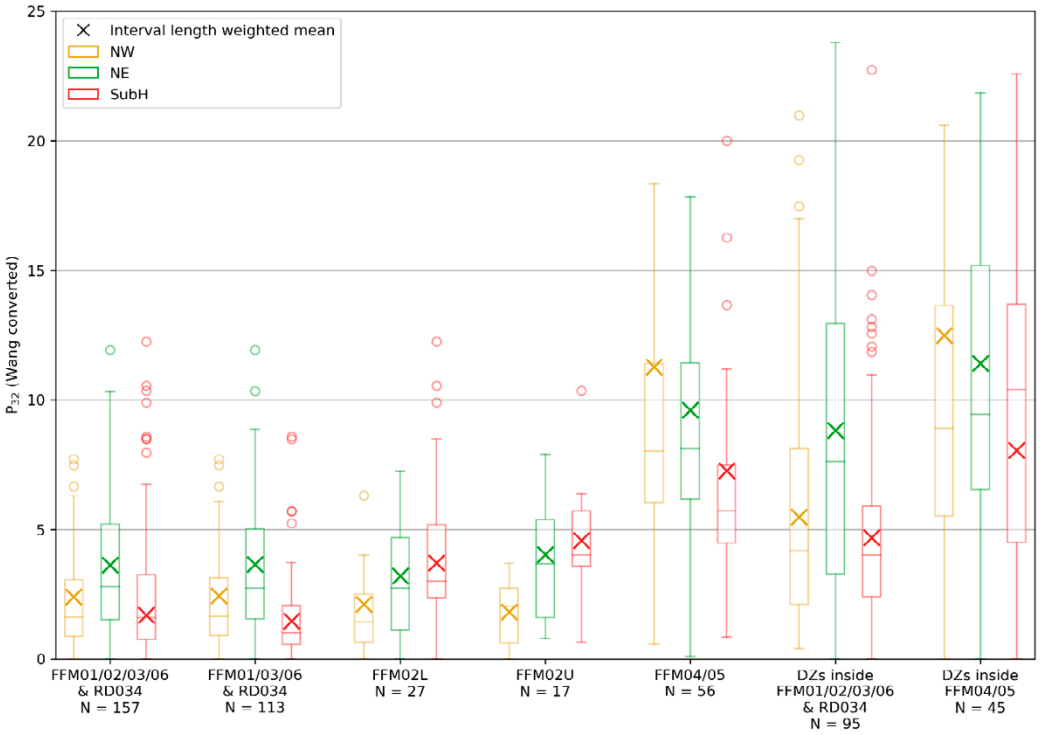

Figure 5-23. *Plot showing the mean estimate P_{32} (Wang 2005) for the main fracture domains weighted by the length of the intervals from which the intensities are calculated, with bar and whisker plots where the number of sampled intervals (N) is > 10. The bars indicate 25, 50 and 75 percentiles, the whiskers 5 and 95 percentiles, and the crosses the mean. The circles show individual values above the 95-percentile. For the KFM boreholes, the DZs are the ESHI DZ assignments. The intensities shown for the named FFM regions exclude the DZ intervals.*

5.4.1 Small (stochastic) DZ swarms

The number of peaks in intensity associated with stochastic DZs (Figure 4-1) is high enough that the computational cost of generating a discrete grid for each DZ midplane (as for the deterministic DZs) would be impractical. Instead, the intensity of the background fractures is redistributed on a grid to emulate increased intensity around the stochastic DZs. This is achieved by generating the stochastic DZ midplanes as a DFN (Figure 5-24 upper) and upscaling their P_{32} onto the grid (Figure 5-24 lower). The upscaled values are then used as relative intensities to generate stochastic DZ-related fractures.

As the grid cells have 10 m side, the thickness of the region of increased intensity around each Small DZ midplane will also be at least 10 m. Using the relationship between DZ and thickness described in Subsection 5.3.1 (structure thickness is approximately 1 % of structure length), would imply clusters associated with Small DZ will be smeared relative to their actual thickness, although Figure 5-14 would suggest that DZ of 200–500 m length have thicknesses of 5–10 m, and so the smearing is not expected to hugely obscure the connectivity of the fracture network. Nonetheless, it does motivate automating a more automated parent-daughter method for generating 1 000 s of stochastic DZ in FracMan (or DFN software) to remove the need to represent DZ-related fracturing on a fixed scale.

The distribution of intensities that arise from upscaling the small stochastic DZ is most sensitive to two factors:

- the intensity of the small DZ midplanes; and
- how the increase in relative intensity of a given grid cell relates to the size of the stochastic DZ that has intersected the cell.

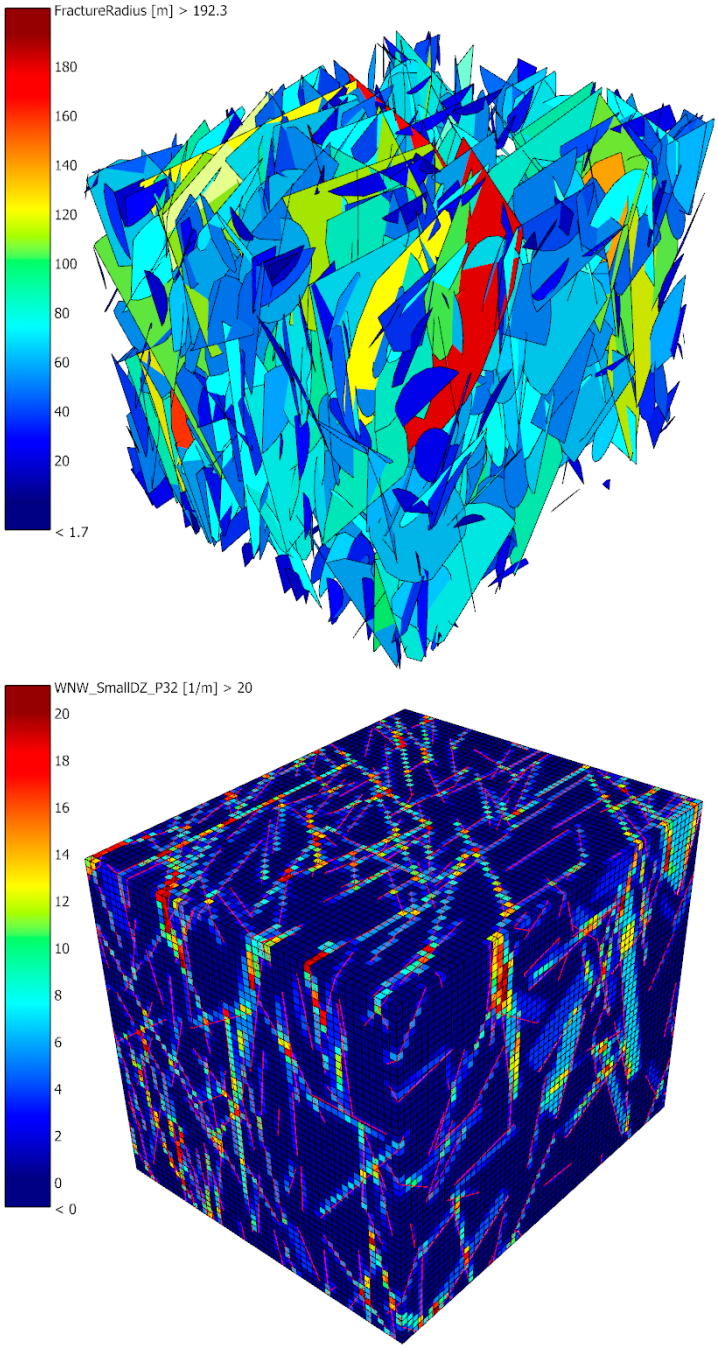

Figure 5-24. *View of a stochastic DZ midplane model for the NW set (upper) and associated upscaled intensity values (lower). Note that the figure shows an early model version, so the fractures and intensity values shown are not necessarily representative of the final model.*

The impact of these two items on the final DFN is both inter-dependent and affected by other parameters such as size distribution, termination probability and the relative proportions of small DZ swarm fractures and homogenous background fractures. Hence, the result is non-unique with other combinations of parameters being equally constrained by the data. For example, terminations only have a significant impact if the intensity and size distribution of the fracture systems cause many DZ intersections to occur. Consequently, the following discussion is limited to the parameters that have most impact in the matching the distribution of fracture intensity on a 10 m scale. The final calibrated recipe for small stochastic DZ is given in Table 5-4.

Table 5-4. Parameters for generating small stochastic DZ (some common parameters are given in Table 5-1).

	NW	NE	SubH	Notes
Target P_{32} ($r_{max} > r > r_{min}$) [m^2/m^3]	0.04	0.06	0.03	Estimated from FFM01/02/03/06 & RD034 P_{32} (for r_0 = 0.038 m)
r_0	50 m			Working assumption for smallest zones
r_{min}	r_0			
r_{max}	250 m			Approx. smallest deterministic DZ
Power-law size scaling k_r (prior to termination)	2.5	2.5	2.5	Typical OSM scaling from (Fox et al. 2007).
Termination probability on intersect with larger fractures	Self: 0.27	Self: 0.27 NW: 0.53	Self: 0.06 NE: 0.11 NW 0.22	As per the Stochastic DZ midplane model.
Orientation	Trend and plunge bootstrapped from the borehole logs with inverse distance weighting.			As per the homogenous background fractures.
Fisher κ	100 (to give a small amount of scatter from the bootstrapped value).			

The prior size distribution of the small stochastic DZ was set equal to the typical OSM scaling exponents from (Fox et al. 2007): power-law size scaling (k_r) of about 2.5. The termination probability was configured to be the same as for the ZFM-scale stochastic DZs.

The power-law relationships allow the extrapolation of the total background P_{32} intensity of fractures inside the lens (shown in Figure 5-23) to the size interval of the Small DZ midplanes. This results in P_{32} intensity estimates of ~0.04, ~0.06 and ~0.03 m^2/m^3 for the NW, NE and SubH sets, respectively. These values were used for the small stochastic DZ both inside and outside the lens.

The intensity of the small DZ controls how many locations receive local increases in intensity. Consider two end-members: a small DZ network with very few fractures will result in swarm fractures located in a very small subset of the modelled region as most of the region will have zero swarm intensity; conversely, a small DZ network with a very high intensity will result in a more homogenous distribution of swarm fractures, with few cells with zero swarm intensity. This behaviour is illustrated by the distribution of relative intensities in Figure 5-25, varying the relative intensity assigned to small DZ versus the background.

Calculating the increase in relative intensity for each grid cell due to intersecting small DZ uses two pieces of information: the area of each DZ that intersects the cell and the size of each of those DZ. Some examples illustrate the result of this:

- A cell that is intersected by many midplanes of a given size will have an associated increase in swarm intensity that is larger than another cell that is intersected by fewer midplanes of the same given size.
- A cell that is fully bisected by a midplane will have an associated increase in swam intensity that is larger than another cell that is only partially intersected by the same midplane.
- A cell that is intersected by a larger midplane will have an associated increase in swam intensity that is larger than another cell that is intersected by a smaller midplane.

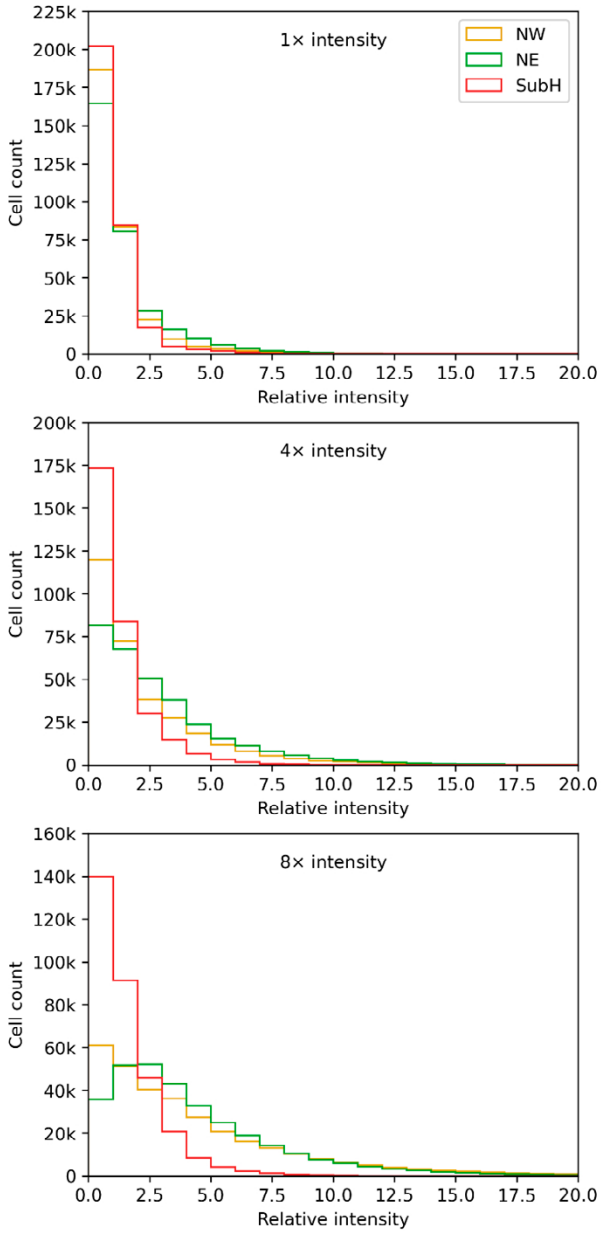

Figure 5-25. *Histograms showing how the distribution of relative intensities from small DZ varies as the intensity multiplier for the small DZ increases. Note that the data displayed here is from an early version of the DFN and is provided only to illustrate how the small DZ intensity impacts the shape of the distribution. Note that as the intensities shown are relative, their contrasting magnitudes between different formulations is inconsequential, it is the shape of the curves that is key.*

Using this information, the relative intensity, denoted I_r, for each cell is then a function of an upscaled intensity parameter, denoted I_u, which is the sum of the area of each small DZ intersecting the cell multiplied by the square root of the equivalent radius of those midplanes. Multiple relationships between I_u and I_r were tested, Figure 5-26 shows some examples and their associated relative intensities. The formulation:

$$I_r = 2 \cdot I_u + {I_u}^2 \qquad \text{Equation 5-3}$$

was selected from these empirical tests as it mimics the observed distribution. When used to drive a heterogeneous fracture generation it was found to give a good fit for the observed data as is demonstrated in Subsection 5.4.3.

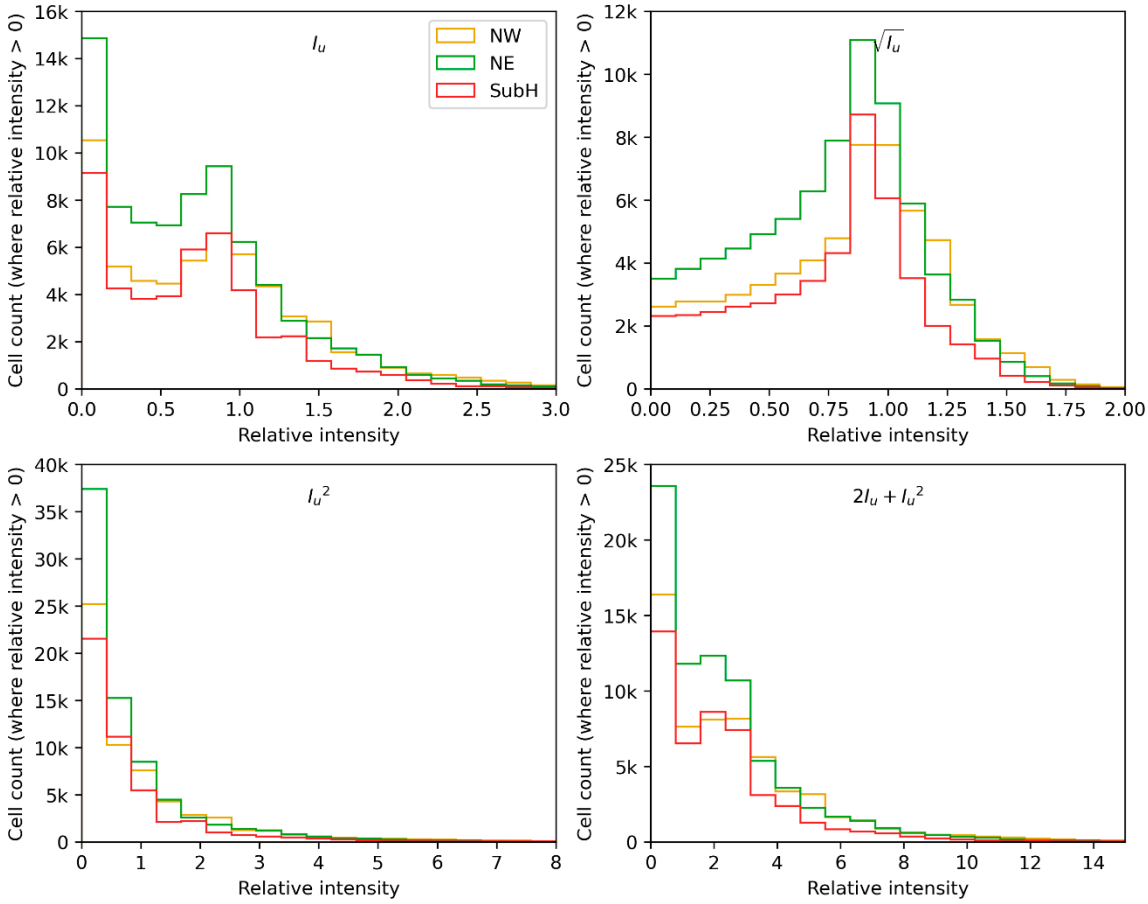

Figure 5-26. *Histograms showing examples of how the formulation of relative cell intensity, I_u, as a function of I_u, can impact the resulting distribution of relative intensity values. Note that as the intensities shown are relative, their contrasting magnitudes between different formulations is inconsequential, it is the shape of the curves that is key.*

5.4.2 Background individual fractures

To better match the observed data, the target intensities for the homogenous background fractures some additional randomness was introduced to the spatial distribution of intensity at the scale of the 10 m cells. For a completely random Poisson point process, where the number of "events" (i.e. fracture centres) per interval is described by a Poisson distribution with a rate parameter, the distribution of the rate parameter (i.e. P_{32}) is the conjugate prior for the Poisson distribution, which is Gamma. When modelling background fractures down to the borehole scale, the number of fracture centres in a 10 m cell is large, described by a large shape parameter in the gamma distribution, giving a similar shape to a normal distribution (due to their exponential form). A simple normal distribution is, therefore, used to give a random scaling factor on the cell based background intensity, using a mean of one, a standard deviation of one and truncated between zero and two. The effect of including this component of background intensity is shown in Figure 5-27: it reduces the count of cells with near-zero intensities and increases the count of cells with low relative intensities.

5.4.3 Combined calibration

The target P_{32} intensities for the background fractures is a combination of the upscaled small DZ fractures and homogenous background fracture intensity. Both the individual contributions of these two sources of intensity distribution and their relative proportions were calibrated in tandem, so that the resulting P_{10} intensities and their distributions match those observed in a statistical sense. The graphs shown below describe relatively subtle changes in intensity, as seen in Subsections 5.4.1 and 5.4.2, illustrating contrasting sensitivities.

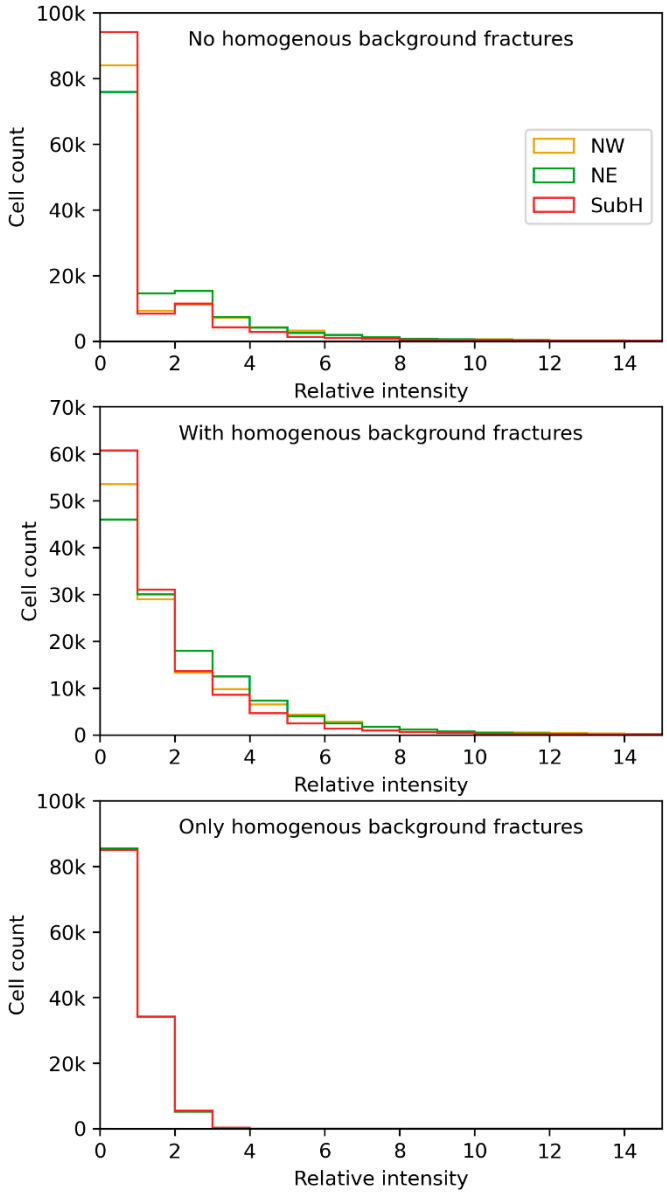

Figure 5-27. *Histograms showing how the distribution of relative intensities varies with different combinations of small DZ, and background fractures, or not. No background fractures corresponds to only small DZ-related fractures. Note that as the intensities shown are relative, their contrasting magnitudes between different formulations is inconsequential, it is the shape of the curves that is key. These can be compared with the observed data shown in Figure 5-21.*

Figure 5-28 and Figure 5-29 show, for inside and outside the lens, respectively, the distribution of modelled intensities for three different versions of the baseline model in comparison to observed intensities. These versions vary the relative proportions of small DZ-related fractures to homogenous background fractures, as indicated by the graph annotations. Note that the logged modelled fractures include some stochastic variability, but it was not practical to produce a big enough sample to remove this variability (the DFNs for Figure 5-29 contained > 1.3 billion fractures), and consequently the upscaled intensities for fractures > 4 m radius were also included.

To model data from inside the lens, it was found necessary to assign a higher fraction of the background intensity to small DZ-related fractures of order 90 % or more. This would suggest only a limited general background fracturing occurs inside the lens which has been subject to relatively low ductile strain, while in the high-strain belts surrounding the lens there is more ubiquitous fracturing on all scales, see Section 2.1. Sensitivity cases clusters around such a high fraction are shown in Figure 5-28. Decreasing the proportion of homogenous background fractures increases the proportion of near-zero intensities in the output intensity distributions. Model v0.12.1 has a logged intensity of near-zero NW fractures that is higher than that observed, but this is in contrast to the other model versions and the upscaled intensity plot, indicating it is a product of the stochastic variability. Based on this, the case with 95 % of background intensity associated to small DZ-related swarms was selected for FFM01/02/03/06.

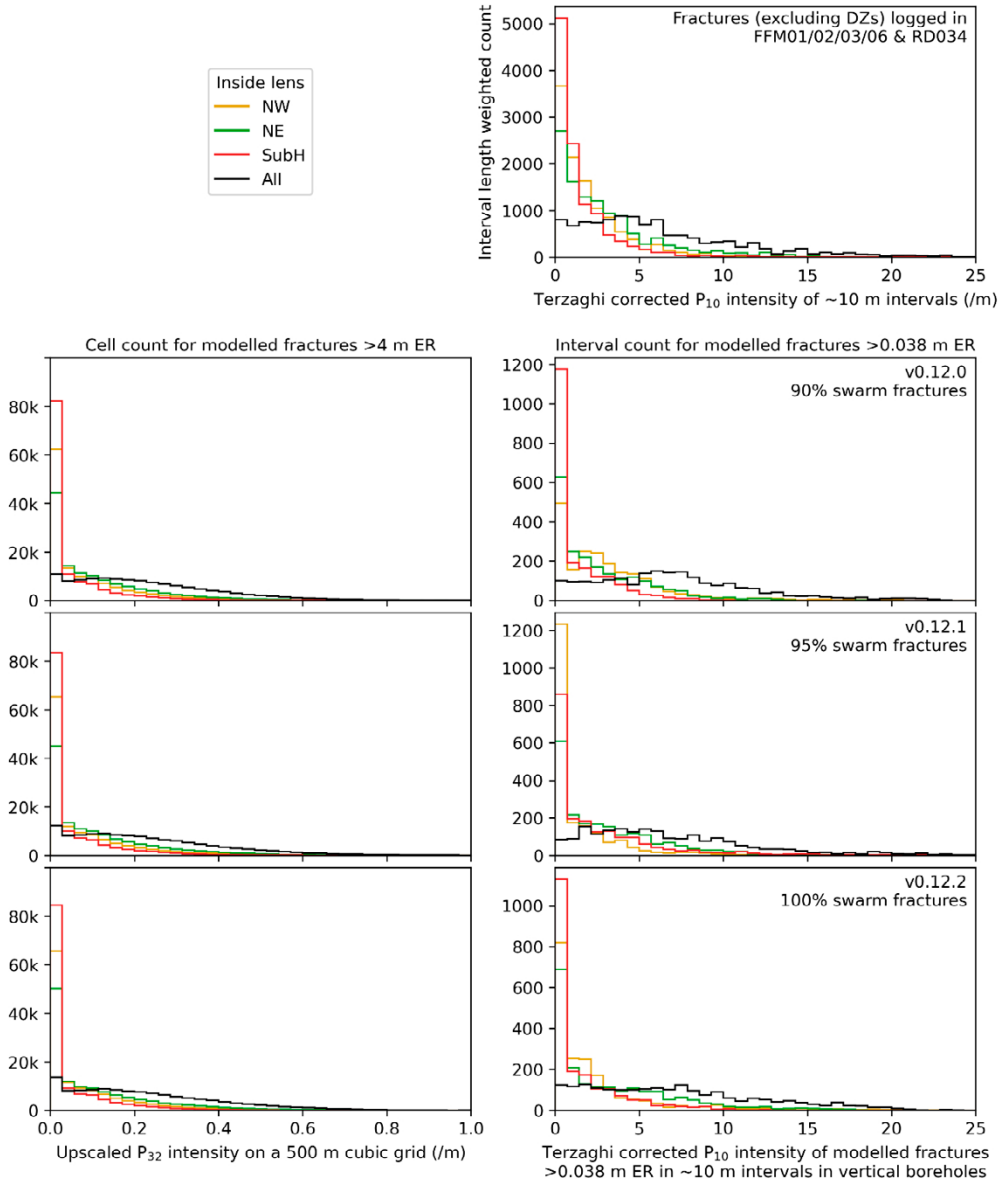

Figure 5-28. *Plots showing the intensity distributions for three different versions of the DFN-BF1 model inside the lens, illustrating the sensitivity of the model to the proportion of DZ-related swarm fractures to homogenous background fractures. The upper right plot shows the observed intensities with its shape of distribution being the calibration target.*

By contrast, domains outside the lens required of the order of 50 % of background fracture intensity to be assigned to small DZ-related swarms. Figure 5-29 demonstrates how increasing the proportion of swarm fractures flattens the intensity distribution curve and increases the count of near-zero intensities. The observed data indicate relatively few near-zero intensities, a (roughly) normally distributed peak in intensities around 18 m^{-1} and steadily decreasing low intensities above ~30 m^{-1}. Based on this, the case with 50 % small DZ-related fractures is selected as the best fit for these FFM04/05.

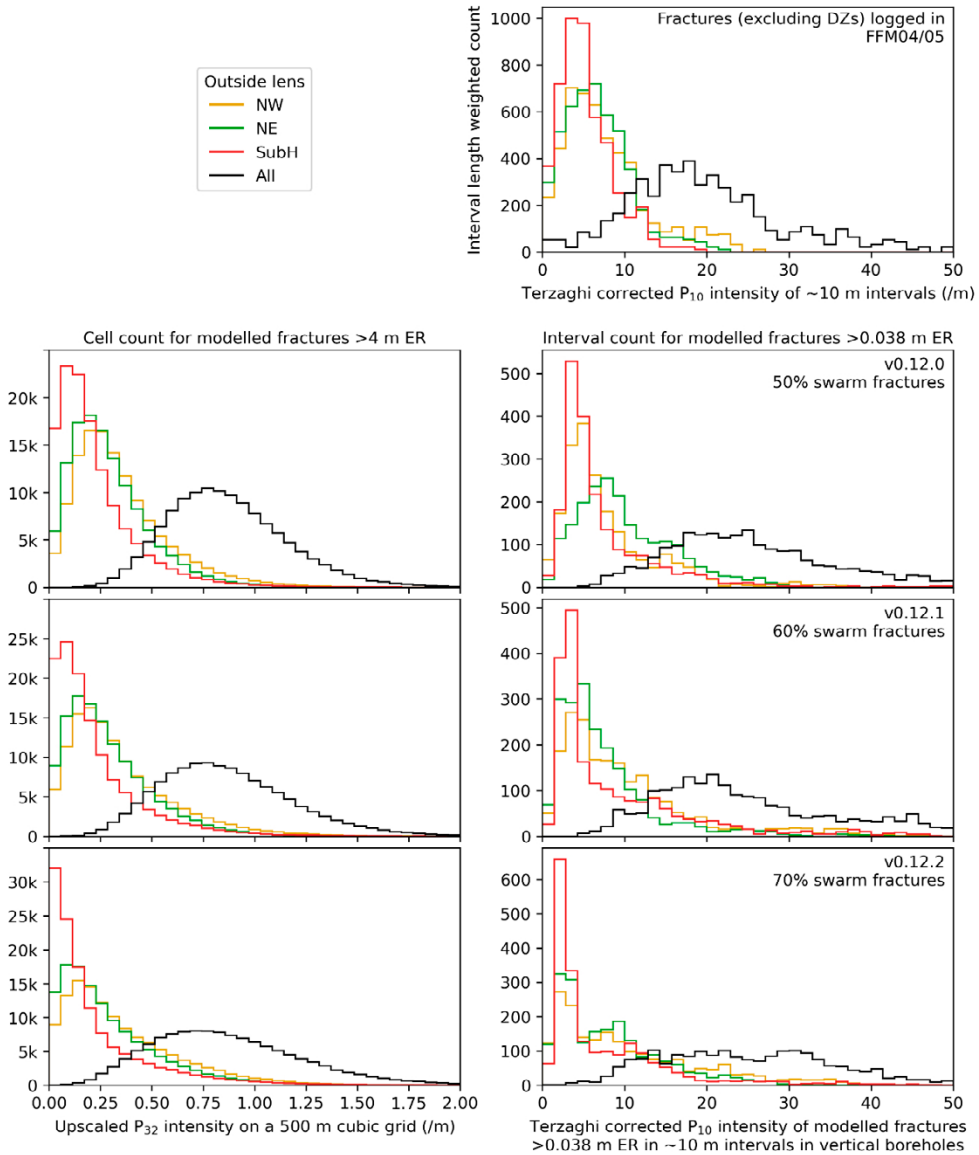

Figure 5-29. *Plots showing the intensity distributions for three different versions of the DFN-BF1 model outside the lens, illustrating the sensitivity of the model to the proportion of DZ-related swarm fractures to homogenous background fractures. The upper right plot shows the observed intensities with its shape of distribution being the calibration target.*

5.4.4 Size distribution and terminations

In the G-DFN model, the distribution of sizes of fractures produced by a given configuration is an emergent characteristic that is sensitive to termination probability as well as the fracture size scaling in the prior model. This is because if growth of a fracture arrests due to terminations, it will not reach its target size. Therefore, to achieve a target size distribution, the size scaling of fractures in the prior model needs to be shallower (small exponent) than what the target size distribution demands. This effect becomes larger the higher the fracture intensity as more potential terminations occur.

Thus, when calibrating the size distribution of a G-DFN, several factors need to be balanced:

- Output size distribution (i.e. aims to be the size distribution that is observed);
- Input size distribution for the prior model (i.e. for power-law size distributions, lower k_r values than the output size distribution, to offset reductions in size from terminations);
- Termination probability (i.e. reduces average size of output size distribution); and
- Input intensity (i.e. controls occurrence of terminations).

Here, we first describe observed constraints on these inputs, before discussing the balance of parameters that was selected.

Terminations of fractures as seen on an outcrop can be quantified by classifying the nodes along traces as either:

- Type I where the fracture ends in isolation;
- Type X where two fractures cross each other without termination:
- Type Y where two fractures cross each and one terminates: or
- Type V where two fractures cross each and both terminate.

The proportions of these types of nodes as seen on an outcrop can be plotted on a ternary diagram as a characteristic of connectivity topology (Sanderson and Nixon 2015; Sævik and Nixon 2017).

This then provides a quantitative metric for model calibration. However, in practice there is uncertainty in converting digital outcrop mapping to such a metric due to the precision with which the traces are mapped and recorded. Unless an outcrop mapping is recorded to high precision, an automated analysis of traces might yield I, T or X for a fracture that ends close to another. Automated methods for calculating connectivity topology have to be trained using an outcrop specific tolerance, but this may still result in subjective results if the mapping precision is variable across the outcrop.

Figure 5-30 indicates the range of possible outcomes according to this tolerance issue for the outcrop data used in SDM-Site. As can be seen, the main uncertainty is between whether nodes are type I or Y/V with about a 40 % shift between high tolerances used. Nonetheless, this information provides a useful additional constrain on fracture size distribution. An estimate of the true connectivity topology might be: 20 % Y, 25 % X and 55 % I. It should be noted that creating G-DFN tracemaps with c. 40 % nodes (i.e. the upper end of this measurement uncertainty) classified as terminating would, for the intensities observed at Forsmark, likely require 100 % termination chance. Hence, an estimate of 20 % for the true percentage of Y nodes seems more plausible. Comparing with connectivity topology for deterministic DZ scale structures in Figure 5-7, networks on this smaller scale tend to have more I type and less X type nodes. Comparison of model results of this type against new drone mapped outcrop data, as a prediction-outcome exercise, is presented in Chapter 8.

To constrain the size distribution of the background fractures, four sources of information were potentially available:

- Historic surface mapped trace data;
- New drone mapped trace data (preliminary data not QA:ed);
- Lineament scale data to support a potential interpolation of size scaling beyond borehole and outcrop scales; and
- Discrete flow logging as a measure of fracture network connectivity.

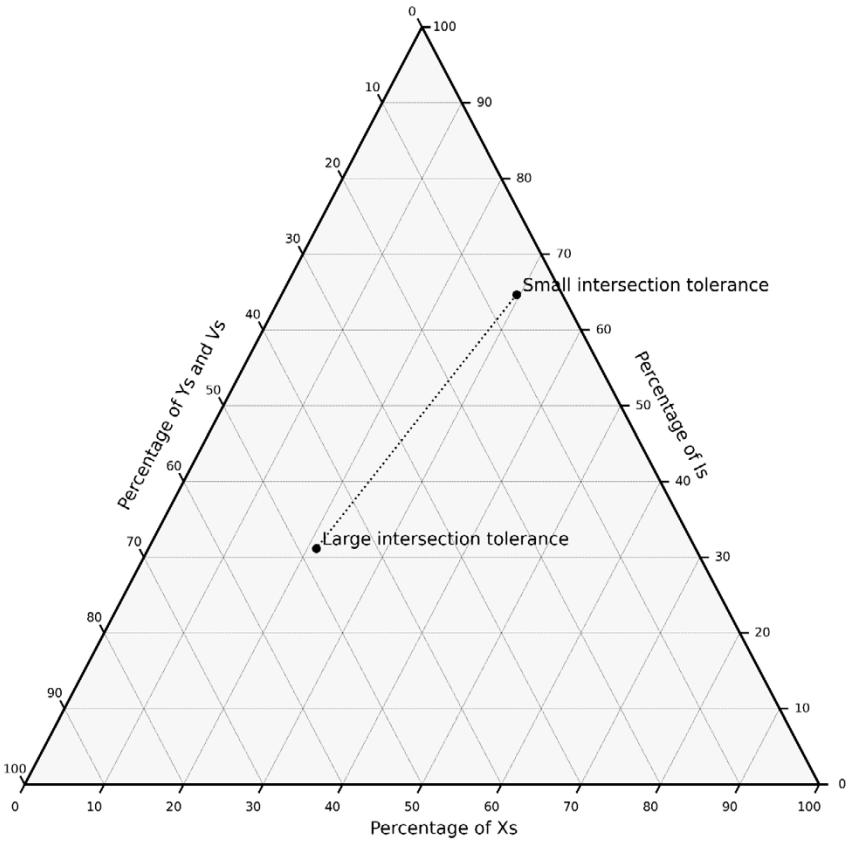

Figure 5-30. *Ternary diagram illustrating the fracture trace topology (Sævik and Nixon 2017) for surface mapped fracture traces.*

Some challenges are present with the interpretation of these data:

- The tracing of the drone mapped data were incomplete during the period of model construction and so were reserved for confirmation/validation purposes (see Chapter 8);
- Both types of trace mapping dataset are representative of fractures in natural outcrops, which, due to their glacial exhumation, have a bias towards being mechanically stronger, and therefore potentially unlikely to include fracture zones, assuming they have become eroded to become located between outcrops;
- The need to extrapolate a size scaling model for single fractures from borehole scale through the outcrop scale (Req~ 10 m) out to the largest single fractures (Req~ 100 m); and
- Flow logging is an indirect observation of the effects of fracture size distribution.

Consequently, and as is a common challenge for DFNs, fracture size scaling is an uncertain component of the DFN-BF1 modelling. Fox et al. (2007) considered the validity of the same sizing model from the borehole to regional lineament scale, the so-called tectonic continuum. Here, we consider a narrower window of scales due to the separate conceptualisations of DZ and single fractures. The scaling model is only required to be valid up to ~ 100 m length. Current outcrops are limited to ~ 10 m scale, so modelling is required to estimate scaling behaviour of 10–100 m fractures where there is a gap in data.

Fox et al. (2007) interpreted k_r values of ~ 2.4 for NW and ~ 2.6 for NE and SubH sets on the outcrop scale; and k_r values of ~ 2.1–2.2 for the oldest NW set and k_r values of 2.8–3.0 for NE and SubH sets for fault scale models. This difference in scaling exponents for the two different scales was also noted by (Darcel et al. 2009), see Figure 5-31. Using a genetic type model, Davy et al. (2013) interpret a scaling exponent of 2.1 for the outcrop scale and 3.0 for the lineament scale, without differentiating between sets. Hence, one can expect that suitable exponents for the outcrop scale are between 2.1 and 2.4, and emergent scaling for the largest fractures might be up to 3. These initial values informed the parameters tested in modelling the background fracturing as a combination of Small DZ-related swarms and a homogenous Poissonian model.

Figure 5-32 shows the size distribution of background fractures (both those associated with small stochastic DZs and by a homogenous Poissonian background) generated in two tectonic domains, one inside the lens and one outside the lens, with the parameters given in Subsection 5.4.5. Note the size range generated is between 4 m to 50 m, here, and hence there is a roll-over ~50 m. These parameters include a prior "average" scaling exponent k_r of 2.7 and variable input k_r values, configured to make their respective fracture sets have an average k_r close to 2.7. The fracture sets inside the lens achieve consistent output k_r trends between 2.6 and 2.7. Outside the lens, the NW set (i.e. generated first) has a similar k_r trend. However, the later sets have increased average k_r trends (i.e. more steeply dipping) due to the termination of fractures.

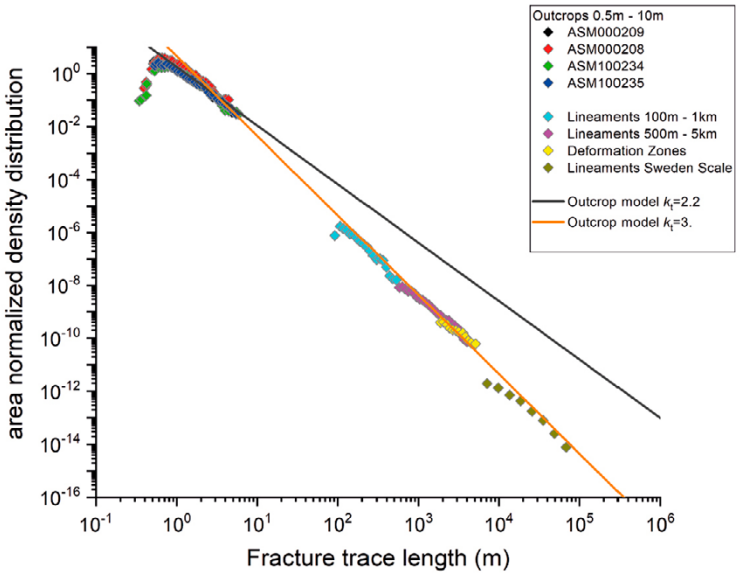

Figure 5-31. *Areal fracture trace length density distribution for different outcrop or lineament maps from the Forsmark area (Sweden), after (Darcel et al. 2009).*

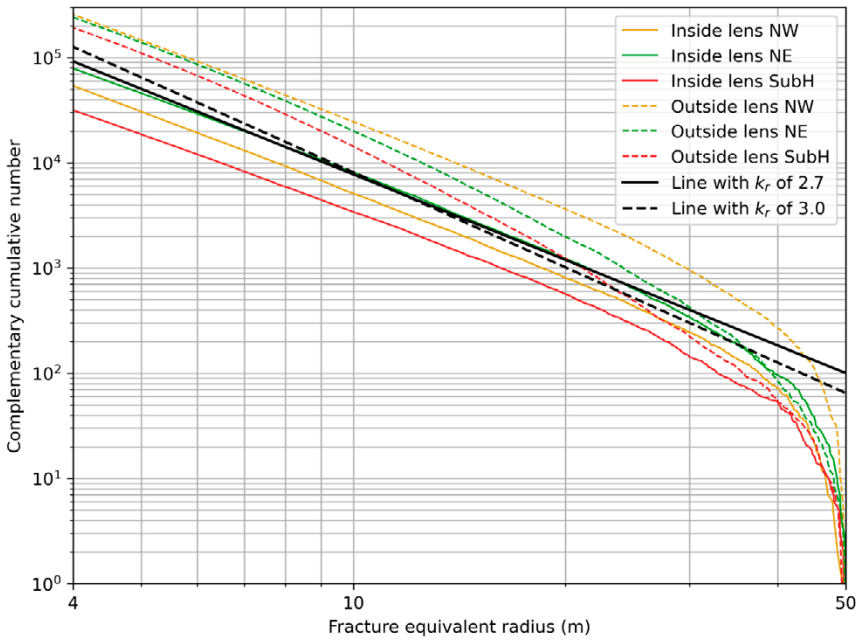

Figure 5-32. *Complementary cumulative number plot for background fractures, r = 4 to 50 m, generated in two 500 m cubic volumes, one inside and one outside the lens. No stochastic DZs were generated in these realisations. Two lines with slopes of particular k_r trends are included for comparison.*

The chosen parameters (Subsection 5.4.5) strike a balance between the observed proportion of fracture trace terminations (indicating a larger proportion of fractures should terminate), the observed fracture trace and lineament size distributions (indicating a larger k_r value), and the results of the flow modelling described in Chapter 7. This is a balance because increasing the termination probability reduces the average fracture size (i.e. increases output k_r). However, for the SubH set (i.e. generated last) outside the lens (i.e. intensity is larger), the k_r value cannot go any lower without invalidating the power-law. We speculate that achieving the observed fracture trace terminations with the observed trace size distribution would require a mechanism for linking of fractures in an evolved version of the G-DFN model.

Changing the power law-size scaling parameters for small DZ, including the location parameter, r_0, would be an alternative way to distribute relative intensity differently between inside and outside the lens. This was not attempted as the approach would provide less insight than keeping the modelling of small DZ the same in both domains and using a different division of fracturing between structure-related and a Poissonian background.

5.4.5 Background fracture parameters

The parameters used for the background fractures are presented in Table 5-5 for both inside and outside lens tectonic domains and to split the total background fracture intensity between small DZ-related swarms and the Poissonian distribution of individual background fractures. Parameters determining the generation of small stochastic DZ (as midplanes) are given in Table 5-4.

Table 5-5. Parameters for background fractures as divided between small DZ-related swarm fractures and the remainder as Poissonian individual fractures. The parameters used to generate the small DZ midplanes are given in Table 5-4. (Some common parameters are given in Table 5-1.)

	NW	NE	SubH	Notes
Target P_{32} ($r_{max} > r > r_0$) [m^2/m^3]	Inside lens: 2.4 Outside lens: 11.3	Inside lens: 3.6 Outside lens: 9.6	Inside lens: 1.5 Outside lens: 7.3	
Spatial distribution	Inside lens: 95 % clustered around small DZ midplanes, 5 % distributed according to a normal distribution. Outside lens: 50 % clustered around small DZ midplanes, 50 % distributed according to a normal distribution.			See Subsection 5.4.3.
Power-law size scaling k_r used for determining P_{32} of small DZ midplanes	2.7			Offsets some of the discrepancy between initial and emergent k_r.
Power-law size scaling k_r (in prior model)	Inside lens: 2.5 Outside lens: 2.4	Inside lens: 2.4 Outside lens: 2.1	Inside lens: 2.3 Outside lens:2.01	Due to truncations, emergent k_r is larger.
Termination probability on intersect with larger fractures	0.4	0.3	0.2	Compromise between observed termination probability and size distribution, see Subsection 5.4.4.
Orientation	Small DZ swarms: trend and plunge of closest midplane in the same set, with Fisher κ of 35. Homogenous background fractures: bootstrapped from log data with inverse distance weighting and a Fisher κ of 100.			The orientation of the small DZ is also bootstrapped from the log data.
r_0	0.038 m			
r_{max}	50 m			
r_{min}	4 m for calibration, but user configurable dependent on scale of model application, e.g. lower around boreholes.			

Figure 5-33 shows an example realisation that spans the two tectonic domains inside and outside the lens, illustrating how the intensity of the fractures increases outside the lens and clusters around small stochastic DZ. Note the midplanes of DZ are only used to seed fractures, they are not incorporated as part of the model. It can be noted that changes in fracturing are coincident with changes in rock type and ductile fabric, see Figure 2-2, rather than bounding regional DZ. The combination of 4–6 times higher intensity outside the lens for NW and SubH sets but less concentrated in DZ, means that the net intensity in DZ inside the lens is about half that outside, as seen in Figure 4-10. This contrast in DZ-related intensity is less in the NE set, about 2/3rds, also as seen in Figure 4-10.

The regional DZ lie within the broader, high-strain belts around the tectonic lens. Further illustrations of the model are given in Section 5.6.

Figure 5-34 and Figure 5-35 shows examples of synthetic logs inside and outside the lens, illustrating how the small DZs cause variations in intensity mimicking the observed data. Note that the location of the peaks in intensity in the modelled logs will vary between DFN realisations.

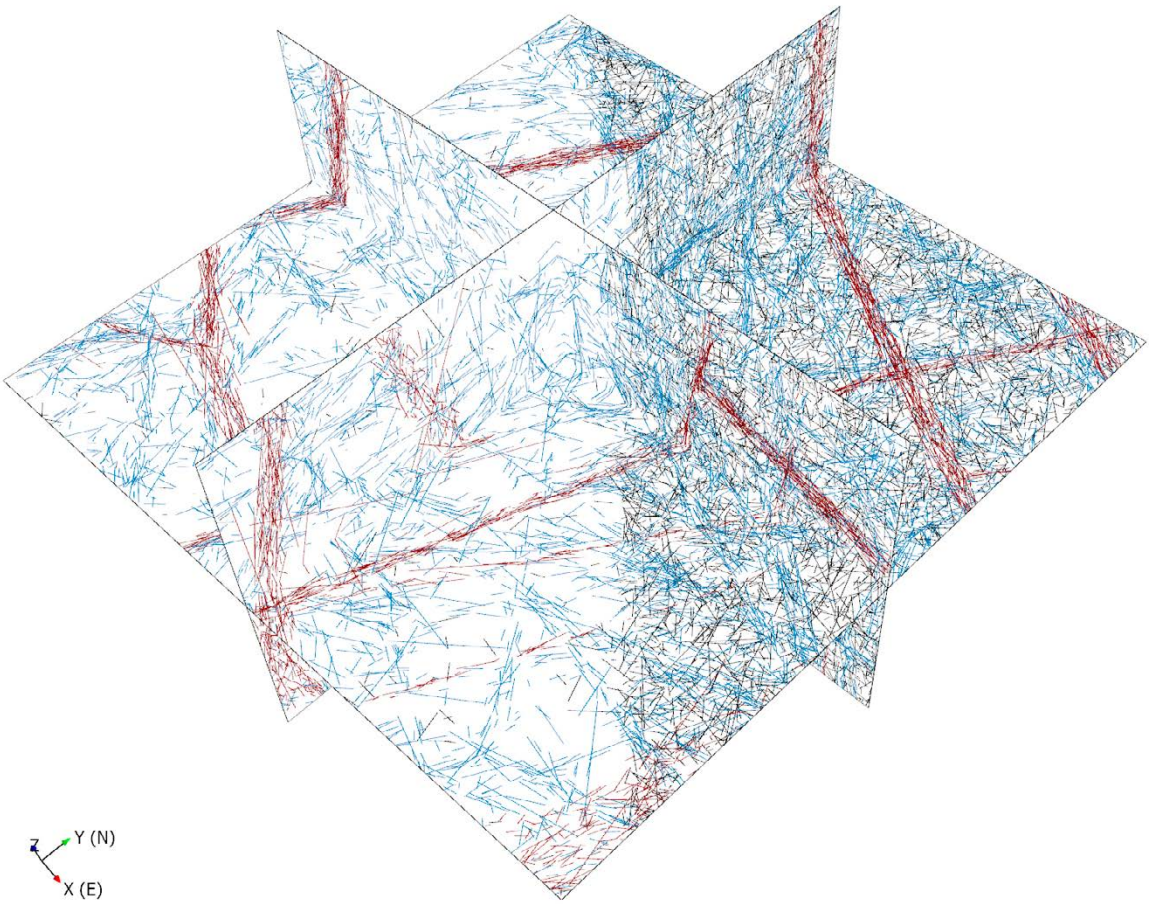

Figure 5-33. *Tracemaps through a 600 m × 600 m × 300 m fractured volume at the north–eastern edge of the lens, showing DZ-related swarm fractures (red), background fractures associated with small DZ-related swarms (blue) and homogenous background fractures (black). The minimum fracture size in the DFN shown is* r_{min} *= 4 m.*

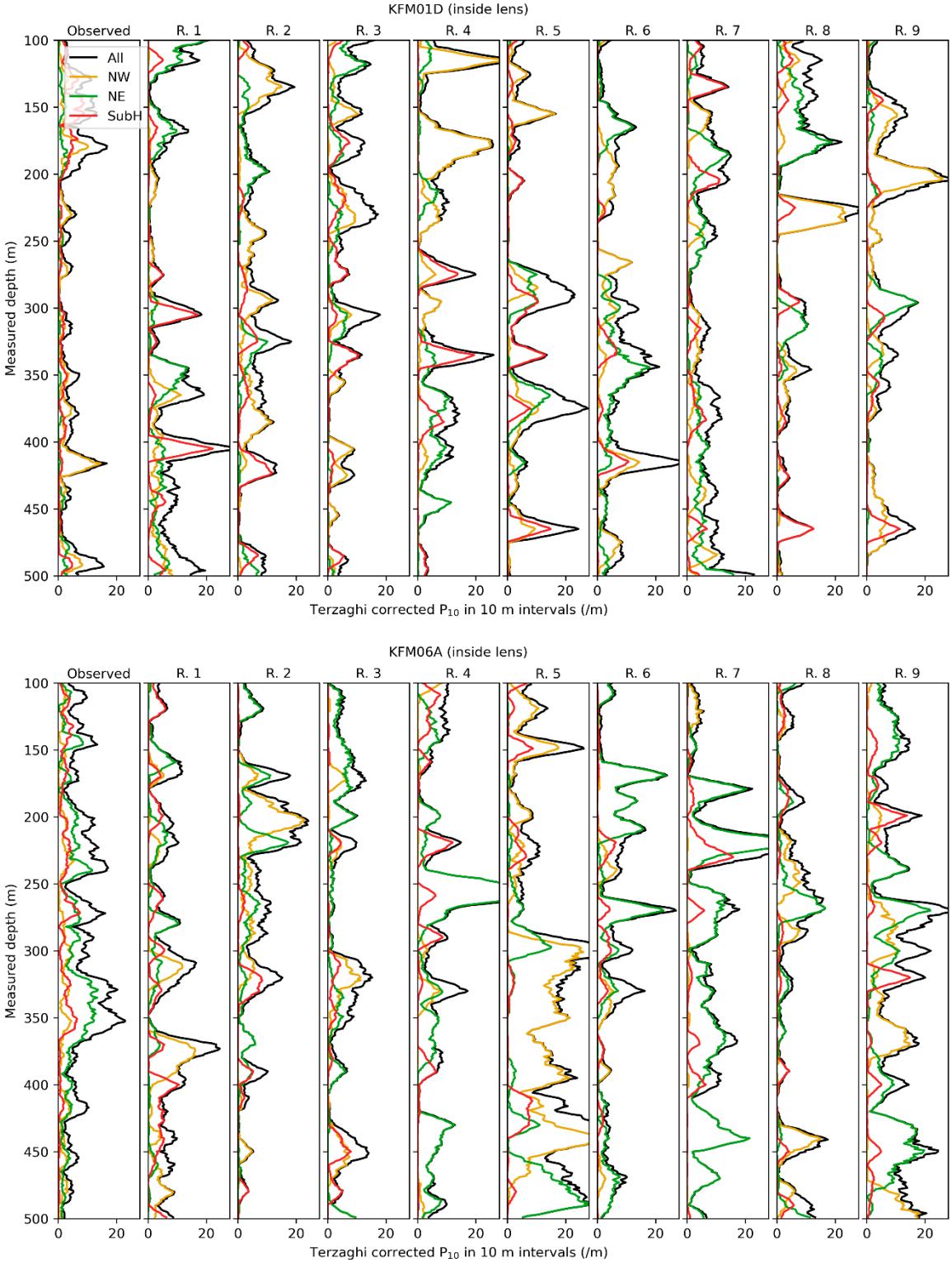

Figure 5-34. *Plots showing a comparison between observed and modelled total fracture intensities for KFM01D and KFM06A (both inside the lens) with nine realisations. The intensities for the individual sets are shown in different colours and all sets, see the legend top left.*

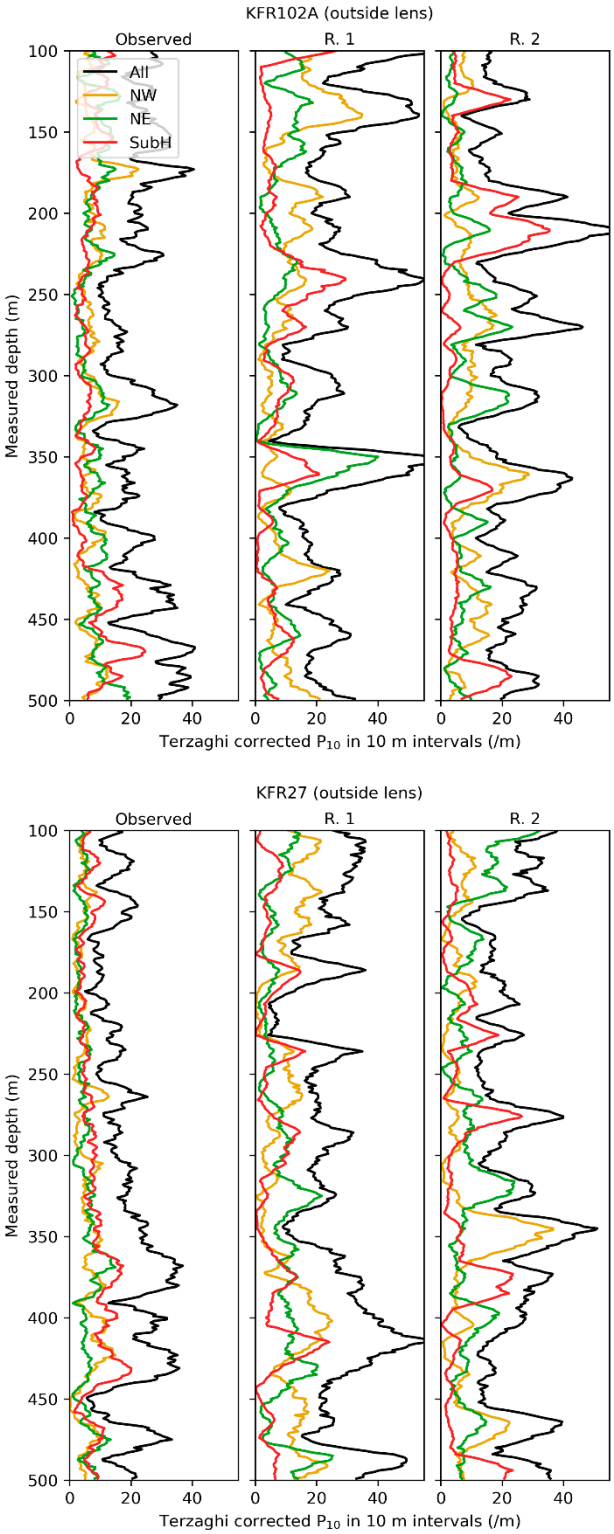

Figure 5-35. *Plots showing a comparison between observed and modelled total fracture intensities for KFR102A and KFR27 (both outside the lens) with two realisations. The intensities for the individual sets are shown in different colours and all sets, see the legend top left.*

5.5 Near-surface fracturing

Evidence for increased fracturing in the near-surface has long been recognised from excavations for the nuclear power plant (Carlsson 1979) and in the SDM-Site modelling through definition of a specific fracture domain, FFM02, and some topography parallel hydraulic ("cage") features inside the lens (Follin et al. 2007b; Fox et al. 2007; Olofsson et al. 2007; Stephens et al. 2008a). The most significant characteristic of this domain is the presence of extensive fractures (sheet joints) parallel to the near horizontal topography as seen on mapping and photographs from the original excavations, see Figure 5-36 and Figure 5-37. Sheet joints, therefore, form a subset of the more broadly defined subhorizontal fractures. Further evidence for these is seen in the borehole log statistics. Figure 4-10 shows that the intensity of SubH fractures is about twice as high in FFM02L as it is in FFM01 and about four times higher in FFM02U (elevation > −30 m). These are thought to have arisen due to subglacial erosional processes of hydraulic jacking and glacial ripping (Krabbendam et al. 2022a; Krabbendam et al. 2022b). The aggregated plot, Figure 5-23, indicates that SubH intensity is higher and less variable across FFM02U than FFM02L, while there is less of a depth trend in FFM01/03/06 & RD034 and FFM04/05 (see Figure 5-21).

That is, intense sheet joints are likely pervasive inside the Forsmark lens in FFM02U, sparser and more erratic in FFM02L and FFM01/03/06, and hard to discern in the borehole data for FFM04/05 from the generally more elevated fracture intensity. Although it should be noted that a lot of the cored data for FFM02U comes from the recent drilling around the access area, as other KFM holes were typically cased in this upper domain, exceptionally high flows during pumping tests in the upper sections of HFM holes inside the Forsmark lens (Follin et al. 2007b) provides evidence that this is a general feature.

The potential for some enhanced sub-vertical fracturing by subglacial beam failure is proposed by (Krabbendam et al. 2021), see Figure 5-36F, G (see sections SKB-036 and SKB-057). A moderate increase in NE sub-vertical fractures, about 50 % in FFM02U compared to FFM01, is seen in Figure 4-10, but the variability between holes overlaps the difference between means for these two domains. Hence, the NE cross-jointing by beam-failure is sporadic, see Figure 5-36C, D, E (see sections SKB-037, SKB-064 and SKB-031). Further, when aggregating data from FFM01/03/06 & RD034 for the purposes of 3D modelling, then there is little difference in the means and variability between FFM02U, FFM02L and FFM01/03/06 & RD034. Hence, it is concluded that such sub-vertical cross-jointing between sheet joints is localised and limited, and so it is neglected here in the DFN-BF1 modelling.

These same characteristics were identified previously by Hartley et al. (2021), and motivated incorporation in a prototype DFN model of near-surface fracturing. Fracture mapping at shallower depths for the new cored holes in the access areas KFM13-27 provided a quantitative basis for splitting P_{32} of SubH fractures into sheet joints and the rest of the set. Sheet joints were modelled as horizontal with a high Fisher concentration to reflect their sub-parallel nature seen in, e.g., Figure 5-36 and Figure 5-37. A higher value of Fisher κ was used here to better honour this feature and mimic the sparsity of self-intersections between the sheet joints. The need to have distinct near-surface zone was already recognise in SR-Site Hydro-DFN (Follin et al. 2007b), where the bedrock was split at −200 m elevation mainly due to a nearly double intensity of SubH open fractures compared to below.

The average P_{10} intensity of SubH fractures logged in FFM02U is 4.6 m^{-1} (Figure 4-10). This contrasts with the significantly lower fracture density values noted in Figure 5-36, due to the different size ranges apparent on the scale of these outcrops relative to boreholes. As in Hartley et al. (2021), SubH fractures are conceived and modelled as two subsets: near-surface sheet joints and pervasive SubH fractures. Since the sheet joints are likely to be reactivated/disturbed by periodic glacial cycles, they are assumed to contain openings (non-sealed). The intensity of open subH fractures was analysed in (Hartley et al., 2021) and so the intensity values in used in the sheet model presented in that study are used here as an initial guess for the sheet joints subset, and then calibrated as discussed in Chapter 7.

The orientations of the sheet joints do not vary much about the horizontal but nonetheless, as seen in Figure 5-36, the variability in dip is sufficient to cause them to intersect. Therefore, the probability of 1 was used for self-termination. No evidence of increased SubH intensity was observed in FFM04 and FFM05 (Figure 5-22). However, the hydrogeological calibration indicated that including some shallow sheet joints outside the lens region provided a better fit with the observed data.

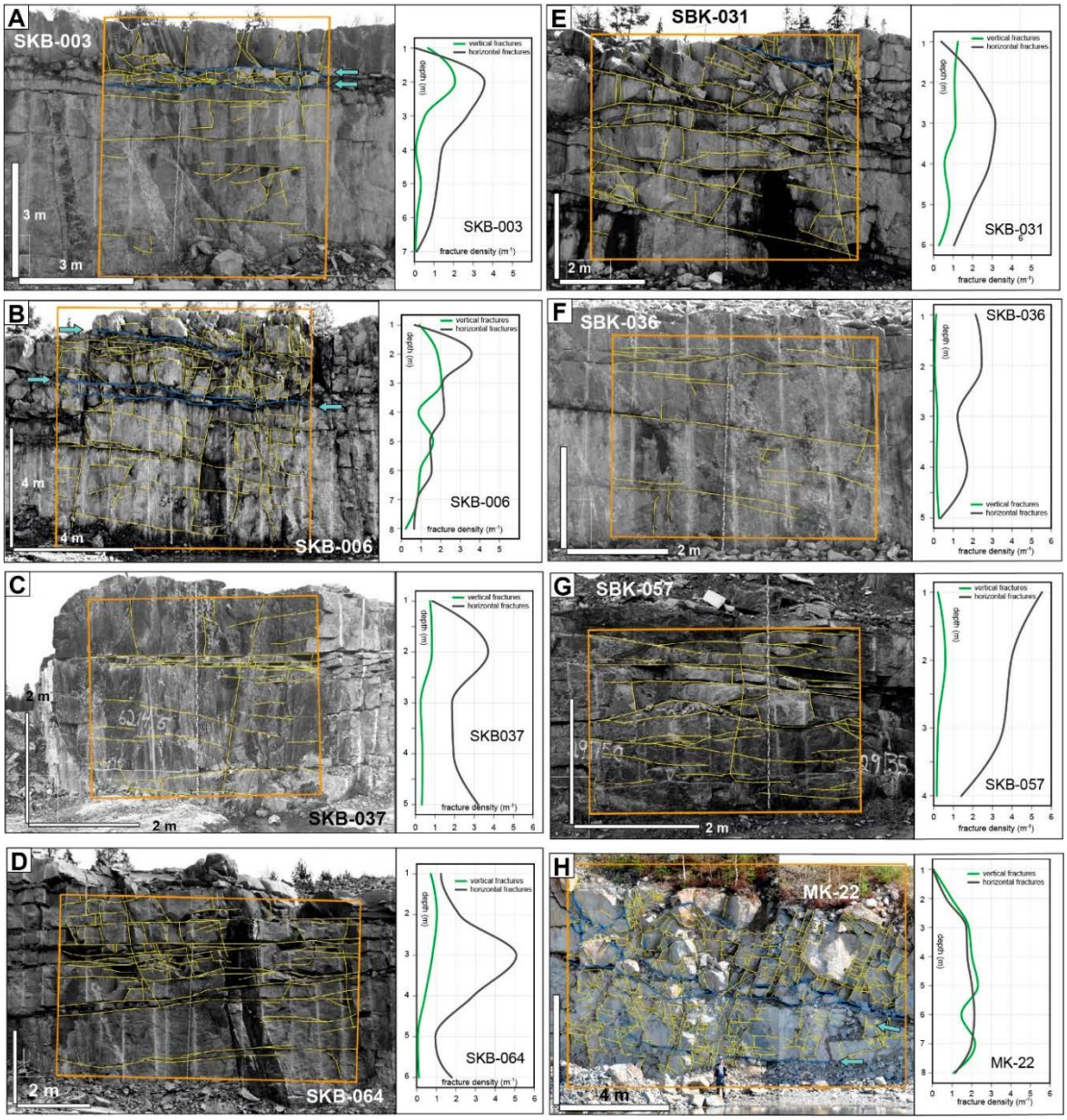

Figure 5-36. *Digitised fracture patterns in the canal excavations at Forsmark (left panels). Blue fractures (with blue arrows) are dilated. Fracture density for subvertical and subhorizontal fractures, against depth (right panels). A-G from Forsmark construction excavations – Photos: Göran Hansson; H: Svagberget quarry, SW of Iggesund. Figure and photos © Svensk Kärnbränslehantering. After (Krabbendam et al. 2021).*

Figure 5-37. *Photograph of the inlet water channel at Forsmark (Follin et al. 2007b).*

The final parameters used in the sheet joint model are presented in Table 5-6. An example realisation is shown in Figure 5-38.

Table 5-6. Parameters for the sheet joints (with some common parameters shown in Table 5-1).

Target P_{32} ($r_{max} > r > r_{min}$) [m^2/m^3] For open sheet joints	FFM02U: 1.85 FFM02L: 0.86 Above −30 m m.a.s.l.: 0.57 Elsewhere: 0	This is 50 % higher than in (Hartley et al., 2021), modified as part of the hydraulic calibration discussed in Chapter 7 in order to better replicate the high flows seen at shallow depths.
Size distribution (r)	Lognormal Mean: 14.7 m Std. 11.9 m (r_{min} 4 m, r_{max} 300 m)	(Hartley et al., 2021)
Orientation distribution	Horizontal	
Fisher κ	500	To give a small amount of scatter from the bootstrapped value
Termination probability	1	To ensure terminations in the rare cases they occur as seen in Figure 5-36.

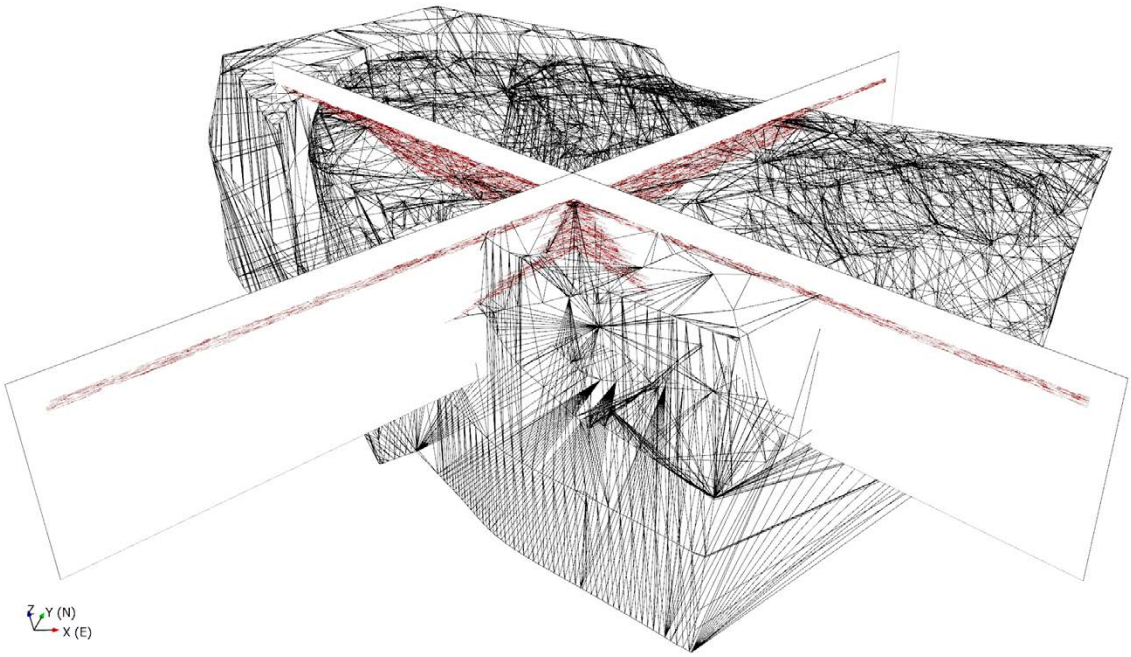

Figure 5-38. *View of FFM01/02/03/06 and RD034 (black wireframes) with two vertical cross sections (along lens and across lens) showing one realisation of open sheet joint fractures (red) going to greater depth in FFM02 in the footwall of ZFMA2.*

5.6 Method of fracture generation and results

Although fractures are created set by set using the G-DFN algorithm, following their relative ages (NW, NE then SubH), it was necessary, for modelling purposes, to generate all large DZ prior to background fractures. This is because growing a large range of fracture scales all at once prohibits the growth of any large DZ in the younger sets, smaller fractures have the chance to terminate on larger ones being one of the rules. Consequently, each set of stochastic DZ midplanes was only able to terminate on midplanes in the same or preceding sets of stochastic or deterministic midplanes, and each set of Small DZ midplanes was only able to terminate on midplanes in same or preceding sets of Small DZ midplanes.

For large DZ, fracture orientation distributions are defined by their associated grids. For small DZ, their presence in a cell increases the relative intensity of the set to which they belong, favouring orientations from distribution for that set. It is not currently possible to grow G-DFN fractures according to different orientation or intensity distributions concurrently, so these fracture sets are grown sequentially. The order of this sequence was chosen to be:

- DZ swarms;
- Small DZ swarms; and then
- background individual fractures.

This order reflects the concentration of fractures in the DZ (swarms) likely reflecting the localisation of stress at the tips of pre-existing larger structures, and that larger brittle structures often coincide with previous ductile deformation or combined with it. This sequence is run for each set in their formation order, as for the midplanes. This means, for example, that individual fractures within the SubH DZ swarms can terminate on the NW homogenous background fractures where the former are larger. The near-surface fractures are generated in last step and can only terminate on themselves.

5.6.1 Implementing tectonic domains

The relative proportions of open and closed swarm fractures (see Section 7.1) and the intensity of the small DZ-related fractures are characterised in two domains: inside and outside the tectonic lens. This reflects the contrasting stress and lithological configurations inside and outside the lens. The domain considered to represent the Forsmark lens is defined as FFM01/02/03/06 and RD034 (Figure 5-39). Figure 2-7 shows how the SE end of the FFM01 and FFM03 geometries is truncated by the limits of the modelled domain. This is problematic for the DFN modelling because this area should be modelled as being inside the lens. Consequently, parts of RFM017 and RFM029R were used to extrapolate the lens to the SE, as shown in Figure 5-39.

Characterisation of the background fractures in individual FFM regions was considered, however there is insufficient borehole data to confidently characterise FFM03, FFM04 and RFM034 individually (Follin et al. 2007b; Olofsson et al. 2007).

The superposition of the near surface fracturing (Section 5.4) with the DZ-related fracture swarms means that there are effectively five domains for fracture intensity:

1. Inside lens and FFM02U including additional near-surface fracturing;
2. Inside lens and FFM0L including additional lower near-surface fracturing;
3. Inside lens including additional near-surface fracturing (i.e. FFM01/03/06, RD034 and expanded lens region above −30 m elevation);
4. Inside lens without near-surface fracturing (i.e. FFM01/03/06, RD034 and expanded lens region below −30 m elevation); and
5. Outside lens.

The variation in intensity between the two domains is in addition to other spatial variabilities such as the localisation of orientations that result from bootstrapping (see Section 5.1) and fracture hydraulic properties (See Chapter 7). The contrasting fracture intensities inside and outside the lens and the higher proportion of homogenous background fractures outside the lens results in a contrasting pattern of fracturing as seen in Figure 5-40.

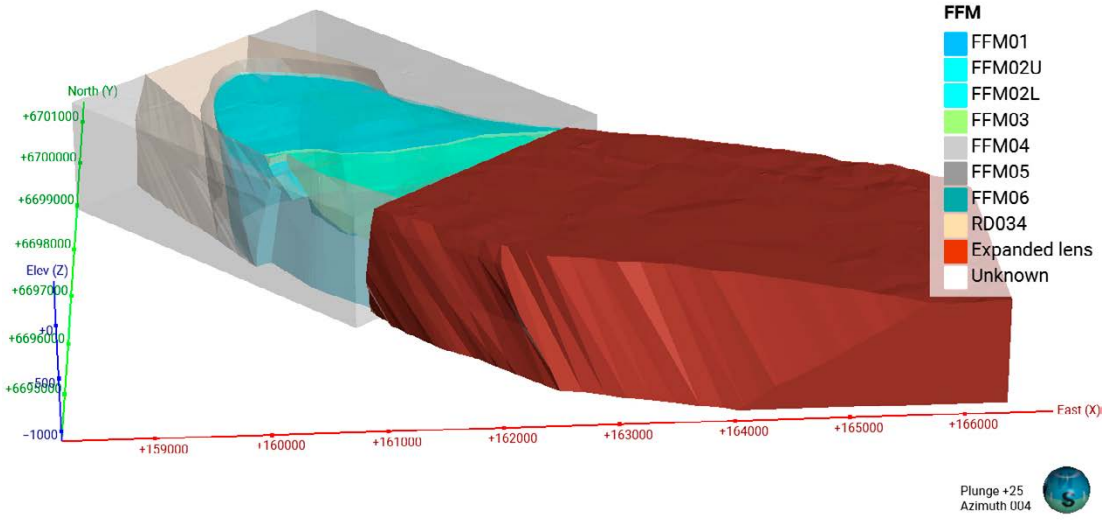

Figure 5-39. *View of the domain subdivided into FFM regions, and the parts of RFM017 and RFM029 considered as being the SE extension of the lens.*

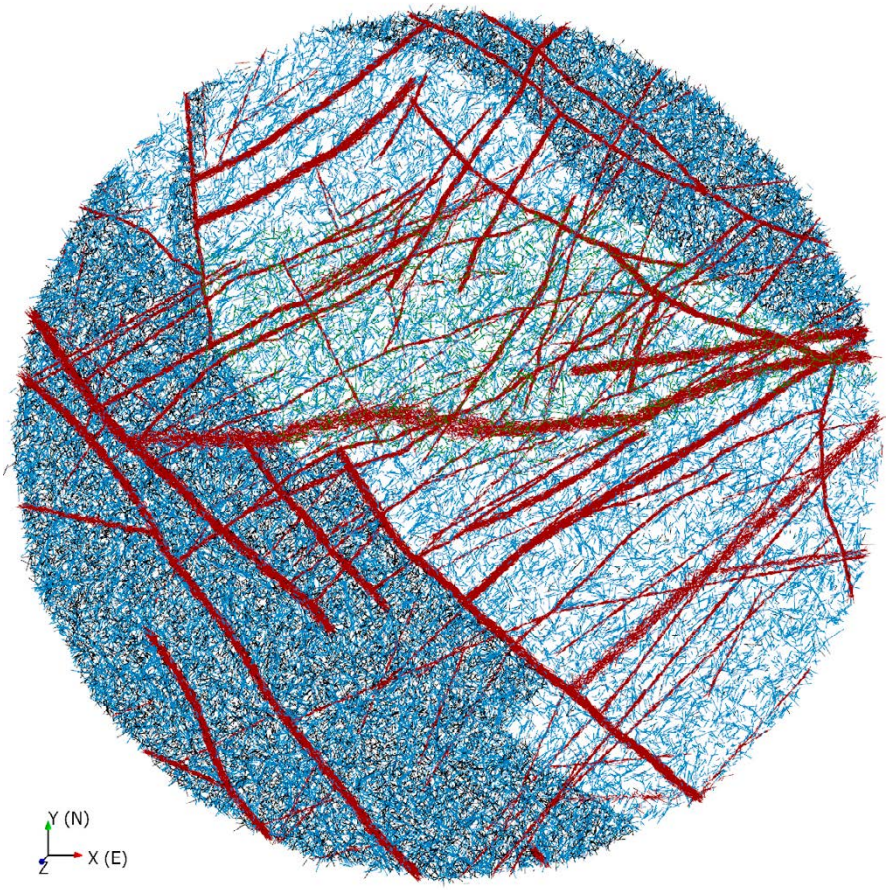

Figure 5-40. *Horizontal tracemap at elevation −60 m through a model of all fractures (open and sealed) in a cylindrical region with a 2 km radius and centred on HFM14 as used in hydraulic interference tests models in Section 7.5. DZ-related fractures are shown in red, small DZ-related fractures in blue, background individual fractures in black and sheet joints in green, for r_{min} = 12 m. The clear change in intensity coincides with tectonic domains based on a mesh representation of rock and fracture domains, cf. Figure 2-2 and Figure 2-6 and Figure 2-7.*

5.7 Summary and potential future refinements

The analyses described in this chapter have provided the basis both for updating the geometric conceptual model for fracturing and for parameterising a DFN model consistent with those concepts. The new concepts developed since the SDM-Site model were inspired by developments in the Geological and DFN modelling methodologies, including:

- Describing fracturing as occurring through a sequence of main deformation phases that are mimicked in the model by generating firstly DZ using a G-DFN for a sequence of sets, and then background DZ and fractures also as a sequence of grown sets;
- Describing variability in orientations by inverse distance weighted bootstrapping fracture orientations within three simplified global sets;
- Representing deformation zones as domains of swarm fractures representing their damage zones and variations in intensity across their core (Choi et al. 2016). Also included is stochastic variability in their size, connectivity and properties creating a mechanism for them to have a zone of influence and in-plane variability;
- Representing additional stochastic deformation zones outside the focus volume for characterisation;
- Representing variability on a continuous range of scales by introducing Small DZ swarms as part of the background fracturing; and
- Identifying differences in fracture characteristics, including spatial variability, between inside the lens and outside, by analysing both KFM and KFR fracture data.

These are the key conceptual elements introduced in the DFN-BF1 model. Potential further refinements of the model are noted below, although it may require additional information from underground investigations and associated modelling needs to warrant their development:

- FFM specific intensities (should additional data be acquired to support them), see Section 5.4;
- Distinct α and β values to introduce asymmetry in the DZ intensity distribution (see Section 5.3) should differences between hanging wall and footwall intensities be observed;
- A target DZ intensity that scales with structure size (see Section 5.3).
- Identifying potential drivers for spatial variability in the sheet joint intensity such as surface curvature, with the additional possibility of a sporadic subvertical joint set where sheet joints are most intense (see Section 5.5);
- Harmonise quantitative information on termination behaviour of interpreted DZ and fractures on their respective scales with the qualitative geological description of deformation phases (see Subsection 5.4.4);
- Inclusion of data from crush intervals (too fractured to be logged) and sealed networks in the calculations of fracture intensity within DZ damage zones (see Subsection 5.4.1);
- NE DZ swarms have more extra intensity than SubH and NW (Figure 4-10.). Implying the DZ-related swarm intensity could be set specific, and might result in more accurate flow predictions;
- Assess the possibility of distinct size scaling and termination behaviour for the background fractures inside and outside the lens based on outcrops and surface mapping in the SFR and SFK facilities; and
- Test the sensitivity to different k_r values when calculating the intensity of the DZ-related swarms.

By way of a summary illustration of the DFN geometries, Figure 5-41 and Figure 5-42 show views of DFN tracemaps in the central SFK and SFR volumes, respectively. The reference repository layouts are superimposed on the DFN model, but these layouts are not optimised against any realisations of the model. The difference in fracture intensity (higher in the SFR region) and fracturing style (more background individual fracturing in the SFR region) may be observed. Recall from Subsection 5.4.3 that inside the lens 90 % of the background fracturing is associated to small DZ shown in blue in Figure 5-41. By contrast 50 % of the background fracturing is associated to individual fractures outside the lens shown in black in Figure 5-42.

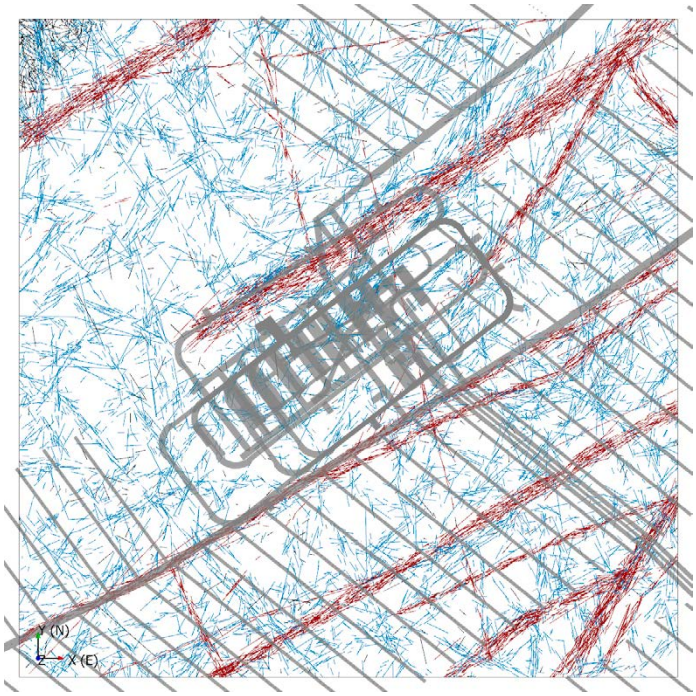

Figure 5-41. *Plan view of a 800 m by 800 m area around the central access tunnels and planned tunnel layout (shown in grey), with fracture traces from a single realisation at −470 m elevation, showing DZ-related fractures in red, Small DZ-related fractures in blue and background individual fractures in black. The r_{min} for the DFN was 4 m.*

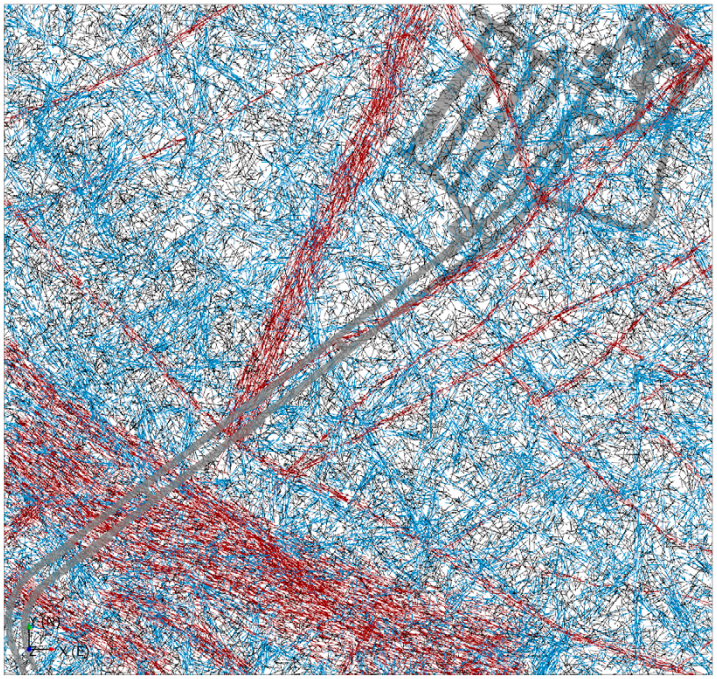

Figure 5-42. *Plan view of a 900 m × 850 m area around the SFR tunnels (shown in grey), with fracture traces from a single realisation at −70 m elevation, showing DZ-related swarms in red, small DZ-related swarms in blue and background individual fractures in black. The r_{min} for the DFN was 4 m.*

6 Rock mechanics description

The geometrical properties of the DFN-BF1 model defined in Chapter 5 provide the spatial framework for describing the main components of rock mechanical, hydrogeological and hydrogeochemical properties of the bedrock through the addition of discipline-specific properties defined on each fracture. These mechanical, hydrogeological and mineralogical properties of fractures are, however, inter-related. For example, large apertures filled or coated with soft clay materials will have a higher slip tendency, likely correlate with higher flows, and provide sorption capacity. The most significant coupling for the current work is that between rock mechanics and hydraulics. The assignment of hydraulic properties of fractures is founded on understanding of the spatial variability of the current *in situ* stress tensor across the site and mechanical properties of fractures, intact rock and the rock mass. The stress field and rock mechanical properties provide an initial estimate for hydraulic properties that can then be calibrated to flow measurements. This approach provides for cross-disciplinary integration with lessons from hydraulic calibration potentially feeding back to the adjustment of fracture mechanical properties and calculation of 3D stress. It also supports a physically-based means to extrapolate likely hydraulic conditions to volumes not characterised, such as between boreholes, at depth and outside areas of direct investigation. The main components required for this coupling are the stress field, a set of suitable hydromechanical models and associated site-specific mechanical properties for both intact rock and structures.

6.1 Site stress model

Two models for the stress field were considered in the DFN Baseline model:

- The in situ stress state model at the Forsmark site (Martin 2007), varying only by elevation (denoted the 1D stress model in the following); and
- The numerically determined stress field model (denoted as the 3D stress model in the following), originally (Hakala et al. 2019), but updated to (Valli et al. 2023) in the final DFN-BF1.

The 1D model is adequate for determining the average anisotropic stress field inside the Forsmark lens in the footwall of ZFMA2, which is the target host volume for the SFK repository, as shown in Figure 6-1. However, typical stress magnitudes are different in the hanging wall of ZFMA2 and outside the lens, such as around SFR. Hence, the 1D stress model is sufficient for modelling on the facility scale, but it is necessary to use the 3D stress model for modelling multiple domains and the regional-scale. The different stress magnitude between the footwall (FFM01/02/06) and the hanging wall (FFM03) is the main reason to expect differences in hydraulic properties between these two domains rather than difference in fracture geometries (see Section 5.4) within the greater lens domain.

The measured data also displays significant local variability within both the footwall and hanging wall, as expected in a high strength rock, e.g. (Martin and Chandler 1993). The 3D stress model is obtained from 3DEC modelling (ITASCA 2022), which includes spatial variability in rock mass properties through inclusion of a deterministic DZ model with different mechanical deformation and strength properties for the deterministic DZ with respect to the background rock mass, and between fracture domains. When subject to a load this structure driven variability creates spatial variations in simulated stress magnitudes and anisotropy consistent with some aspects of measurements. The 3D stress model, therefore, provides initial starting point for mechanistic stress variations, and ultimately flow. The mechanical properties of intact rock and structures and loading boundary conditions have in part been calibrated to describe some of the key features of the observed stress data. These properties provide an initial guess for a suitable parameterisation of the mechanical properties of both DZ and smaller scale fractures in the DFN model when simulating hydromechanical effects. Hence, the 3D stress model can be used both to provide the stress field and a guide to stiffness parameters to use in estimating how fractures and zones respond hydraulically to those stresses. Thereby a degree of integration between mechanical and DFN modelling is achieved. A full integration of the effects of fracture geometries, mechanics and hydraulics back to the regional-scale rock mass and stress calculations is, however, beyond the scope of this study.

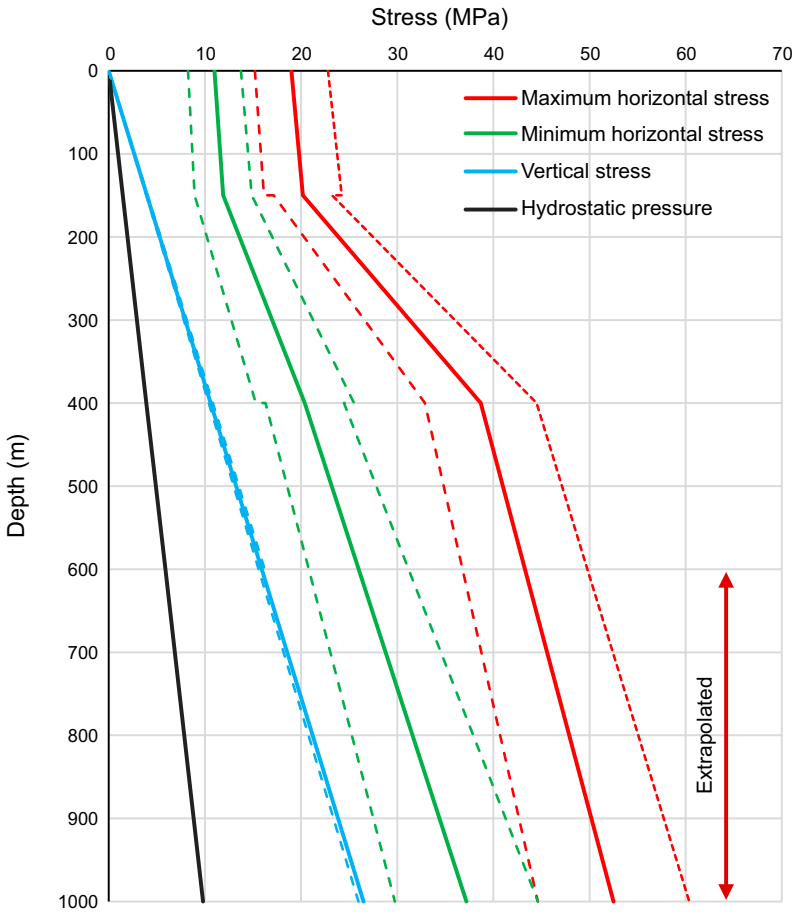

Figure 6-1. *Principal stress components predicted by the 1D stress model (Martin 2007) . Here, the stress is extrapolated below the depth of 600 m.*

The 3DEC modelling was organised into two phases with first phase calibrating the DZ model and boundary conditions against stress measurements, and the second performing a sensitivity analysis. The stress field used here corresponds to the base case from that second phase (Valli et al. 2023), delivered by Diego Mas Ivars on 11/01/23, which corresponds to Case 2-1 of first phase of 3D stress modelling as defined in Table 3-7 of (Hakala et al. 2019). That model had slightly different elastic parameters for fracture domain FFM01/02/06 and the rest of rock mass and was modified by the presence of undulating DZ structures (i.e. represented as triangulated surfaces) with a defined stiffness/strength parameters for each zone, and boundary thrust conditions. The case used a friction angle of 36° for DZ (31.5° for Singö zone) and cohesion 0.7 MPa (0.4 MPa for Singö zone). In the 3DEC model the DZ had no thickness, and so modelled stress changes tend to be abrupt. It should be noted that undulations were introduced to the surfaces with a maximum deviation of 40 m, and so any resulting steps in stress may be offset from the centre of the DZ by up to 40 m.

An illustration of the 3D stress field is shown in Figure 3-6. How the stress field manifests in the locations of selected boreholes is shown in Figure 6-2 through Figure 6-4 for domains FFM01/02/06, the transition from FFM03 to FFM01 and FFM05, respectively. These left-hand set of logs show the magnitudes of principal stresses, S1, S2, S3, pore pressure (equal to hydrostatic pressure), Pp, the middle logs are fracture intensities by set, and the right-hand log shows the depths of discrete flows from PFL logging. It is apparent that the minimum principal effective stress (according to the Terzaghi's principle), S3-Pp, is relatively close to zero in the top 300–400 m of the boreholes and this is where flows are concentrated, especially where there are clusters of SubH fractures that will be experience this low effective normal stress. Increases in pore pressure, such as those induced by an advancing ice front or glacial meltwater, may result in hydraulic jacking of sub-horizontal fractures. Possible indications, in the form of sediment filled sub-horizontal fractures, of hydraulic jacking events occurring during previous glaciations have been found at several Swedish sites including Forsmark to depths of a few tens of metres (Leijon 2005; Hökmark et al. 2006; Lönnqvist and Hökmark 2010).

KFM01A is mostly in the footwall of ZFMA2, with low stresses in the hanging wall of this major structure, moderate stresses above −300 m elevation and relatively high stresses below this (see Figure 6-2). The borehole runs close to and almost parallel to ZFMENE1192A, such that it intersects two splays of this zone. There is limited change in modelled stress across the two splays, and yet there is a cluster of flows associated with the upper splay of this structure. One possible hypothesis is that in reality there is either lower normal or shear stiffness in this zone resulting in more fracture dilation than modelled in the 3D stress modelling.

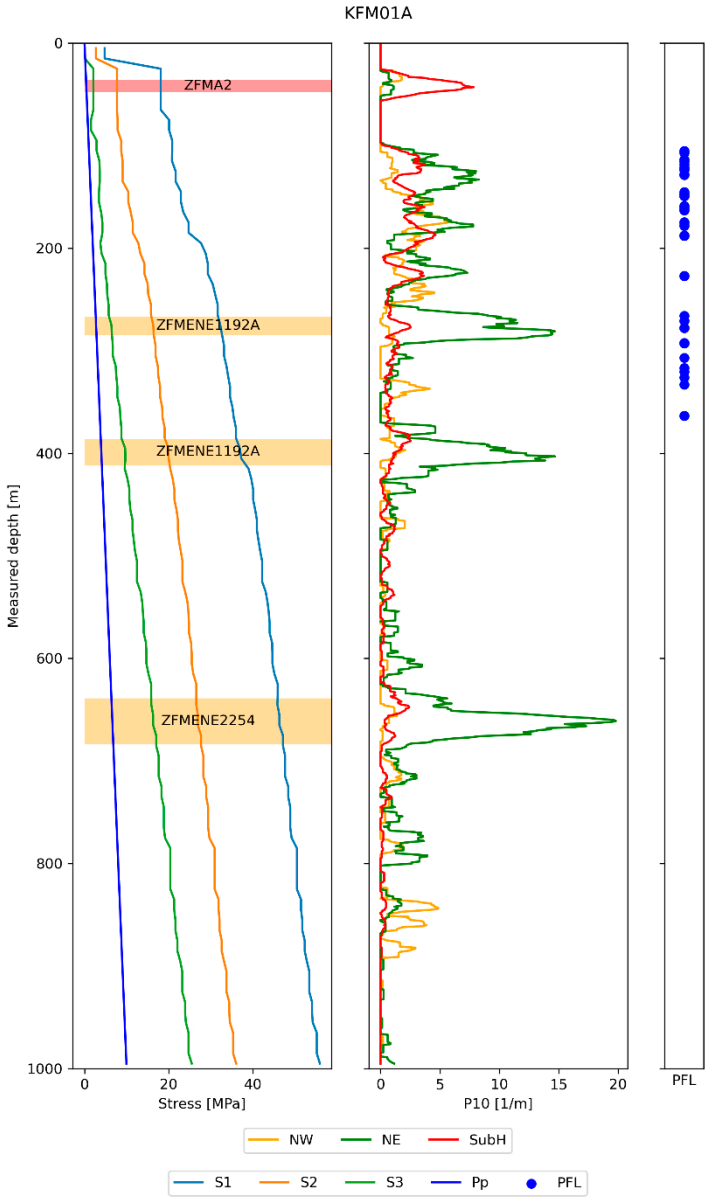

Figure 6-2. *Principal stress components, S_1, S_2, S_3 and pore pressure, P_p, determined by the 3D stress model (Valli et al. 2023) as projected on to KFM01A (for illustration purposes) which is located in FFM01/02/06.*

KFM02A passes from FFM03 in the hanging wall of ZFMA2 to FFM01 at about 425 m depth, see Figure 6-3. A clear increase in modelled stress is seen in the footwall and there are many discrete flows detected coincident with subH fractures swarms. The high flows in ZFMF1 may suggest that this structure is maintaining the relatively lower stresses to greater depth than modelled, recalling the 40 m undulations in the DZ surfaces for the stress modelling. It is noticeable that flows cluster where SubH fractures cluster, which are subject to relatively lower effective normal stress.

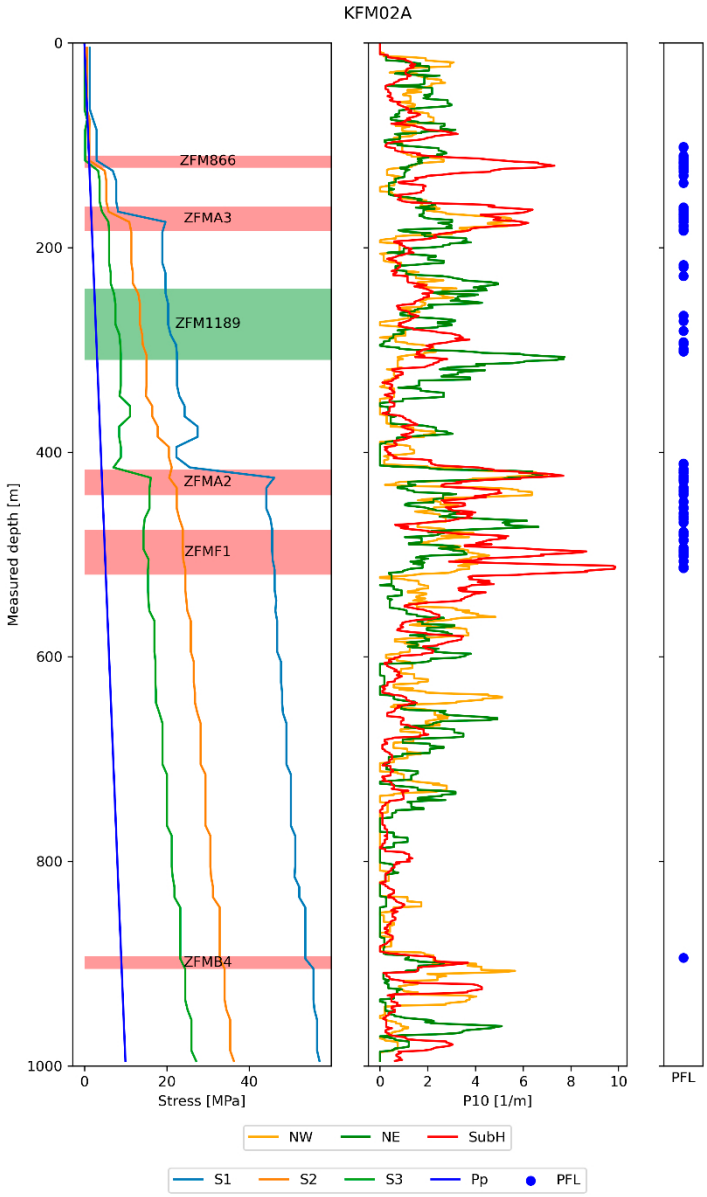

Figure 6-3. *Principal stress components determined by the 3D stress model (Valli et al. 2023) as projected on to KFM02A which crosses from FFM03 into FFM01/06 where it intercepts ZFMA2.*

KFR102A is an inclined hole lying in FFM05 outside the lens, see Figure 6-4. Here, the minimum modelled stress is close to hydrostatic pressure in the upper 280 m in the hanging wall of ZFMNE3122, increasing in the footwall (again recalling the 40 m undulations in DZ surfaces for the stress model). Flows tend to cluster in this region of relatively low stress, particular where there are clusters of SubH fractures or all three sets of fractures in the hanging wall. In the footwall, flows are mainly restricted to a cluster of all three sets of fractures in the hanging wall of ZFMENE3115. The modelled stress looks to have the right behaviour in this borehole, although the flows coincident with hanging wall of ZFMENE3115 may suggest in reality the zone is causing a drop in local stress, perhaps due to a lower local stiffness in the zone.

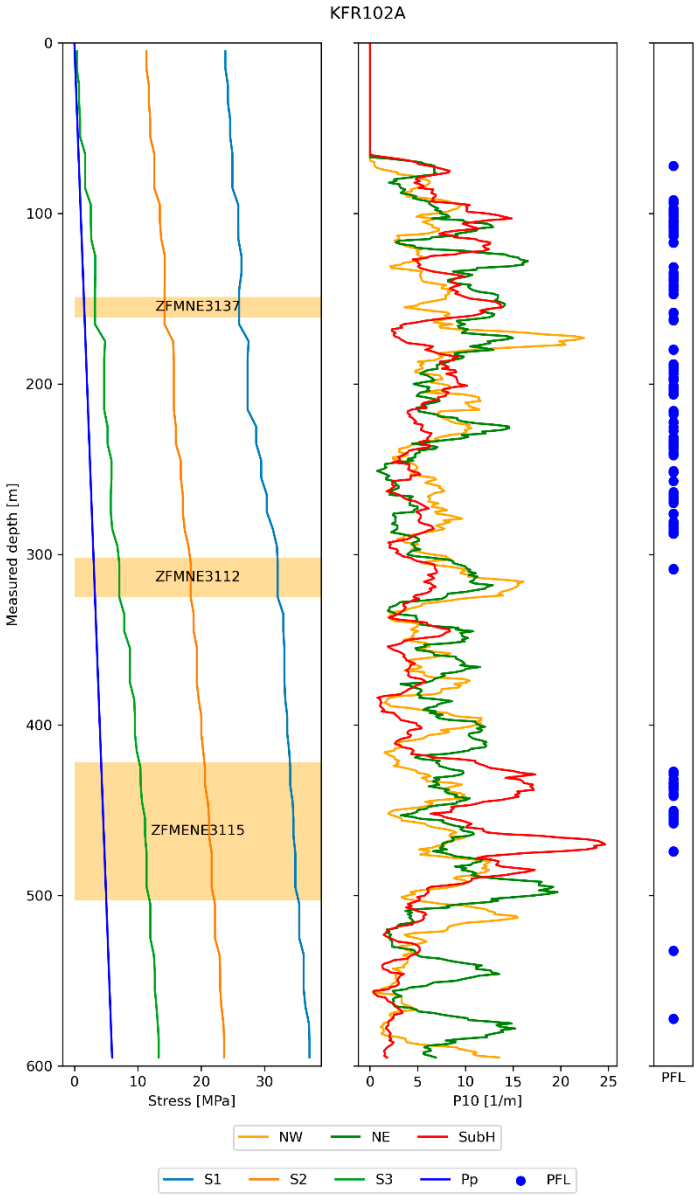

Figure 6-4. *Principal stress components determined by the 3D stress model (Valli et al. 2023) as projected on to KFR102A which crosses through FFM05.*

In summary, the 3D stress model provides a mechanism both to explain some of the observed heterogeneity in flow and to extrapolate predictions of hydraulic conditions across the regional-scale. For example, the main driver for differences in flow characteristics between FFM01 and FFM03, both inside the lens, would seem to be the different stress magnitudes between the hanging wall and foot wall of ZFMA2 rather than a difference in fracturing. Flows often cluster where there are swarms of SubH fracturing that are subject to relatively low effective normal stress. The clustering of flow near some deformation zones may result from a combination of both the increased connectivity that comes with the increased intensity of fracturing in damage zones and a softening of the mechanical properties leading to a reduction in stress and fracture dilation.

The 3D stress model developed by (Valli et al. 2023) was able to calibrate some mechanical properties of deformation zones and loading boundary conditions against broad trends, statistics and variability in measured stress data. Incorporating this 3D stress field into a hydromechanical description of DFN hydraulics provides a one-way coupling of mechanics with flow, but also opens possibilities for further calibration against measured flow measurements, see Chapter 7. In principle, lessons learnt from calibrating a hydromechanical model could be fed back to the rock mechanical model as a basis for a wider integration of bedrock description and uncertainty reduction.

The effects of magnitudes of effective normal stress and stress anisotropy on fracture hydraulics can be examined by calculating the effective normal and shear stress on each fracture logged in the boreholes, plotting them on a Mohr diagram, and highlighting the sub-population of transmissive fractures, see (Hartley et al. 2018; Mattila and Follin 2019), for example. Figure 6-5 illustrates such analysis using the 1D stress model to consider the simplified case where stress magnitudes are only varying by depth. The plots are sorted in three depth zones. It shows that the flows, where they occur, coincide mostly with low effective normal stress for each depth. High shear to normal effective stress ratios on fractures leading to a critical stress state, perhaps also augments flow, but low normal stress seems to be key. Low normal stress is not sufficient by itself, the fracture also needs to be connected and open, see (Mattila and Follin 2019). There are some relatively high flows occurring at higher normal stresses, contradicting the general interpretation. It can be noted that linking discrete flows to individual fractures may not always identify the actual fracture where flow occurs. Alternative nearby candidate fractures are highlighted in the linking process, but an assessment whether these correspond to fractures at lower effective normal stress has not been made here. Also, it can be noted that the in situ stress field of the Forsmark site has variability in magnitude and direction, estimated in Table 7-4 of (Martin 2007) to be order ± 20 % in magnitude and ± 20° in trend, which is not captured when applying the 1D stress field used in these plots. Finally, some fracture surfaces may be unmated after undergoing a significant shear displacement so that they never close even at high stress levels (i.e. some fractures may have a larger residual aperture compared to other fractures).

Sheet joints have low dips and so low effective normal stress, and hence coincide with the clusters of measured transmissivities, although transmissivity and the existence of flow can be highly variable depending on the type of fracture infilling materials and voids in these features.

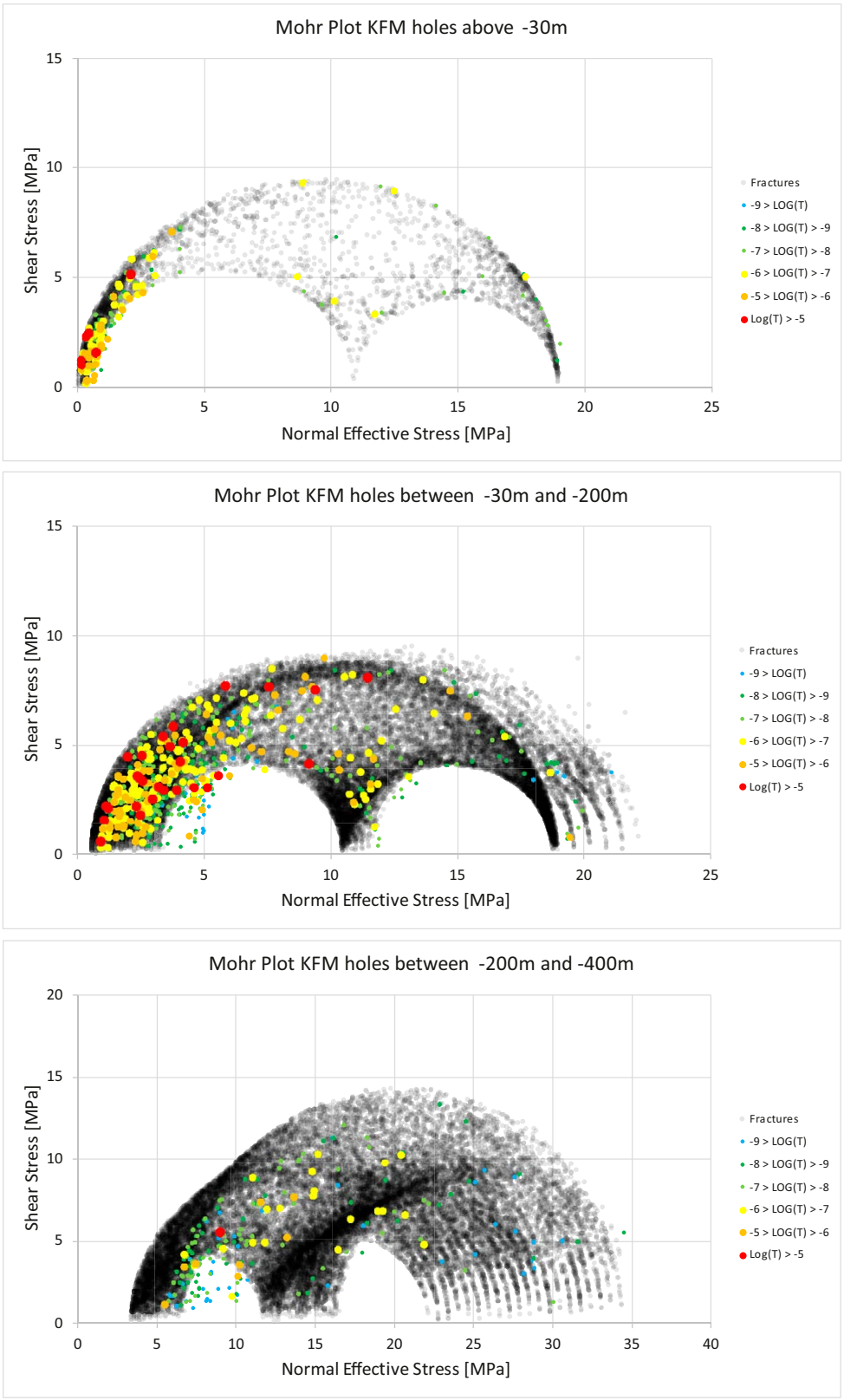

Figure 6-5. *Mohr plots for each observed fracture in KFM boreholes using the analytical 1D stress model. Fractures are sorted by domains: FFM02 above elevation −30 m(top), in FFM01/FFM06 with elevations −30 m to −200 m (middle) and in FFM01/FFM06 with elevations −200 m to −400 m (bottom), and each outside deformation zones transmissive fractures coloured by their magnitude of interpreted transmissivity.*

Figure 6-6 through Figure 6-10 considers the first of these issues by performing the same analysis using the 3D stress model. The heterogeneity in stress in that model results in a blurring of the stress envelope even when dividing the data by elevation. It is seen that the number of transmissive fractures at high normal stresses reduces in this case, presumably because the model includes some softening of deformation zones and therefore lower stresses around these volumes where flow is more likely to occur. Again, most flows cluster around low effective normal stress at all elevations, with magnitudes decreasing as the minimum stress increases with depth. There are some anomalous fractures with flows at moderate normal stress, and again might be due to the 3D stress model not matching the actual stress conditions around all deformation zones, or some actual high residual apertures on unmated fracture surfaces.

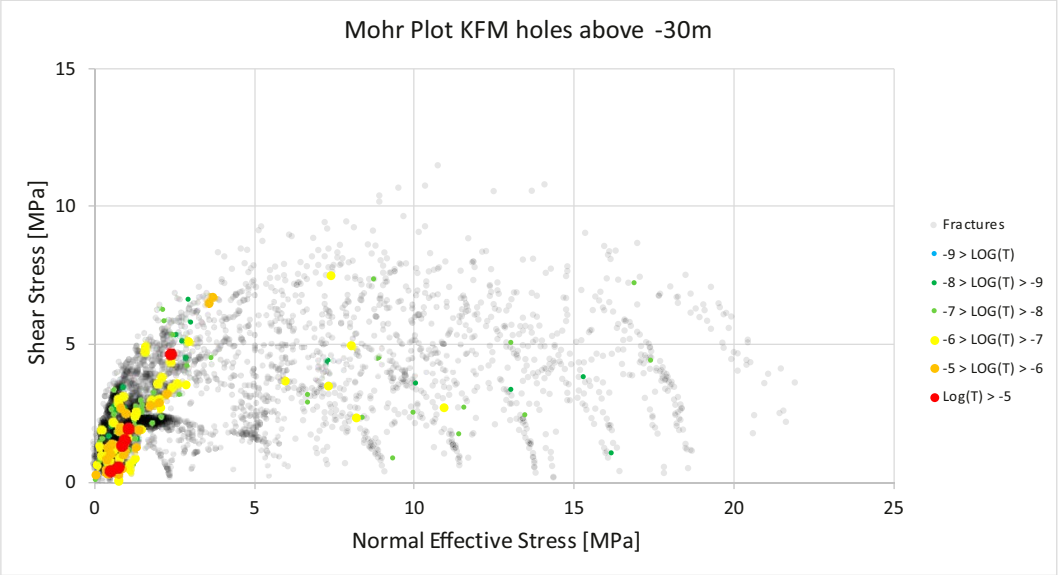

Figure 6-6. *Mohr plots for each observed fracture in KFM boreholes using the 3D stress model (Valli et al. 2023). Only fractures above elevation −30 m are shown and each transmissive fractures coloured by their magnitude of interpreted transmissivity.*

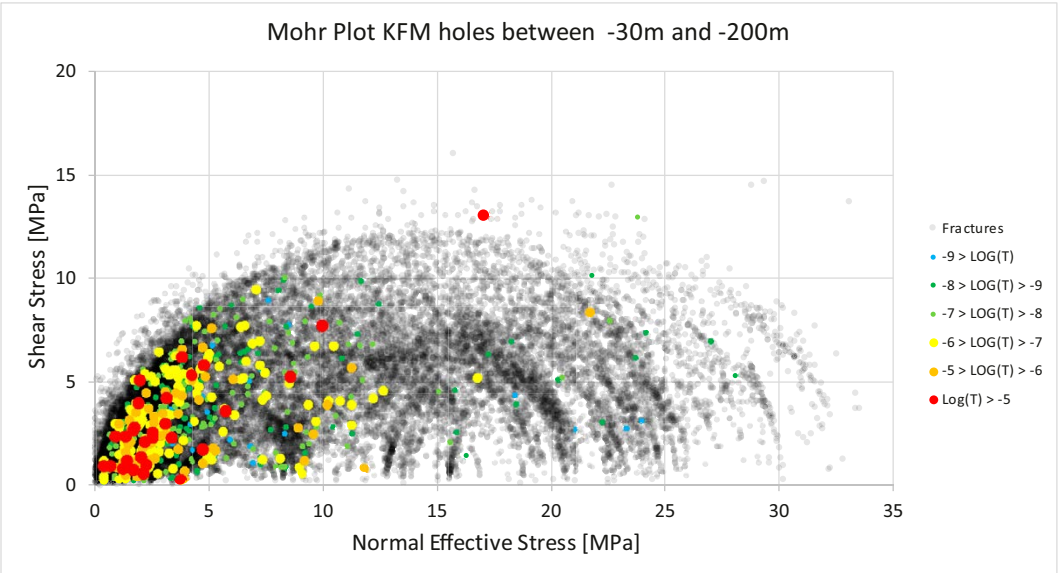

Figure 6-7. *Mohr plots for each observed fracture in KFM boreholes using the 3D stress model (Valli et al. 2023). Only fractures with elevation between −30 m to −200 m are shown and each transmissive fractures coloured by their magnitude of interpreted transmissivity.*

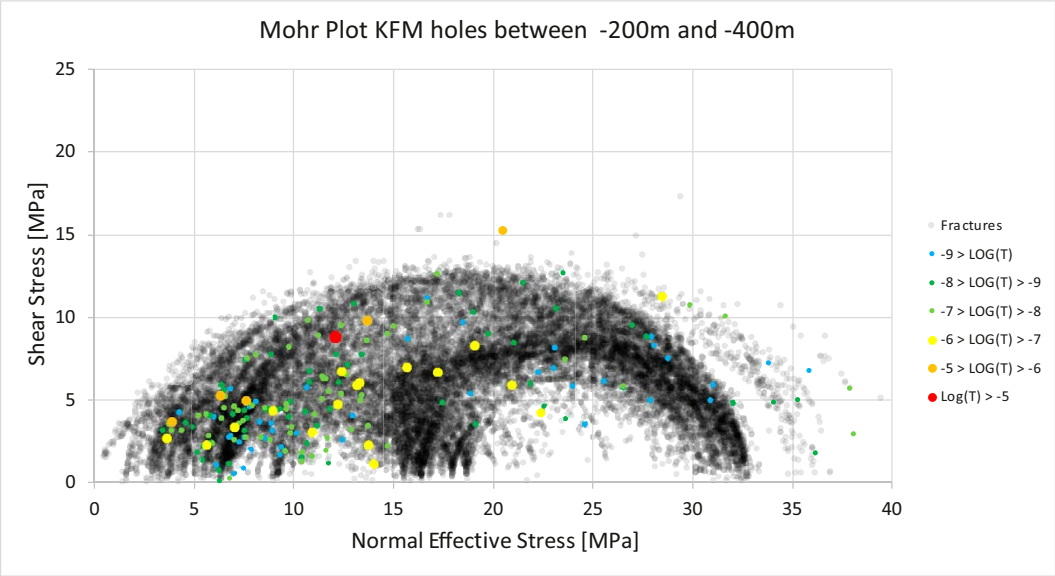

Figure 6-8. *Mohr plots for each observed fracture in KFM boreholes using the 3D stress model (Valli et al. 2023). Only fractures with elevation between −200 m to −400 m are shown and each transmissive fractures overlain coloured by their magnitude of interpreted transmissivity.*

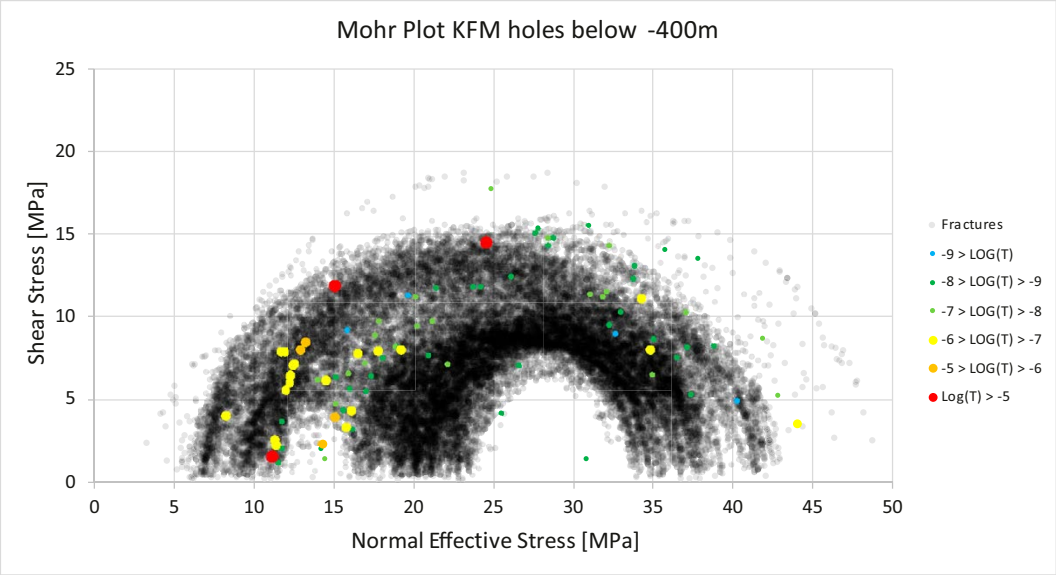

Figure 6-9. *Mohr plots for each observed fracture in KFM boreholes using the 3D stress model (Valli et al. 2023). Only fractures with elevation less than −400 m are shown and each transmissive fractures overlain coloured by their magnitude of interpreted transmissivity.*

Although most transmissive fractures have low effective normal stress, approximately below the midpoint between S_3 and S_2, many are also critically stressed. Hakala et al. (2019) uses a friction angle of 36° for DZ and 31.5° for the Singö zone. Figure 6-10 considers a range of Mohr-Coulomb (M-C) failure envelopes from 163 tilt tests at the Forsmark site with cohesion varying from 0.2–0.8 Mpa (mean 0.5 MPa) and peak friction angle from 26° to 38° (mean 34°), and alternative Barton-Bandis (B-B) failure envelopes (Barton and Choubey 1977) with residual friction angle ranging from 17° to 34° (mean 26°), JRC from 2 to 9 (mean 6), and JCS 33 to 156 MPa (mean 83 MPa). It is seen that many flowing fractures lie above both the mean M-C and B-B curves. The data appears to divide into a majority high branch above the maximum B-B curve (or maximum Mohr-Coulomb but with cohesion around 0.2–0.5 MPa) and a minor low branch around/between the minimum M-C and B-B curves with

friction angles around 20–25°, JRC~2-4 (the curve is less sensitive to JCS). The first branch is consistent with typical values for the rock mass (Glamheden et al. 2007); the second branch is consistent with spatial variability in residual friction angle that has no clear relation to geological domains/structures or depth (Glamheden et al. 2007). Therefore, an alternative to simply assuming that low normal stress is the key driver determining whether a connected fracture has the capacity to flow is that sheared/ reactivated fractures also have a significant contribution. However, this analysis of flow would indicate that water-bearing fractures exist at various structural scales/settings and have undergone different shear cycles. This makes it difficult to develop such a concept at this stage without a lot more understanding of local stress history and fracture mechanics in different structural settings, as might be developed during underground investigations.

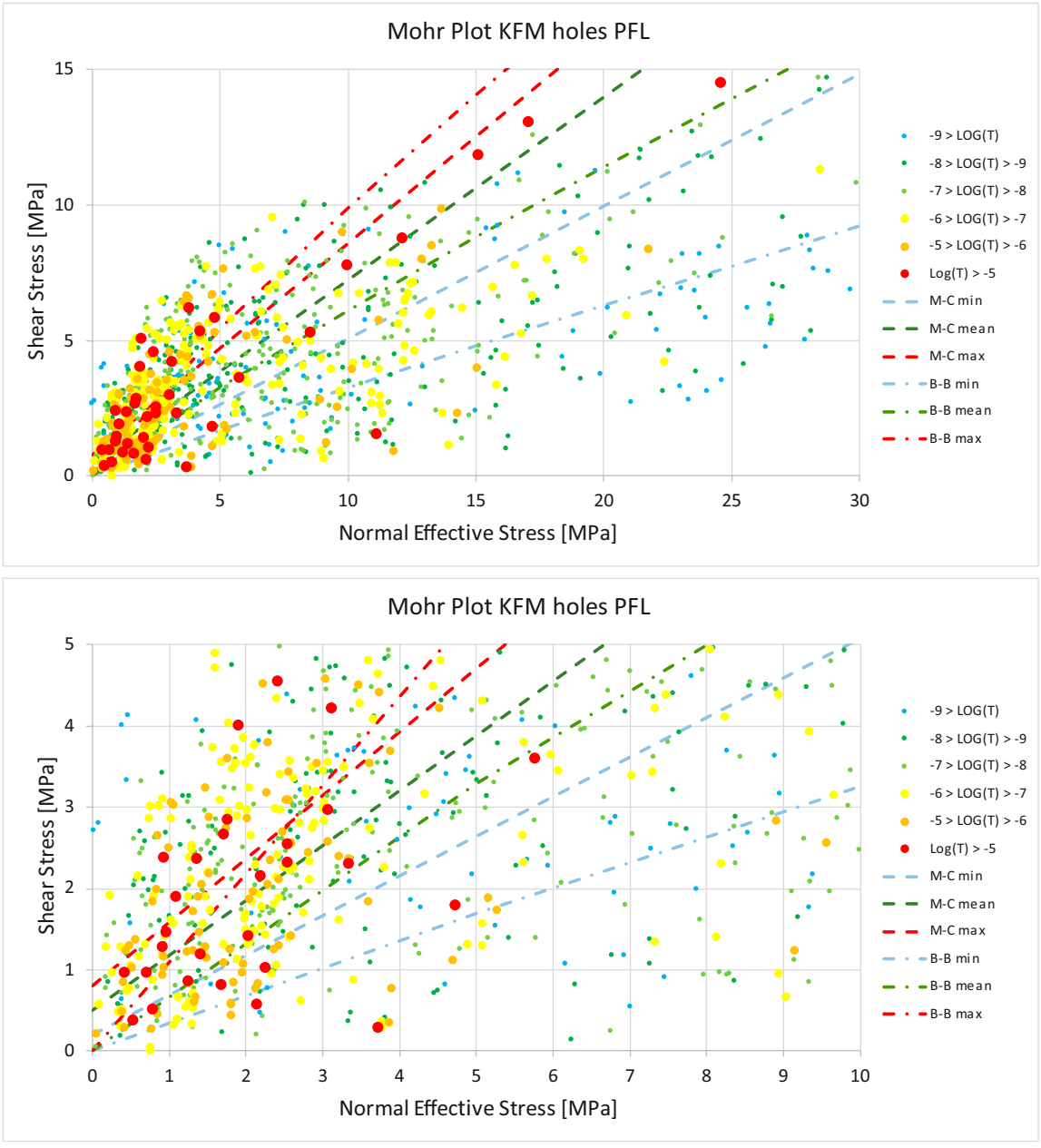

Figure 6-10. *Mohr plots for each observed transmissive fracture in KFM boreholes using the 3D stress model (Valli et al. 2023) at all elevations with three alternative Mohr-Coulomb (M-C) and three alternative Barton-Bandis (B-B) failure envelopes using parameters from tilt tests at the Forsmark site (Glamheden et al. 2007; Mas Ivars et al. 2014). The lower figure zooms in on the origin.*

One illustration of what the implications of critically stressed fractures might have for hydraulics is shown in Figure 6-11 by identifying those parts of the high transmissivity gently dipping ZFMA2 structure which are critically stressed for different values of friction angle using the 3D stress model (Hakala et al. 2019). That is, calculating those areas where the shear stress exceeds the failure envelope. Here, a Mohr-Coulomb failure envelope is used with zero cohesion and a friction angles of 33°, 36° and 39° (top to bottom figure respectively), based on mean and ± standard deviation in peak friction angle across 57 direct shear tests (Glamheden et al. 2007). Using 33° gives 57 % of the area of the structure is critically stressed, with the near-surface particularly affected. This reduces to 39 % as the friction angle increases to 42° (bottom figure). In all cases a larger fraction of the DZ surface is critically stressed near the ground surface. This variability in shear [stress or failure] across a DZ, and the associated potential for shear dilation of apertures, on top of the variability in connectivity when zones are conceptualised as swarms, gives another mechanism to explain the variability seen in the flow properties within a DZ.

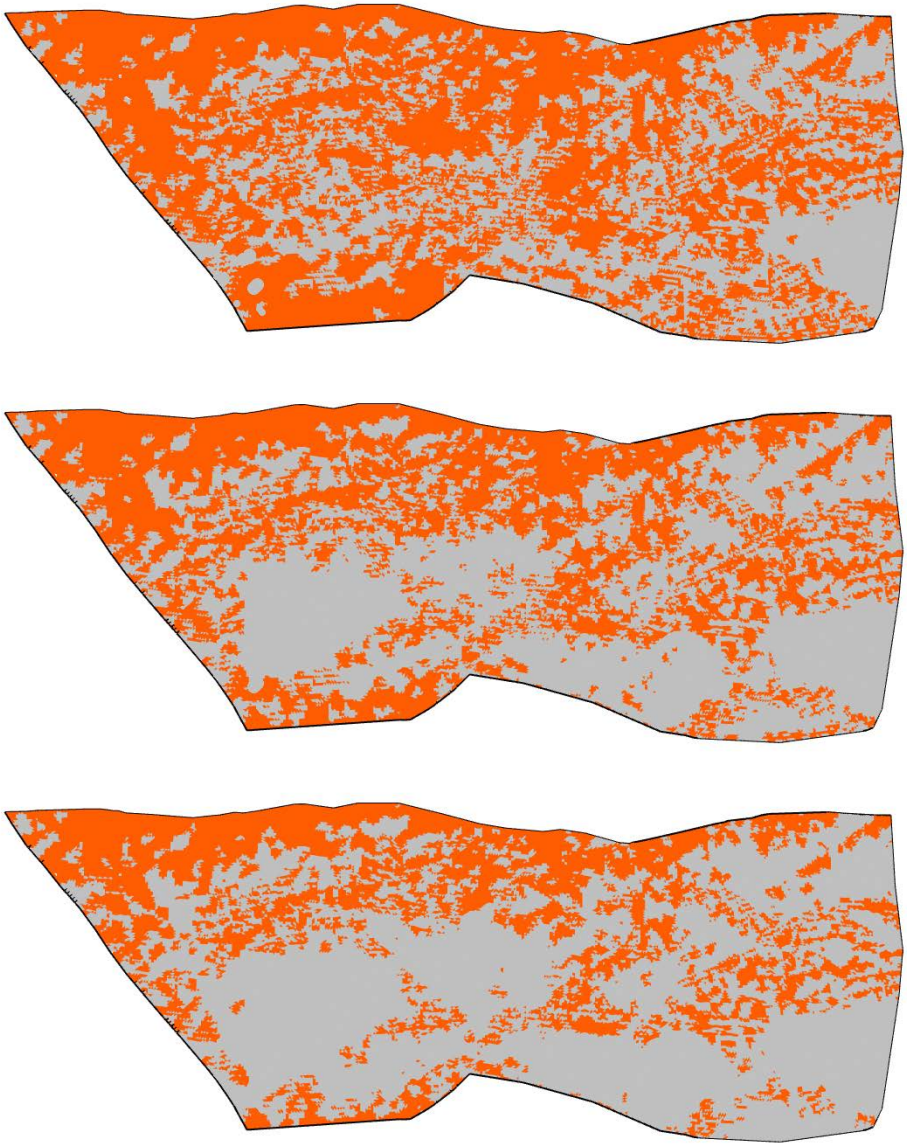

Figure 6-11. *Example of critical stress analysis and its sensitivities on the undulating gently dipping structure ZFMA2 as viewed from the southeast and using the 3D stress model (Valli et al. 2023). Subareas that are critically stressed are coloured orange. Three sensitivity cases are shown for Mohr-Coulomb with 0 cohesion and friction angles of 33° (top), 36° (middle) and 39° (bottom).*

6.2 Hydromechanical coupling

Based on the guidance of the DFN methodology report and the above exploratory analyses, prescription of fracture hydraulic properties are framed within hydromechanical conceptual models, that are first conditioned on current understanding of mechanical properties, used to make forward predictions of hydraulics, and then calibrated. This approach is preferred to a direct statistical calibration of hydraulic parameters, as it yields more insight into the overall fracture system description. The conceptual model components are those of normal displacement, shear displacement, and hydraulic aperture.

6.2.1 Estimating mechanical aperture

In linear elastic fracture mechanics, a fracture is assumed to represent a crack in a linear elastic medium. Under this assumption, the normal displacement (opening) of the fracture can be solved analytically, e.g. (Sneddon and Lowengrub 1969; Pollard and Segall 1987), whereby the distance, or aperture between the two walls of a circular fracture is given by:

$$e = \sigma_d \frac{8(1-\nu^2)}{\pi E}(r^2 - r'^2)^{1/2} \qquad \text{Equation 6-1}$$

and r' is the distance from the centre of the fracture, r is the radius of the fracture, E is the Young's Modulus, and v is the Poisson's Ratio of the linear elastic medium in which the fracture is embedded and σ_d is the driving stress (Mode I). The aperture is non-uniformly distributed, so integrating over the fracture area gives the following area-averaged aperture (Rice et al. 1979) gives:

$$e_{n,max} = \sigma_d \frac{16(1-\nu^2)}{3\pi E} r \qquad \text{Equation 6-2}$$

The driving stress at the circumference of the fracture is given in terms of the stress intensity factor, K_I, (Sih 1973; Anderson 2017):

$$K_I = \sigma_d \frac{2}{\pi}\sqrt{(\pi r)} \qquad \text{Equation 6-3}$$

Assuming critical crack propagation under constant stress intensity factor conditions (Olson 2003; Klimczak et al. 2010), Equation 6-3 can be substituted into Equation 6-2 to give

$$e_{n,max} = K_I \frac{8(1-\nu^2)}{3\sqrt{\pi}\cdot E}\sqrt{r} \qquad \text{Equation 6-4}$$

This model provides an estimate of the area-averaged mechanical aperture correlated to size for circular fractures from insertion of site-specific parameters as provided in Table 6-1 from laboratory mechanical tests on rock samples. Fault displacements can be orders of magnitudes larger than those of opening-mode fractures; however, faults may lack any opening displacements. Therefore, faults can function as barriers or conduits to flow. Despite the fact that faults obey linear displacement/size scaling relationships, their roles in conducting fluid flow depend on several other parameters that cannot easily be generalised. An incorporation of faults into general models for fluid flow is therefore not considered in this study.

The parameters given in Table 6-1 are used to estimate fracture apertures (prior to application of the stress field) in all domains for simplicity, see Section 7.2. These compare with E = 65 GPa (55 GPa for FFM02) and v = 0.24 (0.18 for FFM02, 0.30 for FFM03) for rock mass properties in the 3D stress modelling (Hakala et al. 2019).

Table 6-1. Selected Forsmark specific parameters for normal displacement modelling based on intact rock properties.

Parameter	Mean/st. dev/min.–max.	Notes
E [GPa]	76 / 3 / 69–83	RFM029 / FFM01 Table 3-10 (Glamheden et al. 2007)
v [-]	0.23 / 0.04 / 0.14–0.30	RFM029 / FFM01 Table 3-10 (Glamheden et al. 2007)
K_I [MPa m$^{1/2}$]	1.59 / 0.265 / 1.15–1.99	RFM029 Table 3-5 (Delgado-Martin J. et al. 2021)

It can also be noted that the rock mass modulus is scale dependent below the representative elementary volume (REV), e.g. (Darcel et al. 2021). For note, that study estimated rock mass moduli on scales up to 20 m using a DFN model and predicted $E \sim 60$ GPa, and are the subject further studies. For frictionless fractures at the largest scale considered, 40 m length, they predicted a lower bound around 40 GPa, which is used here for DZ after hydraulic calibration, see Section 7.2.

6.2.2 Hydraulic aperture

The estimates of mechanical apertures given in the previous section are for initially open cracks, failed in tension, prior to application of normal stress. The reduction in mechanical aperture with normal loading can be estimated using several alternative empirical models. For example, by a logarithmic form (Evans et al. 1992; Zangerl et al. 2008), an exponential form (Rutqvist et al. 2002; Min et al. 2004), and a hyperbolic form (Bandis et al. 1983; Willis-Richards et al. 1996).

The ratio between hydraulic and mechanical apertures is less than or equal to one and typically varies with surface roughness, e.g. (Nishiyama et al. 2014). The hydraulic aperture tends to vary linearly with mechanical aperture if it is large or smooth but stabilise around a residual value as the mechanical aperture is closed. The residual value depends on surface roughness, amount of shear and infillings. Here it is assumed that changes in the hydraulic aperture scale linearly with changes in mechanical aperture, see (Witherspoon et al. 1980; Elliott et al. 1985). Also, the exponential form for hydraulic aperture, e_h, is considered following previous THM modelling of Forsmark (Hökmark et al. 2010):

$$e_h = (e_r + e_{n,max} \exp(-\alpha \sigma_n'))/f \qquad \text{Equation 6-5}$$

where e_r is the residual aperture, α is a constant related to fracture normal stiffness, σ'_n is the effective normal stress, and f is a roughness factor used to account for combined flow reduction effects due to roughness and fracture infill. Through the dependence on effective normal stress, this equation implies flow magnitudes vary with fracture orientation (relative to principal stresses) and levels of stress (and hence depth). Table 6-2 collates suitable initial guesses, prior to calibration, from previous studies.

Table 6-2. Initial parameter guesses for hydraulic aperture modelling.

Parameter	Values and suggested range	Notes
e_r [m]	2×10^{-5}, 1×10^{-5} – 4×10^{-5}	Previous SR-Site THM (Hökmark et al. 2010)
α [MPa^{-1}]	0.15, 0.1–0.2	Previous SR-Site THM (Hökmark et al. 2010)
f [-]	10, 1–20	From considerations in DFN methodology report (Selroos et al. 2022)

The hydraulic field parameter used in DFN modelling is fracture transmissivity, from which the equivalent hydraulic aperture can be calculated:

$$T = \frac{\rho g}{12\mu} e_h^3 \qquad \text{Equation 6-6}$$

From these equations it can be seen that the DFN hydraulic parameters and their dependencies on fracture size, orientation and location due to spatially varying 3D stress can be estimated *a priori*. Calibration of these parameters to match flow observations, therefore, reflects on these underlying hydromechanical parameters.

The form of Equation 6-5 implies a steep drop off in hydraulic aperture/transmissivity with depth, reaching the asymptote of residual aperture below an effective normal stress of about 20 MPa, which occurs for a majority of fractures below approximately 600 m depth with the 1D stress model. The form of aperture-stress coupling has a specific effect below this depth. The exponential form decays to the residual aperture, while the alternative hyperbolic form for transmissivity suggested by Hökmark et al. (2010) would predict that transmissivity continues to fall with depth, assuming a smaller or zero residual aperture.

6.2.3 Alternative model with addition of shear displacement

The normal displacement model above describes a depth trend with approximately one order of magnitude reduction in hydraulic aperture or three orders of magnitude in transmissivity, whereas variations in typical measured discrete flow magnitudes between the top 100 m and below 500 m depth can be four or five orders of magnitude. An alternative model including additional aperture dilation due to shear would provide one mechanism for explaining this higher degree of variability with depth. Figure 6-10 illustrates how many of the highest transmissivity fractures (red-orange) are critically stressed. The additional maximum shear displacement can be estimated as a function of excess shear and length ($L = \sqrt{\pi \cdot r}$):

$$e_{s,max} = (\tau - \tau_c)\frac{2(1-\nu^2)}{E}L \qquad \text{Equation 6-7}$$

where τ is the shear stress on a fracture and τ_c the shear strength (Schultz 2003; Schultz et al. 2006), which for simplicity can be estimated from a Mohr-Coulomb criterion based on specified friction angle and zero cohesion (based on exploration of possible failure envelopes for open water-bearing fractures in Figure 6-10, where low cohesion in the range 0.2–0.5 MPa seems appropriate). Shear displacement is then a threshold parameter on whether a fracture is critically stressed:

$$e_s = \begin{matrix} 0 & \tau \le \tau_c \\ e_{s,max} & \tau > \tau_c \end{matrix} \qquad \text{Equation 6-8}$$

$$\tau_c = [tan(\varphi_r)]\sigma_n' + c$$

where φ_r is the friction angle and c is the cohesion of the fracture.

Combining this component into Equation 6-5 gives

$$e_h = \left(e_r + (e_{n,max} + e_{s,max})\exp\left(-\alpha\sigma_n'\right)\right)/f \qquad \text{Equation 6-9}$$

This extra component increases with shear stress above critical stress and with the size of fracture. It, therefore, tends to significantly increase the transmissivity in a minority of large fractures that are critically stressed, i.e. mostly gently dipping fractures at shallow depths. This gives rise to a greater variation in transmissivity with depth with particularly strong heterogeneity in the near-surface. The elevated flows an give rise to tend to be concentrated in deformation zone structures near-surface whose increased intensity gives an increased likelihood of large high transmissivity fractures connecting rather than being choked by lower transmissivity bottlenecks.

This shear component of the hydromechanical model was not part of the initial hydrogeological model, but eventually proved to be a useful sensitivity case when attempting to mimic aspects of the high spatial variability in flow magnitudes observed, introducing necessary additional calibration parameters, see Sections 7.4 and 7.5.

For the sensitivity analysis a cohesion of zero was used and friction angles in the range 30° to 40° based on indications from Figure 6-10 and values used in (Hakala et al. 2019).

7 Hydrogeological description

This chapter describes the data analysis and numerical modelling used to conceptualise and parameterise the hydraulic properties of the natural fracture system at Forsmark. Quantifying this characterisation is achieved by a multi-objective calibration process to match model simulation results to discrete flow logging in single-hole hydraulic tests and multi-hole pressure responses to long-term pumping tests. The geometric framework for this comes from the DFN structural description and numerical recipes given in Chapter 5. An initial guess for the hydraulic properties comes from the hydromechanical concepts and site-specific mechanical data given in Chapter 6. Some additional input parameters derived from data analysis is described here. The model calibration process involves parametric sensitivities tests within the uncertainty windows proposed in Chapter 6. It also tests sensitivities to key uncertain parameters outlined in Chapter 5, such as those relating to size scaling and spatial limits on sheet joints. Finally, sensitivities to boundary conditions are also considered in the simulation of the interference tests.

7.1 Spatial distribution of apertures

Only a subset of the fracture surface area logged at Forsmark is classified as being open to flow. Every observed fracture in the cored boreholes is recorded as open, partly open or sealed on the scale of the borehole core. Whether an open fracture remains open away from the borehole is a basic uncertainty that can only be addressed through hydraulic testing, with apertures being connected being a necessary condition for flow to occur. Experience from mapping traces of minor zones and single open fractures in excavations at Äspö (Stanfors 2006) indicates that there are different types of fracture in terms of openness as well as variations in apertures across the surfaces. The connectedness of openings is manifest in observations of inflows on tunnel walls, e.g. (Palmqvist 1990; Ahokas et al. 2014) in Sweden and Finland. A common observation in these examples is that inflows are more common and extensive on fracture traces where large subhorizontal fractures intersect the tunnels, which is consistent with borehole records on openness at Forsmark, see Figure 7-2.

Assuming that the boreholes overall are not biased towards intersecting volumes that tend to have more or less than typical fractions of open vs. sealed fractures, i.e. boreholes don't all target major DZ, then the core data can be used to estimate the overall fraction of fracture area that is open and assess trend in this statistic. It also provides an upper bound for the fraction that is open and connected, i.e. water-bearing. The calculation of the fraction is Terzaghi weighted to reduce bias with the orientation of drilling. When calculated as a fraction within an individual set, the fractions are less sensitive to relative biases within a set than between sets. The fraction is equated to a proportion of surface area rather than simply a proportion of fractures as recognition that openness as observed in core is on the scale of the borehole diameter, allowing that openness could vary over the area of some fractures as well as between them.

It is also noted there is some uncertainty in this fraction due to core loss in crush zones or conversely filled fractures maybe flushed of soft fillings during drilling, for example. Discrete flow measurements provide a lower bound on the fraction of fracture area that is open and connected, recognising that flow logging misses small flows below detection limits. These two fractions provide quantitative constraints on the participation of the fracture network in flow. Quantifying how these fractions vary by depth, structural location (inside / outside DZ), depth, and by set provide further insight into spatial variations in the degree to which fractures conduct flow. However, it is much more difficult to infer the spatial structure of apertures across fracture surfaces and how they persist across or along fracture intersections.

Mineral chronology on fracture surfaces will give some indications of expected apertures, see Table 2-1. A main part of the mapped sealed fractures is very old (generation 1 and 2), very thin and very strong with no aperture for flow. Open fractures, slickensides and the presence of low temperature minerals are all potential indicators of more dynamic mechanical and hydrogeochemical parts of the system where flow may occur or has occurred periodically due to tectonic or climate-driven processes. Some indications can be obtained from transient hydraulic tests and hydraulic interference tests, in particular, and also grout injection and tracer tests. In any case, the intra-fracture and inter-fracture

spatial distribution of apertures is a subject for conceptual model testing and sensitivity analysis. As discussed below, both concepts were explored initially, but DFN-BF1 only includes inter-fracture variability for the reasons explained.

Figure 7-1 illustrates the depth dependency of openness. It should be noted that much of the local variation at depth is due to the small number of boreholes that penetrate these depths (Figure 3-1), compare with Figure 5-21 showing the general lack of depth dependency in the intensity of all fractures (open and sealed). For the inside lens, it is seen that the main changes occur in the top 200 m with a smaller decline to −400 m and little change below that. The outside lens data is noisier but follows a similar trend. From this it can be hypothesised that a residual 20–25 % of fracture surface remains open over very long time-scales, but the upper 200 m of bedrock is progressively more reactivated by periodic glacial loading/unloading and weathering toward the topographic surface.

To further tease out trends, the data is split by set and DZ intervals and divided into the depth intervals shown in Figure 7-2. It is seen that openness of NW and NE sets does not have a significant depth dependency below −30 m. It is the SubH fractures that have the greatest depth trend, suggesting that glacial-related reactivation mainly extends or opens subH, sheet joint type fractures. DZ-related fractures are also more open, except below −400 m.

For modelling purposes, the open fractions are assigned to a domain and interpolated by elevation between these piecewise averaged values. These fractions are taken as known constraints, with some sensitivity experiments made as part of the model calibration process.

Of possible alternative conceptual hypotheses, two are trialled for the spatial model for apertures:

1. The first considers each fracture as being 100 % open or 100 % sealed to flow (Figure 7-3 left).
2. In the second, there are volumes where all the fracture surface belonging to the same set is open, and the rest where all fracture surface is sealed.

To implement the second of these, 3D space is divided into a regular volume mesh of scale 5 m and a open/sealed binary attribute is sampled randomly according to the fraction of open fractures at that depth. Fractures are then meshed into Voronoi cells of similar scale (see Appendix A3) and all fracture mesh cells of the same set within the same volume mesh are set to the open/sealed attribute for that cell. Other alternative implementations of flow within a DFN structural/geometric framework, including ones that produced highly channelised flow, have been explored recently in (Baxter et al. 2021; Doolaeghe et al. 2023), for example.

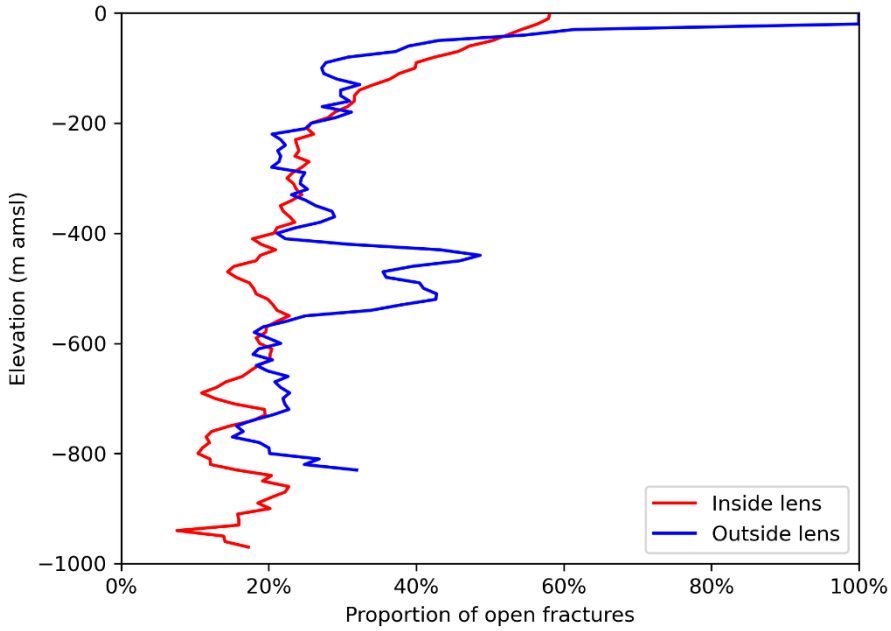

Figure 7-1. *Graph showing how the proportion of open (open and partially open) fractures logged in KFM and KFR boreholes varies with depth. The openness is calculated in intervals spanning 40 m.*

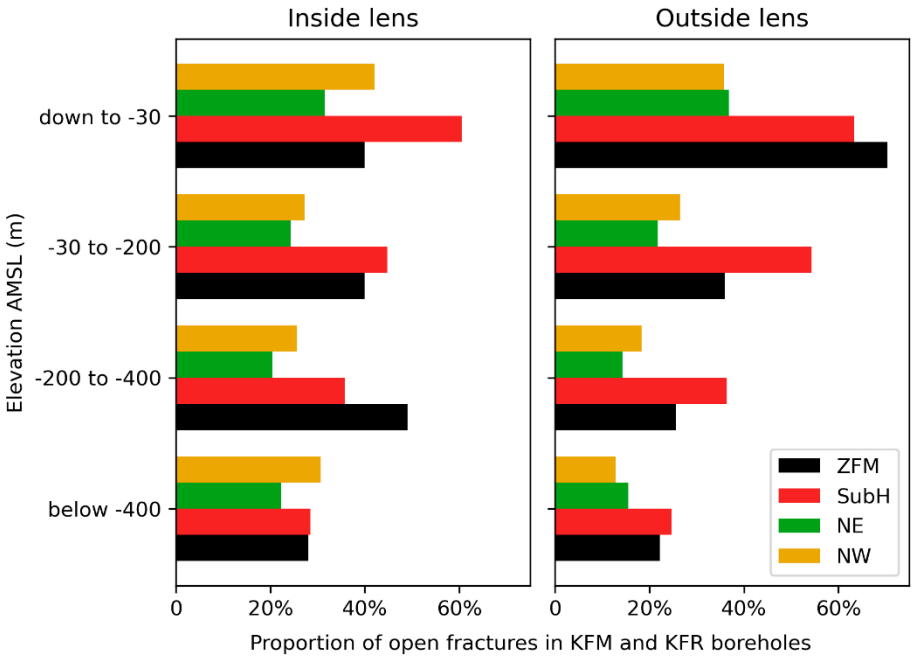

Figure 7-2. *Bar plot showing the proportion of open (open and partially open) fractures in KFM and KFR boreholes in each fracture set outside DZ intervals and inside DZ (ZFM, irrespective of orientation) in different elevation categories.*

An example of each model type is shown in Figure 7-3. The foundations for these methods are given in the DFN methodology report (Selroos et al. 2022).

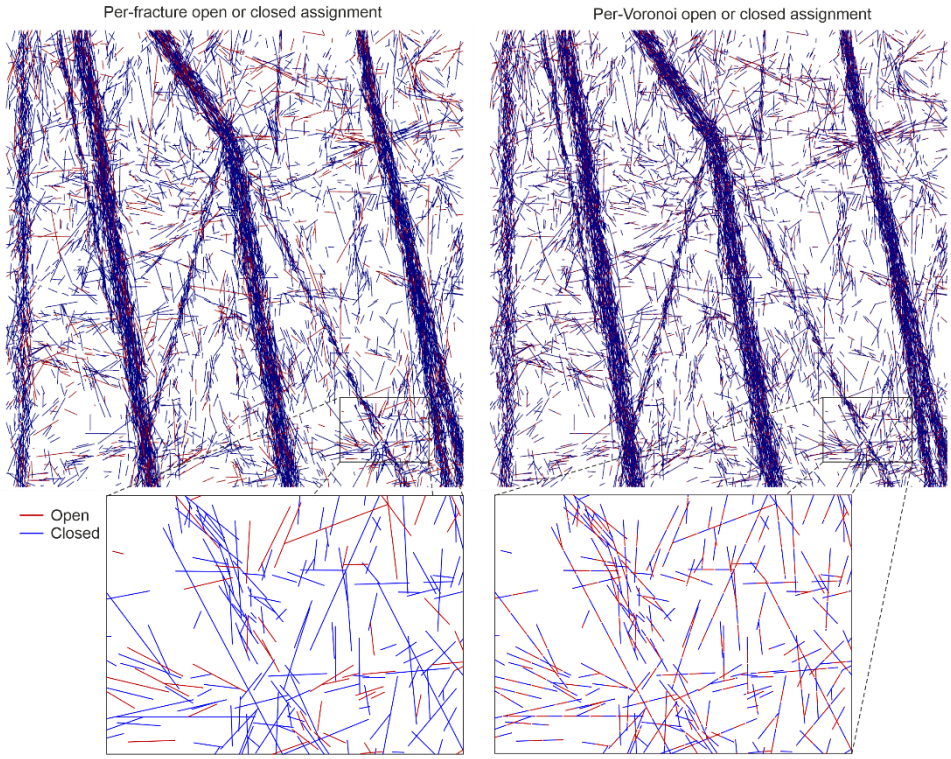

Figure 7-3. *Tracemaps on a N–S vertical cross-section on a 500 m × 500 m scale through a DFN model showing the open (red) and sealed (blue) fractures after discretisation to a Voronoi mesh. Note that the model shown here is an early version and so is not indicative of the final model.*

There are advantages to both methods:

- Per fracture
  - Conceptually simpler.
  - Computationally cheaper.
- Per Voronoi cell
  - An alternative with strong intra-fracture variability (as experience in the dense drilling of grouting probe holes for Olkiluoto shafts (Hartley 2022b)).
  - Flows is more channelised as can be expected in nature.

A disadvantage of the second method is that it introduces an extra unknown, the average correlation scale for apertures. From the experience at Olkiluoto, strong variability occurs on scales smaller than that diameter of the shafts, ~5 m. An isotropic variability in openness on the scale of 5 m was, therefore, used here. It is also about the smallest practical scale for modelling intra-fracture variability in a facility-scale model.

Considering percolation within single fractures, if openness lacks a spatial correlation and is variable on scales much smaller than size, then below a fraction of openness of 50 %, which is the case everywhere but the top 30 m, apertures will not percolate in 2D, such that percolation only occurs through 3D connectivity around fracture intersections. Baxter et al. (2021) showed that the per cell case is less connected than per fracture when the length scale of apertures is less than the spacing of connected open fractures. The two models give similar results if the length scale of apertures is greater than this spacing, but that in turn depends on the geometric size scaling of fractures.

Early sensitivity tests revealed that discretising the openness of fractures on a per fracture basis produces networks outside of DZs that have an intensity of flows that varies with depth consistent with observations, with sporadic flows above the detection limit at < 0.1 m^{-1}, see Figure 7-12. while assigning openness on a 5 m cell basis gave background networks that did not connect at all below −200 m, see Figure 7-4. This would imply that either apertures are persistent across the scale of fractures, or at least over a scale much bigger than 5 m (see Figure 7-12.). Therefore, only the per fracture model was pursued further in the hydraulic calibration.

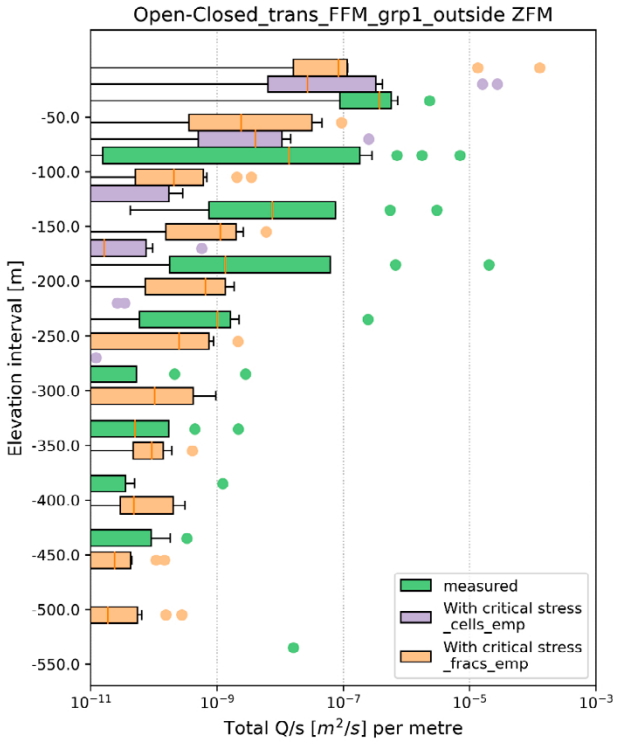

Figure 7-4. *Bar graph showing the distribution of flow on 50 m elevation intervals aggregated over all PFL logged boreholes and divided between inside the lens and outside DZ for measured (green) and simulated single-hole tests. Two model cases are shown: per fracture (orange) and per Voronoi cell (purple). Note that the model shown here is an early version and so is not necessarily indicative of the final DFN-BF1 model parameterisation.*

7.2 Spatial distribution of transmissivity

The starting point for transmissivity model is that expected from the hydromechanical models given in Section 6.2, with fine-tuning of parameters to calibrate on the flow measurements. The analysis made in Section 6.1 explains the justification for taking a mechanistic rather than statistical approach to describing transmissivity. The main assumptions are:

- The observed depth trends in transmissivity can be linked to generally increasing stress magnitudes;
- There is wide variability in transmissivity mainly due to the limited fracture connectivity of the sparse network, but also due to variations in fracture size to which it is correlated, and to variations in fracture orientation which determines the incident stresses on a fracture and variations in fracture infills and normal stiffness;
- SubH fractures are more likely to be open and subject to lower normal stress and higher shear stress making them more likely to have larger aperture and hence flow;
- SubH fractures being far fewer inside the lens (FFM01/03/06) than outside (FFM04/05) is the main reason for the difference in flow intensities and magnitudes between these two domains;
- Stress perturbations about major structures such as ZFMA2 leading to lower stress in their hanging wall and hence higher transmissivities;
- Transmissivities in DZ-related fractures are not necessarily higher than background fractures, except where they experience the stress perturbations mentioned above; and
- DZ-related fractures are, however, far more likely to be connected, and therefore, carry flow.

Table 7-1 gives the range of parameters considered and final values after calibration.

Table 7-1. Values used to calculate a transmissivity value for each fracture.

Parameter	Data values considered Mean/st. dev/min.–max.	Findings from calibration	Final value
E [GPa]	76 / 3 / 69–83	Needed a lower value in DZ to reduce closure at depth	76 outside DZ 40 inside DZ
ν [-]	0.23 / 0.04 / 0.14–0.30	Limited sensitivity for range considered compared to other parameters	0.23 everywhere
K_I [MPa m$^{1/2}$]	1.59 / 0.265 / 1.15–1.99	Used a higher value in DZ to boost transmissivity	1.59 outside DZ 1.89 inside DZ
e_r [m]	2×10^{-5}, $1 \times 10^{-5} - 4 \times 10^{-5}$	Increased to give some flow at depth. This could be smaller if using a hyperbolic instead of exponential model for normal closure	3×10^{-5}
α [MPa^{-1}]	0.15, 0.1–0.2	Not tested. 0.15 gives a drop off in transmissivity below −200 m as observed	0.15
f [-]	10, 1–20	Values of 1–3 needed to have flows of correct magnitude	3 outside DZ 1 inside DZ
φ_r	30–40°	Lower angle in DZ gave more transmissivity near the surface	36° outside DZ 31° inside DZ
k_r in prior model	2.2–3.0	This is an important parameter controlling scaling behaviour of flow. 2.6–2.7 work best.	2.7 outside DZ Table 5-5 2.6 in DZ Table 5-3

An illustration of the assignment of transmissivity across the DFN model of all fractures is shown in Figure 7-5 with the majority sealed fractures coloured grey and open fractures coloured by their transmissivity.

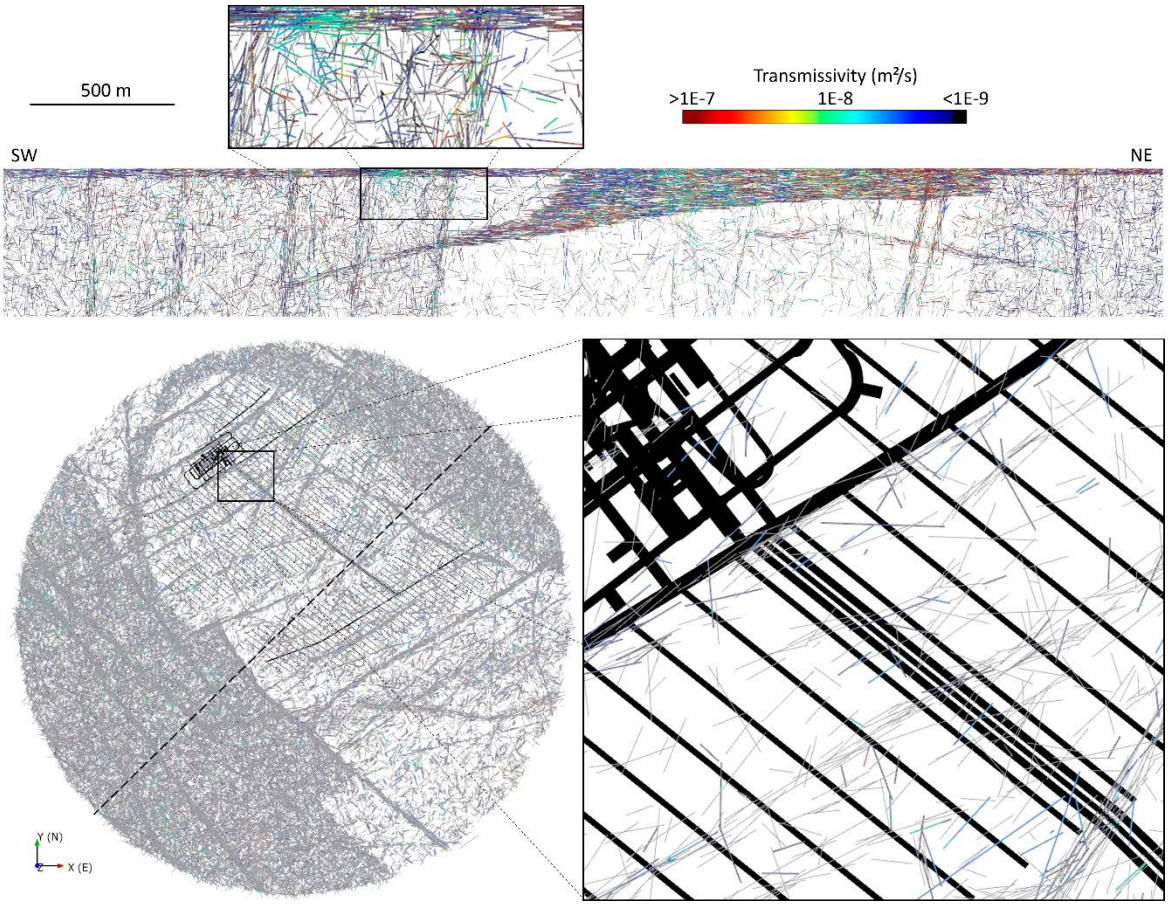

Figure 7-5. *Vertical cross section aligned across the lens (upper) and a plan view cross section at −450 m elevation (lower) showing open fracture traces coloured by their transmissivity value and sealed fractures shown in grey, with insets showing detail. The plan view cross section also shows the planned tunnel layout in black and the location of the vertical cross section with a dashed line. The DFN realisation shown has an of* r_{min} *of 12 m.*

7.3 DFN connectivity

The low intensity of fractures inside the lens together with the low fraction of open fractures are major contributors to only a subset of the open fractures being connected. This results in significant compartmentalisation of the hydraulic network. An example view of such a system around part of the SFK repository is shown in Figure 7-6, and a tracemap of the same network shown in Figure 7-7. Here, 'clusters' are groups of fractures geometrically connected to each other. It may be observed that within the fractured volume there are two main fracture clusters and numerous smaller isolated clusters in which flow will be severely baffled by the low permeability matrix cannot develop (Figure 7-6). The open fractures are sufficiently sparse that there are significant regions that only contain fractures that do not belong to any clusters with more than 20 fractures (Figure 7-7). Note that in a larger DFN some of these isolated clusters may be connected to the wider network through connected parts of the network not considered in the figure.

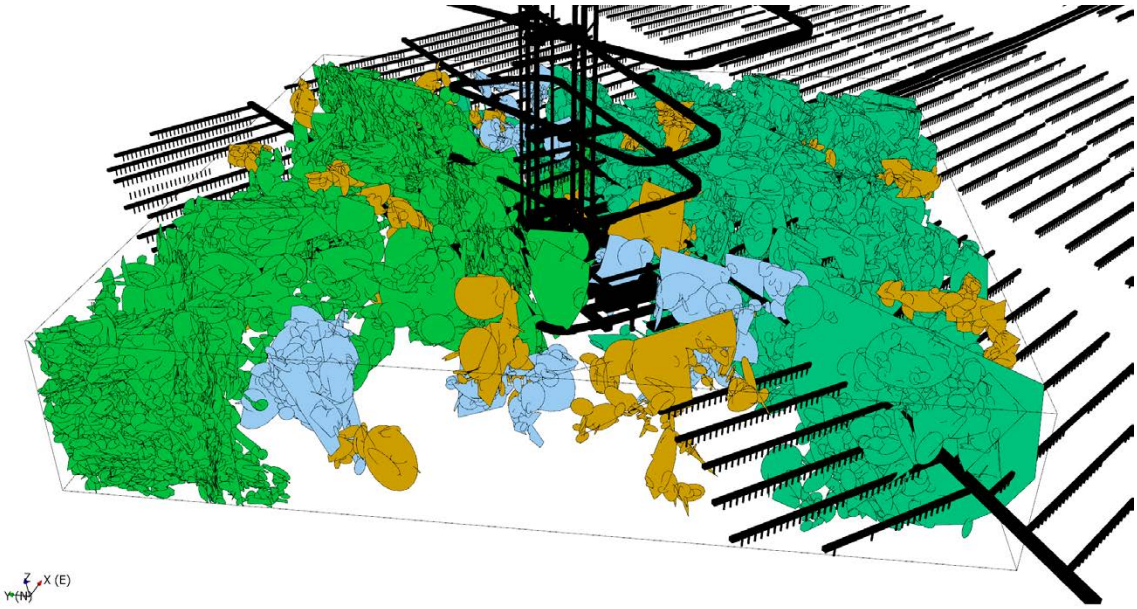

Figure 7-6. *Illustration of connected open fracture clusters on a part-facility scale using 800 m × 800 m × 150 m generation region (black outline) for a single DFN realisation with r_{min} = 4 m. The two largest connected fractures clusters are coloured green and turquoise, clusters with 50 to 100 fractures are coloured light blue and clusters with 20–50 fractures are coloured orange. The planned tunnel layout is shown for context. A tracemap through this network is shown in Figure 7-7.*

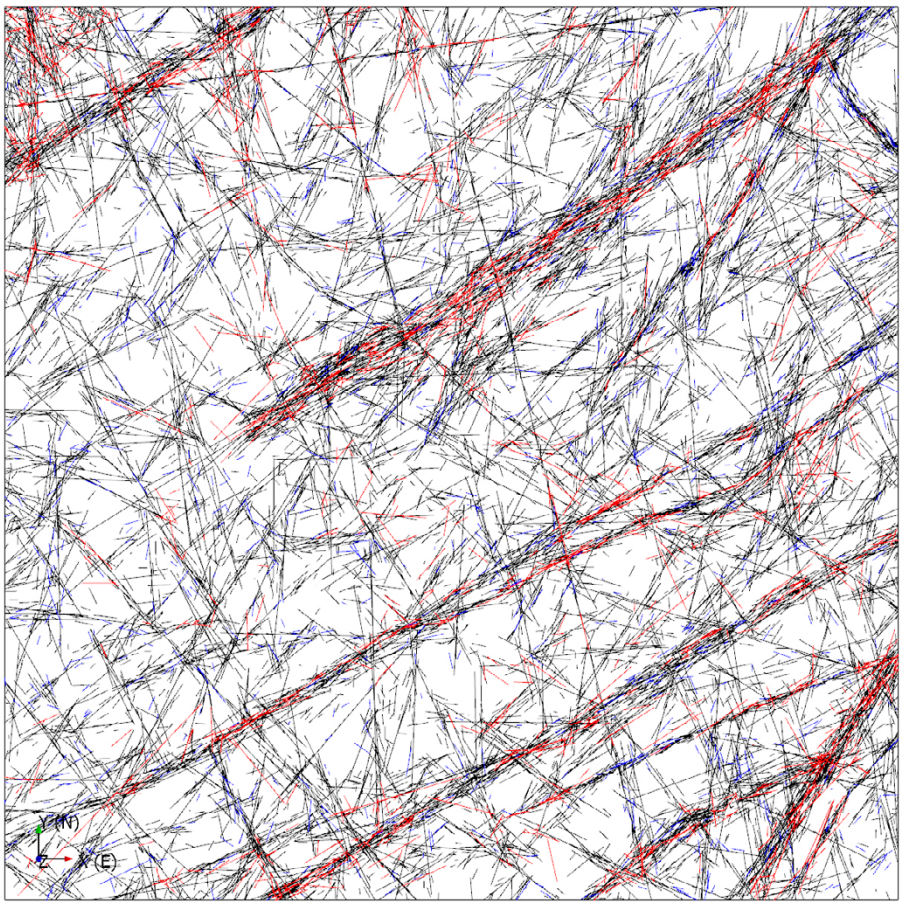

Figure 7-7. *Plan view tracemap through the fractured volume shown on Figure 7-6 illustrating the tracemaps of sealed fractures (black), open fractures not connected to more than 20 other open fractures (blue), and open fractures connected to at least 20 other open fractures (red).*

7.4 Calibration on single-hole hydraulic tests

Although some initial testing of the formulation of DFN's combined geometric and hydraulic properties was made against the combined dataset from PFL single-hole testing it was soon found that it was essential to compare model predictions against both single-hole and interference tests as multiple calibration objectives. This is because single-hole tests characterise the near-hole connectivity and transmissivity, while the interference tests characterise network or facility-scale connectivity and transmissivity. The model needs to find a balance in describing both sorts of characteristic, as improving one near-hole properties can be at the detriment to honouring network properties. Therefore, each time a model sensitivity case was tested, simulations were made of both single-hole and interference hydraulic tests and the results checked by the modeller against calibration metrics (see Subsections 7.4.2 and 7.5.2) for both scales of model to make a holistic judgement on model performance. Figure 7-8 is a schematic of this cycle of multiple objectives evaluated for each model case simulated. In each cycle, multiple realisations of a DFN model on the scale shown in Figure 5-40 with the whole model being used to simulate the interference tests and a "cut-out" model extracted to simulate single-hole flows in every deep KFM and KFR hole in which PFL logging was performed.

The setup and metrics used for the single-hole tests are described in this section. Those for the interference tests are described in Section 7.5.

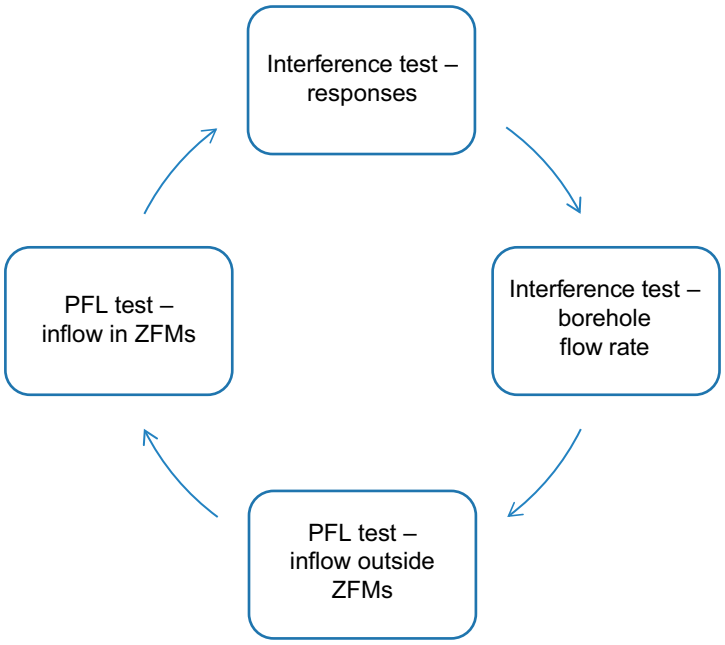

Figure 7-8. *Schematic of a cycle of multiple objectives evaluated for each simulated model case including comparison to PFL inflows inside and outside ZFMs and interference test responses and pumped borehole flow rate.*

7.4.1 Model setup

There are 23 KFM holes with intervals inside the Forsmark lens that were characterised with PFL testing, and 14 with intervals outside the lens. Each test was simulated explicitly by modelling the flow setup during the test with the boreholes in their actual locations and whatever DZ or semi-stochastic DZ structures have been interpreted for them.

Ten realisations of the complete DFN with all structural components were modelled down to r_{min} of 4 m for the region shown in Figure 5-40. Fractures were assigned as being open or sealed probabilistically according to the fractions described in Section 7.1. For each PFL tested KFM/KFR hole, the open fractures inside a cylindrical region (12 sides) with a 250 m radius centred around the tested borehole were extracted and clipped to the boundary, as presented in Figure 7-9. The end of the cylinder extends 50 m below the end of the borehole.

The hydraulic simulations were setup to mimic PFL tests. Since the PFL tests were performed after several days of pumping, they were simulated as steady state, with a constant head boundary on all sides of the cylindrical region and a 10 m drawdown in the tested borehole. A no-flow boundary was applied to the top and bottom of the cylindrical region. The fractures were meshed using target triangle side of 2.5 m side with refinement down to 0.1 m scale graded within a 5 m radius around the hole. An illustration of this type of meshing methodology is shown in Appendix A3.

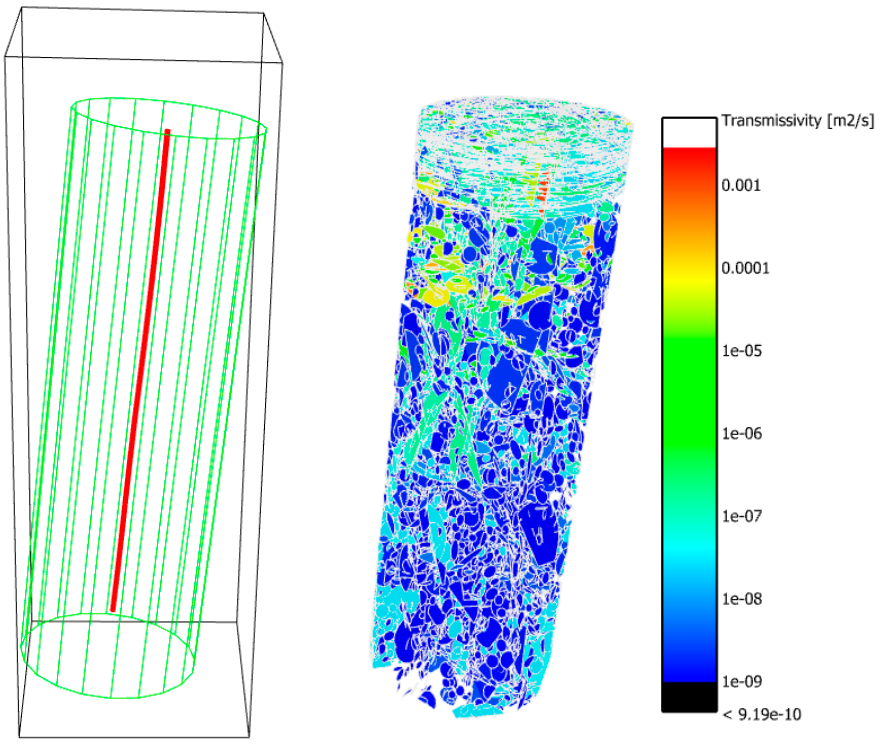

Figure 7-9. *Sketch showing the region (green) used to clip the fractures around a borehole (red) when simulating single-hole PFL tests. Open fractures coloured by transmissivity are shown on the right.*

7.4.2 Results interpretation

For both the measured and simulated discrete flows along the borehole, the effective transmissivity was calculated as

$$T = \frac{Q_s}{h} \qquad \text{Equation 7-1}$$

where T represents effective transmissivity, Q_s the volumetric inflow at each fracture intersection and h the drawdown (corresponding to 10 m in the simulation setup). It has to be recognised that simulations can produce flows down to the accuracy of the numerical method, while data is limited by the detection limit of the tool. This detection limit depends on the seal between two rubber disks and the borehole wall, any degassing effects, and the local drawdown, and so varies within and between holes. Filtering simulated flows below an assumed threshold to compare frequency of flows is, therefore, an approximation. A typical detection limit has been assumed to be equivalent to a transmissivity of order 10^{-9} m^2/s for 10 m drawdown, but because drawdowns and leakages of the disks can vary, then the range of this limit is 10^{-10} to 10^{-8} m^2/s for surface drilled holes (Follin et al. 2011). Here, a threshold of 5×10^{-9} m^2/s is applied when comparing the number of modelled water-bearing fractures with data.

The simulation results are compared to PFL measurements using the following numerical and visual comparison metrics (all being subdivided in inside/outside DZ identified and inside/outside of the lens):

1. The magnitude of the sum of PFL flows for each KFM/KFR borehole with PFL testing;
2. Statistics of the intensity of inflows above the detection limit across borehole intervals within each 50 m elevation band;
3. Statistics of the distribution of total inflows per 50 m elevation band normalised by borehole length (because different holes have different lengths outside of DZ) across each borehole; and
4. Total flows within each individual DZ intersect;

The first metric tests that the sum of PFL flows over all depths are spanned by realisations and whether differences between holes due to deterministic structures are captured. The second metric ensures that the sparsity of flow, and depth trends therein, are matched. The third metric ensures the magnitudes of flows, and depth trends and spatial variability therein, are mimicked. The fourth metric checks that flows with DZ and their depth trends are reproduced. The division into four main structural domain types requires that recognised differences, see Chapters 4 and 5, are honoured.

7.4.3 Calibration results

The following figures present the final results for single-hole tests according to the four metrics listed above and the parameters given in Table 7-1. The measured and simulated total inflows in the holes (outside of DZ) are compared in Figure 7-10 for FFM01/02/06 and in Figure 7-11 for FFM03/04/05. The geometric mean, minimum and maximum total inflows are calculated from ten realisations to compare with the measured outcome. It is seen that the model realisations span the measurements for many holes. These total specific capacities tend to be dominated by single flows per borehole with outlying transmissivities above 1×10^{-5} m^2/s in the top 150 m of bedrock, see Figure 5-12 of (Follin et al. 2011). Total flows vary by three orders of magnitudes between 100 m sections of boreholes at the same elevation, see Figure 5-13 of (Follin et al. 2011). These magnitudes of sporadic flows are replicated in the arithmetic mean over realisations, but difficult to reproduce consistently across a majority of stochastic realisations due to their sparsity.

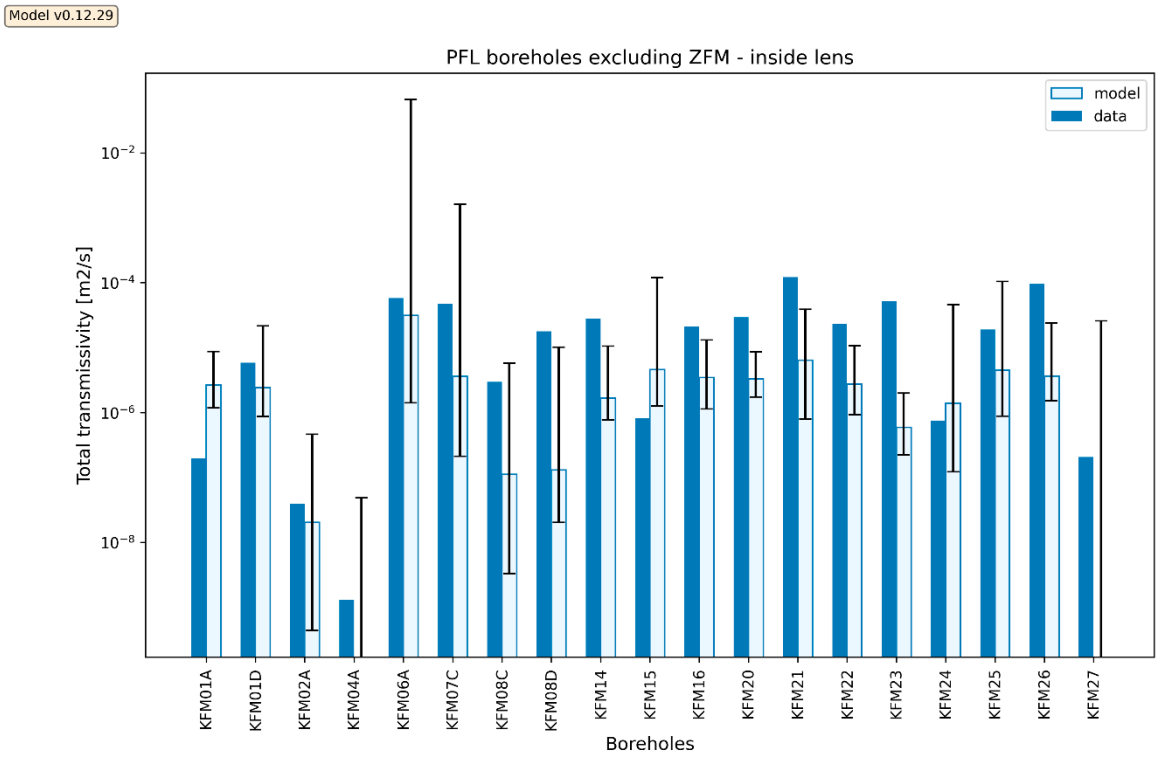

Figure 7-10. *Geometric mean values for Total Q/s outside deformation zones and in FFM01/02/06 for 10 realisations. Error bars indicate the minimum and maximum of 10 realisations. Data is shown in dark blue.*

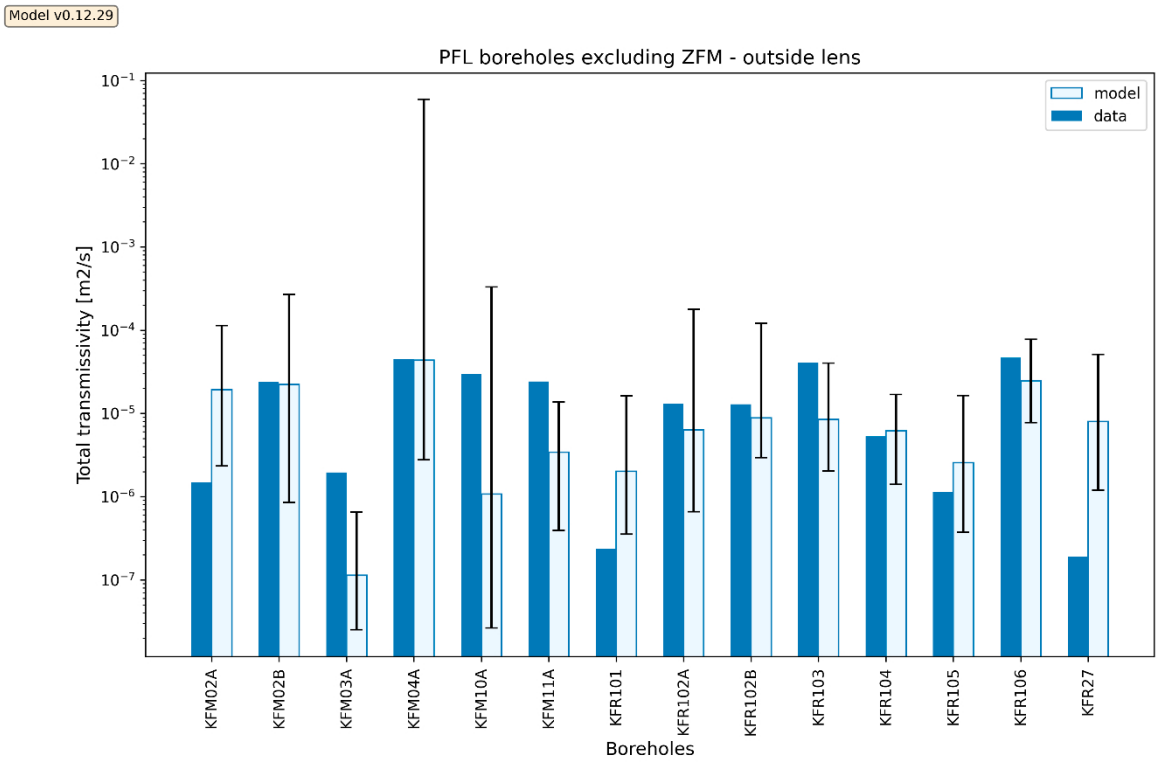

Figure 7-11. *Geometric mean values for Total Q/s outside deformation zones and in FFM03/04/05 for 10 realisations. Error bars indicate the minimum and maximum of 10 realisations. Data is shown in dark blue.*

The comparison of intensity of inflows above the detection limits is shown Figure 7-12 for FFM01/02/06 and in Figure 7-13 for FFM03/04/05. FFM03 is here lumped with the outside lens domains as the lower stresses in the hanging wall of ZFMA2 make the flow magnitudes in this domain more analogous to FFM04/05. For comparison, only three realisations with total flows closest to measurements are presented to illustrate the variability between realisations. The high intensity of flows, P_{10PFL} 0.3–0.5 m^{-1} in the top 50 m followed by a fall-off to 0.0 to 0.2 m^{-1} down to −150 m and again to 0–0.02 m^{-1} below that inside the lens (and outside DZ) is honoured by the model. These discrete flow intensities are consistent with previous statistics in SDM-Site, see Table 5-13 of (Follin et al. 2011). The modelling of sheet joints and FFM02 (see Section 5.5) provide the agreement with the top 50 m. The graded reduction in fraction of openness (see Section 7.1) and hydromechanical effects (see Section 6.2) provide the mechanisms for the lower depth trends.

The slightly lower intensity, 0.0 to 0.2 m^{-1}, in the top 50 m outside the lens is also reproduced, which comes from the absence of a domain equivalent to FFM02 (see Figure 5-22). The gentler drop-off in P_{10PFL} outside the lens is honoured by the model as a result of the higher background intensity (see Figure 5-22) and lower stress magnitudes (see Section 6.1).

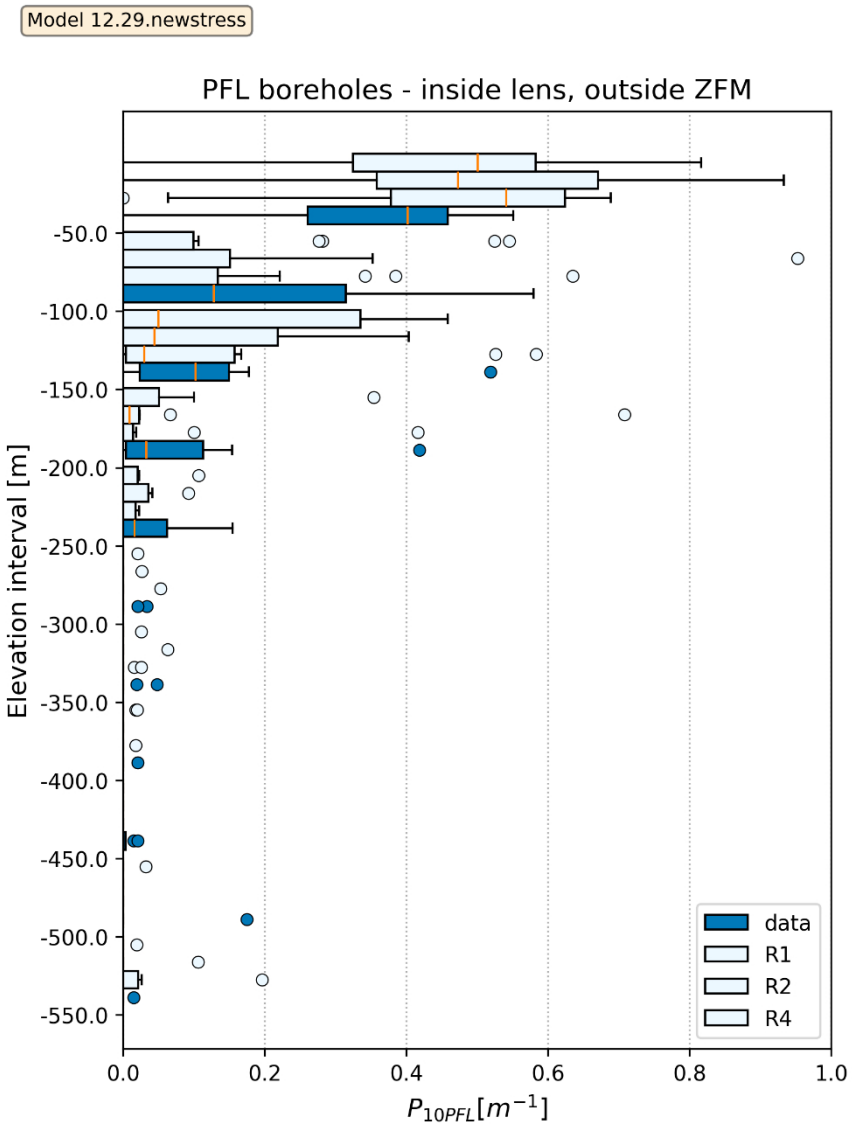

Figure 7-12. *Intensity (Terzaghi corrected P_{10}) of fractures with $Q/s > 5 \times 10^{-9}$ m^2/s per elevation interval aggregated over all PFL logged boreholes and outside deformation zones and in FFM01/02/06 for 3 realisations with total flows closest to PFL measurements. Each box extends from the lower (Q1) to upper (Q3) quartile while the whiskers extend from the box to the farthest data point lying within 1.5 × (Q3–Q1) from the box. Flier points are individual holes with values higher than the end of the whiskers.*

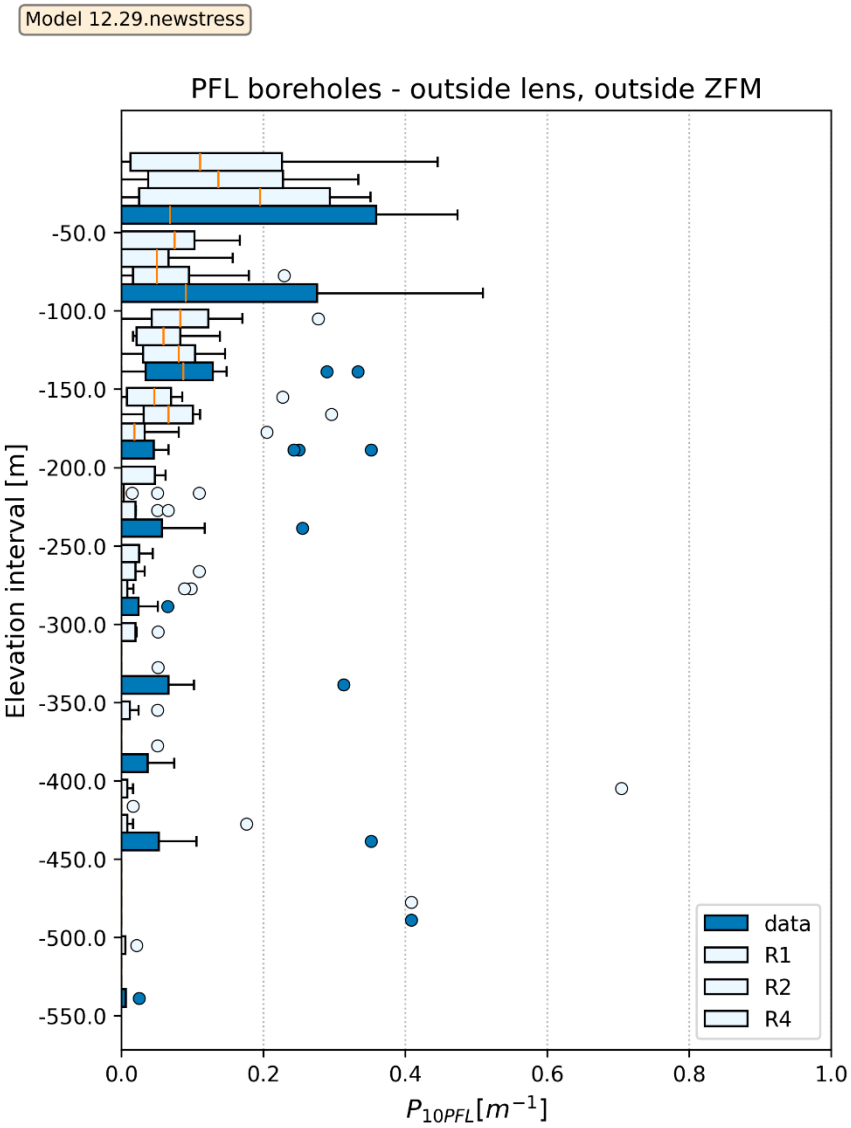

Figure 7-13. *Intensity (Terzaghi corrected P_{10}) fractures with $Q/s > 5 \times 10^{-9}$ m^2/s per elevation interval aggregated over all PFL logged boreholes outside deformation zones and in FFM03/04/05 for 3 realisations with total flows closest to PFL measurements. Each box extends from the lower (Q1) to upper (Q3) quartile while the whiskers extend from the box to the farthest data point lying within 1.5 × (Q3–Q1) from the box. Flier points are individual holes with values higher than the end of the whiskers.*

The comparison of depth trends and statistics for magnitude of transmissivity per metre (i.e. effective hydraulic conductivity) for up to 50 m elevation intervals outside of DZ are shown for inside the lens in Figure 7-14 and outside the lens in Figure 7-15. For the data, for each borehole the sum of transmissivities is made over all flows within each 50 m elevation range and divided by the logged borehole length in that same elevation range. Statistics across all boreholes logging this elevation range are then calculated. The overall shape of the decrease in flow magnitudes with depth can be compared to SDM-Site results in Figure 5-12 of (Follin et al. 2011) and sparsity of flow at depth can be compared to Figure 5-13 of the same report.

The overall trend of effective hydraulic conductivity of 10^{-7} m/s in the upper 50 m reducing to about 10^{-9} m/s by −150 to −250 m and down to ~10^{-11} m/s below −250 m is reproduced in the model due to the combined effects of connectivity (as intensity and openness decrease) and reduced transmissivity (due to higher closure stress and reduced incidence of critically stressed fractures). The less dramatic depth trend seen outside the lens with a more gradual reduction from 10^{-8} to 10^{-7} m/s in the upper bedrock to ~10^{-10} m/s below −200 m is also reproduced (due to the higher intensity and lower stress magnitudes).

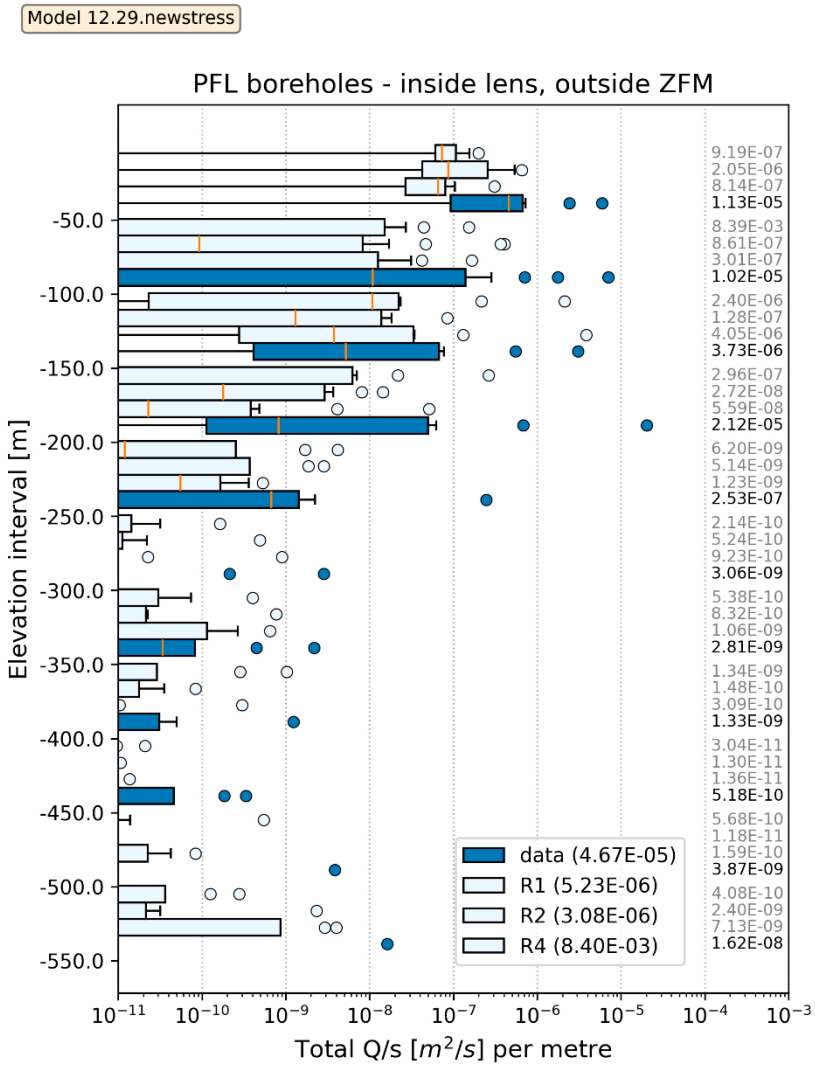

Figure 7-14. *Normalised Q/s per metre (as averaged over each 50 m elevation interval) aggregated over all PFL logged boreholes outside deformation zones in FFM01/02/06 for 3 best realisations (R1, R2 and R4). Each box extends from the lower (Q1) to upper (Q3) quartile while the whiskers extend to 1.5 × (Q3–Q1) beyond the box. Flier points are individual holes with values higher than the end of the whiskers. Numeric values on the right-hand border represent total sum per interval over all logged boreholes, and in the legend, they are the sum of sums over all intervals.*

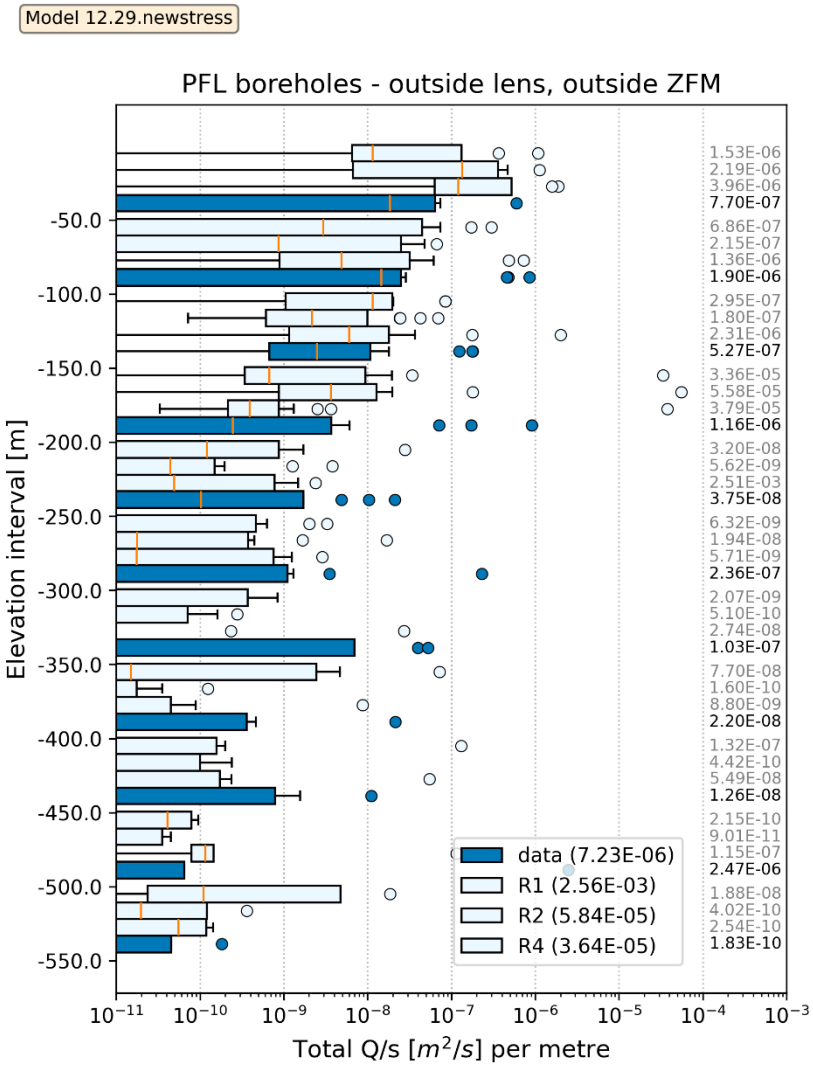

Figure 7-15. *Normalised Q/s per metre (as averaged over each 50 m elevation interval) aggregated over all PFL logged boreholes outside deformation zones in FFM03/04/05 for 3 best realisations (R1, R3 R8). Each box extends from the lower (Q1) to upper (Q3) quartile while the whiskers extend to 1.5 × (Q3–Q1) beyond the box. Flier points are individual holes with values higher than the end of the whiskers. Numeric values on the right-hand border represent total sum per interval over all logged boreholes, and in the legend, they are the sum of sums over all intervals.*

The magnitudes of flows in DZs are also displayed relative to elevation but shown as discrete DZ intersects rather than lumped together. DZs are split into hanging wall and footwall of A2 structure in Figure 7-16 and Figure 7-17 respectively. Individual transmissivities are summed across the SHI intervals for each DZ intercept shown as squares for data and circles or triangles for the three modelled realisations. This can be compared to similar such plots in SDM-Site, see Figures 5-1 through 5-3 in (Follin et al. 2011). Plotting according to elevation reveals the generally triangle-shaped envelope of transmissivities. It is notable that many of DZ intercepts have a measured transmissivity below the detection threshold, indicating the strong variability and channelling within DZ. Here, conceptualised as being caused by variable connectivity within the damage zone of the DZ. The general trends in magnitudes, values of individual intercepts and variability are all surprisingly well honoured, given the complexity of the data. Consideration of the spatial structure of connected open fractures inside DZs as illustrated in Figure 7-7. helps appreciate the random nature of flow measurements in model's conceptualisation, and what this will imply for flow channelisation. The under-prediction of transmissivity of ZFMA2 at depth is thought to be due to the 3D stress model not getting the stress reduction in the hanging wall of this zone entirely correct, see Figure 6-3.

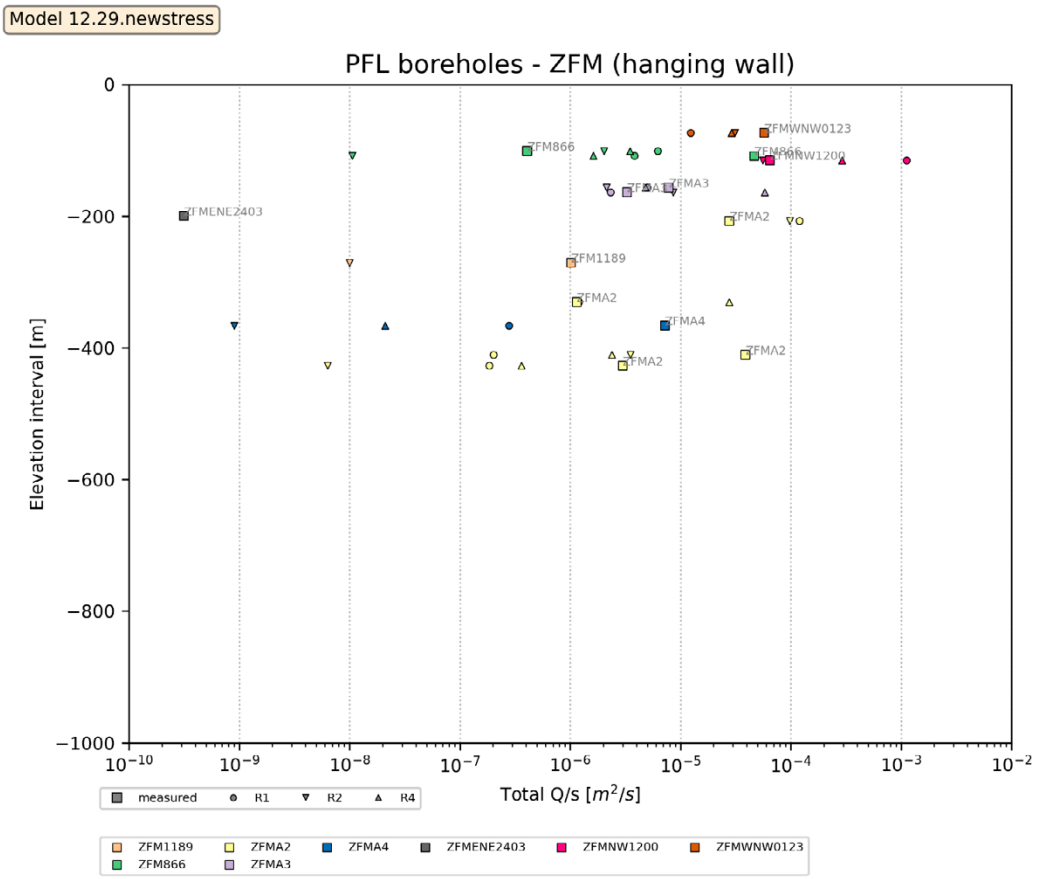

Figure 7-16. *Total Q/s over each DZ interval (SHI) in hanging wall of DZ-A2 structure per individual borehole intersect for measured (square) and three chosen realisations (triangles and circles), order by elevation. DZ intersects where there was no flow or was below the detection limit are plotted as transmissivity* 5×10^{-9} m^2/s.

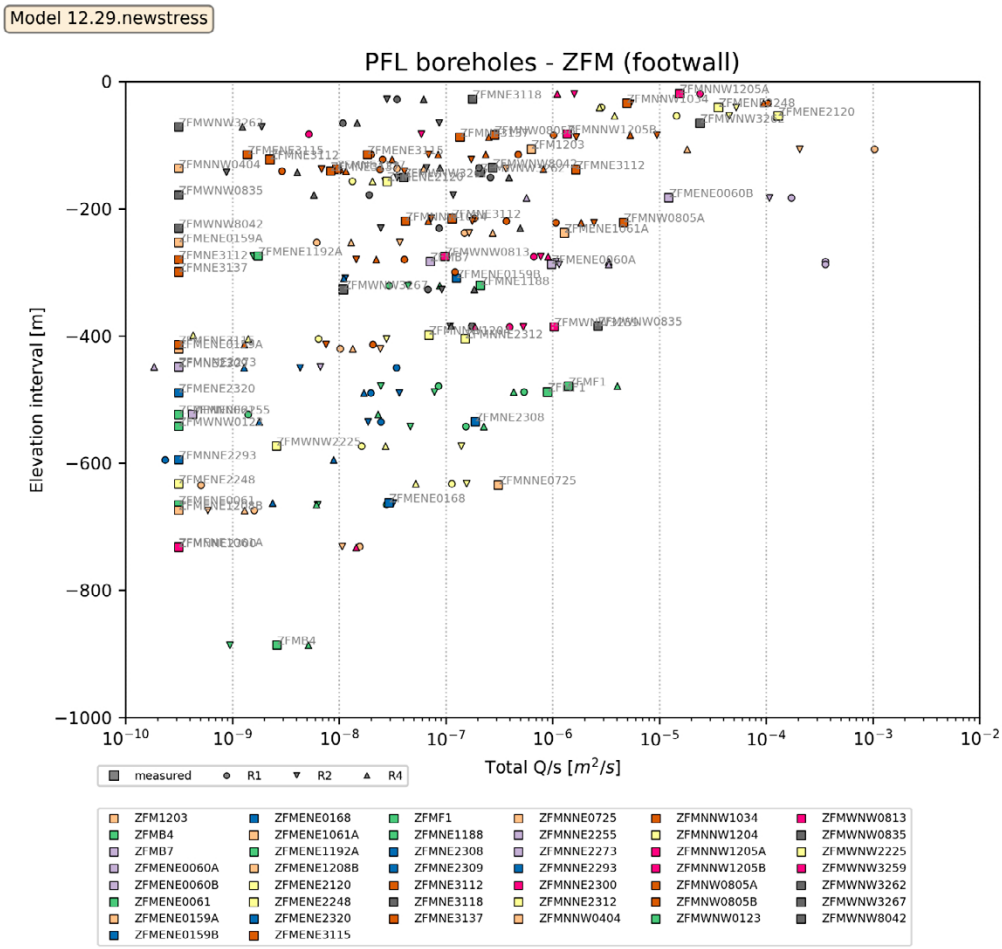

Figure 7-17. *Total Q/s over each DZ interval (SHI) in footwall of DZ-A2 structure per individual borehole intersect for measured (square) and three chosen realisations (triangles and circles), order by elevation. DZ intersects where there was no flow or was below the detection limit are plotted as transmissivity* 5×10^{-9} m^2/s.

7.5 Calibration on interference tests

Figure 7-10 through Figure 7-16 illustrate the calibration of the DFN model's hydraulic parameters based on single-hole tests which constrains how the model describes connectivity of the DZ and background fractures and the transmissivity distributions on the scale of boreholes. Interference tests, on the other hand, tend to constrain the connectivity and transmissivity of the most conductive structures on the scale of the test, which is the DZ for the tests performed at Forsmark. The interference tests most suited to this purpose were the large-scale, long-term pumping tests performed in HFM14. Tests performed first in 2006 (Gokall-Norman and Ludvigson 2007) and repeated in 2007 (Gokall-Norman and Ludvigson 2008). In the 2006, the main test involved pumping for 3 weeks with some monitoring holes instrumented as open holes. In the 2007, the main tests lasted 15 weeks with more holes instrumented with multiple screened sections to give more resolution as to the 3D structural controls on hydraulic communication. This same interference test was also prioritised in the SDM-Site modelling (Follin et al. 2008).

As indicated in Figure 7-8 calibration on the interference tests was performed simultaneously with that on the single-hole tests since it was found that improvements to matching one calibration metric could be the detriment of the other, and so multiple calibration objectives were balanced.

7.5.1 Model setup

Pressure responses were monitored in 185 intervals in 49 boreholes, both cored and percussion drilled. They covered an area with a radius of about 2 km, and hence a 12-sided cylindrical region centred around borehole HFM14, with a radius of 2 000 m and a depth of 500 m was used for DFN modelling. Model boundaries and monitored boreholes are shown in Figure 7-18 and full DFN network prior to removal of sealed and unconnected fractures in Figure 5-40 (Figure 7-7 shows zoomed in area).

All boreholes monitored in the 2006 and 2007 campaign inside the modelled region were included to permit comparison with the observed data and were subdivided into segments according to the screens monitored. Any monitored boreholes intersecting the model outer boundary were excluded from the simulation to avoid numerical problems with mesh refinement near the boundary. The monitored intervals were modelled as passive observation boreholes since they were installed with multiple packed of flowing intervals limiting the amount of cross-flows within boreholes. Results were extracted as simulated drawdowns at fracture intersections within the monitored intervals.

The simulation was run as steady-state with a constant head (0) boundary on the sides of the cylindrical region, as response times were interpreted to be no more than a few days in (Gokall-Norman and Ludvigson 2008), even to 2 km distance. No-flow boundaries were set on top and bottom of the cylinder, i.e. assuming little recharge on the top, and a drawdown of 10 m in the pumped borehole. An alternative boundary condition with zero head on the top surface covered by the sea was also tested, recognising that there are also some lakes inland. Freshwater, constant density, conditions were assumed.

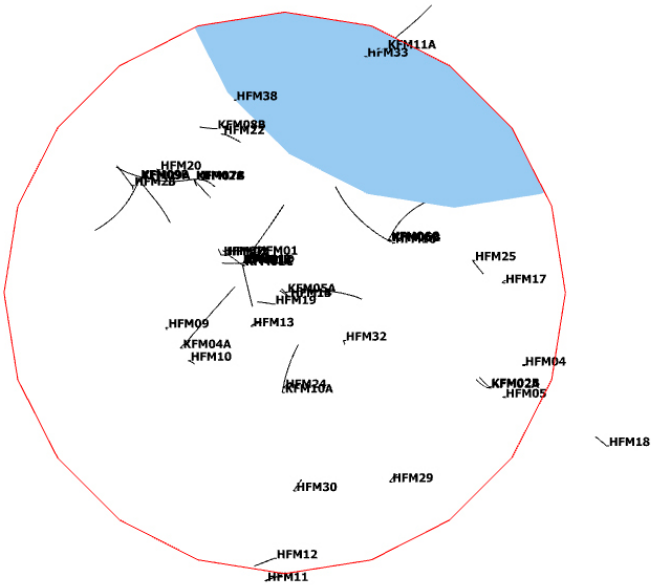

Figure 7-18. *Cylindrical domain used for simulating the HFM14 interference test, at the centre, with a 2 km radius. The monitoring boreholes are shown as black lines. A fixed pressure boundary is applied on the vertical sides (red) and no flow on the top and bottom. Sensitivity to the top boundary condition was tested by setting a fixed pressure on the approximate top surface covered by the sea (blue) as an alternative to no flow over the whole top surface.*

7.5.2 Results interpretation

For each simulated realisation, the calculated pressure drawdown at each monitored borehole interval was exported from the results. Ten realisation were performed per parameter sensitivity test as a reasonable comprise of convergence in overall error metrics and simulation time. If a monitored interval contained multiple intersecting fractures a maximum value of pressure change was considered as the drawdown for the whole interval. These were then compared to the measured maximum drawdown reported in (Gokall-Norman and Ludvigson 2007, 2008), as appropriate.

In the 2007 campaign, the measured drawdown in the pumped HFM14 borehole was 12.5 m (Gokall-Norman and Ludvigson 2008). To compare the measured data with simulation results (where the modelled drawdown was 10 m), the results are normalised by pressure drawdown in the pumped borehole, as the key metrics used for comparison were whether an interval responded or not and whether the response was similar to that at the pumped hole or significantly attenuated.

The results are plotted such that the monitored intervals are sorted by horizontal distance from borehole HFM14 with the distance plotted on the left part of the plot, see Figure 7-19, for example. Moving left to right: the blue squares indicate those intervals intersected by deterministic DZ; the vertical dashed line is an approximate indication of a threshold for clear response; symbols represent the observed and three realisations of simulated normalised drawdowns; in the comparison, the blue bars indicate interpreted responses and the grey a lack of response, the bars under R1–R3 colour code the consistency of the simulated response. A sequence of green modelled responses is good where the measured result saw a response blue, or white/grey/pink modelled responses where measured responses were absent (grey) or small. For each realisation the error metric indicating the match between measured and modelled responses is presented in the parenthesis in figure legend. The metric is calculated as follows:

$$\varepsilon_i = \frac{\left| r_{i,measured} - r_{i,modelled} \right|}{\max(r_{i,measured}, r_{i,modelled})} \qquad \text{Equation 7-2}$$

$$\mathrm{E} = \frac{1}{n}\left(\sum_{i}^{n} \varepsilon_i\right)$$

where r_i represents ratio between the pressure drawdown at monitored location i and drawdown at borehole HFM14. Presented error value for each realisation is calculated as mean of all errors ε_i for all monitored intervals. A better match between measured and modelled data is indicated by a lower E value.

Figure 7-19 shows that for the 2006 test, the pattern of responses or their absence is in good agreement with an absence or varying responses simulated in the correct intervals. The variability in individual responses between modelled realisations is large, but the overall error metric (in the legend here) is consistently around 0.6–0.7. R1 provides the closest match, with the error metric of 0.568, with responses dropping off with distance in a pattern close to that of the data.

The simulations are computationally intensive, and several model variants were necessary to find the set of parameters in Figure 7-19 that provided a balance of matching all calibration targets. Hence, running a large number of realisations repeatedly was not a tractable option. The different levels of drawdown at similar distances but with some holes that respond at various distances are an indication of the discrete and heterogeneous flow system with a few hydraulically dominant but spatially confined connections, as simulated by the model. Modelled discrepancies or variability for some intervals are indicative of the sensitivity to whether particular DZs connect or not. The simulated pump rates also spanned the measured flow-rate, within a factor two either way.

Figure 7-20 shows the equivalent comparison for the 2007 test with additional screened intervals in the monitoring, which improves the characterisation of pressure communication to depth. This confirms the consistent match to those intervals that respond and those that don't or are variable between realisations. R1 is again distinctly the best of the realisations. It can there is a poor correlation between blue boxes on the left indicating DZ connections with measured responses. Although a few key DZ such as ZFMA2 provided dominant hydraulic connections, not all DZ are connected to this flow system, while non-deterministic DZ do provide connections between monitored sections and the dominant flow system that results in responses. Thus, the hydraulic interferences are a test of both deterministic and stochastic descriptions of the fracture system.

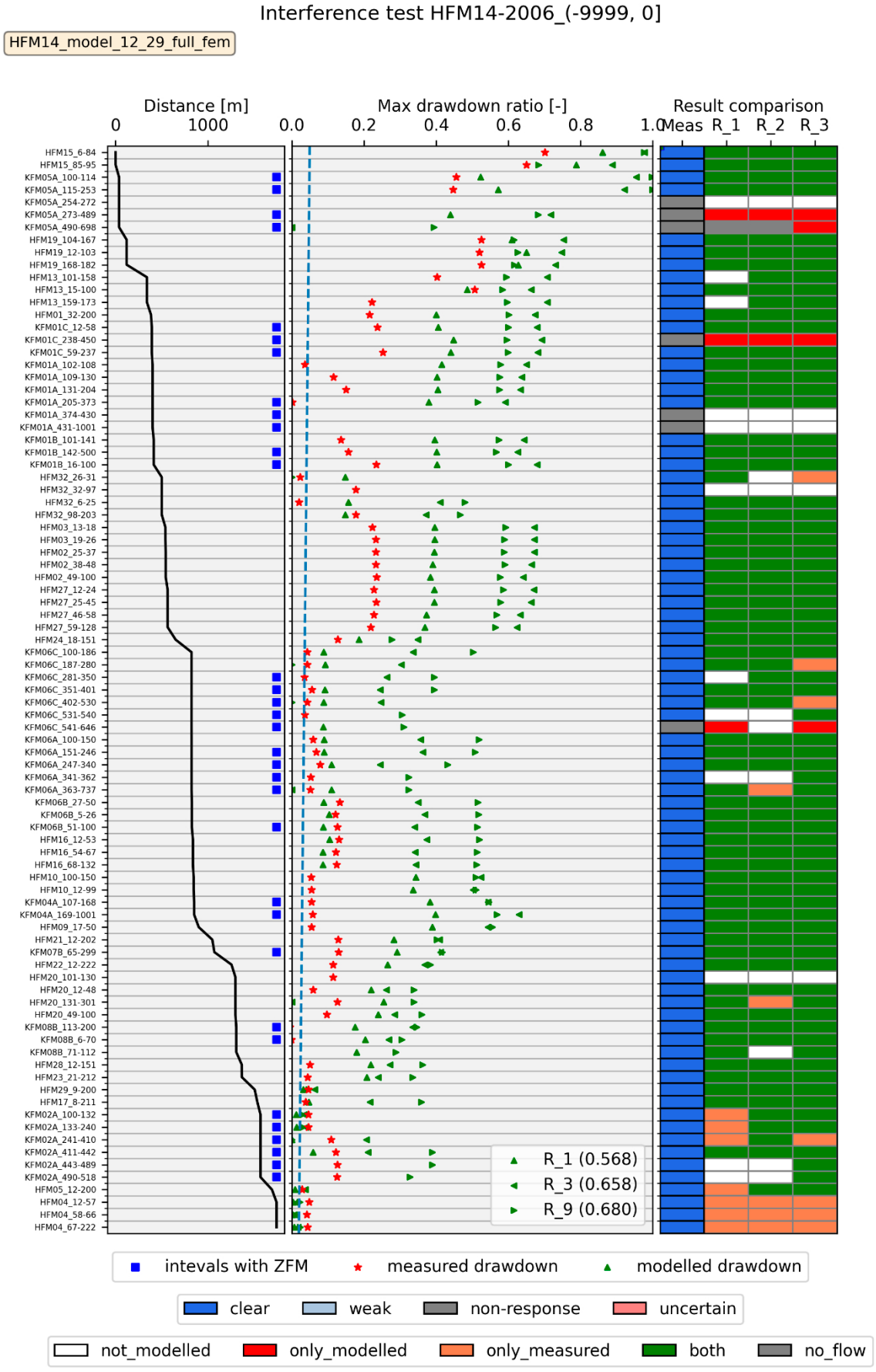

Figure 7-19. *Comparison of measured (red stars) and simulated (green symbols) normalised drawdowns for the 2006 interference test in HFM14. Case with no flow on top boundary. See text for details.*

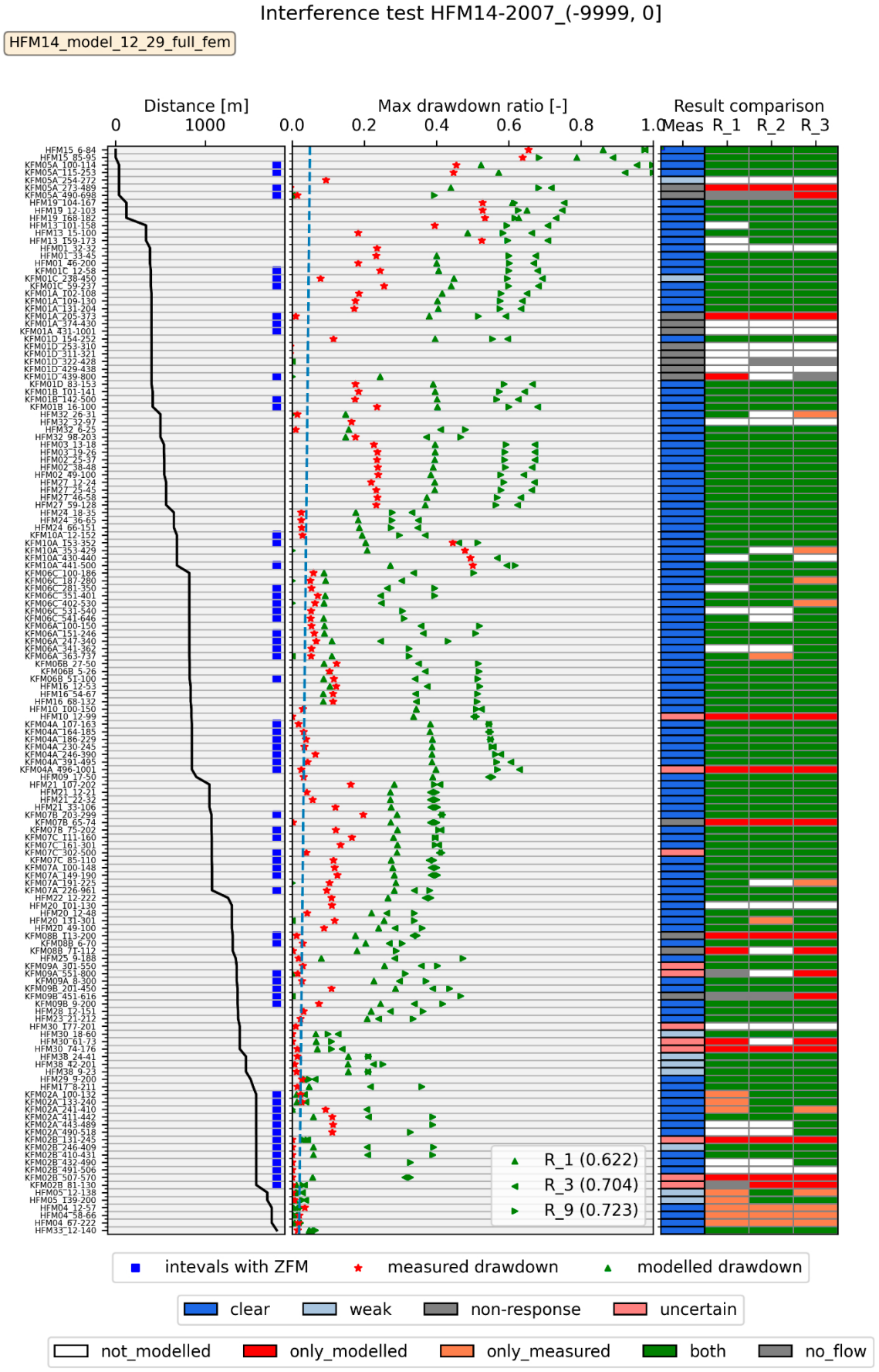

Figure 7-20. *Comparison of measured (red stars) and simulated (green symbols) normalised drawdowns for the 2007 interference test in HFM14. Case with no flow on top boundary. See text for details.*

Figure 7-21 and Figure 7-22 show the equivalent plots for the sensitivity case with a fixed head boundary on the north–east corner of the top surface to approximate the fixed head of the seabed.

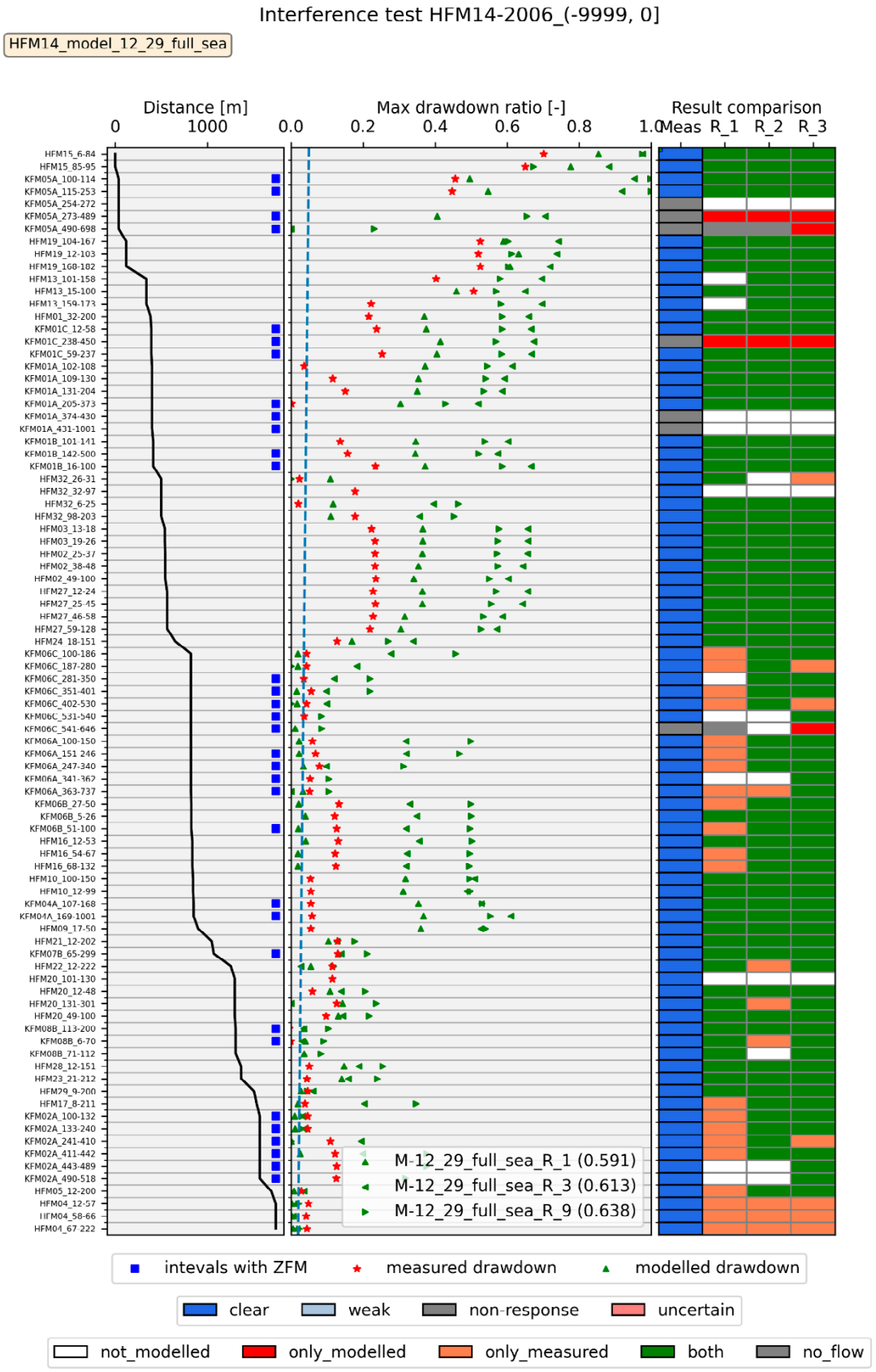

Figure 7-21. *Comparison of measured (red stars) and simulated (green symbols) normalised drawdowns for the 2006 interference test in HFM14. Case with partial fixed head on top. See text for details.*

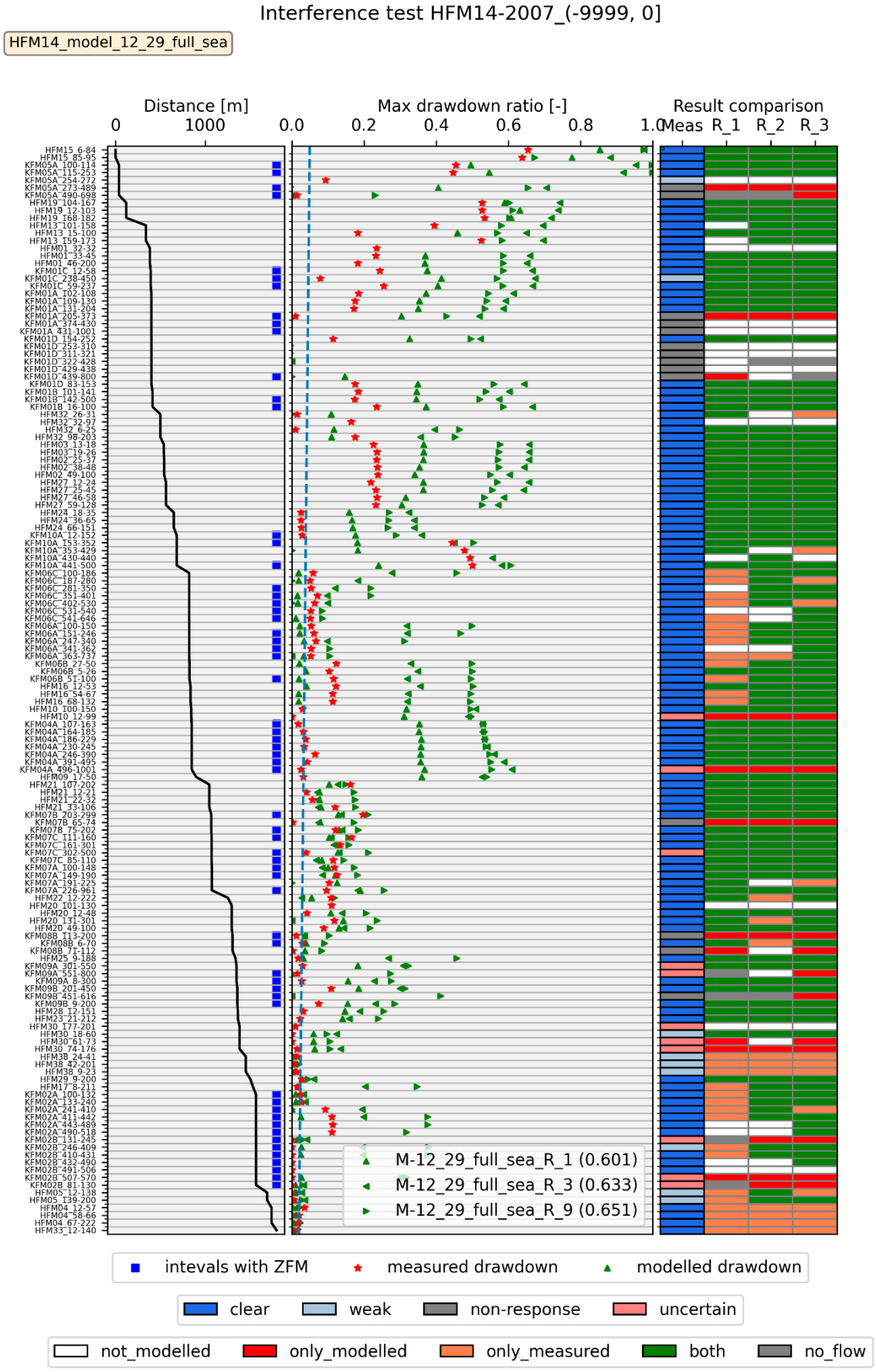

Figure 7-22. *Comparison of measured (red stars) and simulated (green symbols) normalised drawdowns for the 2007 interference test in HFM14. Case with partial fixed head on top. See text for details.*

These produce a slight improvement in the modelled results in the far-field with a reduced over-prediction of drawdown. It is possible that the fixed head associated with lake Bolundsfjärden near to HFM14, and more distant Eckarfjärden, also has an attenuating effect on the measured drawdowns.

It is interesting to compare these results using a DFN model to simulate a large-scale interference test directly to previous modelling versions that have first upscaled the DFN to an equivalent continuous porous medium (ECPM). The same HFM14 interference test was simulated using the Forsmark version 2.3 DFN upscaled to an ECPM, see Figure 5-6 of (Follin et al. 2008). This was able to accurately reproduce pressure responses out to about 700 m from the pumped holes, but then tended to under-predict responses at greater distance. This is presumably a result of the upscaling process smearing properties to give a more uniform and isotropic system than both reality and the underlying DFN model. By contrast the DFN-BF1 model tends to over-predict far-field drawdowns due to its long range connectivity and the low pressure diffusivity outside of main conduits. The DFN model also predicts far more variability between realisations, resulting from the stochastic creation and connectivity of different structural compartments. This variability is far greater than in the F2.3 ECPM model, see Figure 7-2 of (Follin et al. 2008). That study did identify the properties of ZFMA2 as being the main control on the magnitudes of drawdowns, as seen in Figure 7-5 of (Follin et al. 2008). That is a useful indicator that the absolute magnitudes of drawdowns could be improved in the DFN-BF1 model, by some fine-tuning of the properties of ZFMA2. Figure 7-5 of (Follin et al. 2008) would suggest drawdowns are reduced when the transmissivity of ZFMA2 is increased. It is noted that the simulated transmissivity of the upper intervals in ZFMA2 is about half an order of magnitude low in Figure 7-16. The hydraulic calibration here has tried to adjust the DFN properties of DZs as a whole rather than individual zones, but it appears that ZFMA2 would benefit from its own specific parameterisation.

A similar interference test in HFM43 was simulated in the prototype DFN modelling of the upper bedrock (Hartley et al. 2021) using an upscaled ECPM. That was able to reproduce the general pattern of drawdowns with distance, see Figure 4-22 of that report, but again failed to reproduce the lack of responses in some intervals. This again shows that upscaling tends to average out the hydraulic compartmentalisation of discrete fracture systems. Comparison with this interference test could also be considered in future updates of the DFN model.

In summary, the power of modern computers and numerical methods has demonstrated that direct simulation of large-scale interference tests using DFN's directly does improve the representation of discrete compartmentalised fracture systems over previous upscaled ECPM based approaches. The increased parametric complexity, does however, bring some additional logistical challenges.

Implementing a structural recipe as complex as that described in Chapters 5, 6 and Sections 7.1 and 7.2 on a scale of this interference test created challenges that had not been faced before, and so several cycles of model building and sensitivity analyses had to be trialled. Learnings from these sensitivity tests are, therefore, captured in Table 7-2 as a qualitative narrative rather than a detailed control set of analyses.

Table 7-2. Summary of sensitivity testing during calibration process against both single-hole PFL and hydraulic interference tests.

Property	Summary of sensitivity testing
k_r of DZ-related swarms	The size scaling exponent for the prior model for DZ-related fracture swarms. This was the most critical geometric parameter tested as it controls the backbone connectivity of the hydraulic system. Using values of around 2.0 makes for an overly connected system with high drawdowns extending far through the system. Using high values around 3 breaks connectivity, eliminates responses and chokes flow to much lower magnitudes in the PFL tests. Optimal values around 2.6–2.7.
Open fraction	The fraction of open surface area has a strong control on connectivity. The values interpreted from core provide constraints on this parameter that lead to a model that largely has the correct connectivity. Some small, 10–20 %, relative reduction in the fraction of open fractures was found to improve the matching of the low connectivity at depth seen in PFL and interference tests. This calibration is non-unique since same effect could be mimicked by changing the scaling model of fractures at depth or the aperture closure model for normal stress.
K_I	The Mode I fracture toughness. This was increased within the DZ according to the site data range to make a bigger contrast between DZ and background fractures in order to better match the PFL flows inside DZs.
E	The Young's modulus. This was decreased within the DZ within the site data range to make a bigger contrast between DZ and background fractures in order to better match the PFL flows inside DZs. Compounds change made to K_I. Reducing Poisson's ratio would also have a small effect in this direction.
e_r	Residual aperture. Increased slightly to maintain some background connectivity for the single-hole tests. It has the implication of maintaining transmissivity and connectivity at depth when using the exponential closure model. An alternative hyperbolic closure model would result in lower transmissivities at depth.
f	Aperture roughness factor. This was decreased in background and further decreased in DZ to make a bigger contrast and increase transmissivity.
φ_r	Friction angle. Values were decreased in DZ to get the higher flows near the surface and in relatively low stress areas. This improved the PFL flows seen in the top of the bedrock and flow rate measured in HFM14.
Inclusion of sheet joints	Sheet joints were included in top 30 m outside the lens to avoid a choking of flows in the interference tests giving high drawdowns far away from HFM14.
α	The rate of decrease of aperture/transmissivity with stress in the exponential normal closure model. This was not changed from the initial guess as it matches the correct reductions in transmissivity below −200 m elevation.
Alternative normal closure model	Only the exponential normal displacement model was tested. This gives a sharp drop-off in transmissivity becoming a constant determined by the residual aperture. An alternative is to use a hyperbolic form that gives a continuous drop-off in transmissivity with depth, allowing a lower residual aperture/transmissivity to be used.
Inclusion of surface water as boundary conditions	An alternative top surface boundary of zero head on the top surface approximating the sea trialled for the interference test, which made a small improvement. Other lakes closer to the pumping hole might have a more significant effect. Although fine-tuning the transmissivity of ZFMA2 would likely have a greater effect.

7.6 Summary and potential future refinements

The integration of the structural recipe defined in Chapter 5 with the spatial distribution of apertures within the fracture system quantified in Section 7.1 and transmissivity distribution defined in Section 7.2 according to links to the 3D stress field described in Chapter 6 has after calibration yielded a model that mimics the connectivity, spatial structure and distribution of magnitudes of the observed flow field under different forced conditions. The model matches these key hydraulic characteristics in a statistical sense including observed differences between statistical domains relative to the lens (SKF) and outside lens (SFR), relative to inside / outside DZ and depth variations. This is true both for the intensity and magnitudes of flow. Key conceptual changes in the modelling methodology DFN-M2022 relative to SDM-Site (DFN-M2008)) include:

- Heterogeneity/channelling of connectivity and flow within DZ due to them being modelled as swarms;
- More structural domain and orientation specific distributions of the fraction of fracture open surface area to control trends in open fracture connectivity and hence flow;
- Integration with a 3D rock mass mechanical model and 3D stress field to describe the drivers for spatial controls and variability in flow rather a purely statistical description;
- Inclusion of rock mechanical parameters via hydromechanical models in the hydraulic calibration opening the possibility of a holistic structural-mechanical-hydraulic calibration;
- Use of borehole-specific DFN structural models for each PFL tested hole for use in calibration rather than generic vertical boreholes; and
- Use of DFN models directly in the calibration of large-scale interference tests to better match the compartmentalisation and channelisation of pressure communication observed as spatial variability in pressure responses.

Further potential improvements of the methodology and its implementation include:

- The calibration of DFN structural-hydromechanical parameters against hydraulic data on its own results in a multitude of possible parameter combinations, i.e. non-uniqueness. Using the DFN model as a basis for an upscaled earth (synthetic rock mass) model to calibrate on both measured stress and hydraulic conditions would reduce these uncertain combinations and provide a two-way integration. This is particularly important for the DZ scale structures that have strong effects on both the stress and flow fields;
- The normal displacement model has only considered an exponential form. This may be adequate for describing the reduction in transmissivity over the top 200 m of bedrock, but this may not adequately describe if transmissivity asymptotes or continues to fall below this depth. Figure 7-16 would suggest that the envelope of transmissivity values continues to fall with depth, which is more consistent with a hyperbolic form for normal displacement at high stresses seen at greater depths. Another hypothesis to consider is that openness of fractures continues to fall with depth due to self-sealing. More experiments need to be made in describing the deep hydraulic system;
- Testing of parameters describing DZ as swarms have been made using the same parameters for all DZ apart from their thickness varying with size. More specific parameterisations according to orientation of DZ and or key zones such as ZFMA2 and Singö should be tested;
- The HFM14 interference test would support fine-tuning of ZFMA2. Other interference tests such as HFM43 in the accesses area could further constrain the sheet joint hydraulics and the KFR27/103/105 interference tests could further constrain the outside lens domain hydraulics; and
- Beyond these proposed exercises to take a more holistic/integrated approach to uncertainties in hydromechanical properties, reduction in uncertainty regarding structural parameters, such as size scaling, can only be tackled through further detailed mapping of fracture patterns on the surface and, more importantly, underground. Some first exploration of new surface mapping data is presented in the next chapter, but the present maturity of that data does not provide conclusive feedback to the hydraulic modelling yet. The sensitivity to geometrical parameters can be explored alongside planning of further phases of structural mapping as prediction-outcome exercises. The hydraulic data from PFL and interference tests provide a permanent set of metrics that new DFN models can be tested against as they become more constrained by structural mapping and flow logging data at depth.

8 Model validation against new outcrop data

8.1 Introduction

Here, we compare modelled fracture trace data with the fracture traces mapped from the drone orthophotos shown in Figure 3-5. It is reiterated that at the time of writing the mapping of these traces is incomplete, and consequently they have not been quality checked. Nonetheless, they still provide value when used for illustrative comparisons.

In most of the areas mapped by drone data, a large proportion of the traces are truncated by the limits of the bedrock exposure (Figure 3-5). However, AFM001702 covers a sufficiently large contiguous area that many traces do not finish at the limits of the exposure (Figure 8-1). Consequently, it is the most suitable outcrop for analysis of the traces. However, it should be recognised that the mapping is ongoing, and the methods are being tested and refined (see Figure 8-2) as discussed where appropriate.

To compare the modelled tracemaps with those observed, polygons describing the approximate surveyed area were interpreted (e.g. Figure 8-1). These interpretations are based on both the orthophotos (e.g. excluding areas of non-exposure) and limits of the mapped traces (i.e. to exclude areas of exposure where no traces were mapped). Using the intersection of the DFNs with these polygons ensure that the modelled traces are subject to the same approximate truncations by the limits of the surveyed area, permitting an equivalent comparison.

No DZs or sheet joint fractures were included in the DFNs used to make predictions in this chapter. Based on the observed size distribution shown in Section 8.4, a r_{min} of 1 m was selected. Otherwise, the parameters used match those described in Chapter 5.

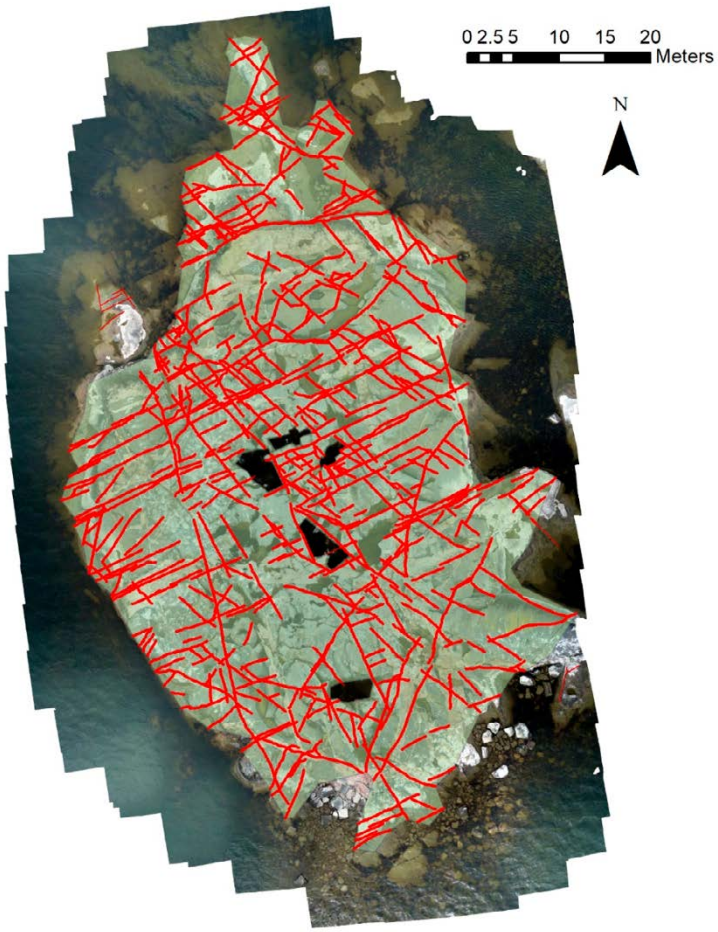

Figure 8-1. *Drone-sourced orthophoto of AFM001702 (see Figure 3-3 for site location) overlaid with mapped fracture traces (red) and estimated mapped area (transparent green).*

8.2 Intensity

As mentioned, the drone trace mapping is incomplete (Figure 8-2), and so provides only a lower estimate for the true intensity of fracture traces. AFM001702 has the most complete mapping of the drone surveyed outcrops, and also covers the largest area of clear exposure (Figure 8-1). Consequently, it was selected to calculate the observed fracture intensities. The interpreted mapped region shown in transparent green on Figure 8-1 has an area of ~2 619 m^2 and contains mapped fracture traces with a total length of ~2 031 m. This is a P_{21} intensity of ~0.8 m^{-1}.

A comparison of predicted and observed fracture trace intensities in AFM001702 are shown in Figure 8-3. A tracemap of an example fracture realisation is shown in Figure 8-4. The data value is highly by fracture visibility and censoring effects.

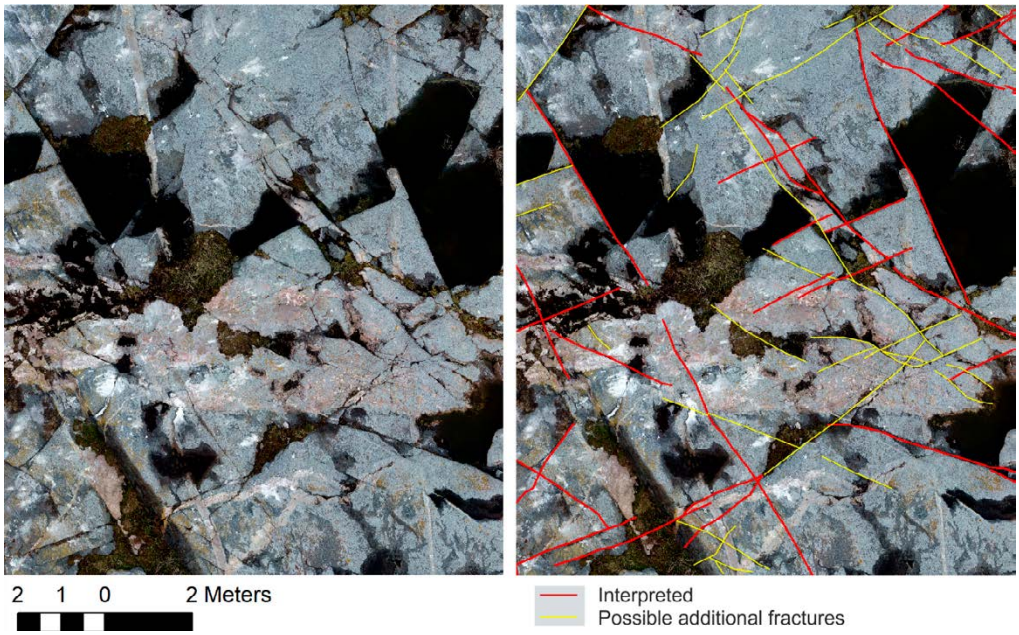

Figure 8-2. *View of part of AFM001702, with traces interpreted in the data delivery (red) and possible additional traces (non-exhaustive) marked (yellow).*

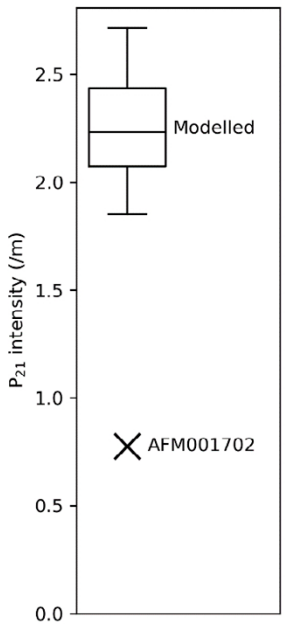

Figure 8-3. *Boxplot showing the distribution of intensities modelled in ten different realisations for the surveyed area at AFM001702 in comparison to that observed.*

The intensity of the predicted traces is around three times higher than those observed. However, as well as the incomplete mapping (Figure 8-2), there are three other factors that may reduce the mapped intensities.

The first is that AFM001702 is a small high point in a glaciated landscape, which to exist as such must have been more resistant to erosion than the surrounding areas. Relatively high erosion resistance corresponds to relatively high mechanical strength, something influenced by relatively low fracture intensity. The second factor is that pieces of bedrock underlain by shallowly dipping fractures are less resistant to the abrasive erosion of an overlying glacier, as they have a pre-existing mechanical break with the underlying bedrock. Therefore, the rock above a shallowly dipping fracture will have been preferentially removed, also removing the features that would have allowed the shallowly dipping fracture to have been mapped. Consequently, in a glacially exhumed outcrop the intensity of mappable shallowly dipping fractures is reduced. The third factor is that due to the geometries involved, shallowly dipping features are less likely to have a near-linear signature on a shallowly dipping bedrock surface. This means that their signature is harder to identify, resulting in a lower mapped intensity. These factors do not occur in the simulated fracture mapping, creating a bias.

It should also be noted that in most DFN scenarios, it is typical for a model calibrated to intensities observed in borehole data to produce higher intensities than those observed in outcrop. This is influenced by a number of factors that includes those described above, but also the uncertain size distribution of the fractures and the difference in scale between fractures logged in boreholes and fractures mapped on outcrop. Experience in predicting fracture intensity seen in subsurface tunnel mapping from DFNs and comparing to tunnel pilot hole amping has been gained from ONKALO® (Hartley 2022a). It was found that intensity of fracture traces above an effective lower size limit can be accurately matched, and its value is relatively consistent between different tunnel sections, whereas fracture intensity in boreholes/ pilot holes is more spatially variable.

Figure 8-4. *Example realisation of fracture traces modelled at AFM001702 for comparison with Figure 8-1.*

8.3 Orientation

The mapped trace data has the orientation distributions shown in Figure 8-5. These are generally bimodal distributions with a bias toward a dominant mode due to the elongated shape (shorelines) for most of the surveyed areas (Figure 3-5). Modelled distributions for these surveyed areas are shown in Figure 8-6. The rose plots for the compiled realisations show a range of orientations that is much more distributed than the observed data reflecting. About two thirds of the realisations for each outcrop have a dominant trend mostly in either the NW or NE quadrants, with the remainder of realisations showing mixed mode orientations. The data also shows each outcrop is dominated by one of these two modes/ sets. In that sense, the clustering of background fracture orientations around small DZs is confirmed as being an important component of the DFN conceptualisation when describing fracturing on the scale of these outcrops 10–100 m. However, the model has no mechanism for predicting which orientation of small DZ is most likely in a particular location on this scale, and so comparing predictions and data for individual outcrops has little meaning, especially where it is only been possible to map subareas of each. The main value is this comparison then is to confirm the value of having small DZ swarms as a component of the DFN-BF1 model rather than a pure Poissonian background fracturing.

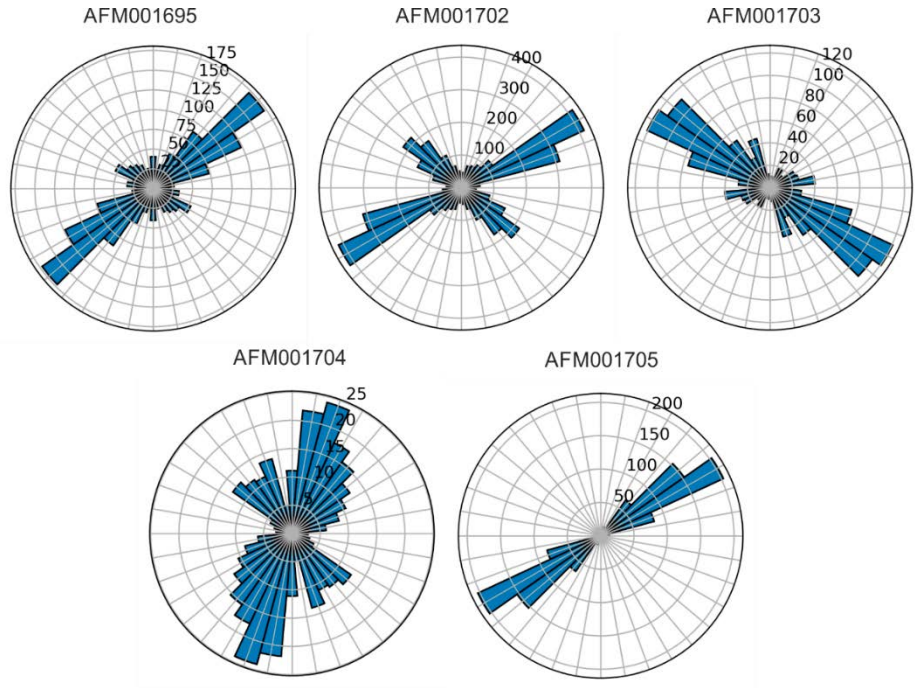

Figure 8-5. *Rose diagrams showing the orientation distribution of the traces mapped from drone-sourced orthophotos (see Figure 3-5). The radial axes are the segment-length weighted fracture counts.*

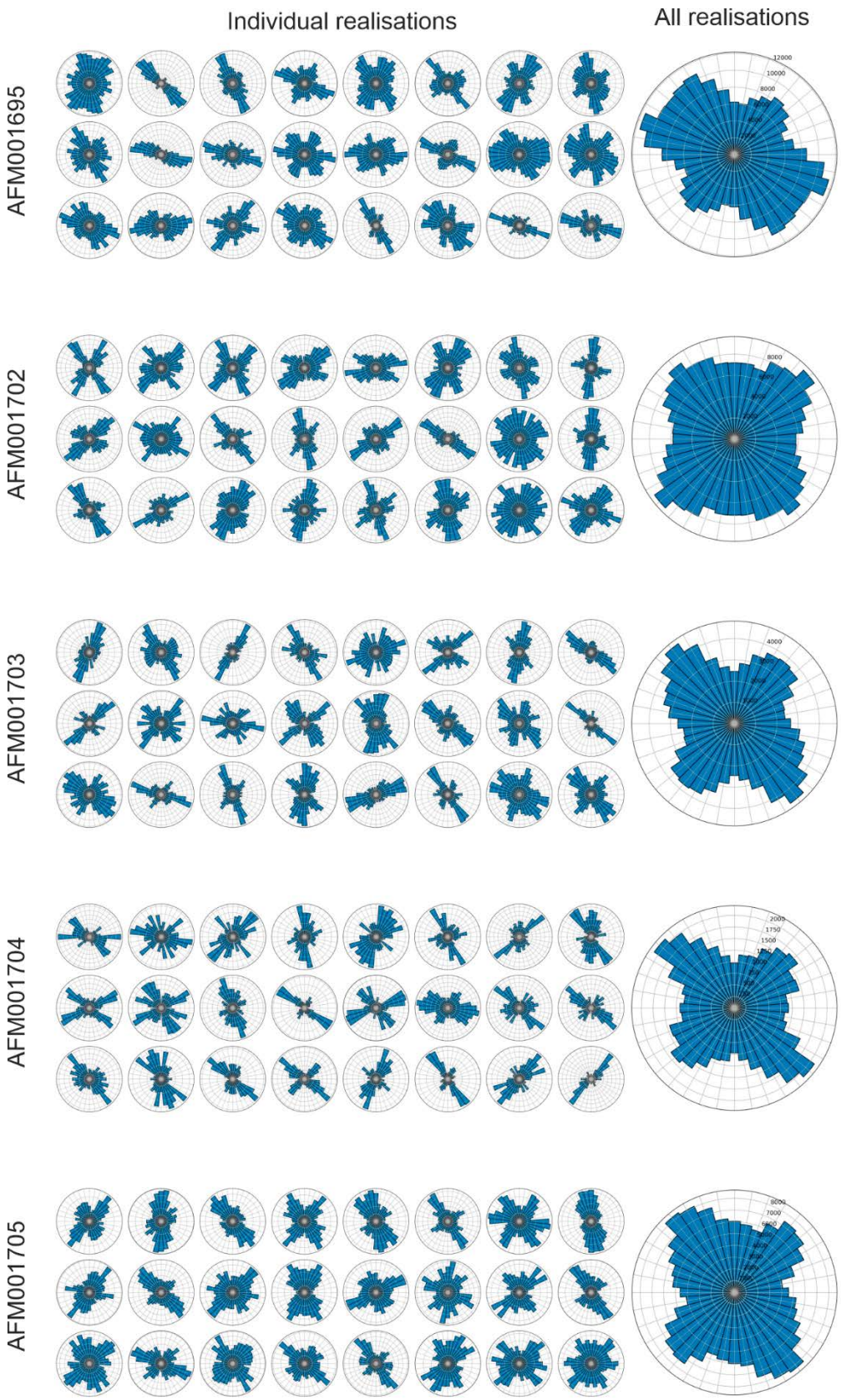

Figure 8-6. *Rose diagrams showing the orientation distribution of 24 realisations of modelled fractures traces that intersect each surveyed areas, and rose diagrams showing the compiled traces for all realisations. The radial axes are the segment-length weighted fracture counts.*

8.4 Size distribution

To compare the modelled trace size distribution, fracture intersections were calculated for the area of outcrop surveyed in AFM001702 (Figure 8-1). Figure 8-7 compares the size distribution of the observed traces at AFM001702 outcrop with ten realisations of modelled traces. Several features can be noted on this graph. Firstly, there is a rollover at trace lengths below 1–1.5 m indicating an effective r_{min} below which it is difficult to detect and map all traces of such size. There is then a window ~1–5 m with a power-law exponent of ($k_t \sim 1.5$, $k_r \sim 2.5$) where fractures have grown mostly without encountering larger ones, and a window 5–15 m where the exponent increases ($k_t \sim 2.7$, $k_r \sim 3.7$) due to terminations. Beyond 15 m, the mapped size distribution is heavily censored by the restricted sizes of the exposure and obscuring features such as water and vegetation (Figure 8-2), and so the distribution tails off compared to the model. Otherwise, the modelled size distributions are a reasonable match for the observed data. The key conclusion is that fracture terminations have important effects on the size distribution on fractures larger than ~5 m, likely having significant effects on network connectivity and tortuosity of transport pathways, and so endorses consideration of a G-DFN to assess these issues.

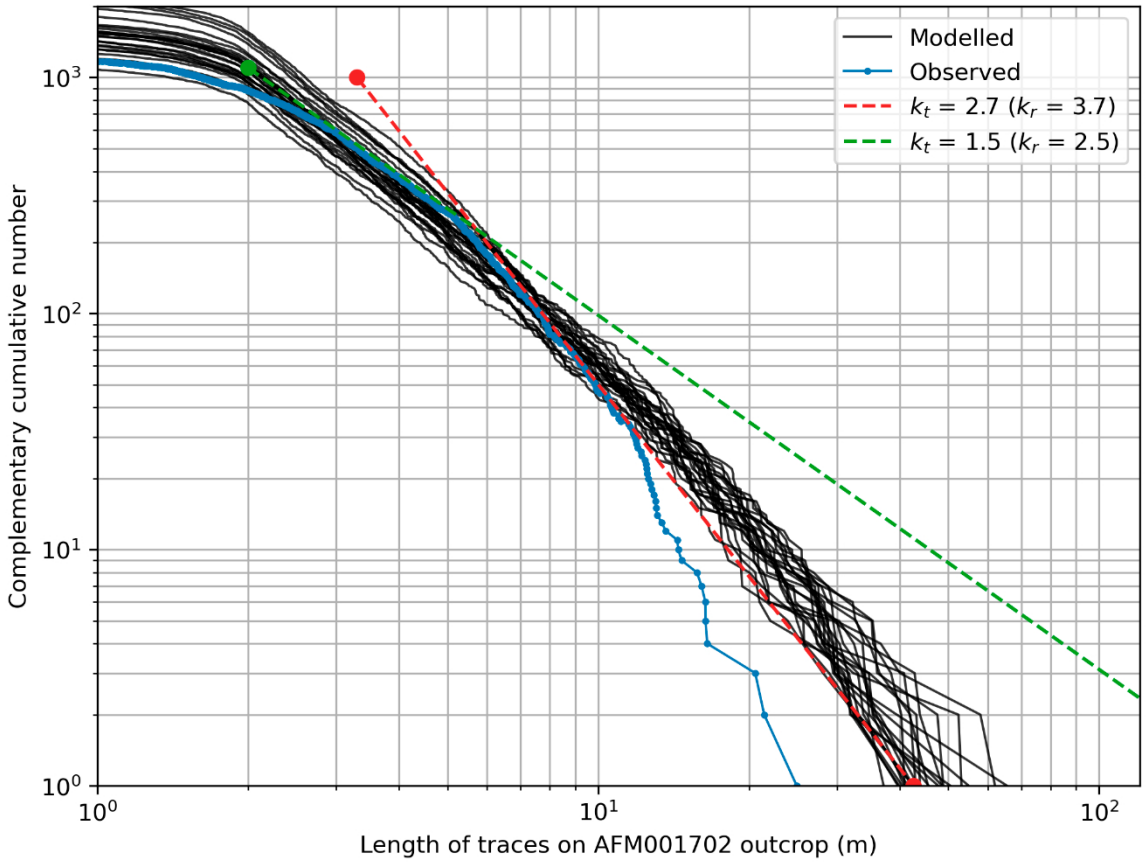

Figure 8-7. *Complementary cumulative distribution plot showing the distribution of fracture trace lengths observed in the AFM001702 outcrop, and ten realisations of modelled fractures for the same outcrop area.*

8.5 Terminations

Connectivity topology is discussed as a metric of the importance of terminations in Subsections 5.2.3 and 5.4.4 on DZ scale and background fracture scale, respectively. Subsection 5.2.3 showed that fracture node end types I/X/Y have ratios about 10/70/20 on the DZ scale, i.e. most DZ terminate on another but cross several DZ before eventually terminating. This is a scale dependent characteristic, with more I type intersections expected for smaller scale fracturing. Here, a collation of connectivity topology for the various outcrops is compared with model results (see Figure 8-8). Variations between outcrops are large, which reflects the sub-optimal shape and obscuration of most outcrops. Still, the data suggests points to I/X/Y ratios of about 50/15/35 with most uncertainty between the X-Y fractions. The model predicts 40 % I nodes (40/45/15), with a bias to under-prediction because smaller metre scale fractures are easier to model than to measure and these are more likely to end in I nodes. This fraction between isolated and connected end nodes is the key characteristic, along with intensity, determining connectivity. The measured high ratio of Y/X nodes again confirms that terminations are an important characteristic of the network, if secondary to the forementioned properties, and so again justifies including them in the model conceptualisation. The censoring effects of mapping towards larger fractures tends to also reduce the number of observed X nodes and incomplete mapping and the presence of obscured parts of the mapping area tends to promote Y nodes. Further sensitivity studies varying fracture size and termination parameters (Table 5-5) as well as uncertainties in calculating the connectivity topology might improve this comparison alongside the size distribution comparison. Moreover, this example illustrates the value of outcrop mapping, especially once it is possible underground, for reducing model uncertainties.

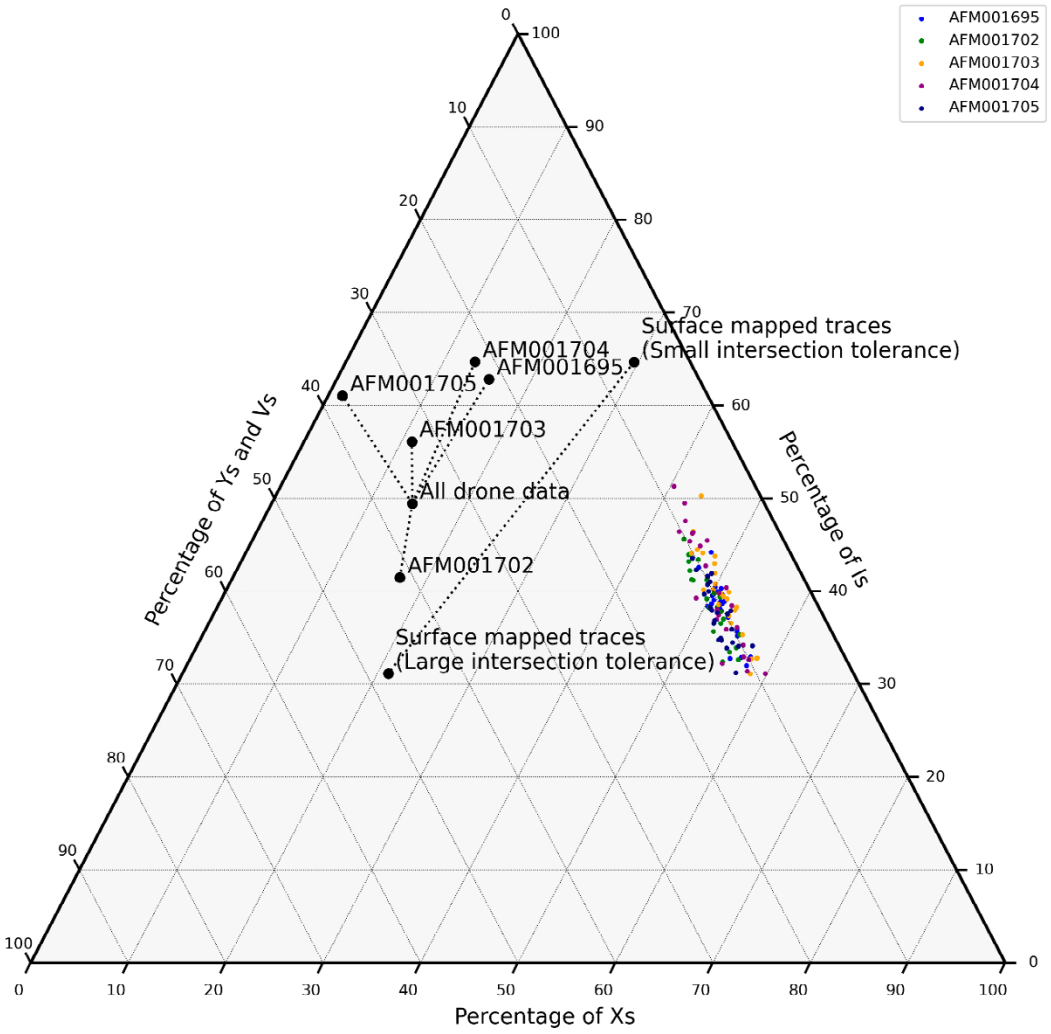

Figure 8-8. *Ternary diagram illustrating the fracture trace connectivity topology (Sævik and Nixon 2017) for traces interpreted from drone and modelled mapped fracture traces (coloured dots). For comparison, the surface mapped traces from Figure 5-30 are included.*

8.6 Summary

Recognising the preliminary nature of the drone data interpretations, the predicted modelled fracture traces show a promising degree of compatible with those observed in outcrop for all the tested metrics: intensity, orientation, size and connectivity. The incomplete fracture trace mapping and the absence of clear limits on the areas that have been mapped has caused (in a best-model-performance end-member) or exacerbated (in a worst-model-performance end-member) discrepancies between observed and modelled fracture trace data. However, if both these issues were resolved, the model outputs would be more similar to the observed traces, and it is feasible that some of the metrics would be very comparable to the observed data.

One notable aspect of the comparison is that the stochasticity of having Small DZ-related swarms in the Baseline DFN is that the DFN-BF1 model yields local scale variations in predicted orientations driven by the chance of occasional (0, 1 or 2) small DZ dominating individual outcrops on this scale. That is a feature seen in both these new drone-mapped outcrops and the original outcrops cleared for SDM-Site. Small scale variability of this type could not be predicted by the DFN models developed for SDM-Site as they used a homogeneous Poissonian spatial model within each fracture domain. Hence, this ability to predict geometrical spatial variability at the surface holds promise for the DFN-BF1 model's ability to also predict variability in the subsurface on the scale of spacings between deposition holes and tunnels. It is recommended that prediction-outcome exercises similar to those explored here be performed for data from mapping excavations once construction begins.

9 Upscaling of DFN to continuous property models

The flow modelling described in Chapter 7 uses a DFN representation throughout. ECPM models represent an alternative modelling approach that can be computationally less costly as multiple discrete fractures can be represented by a single ECPM cell, however, this smears sub-cell-scale aspects of the DFN, such as directional connectivity and channelling. The current limits of computational power mean that for local- and regional-scale models (e.g.10s km), ECPM models can represent the only practical solution/approach. Accurate Upscaling methods that produce heterogeneous and anisotropic cell-based permeabilities, as well as porosities and fracture surface area per unit volume, can produce a reasonable approximation of bulk flow and (but to a lesser extent) reasonable solute transport properties. Accurate upscaling methods must capture the connectivity and orientations of fractures (Jackson et al. 2000; Ahmed Elfeel and Geiger 2012; Lei et al. 2015; Chen et al. 2018).

9.1 Domain grid upscaling

This subsection illustrates the upscaling of a DFN created for the interference tests described in Chapter 7. This DFN covers a cubic region measuring 1 500 m × 1 500 m × 500 m and has a minimum fracture size of 12 m radius (r_{min} = 12). The resolution of the grid, D, on which the upscaled values were calculated is 20 m (hexahedra). (To represent DFN discontinuity, it is advisable to choose $D < 2\ r_{min}$.) Two methods are tested and compared: The Oda method (Oda 1985) and a flow-based method (Jackson et al. 2000; Zou et al. 2017), known as Block k and implemented in FracMan.

The Oda method calculates permeability tensors in three dimensions and all directions for each cell of a given grid. The Oda tensor represents a simplification of Darcy's Law for laminar flow through a porous medium. It works by projecting the uniform fracture intrinsic permeability onto the plane of the fracture, then scaling it by the ratio between the fracture volume (i.e. aperture and area) and the volume of the simulation grid cell. The result is a 3 × 3 matrix describing the directional permeability in each fracture; these matrices can be summed to give a full symmetric net permeability tensor for the grid cell. Alternative forms of output are this tensor or its principal components. The principal permeabilities and flow directions can then be found by eigenvector analysis of the symmetric net permeability tensor. If only the axial components of the tensor are required, these can be scaled by the cube root of the determinant of the full matrix.

The flow-based method can be applied to grids with cubic cells to resolve a permeability value for each axis of each cell. When the method is run, FracMan first meshes the parts of the fracture network within each cell. Then, for each axis of the cell, a linear head gradient is applied along that axis and a steady state flow solution found. These flows are then used to determine an equivalent permeability for that part of the DFN. See (Ahmed Elfeel and Geiger 2012), for example, for a comparison of the two methods.

Figure 9-1 compares the permeability values that result from the two methods for the entire interference tests model of Section 7.5. On average, the Block k method results in both lower permeabilities and a significant number of cells with essentially zero permeabilities. This latter observation is key, as it represent cells where there is no fracture geometric connectivity across the cell, an aspect which is identified by the Block k method but not by the Oda method. (Again, to accurately represent DFN discontinuity is an important feature of ECPM modelling.)

Figure 9-2 illustrates how the upscaled permeabilities decrease with increasing depth, with median permeabilities decreasing monotonically for both methods due to the increasing mean stress. The Oda method always gives slightly higher median and 75-precentile values, but the Oda method can be seen to provide a good approximation of statistics at all depths and directions. The larger spread in ranges at elevation −500 m is probably caused by larger variation of stresses due to the boundary effect of the 3D stress model (Section 6.1).

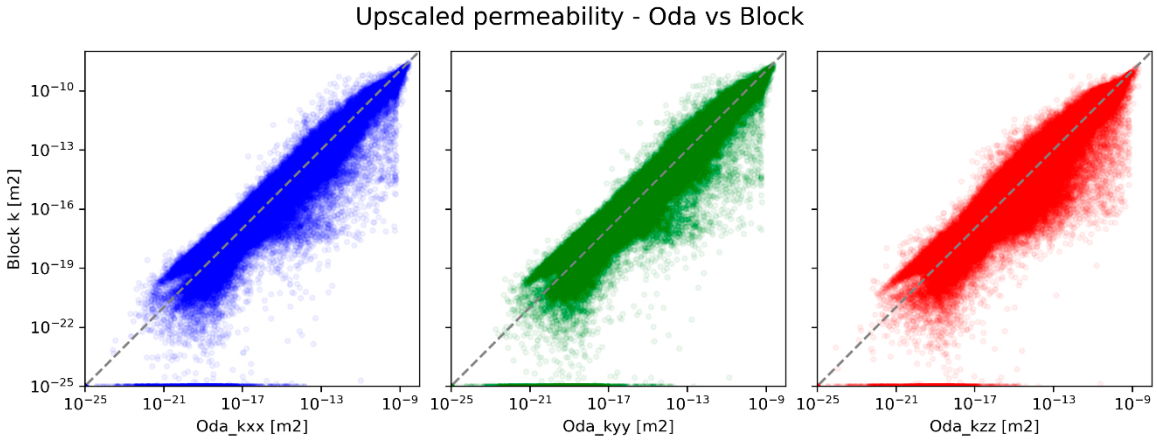

Figure 9-1. *Scatter plots comparing upscaled permeabilities generated using the Oda and Block k methods for the DFN used in the interference tests of Section 7.5. The three plots represent the three axial directions.*

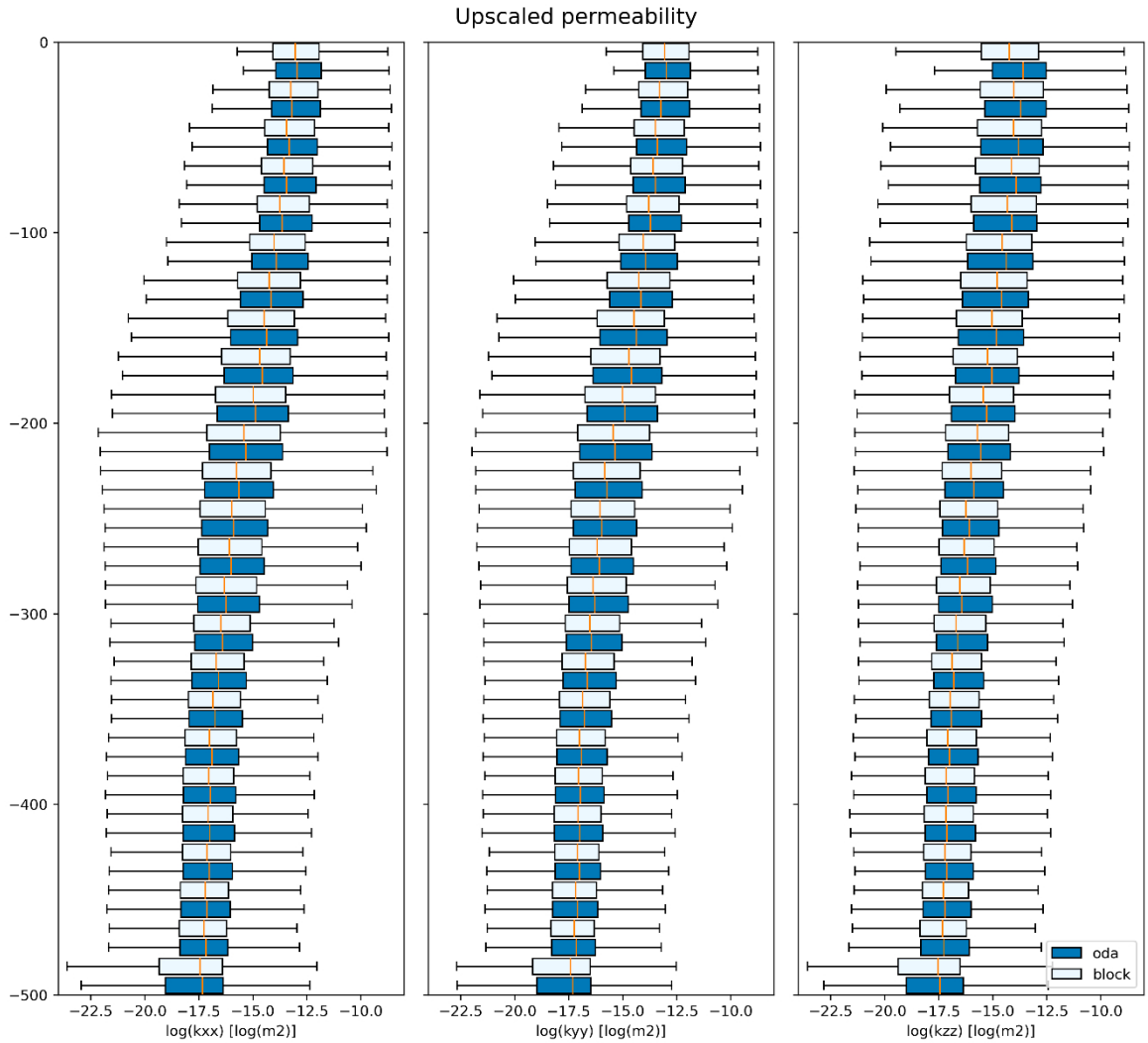

Figure 9-2. *Box plots plotting upscaled permeabilities against elevation for the Oda and Block k methods for the DFN used in the interference tests of Section 7.5. The three plots represent the three axial directions. The bars show quartile ranges, the whiskers show minimum/maximum.*

9.2 Deformation zones upscaling

In the DFN-BF1 model methodology all deformation zones (deterministic, stochastic and semi-stochastic) are modelled as fracture swarms as described in Section 5.3. This modelling approach results in much larger number of fractures compared to previously used DFN models, e.g., (Follin et al. 2007a). Even though this modelling approach results in more realistic geological representation of deformation zones, it increases model complexity which could be hard to handle by some flow simulation programs. Such programs prefer to represent the DZs as meshed surfaces with upscaled heterogeneous properties that capture to some extent the hydraulic properties of the DZ-related damage zones. The resulting midplane properties might be used either explicitly in either simplified DFN models (i.e. DZ modelled as essentially "2D" structures) or implicitly in ECPM models.

Methods to do this have been demonstrated by Baxter et al. (2019). A similar implementation has been developed here. Although here the upscaling is performed on a zone-specific localised structured mesh around each DZ, rather than a global structured mesh whose properties are then projected onto the DZ surfaces as used by Baxter et al. (2019). This is to avoid the necessity of having to create the whole site-scale DFN and upscale to a fixed mesh, instead the upscaling can be performed specifically for a subset or all DZ. The method is essentially similar to Oda but performed on a zone-specific mesh as described in following steps:

1) Create a zone-specific 3D grid around a midplane representing the core of a deformation zone consisting of a mesh of triangles with 10 m side is used. The shape of the grid cells is defined by surface tessellation and the cell thickness corresponds to the thickness of the deformation zone.
2) A three-dimensional conductivity tensor in the global coordinate system XYZ is computed by Oda hydraulic upscaling of all fractures representing the DZ-related fracture swarm into the grid.

$$K_{glob} = \begin{bmatrix} K_{xx} & K_{xy} & K_{xz} \\ K_{yx} & K_{yy} & K_{yz} \\ K_{zx} & K_{zy} & K_{zz} \end{bmatrix} \quad \text{Equation 9-1}$$

3) The natural and convenient way to characterise flow in DZs is to parameterise the distribution of hydraulic properties within and across the local plane of the DZ. This is done using the equations for 3D tensor rotation, the global conductivity tensor is rotated into the local coordinate system of the DZ surface such that local z' direction is aligned with surface normal and the local x' and y' directions being parallel to the surface. Note that the rotation of the conductivity tensor to the local coordinate system is calculated on each surface cell which makes it possible to apply the method also to non-planar surfaces.

$$K_{loc} = R * K_{glob} R^T \quad \text{Equation 9-2}$$

$$R = \begin{bmatrix} \cos\theta + u_x^2(1-\cos\theta) & u_x u_y(1-\cos\theta) - u_z \sin\theta & u_x u_z(1-\cos\theta) + u_y \sin\theta \\ u_y u_x(1-\cos\theta) + u_z \sin\theta & \cos\theta + u_y^2(1-\cos\theta) & u_y u_z(1-\cos\theta) - u_x \sin\theta \\ u_z u_x(1-\cos\theta) - u_y \sin\theta & u_z u_y(1-\cos\theta) + u_x \sin\theta & \cos\theta + u_z^2(1-\cos\theta) \end{bmatrix} \quad \text{Equation 9-3}$$

where u represents a rotation axis defined as the cross-product between surface cell normal vector n and vertical vector (0,0,1), and θ the rotation angle between the two vectors.

4) Hydraulic conductivities parallel and orthogonal to the surface cells are calculated as follow. Transmissivity in parallel direction can be obtained by multiplying $K_{parallell}$ by the zone thickness:

$$K_{parallel} = \frac{K_{loc,xx} + K_{loc,yy}}{2} \quad \text{Equation 9-4}$$

$$K_{ortho} = K_{loc,zz} \quad \text{Equation 9-5}$$

A simple illustration of the upscaling method is shown in Figure 9-3 where the DZ midplane is a simple square and there are three large DZ-related fractures with $T = 10^{-6}$ m^2/s generated in the damage zone. Two fractures are sub-parallel to the midplane surface placed on each side of the midplane while the third fracture is orthogonal to this surface. The resulting upscaled and projected transmissivity by using the method described above is shown on right. The transmissivity of individual fractures is correctly

projected into the centre surface, but the method results in a higher transmissivity in the area where fractures overlap and resulting in an artificial connection between the two fractures. An alternative would be to use flux-based with cells of thickness equal to that of the damage zone associated to the DZ, and thereby capture some connectivity effects. However, given the results presented in Figure 9-2, geometrical upscaling seems adequate when applied on the scale of 10–20 m cells and for fracture size scaling and size-property correlations used in the DFN-BF1 model.

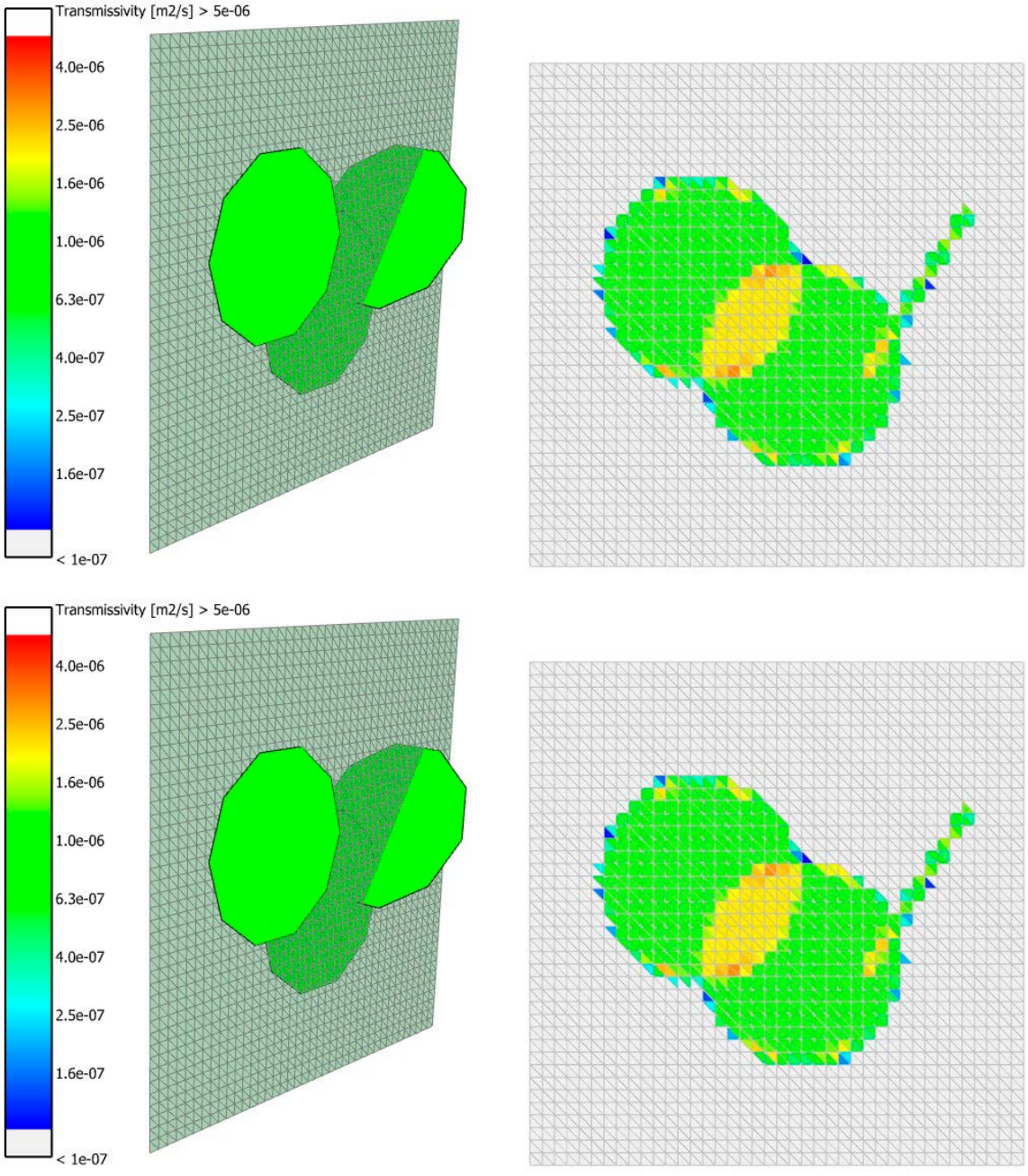

Figure 9-3. *Schematic type of the geometric-type method used to upscale DZ damage zone hydraulics to heterogeneous properties projected onto the midplane. The triangulated mesh is created to discretise heterogeneity across the midplane. The left figure shows three example DZ-related fractures. The right figure shows the resulting upscaled transmissivity (in-plane component) as projected onto the midplane.*

An important point is that the DZ upscaling method is only applied to DZ-related fractures around each midplane. It does not include any contribution from the background fractures. This is because it is envisaged that end users will import a representation of the background separately, and so the upscaled DZ model need only represent the component above the background level, to avoid double counting. On the reverse side of that argument is that the combined network may have a higher hydraulic conductivity than the sum of its parts due to enhanced connectivity. This is less of a concern when using geometric upscaling, as it is not sensitive to connectivity and on a reasonably fine mesh. Elaborations can be added to the methodology for different circumstances, such as generating the entire DFN, doing a global connectivity analysis to identify the connected open fractures, and then applying the DZ upscaling only to the connected open DZ-related fractures.

Figure 9-4 presents the results of the DZ upscaling for the in-plane transmissivity for DMS model and for ZFMA2 (2 km radius model used for interference tests). This demonstrates the depth trends in transmissivity that result from the hydromechanical model, and the heterogeneity that results from the random sampling of DZ-related fracture sizes and their correlation to individual fracture transmissivity, see the underlying DFN for ZFMA2 shown in Figure 9-5 Upscaled transmissivities are higher in the near-surface as the dense fracturing sums within cells. The dependence on orientation can also be seen with higher transmissivity for gently dipping structures. Size dependence of transmissivity is the main cause for localised higher transmissivities at depth, however, the flows in these areas will be hydraulically choked by a lack of supply of water from the surrounding structure, except where multiple DZ intersect perhaps.

Statistics of the results are summarised in Figure 9-6 to show the trends mentioned above in a quantitative way. SubH zones have highest transmissivity experiencing the least normal stress and most shear/normal stress ratio. Next is the NW zones since they are sub-parallel to the maximum horizontal stress and NE are least as experiencing the highest normal stress, although the two sub-vertical sets overlap in the top 100 m as the stress magnitudes are lower. This is consistent with earlier trends noted in (Follin and Stigsson 2014), see Figure 6 therein. The ZFMA2 plot shows that higher transmissivities persist in about the top 200 m, which is due to a combination of increased openness of fracturing and some critically stressed fractures in the lower stressed hanging wall of ZFMA2, having a shear contribution to aperture in the model. Below −200 m elevation there is a more gradual reduction in equivalent transmissivity due to normal closure.

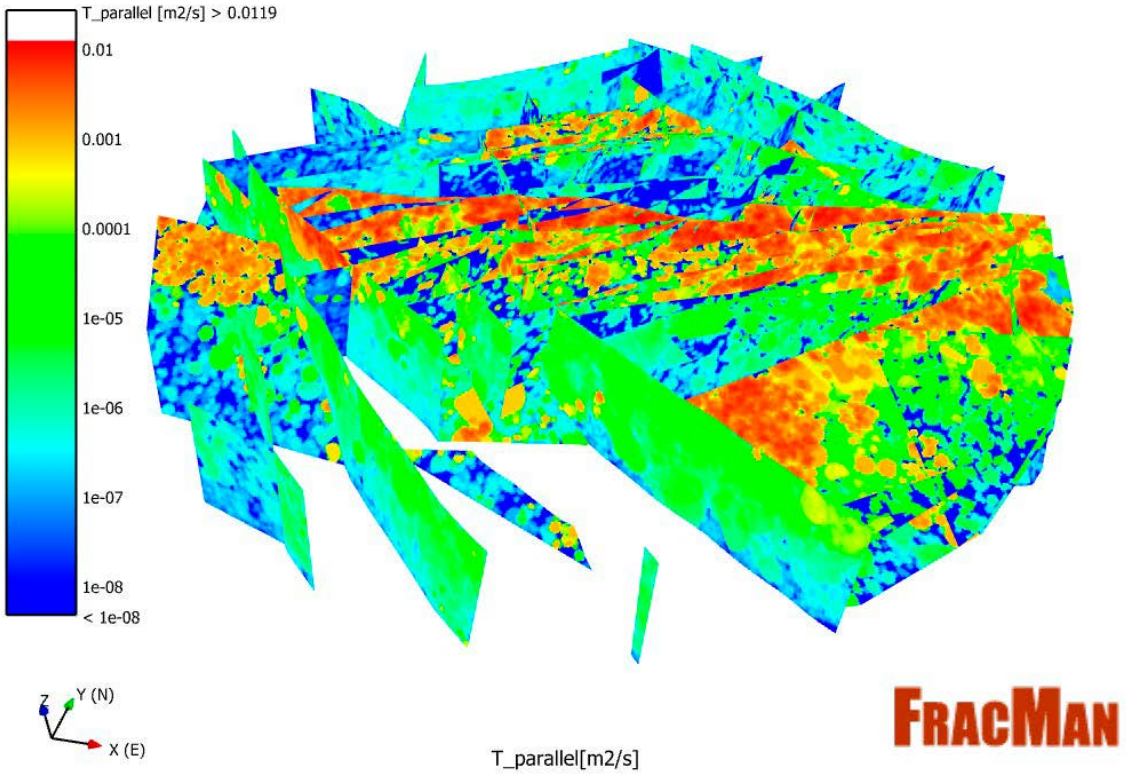

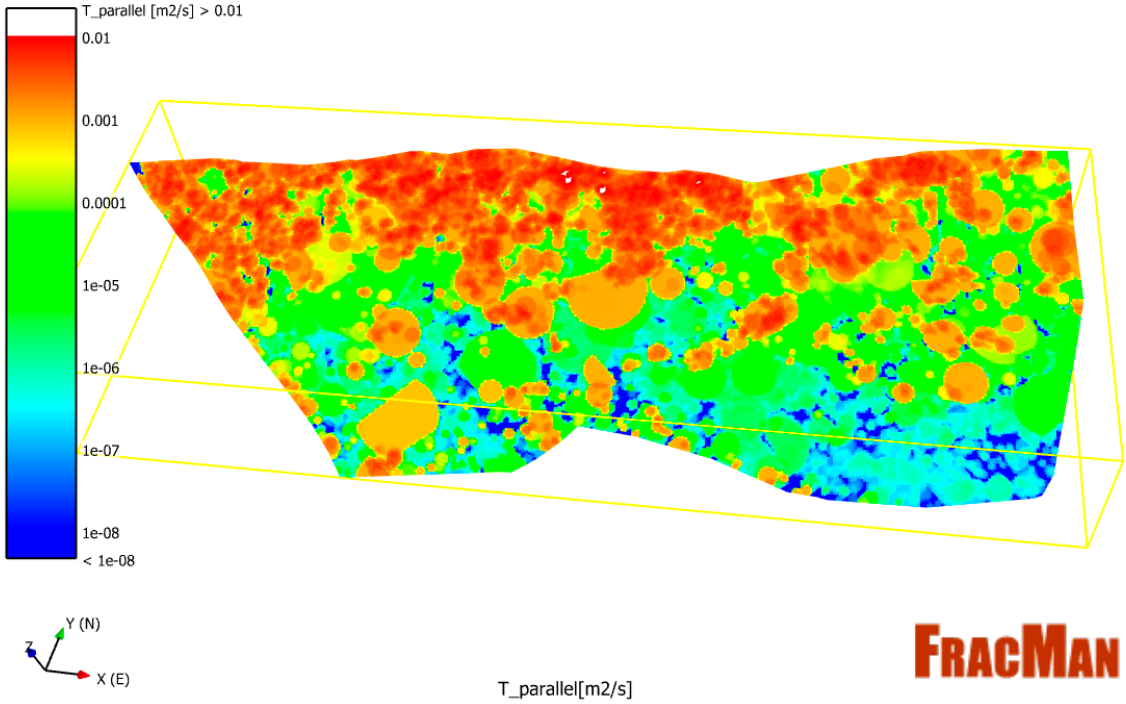

Figure 9-4. *Results of upscaling a single realisation of the DZ-related fracture swarms and projecting their hydraulic properties on to midplanes. The top shows all DZs, and the bottom focuses on ZFMA2. Here, the in-plane transmissivity (parallel to midplane) is shown, calculated as conductivity in the plane multiplied by zone thickness, this compare to the DFN-M2008 methods, e.g. Figure 7 of (Follin and Stigsson 2014).*

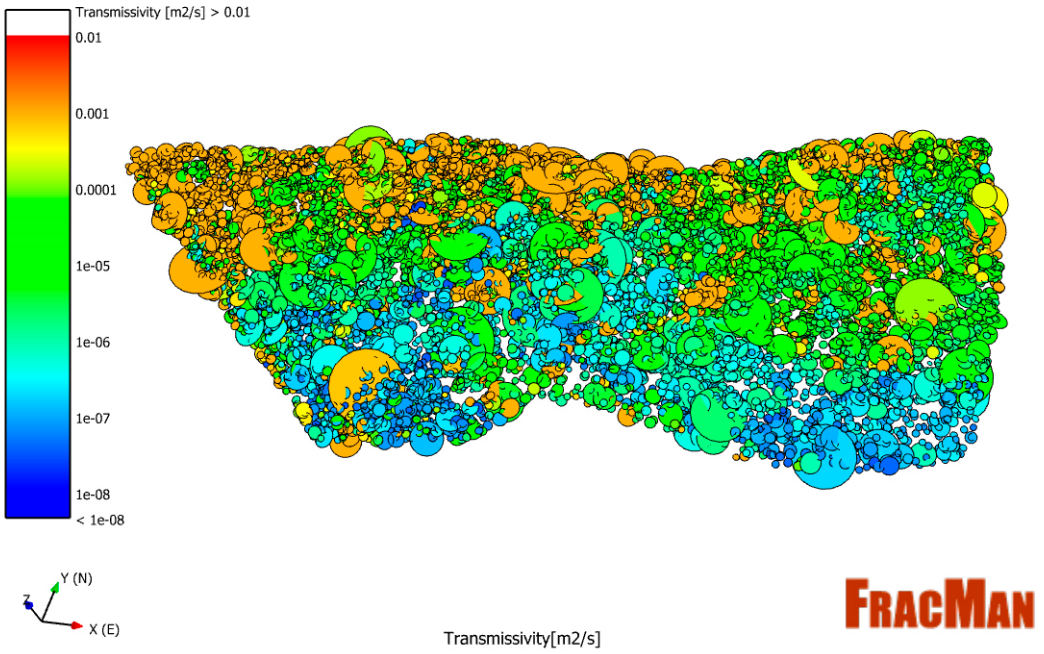

Figure 9-5. *A realisation of the DZ-related fractures and transmissivities for ZFMA2. DZ fractures are generated with size Rmin = 2 m and Rmax = 50 m with hydraulic properties derived according to hydromechanical workflow described in section 6.2. In this example fracture connectivity is not considered.*

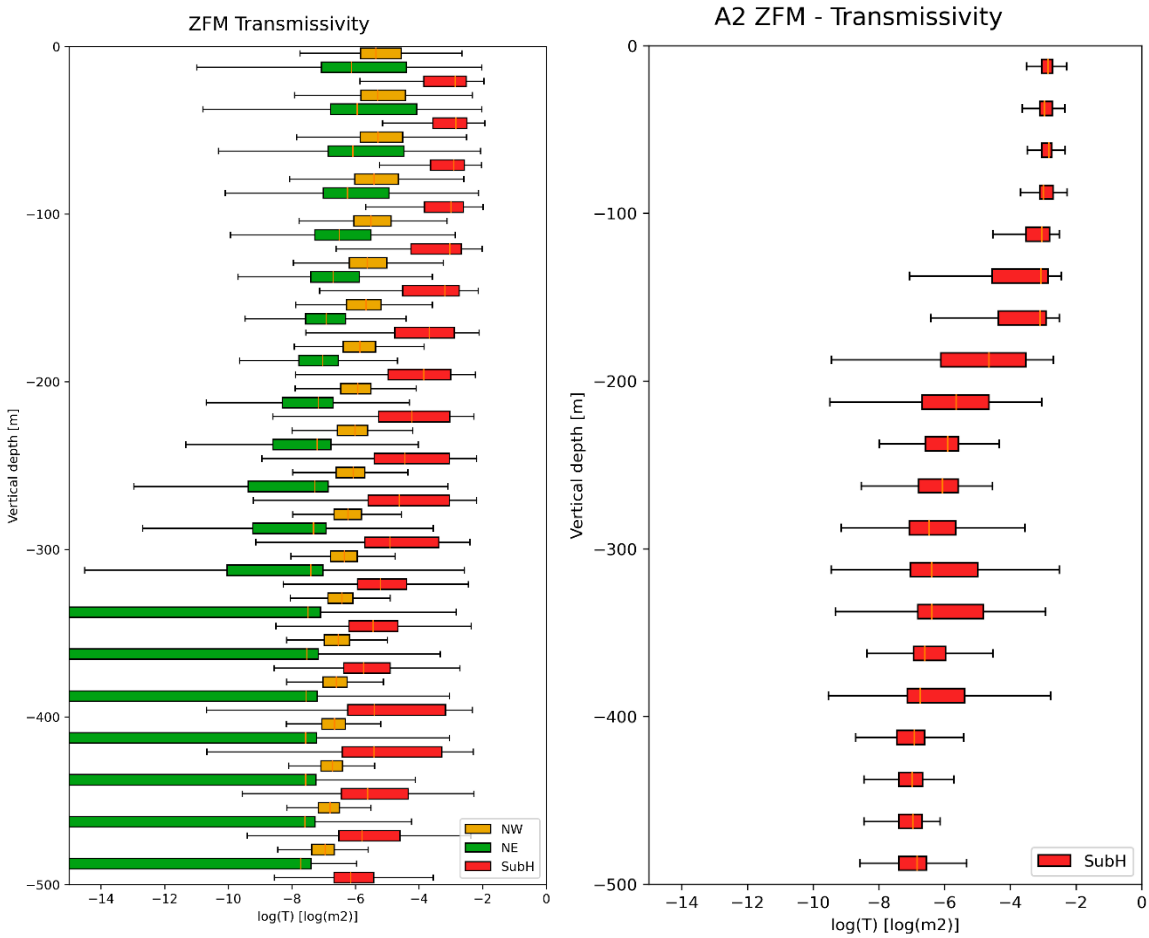

Figure 9-6. *Statistical results of upscaling a single realisation of the DZ-related fracture swarms and projecting their hydraulic properties on to midplanes. The left figure shows results across all DZs but subdivided by orientation set (showing quartiles as bars and minimum/maximum as whiskers). The right figure is specific to ZFMA2 for one realisation.*

10 Conclusions

A Baseline DFN model has been created as an alternative to earlier SDM-Site DFN and SDM-PSU models for Forsmark fully deploying the alternative latest modelling DFN methodology as defined in (Selroos et al. 2022). A more holistic approach has been taken in the current modelling relative to SDM-Site and SDM-PSU. The model makes a seamless integration of deterministic, stochastic and semi-stochastic structural modelling across scales from metres to several kilometres. Geometric, geomechanical and hydraulic properties of fractures and physical dependencies between them are all incorporated in the same model to ensure consistency of conceptual descriptions. This opens new possibilities to identify inter-dependencies between these parameters and how they can be constrained. It is expected that such inter-disciplinary conditioning will eventually lead to improved understanding and confidence in models, and critically as new opportunities for bedrock characterisation and model testing are realised during underground construction of SFK and SFR facilities.

The main novel concepts as applied to Forsmark in the geometric DFN description include:

- Describing fracturing as occurring through a sequence of main deformation phases and mimicking these phases through use of a G-DFN for both deformation zones and individual fractures;
- Describing variability in mean fracture orientations using an inverse distance weighted bootstrapping against borehole data and three Fisher distributed global fracture sets (describing site scale variability by rotations in mean poles and local variability of through the bootstrap sampling of three sets, rather than describing variability through six or more sets);
- Representing deformation zones as domains of individual fractures of elevated intensity representing their damage zones with stochastic variability in their size, connectivity and properties creating a mechanism for them to have a zone of influence and in-plane variability;
- Representing additional stochastic and semi-stochastic deformation zones outside the volume of focused characterisation to give realisations of a structurally consistent model across the regional-scale volume;
- Representing structural variability on a continuous range of scales by introducing deformation zones of relatively intense background fracturing; and
- Identifying differences in fracture characteristics, including spatial variability, between inside the Forsmark tectonic lens and outside, by analysing both KFM and KFR fracture data.

The main novel concepts and methods as applied to Forsmark in the hydromechanical DFN description include:

- Representing the heterogeneity/channelling of connectivity and flow within deterministically modelled deformation zones through their being modelled as grown fracture swarms;
- Describing structural (inside/outside lens) domain- and orientation-specific statistical distributions of the fraction of open fractures to reproduce observed trends in open fracturing and the sparsity of discrete flows;
- Integrating a 3D stress model to describe the drivers for spatial controls of fracture openings and variability in flow between fractures, and hence within deformation zone swarms, improving on earlier pure statistical descriptions;
- Integrating fracture geomechanical parameters via hydromechanical models in the hydraulic calibration, opening the possibility of performing a combined structural-mechanical-hydraulic calibration to reduce uncertainties beyond what can be achieved through individual/partial system calibrations;
- Simulating single-hole flow tests in borehole-specific DFN models for each PFL tested hole including location specific details of deformation zones, borehole trajectory and boundary conditions and thereby improve consideration of flow conditions and statistics in fracture domains, DZs and background rock; and
- Utilising DFN models directly in calibration on large-scale interference tests to better match the compartmentalisation and channelisation of pressure communication observed as spatial variability in pressure responses, and considering the sensitivity to top surface hydraulic boundary conditions.

Going forward, the importance of demonstrating reliability of various aspects of the DFN is recognised as a key activity in maintaining and applying models. In the absence of new underground data, a prediction-outcome exercise has been trialled using preliminary drone data currently being processed and interpreted. This shows a promising degree of compatibility for those metrics appropriate to surface mapping data: intensity, orientation, size and connectivity. The Baseline the DFN-BF1 model is able to predict outcrop-scale variability in these metrics that were noted in SDM-Site (e.g. fractal clustering on scales less than 30 m) but not included formally in the recipes of DFN models developed for SDM-Site and SDM-PSU as they used a homogeneous Poissonian spatial model within each of the delineated fracture domains.

There remain two main tasks to complete the inter-disciplinary integration conceived in the recent site descriptive modelling methodologies:

1. The deterministic modelled structures (DMS) and stochastic structural (DFN) model have now been integrated and implemented across the whole regional-scale model. To fully integrate the hydro-mechanical DFN with the rock mechanical model (RMM) some combined iterative mechanical-hydraulic calibration of models and their parameters. This is the final step required to synchronise a combined hydro-structural-mechanical description as a baseline for future site descriptions of the fractured bedrock at Forsmark; and
2. Such a baseline fractured bedrock system model would then provide the foundations for further integrations with site hydrogeological, hydrological, hydrogeochemical and solute transport models. This would provide opportunities to confirm the hydro-structural-mechanical model or provide additional metrics for its calibration.

Beyond these proposed exercises to reduce uncertainty in hydromechanical properties, hypothesis testing regarding structural parameters, such as size scaling, are most effectively tackled through further detailed mapping of fracture patterns and monitoring hydraulic connectivity underground. The sensitivity of DFN predictions to geometrical parameters can be explored alongside planning of further phases of structural mapping as prediction-outcome exercises. The existing surface-based hydraulic data from PFL and interference tests provide a permanent set of metrics that new DFN models can be tested against as it becomes possible to better constrain the structural and connectivity properties on mapping data from depth. Underground tunnel surface mapping, geological characterisation and hydraulic data will also provide new insights on the scaling and correlation behaviours of hydro-structural-mechanical properties.

Some potential future refinements specific to the alternative DFN methodology presented here include:

- Exploring potential drivers for spatial variability in the sheet joint intensity such as surface curvature, with the additional possibility of a sporadic subvertical joint set where sheet joints are most intense;
- Improving understanding of termination properties between different types of fractures and on different scales. In particular, assessing the possibility of distinct size scaling and termination behaviour for both deformation zones and individual fractures inside and outside the lens based on outcrops and surface mapping in openings of the SFR and SFK facilities. This amounts to a consistent approach to conceptual and modelling methodology across the different structural domains relevant to SFR and SFK facilities;
- Further analysis of the apparent higher DZ-related fracture intensity in NE DZ than SubH and NW. Implying the DZ-related swarm intensity could be set specific, recognising that NE fractures are perpendicular to the regional horizontal stress and so less likely to be open and transmissive;
- Considering an alternative hydromechanical coupling model whereby connected fractures that have been subject to shear/reactivation also have a significant transmissivity; and
- Developing DZ-specific parameterisations for key zones such as ZFMA2, ZFMENE0060A-C, and ZFMWNW0001 (Singö) should be tested.

References

SKB's (Svensk Kärnbränslehantering AB) publications can be found at www.skb.com/publications. SKBdoc documents will be submitted upon request to document@skb.se.

Abdelkader A, Bajaj C L, Ebeida M S, Mahmoud A H, Mitchell S A, Owens J D, Rushdi A A, 2020. VoroCrust: Voronoi meshing without clipping. ACM Transactions on Graphics (TOG). Volume 39, issue 3, p. 1–16.

Ahmed Elfeel M, Geiger S, 2012. Static and dynamic assessment of DFN permeability upscaling. Proceedings of SPE Europec/EAGE Annual Conference, 2012. OnePetro.

Ahokas H, Nummela J, Turku J, 2014. Analysis of ONKALO Water Leakage Mapping Results. Posiva Working Report 2014-17, Posiva Oy.

Andersson J, 2003. Site descriptive modelling – strategy for integrated evaluation. SKB R-03-05, Svensk Kärnbränslehantering AB.

Anderson T L, 2017. Fracture mechanics: fundamentals and applications. CRC press. ISBN: 1315370298.

Bandis S, Lumsden A, Barton N, 1983. Fundamentals of rock joint deformation. Proceedings of International Journal of Rock Mechanics and Mining Sciences & Geomechanics Abstracts, 1983. Elsevier.

Barton N, Choubey V, 1977. The shear strength of rock joints in theory and practice. Rock mechanics. Volume 10, issue 1-2, p. 1–54.

Baxter S, Hartley L, Hoek J, Myers S, Tsitsopoulos V, Williams, T, 2019. Upscaling of brittle deformation zone flow and transport properties. SKB R-19-01, Svensk Kärnbränslehantering AB.

Baxter S, Bym T, Doe T, Hartley L, Libby S, Shi C, 2021. Alternative Conceptual Models for Flow and Transport in Olkiluoto Fracture Systems. Posiva Working Report 2021-15, Posiva Oy.

Berglund S, Selroos J-O, 2004. Transport properties site descriptive model. Guidelines for evaluation and modelling. SKB R-03-09, Svensk Kärnbränslehantering AB.

Billaux D, Chiles J, Hestir K, Long J, 1989. Three-dimensional statistical modelling of a fractured rock mass—an example from the Fanay-Augères mine. Proceedings of International Journal of Rock Mechanics and Mining Sciences & Geomechanics Abstracts, 1989. Elsevier.

Bym T, Hartley L, 2023. Development of new methods to build progressively deterministic DFN models using data from underground construction and operations. SKB R-23-02, Svensk Kärnbränslehantering AB.

Bym T, Hermanson J, 2018. Methods and workflow for geometric and hydraulic conditioning. DFN-R – status report 2013–2015. SKB R-17-12, Svensk Kärnbränslehantering AB.

Carlsson A, 1979. Characteristic features of a superficial rock mass in southern central Sweden – horizontal and subhorizontal fractures and filling material. Striae. Volume 11, p. 1−79

Chen T, Clauser C, Marquart G, Willbrand K, Hiller T, 2018. Upscaling permeability for three-dimensional fractured porous rocks with the multiple boundary method. Hydrogeology Journal. Volume 26, issue 6, p. 1903-1916. doi:10.1007/s10040-018-1744-z

Chilès J P, 1988. Fractal and geostatistical methods for modeling of a fracture network. Mathematical geology. Volume 20, issue 6, p. 631–654.

Chilès J-P, Wackernagel H, Beucher H, Lantuéjoul C, Elion P, 2008. Estimating fracture density from a linear or aerial survey. Proceedings of Proceedings of the VIII International Geostatistics Congress, ed. J. Ortiz and X. Emery, 2008.

Choi J-H, Edwards P, Ko K, Kim Y-S, 2016. Definition and classification of fault damage zones: A review and a new methodological approach. Earth-Science Reviews. Volume 152, p. 70–87. doi:10.1016/j.earscirev.2015.11.006

Darcel C, Davy P, Bour O, De Dreuzy J R, 2006. Discrete fracture network for the Forsmark site. SKB R-06-79, Svensk Kärnbränslehantering AB.

Darcel C, Davy P, Le Goc R, de Dreuzy J R, Bour O, 2009. Statistical methodology for Discrete Fracture Models – including fracture size, orientation uncertainty together with intensiy uncertainty and variability. R-09-38, Svensk Kärnbränslehantering AB.

Darcel C, Davy P, Le Goc R, 2012. Statistical Fracture Domain Methodology For DFN Modeling Applied to Site Characterization. Proceedings of EUROCK 2012, Stockholm, Sweden, 28–30 May, 2012, 2012. BeFo (Bergteknisk Forskning) and International Society for Rock Mechanics (ISRM).

Darcel C, Le Goc R, Davy P, 2013. Development of the statistical fracture domain methodology – application to the Forsmark site. SKB R-13-54, Svensk Kärnbränslehantering AB.

Darcel C, Le Goc R, Doolaeghe D, Ghazal R, Davy P, 2021. Rock mass effective properties from a DFN approach. Phase 1 – Elastic properties SKB R-20-05, Svensk Kärnbränslehantering AB.

Davy P, Le Goc R, Darcel C, 2013. A model of fracture nucleation, growth and arrest, and consequences for fracture density and scaling. Journal of Geophysical Research: Solid Earth. Volume 118, issue 4, p. 1393–1407. doi:10.1002/jgrb.50120

Delgado-Martin J, Muñoz-Ibáñez A, Herbón-Penabad M, Alejano R L, 2021. Fracture toughness using pseudo-compact tension (pCT) test and semi-circular bending specimen (SCB) test. P-21-02, Svensk Kärnbränslehantering AB.

Dershowitz W, Herda H H, 1992. Interpretation of fracture spacing and intensity. Proceedings of Proc. U.S. Symp. Rock Mech., 1992.

Dershowitz W, Lee G, Geier J, Foxford T, La Pointe P, Thomas A, 1998. FRACMAN-Interactive Discrete Feature Data Analysis, Geometric Modeling, and Exploration Simulation. User Documentation, version 2.6. 923–1089, Golder Associates Inc.

Doolaeghe D, Darcel C, Selroos J O, Davy P, 2023. Controls on fracture openness and reactivation in Forsmark, Sweden. Scientific Reports. Volume 13(1). doi:10.1038/s41598-023-33619-9

Earon R, 2022. Watershed analysis of SAR Model Area. Spatial analysis of overland runoff relating to Site Modelling – Forsmark area. SKBdoc 1940271 ver 1.0, Svensk Kärnbränslehantering AB.

Efron B, 1982. The jackknife, the bootstrap and other resampling plans. Society for Industrial and Applied Mathematics (SIAM) Philadelphia Pennsylvania USA.

Elliott G M, Brown E T, Boodt P I, Hudson J A, 1985. Hydromechanical behaviour of joints in the Carnmenellis granite, SW England-A keynote lecture. In International symposium on fundamentals of rock joints. p. 249–258.

Evans K F, Kohl T, Rybach L, Hopkirk R J, Campbell R, 1992. The effects of fracture normal compliance on the long term circulation behavior of a hot dry rock reservoir; a parameter study using the new fully-coupled code “fracture”. Transactions – Geothermal Resources Council. Volume 20, p. 449–456.

Faulkner D R, Mitchell T M, Jensen E, Cembrano J, 2011. Scaling of fault damage zones with displacement and the implications for fault growth processes. Journal of Geophysical Research. Volume 116, issue B5. doi:10.1029/2010jb007788

Follin S, 2008. Bedrock hydrogeology Forsmark. Site descriptive modelling, SDM-Site Forsmark. SKB R-08-95, Svensk Kärnbränslehantering AB.

Follin S, 2019. Multidisciplinary description of the access area of the planned spent nuclear fuel repository in Forsmark prior to construction. SKB R-17-13, Svensk Kärnbränslehantering AB.

Follin S, Stigsson M, 2014. A transmissivity model for deformation zones in fractured crystalline rock and its possible correlation to in situ stress at the proposed high-level nuclear waste repository site at Forsmark, Sweden. Hydrogeology Journal. Volume 22, issue 2, p. 299–311.

Follin S, Johansson P-O, Hartley L, Jackson P, Roberts D, Marsic N, 2007a. Hydrogeological conceptual model development and numerical modelling using CONNECTFLOW. Forsmark modelling stage 2.2. SKB R-07-49, Svensk Kärnbränslehantering AB.

Follin S, Levén J, Hartley L, Jackson P, Joyce S, Roberts D, Swift B, 2007b. Hydrogeological characterisation and modelling of deformation zones and fracture domains, Forsmark modelling stage 2.2. SKB R-07-48, Svensk Kärnbränslehantering AB.

Follin S, Hartley L, Jackson P, Roberts D, Marsic N, 2008. Hydrogeological conceptual model development and numerical modelling using CONNECTFLOW, Forsmark modelling stage 2.3. SKB R-08-23, Svensk Kärnbränslehantering AB.

Follin S, Ludvigson J-E, Levén J, 2011. A comparison between standard well test evaluation methods used in SKB's site investigations and the generalised radial flow concept. SKB P-06-54, Svensk Kärnbränslehantering AB.

Fox A, La Pointe P, Hermanson J, Öhman J, 2007. Statistical geological discrete fracture network model. Forsmark modelling stage 2.2. SKB R-07-46, Svensk Kärnbränslehantering AB.

Fox A, Forchhammer K, Pettersson A, La Pointe P, Lim D-H, 2012. Geological discrete fracture network model for the Olkiluoto site, Eurajoki, Finland. Version 2.0. Posiva Oy, Eurajoki, Finland.

Glamheden R, Fredriksson A, Roeshoff K, Karlsson J, Hakami H, Christiansson R, 2007. Rock mechanics Forsmark. Site descriptive modelling Forsmark stage 2.2. SKB R-07-31, Svensk Kärnbränslehantering AB.

Glamheden R, Lanaro F, Karlsson J, Lindberg U, Wrafter J, Hakami H, Johansson M, 2008. Rock mechanics Forsmark. Modelling stage 2.3. Complementary analysis and verification of the rock mechanics model. SKB R-08-66, Svensk Kärnbränslehantering AB.

Gokall-Norman K, Ludvigson J-E, 2007. Hydraulic interference test in borehole HFM14. Forsmark site investigation. SKB P-06-196, Svensk Kärnbränslehantering AB.

Gokall-Norman K, Ludvigson J-E, 2008. Large-scale interference test with borehole HFM14 used as pumping borehole, 2007. Forsmark site investigation. SKB P-07-228, Svensk Kärnbränslehantering AB.

Golder, 2020. FracMan. Available at: https://www.golder.com/fracman/

Hakala M, Ström J, Valli J, Juvani J, 2019. Structural control on stress.

variability at Forsmark. SKB R-19-23, Svensk Kärnbränslehantering AB.

Hakami E, Mas Ivars D, Darcel C, 2022. Methodology for rock mechanics modelling of the Forsmark site. R-20-13, Svensk Kärnbränslehantering AB.

Harrström J, Hedberg S, Öhman J, 2019. Hydraulic interference tests in KFR27, KFR103, and KFR105. Site investigation SDM-PSU. SKB P-17-20, Svensk Kärnbränslehantering AB.

Hartley L, 2022a. Summary of Prediction-Outcome Exercises (2017–2021) on the Discrete Fracture Network (DFN) Model for the Olkiluoto Bedrock. Posiva Oy, Eurojoki, Finland.

Hartley L, 2022b. Discrete Fracture Network Model for the Olkiluoto Bedrock. Posiva Oy, Eurojoki, Finland.

Hartley L, Baxter S, Hoek J, Joyce S, Mosley K, Williams T, Fox A, Cottrell M, La Pointe P, Gehör S, Darcel C, Le Goc R, Aaltonen I, Vanhanarkaus O, Löfman J, Poteri A, 2018. Discrete Fracture Network Modelling (Version 3) in Support of Olkiluoto Site Description 2018. Posiva Oy, Eurojoki, Finland.

Hartley L, Baxter S, Carty J, Libby S, 2021. Exploratory integration of discrete fracture network models and 1D stress models with data from hydraulic tests for the shallow bedrock at the Forsmark site. R-21-13, Svensk Kärnbränslehantering AB.

Hazewinkel M, 2013. Encyclopaedia of mathematics: volume 6: subject index—author index. Springer Science & Business Media. ISBN: 9400903650.

Hermanson J, Petersson J, 2022. Methodology for deterministic geological modelling of the Forsmark site Application to the development of the final repository for spent nuclear fuel. SKB R-20-10, Svensk Kärnbränslehantering AB.

Hermansson T, Stephens M B, Corfu F, Andersson J, Page L, 2007. Penetrative ductile deformation and amphibolite-facies metamorphism prior to 1851Ma in the western part of the Svecofennian orogen, Fennoscandian Shield. Precambrian Research. Volume 153, issue 1-2, p. 29–45. doi:10.1016/j.precamres.2006.11.009

Hermansson T, Stephens M B, Corfu F, Page L M, Andersson J, 2008a. Migratory tectonic switching, western Svecofennian orogen, central Sweden: Constraints from U/Pb zircon and titanite geochronology. Precambrian Research. Volume 161, issue 3-4, p. 250–278. doi:10.1016/j.precamres.2007.08.008

Hermansson T, Stephens M B, Page L M, 2008b. 40Ar/39Ar hornblende geochronology from the Forsmark area in central Sweden: Constraints on late Svecofennian cooling, ductile deformation and exhumation. Precambrian Research. Volume 167, issue 3-4, p. 303–315. doi:10.1016/j.precamres.2008.09.003

Hökmark H, Lönnqvist M, 2014. Reply to comment by Christopher Talbot on "Approach to estimating the maximum depth for glacially induced hydraulic jacking in fractured crystalline rock at Forsmark, Sweden. J. Geophys. Res. Earth Surf. Volume 119, p. 955–959. doi.org/10.1002/jgrf.20106

Hökmark H, Fälth B, Wallroth T, 2006. T-H-M couplings in rock. Overview of results of importance to the SR-Can safety assessment. SKB R-06-88, Svensk Kärnbränslehantering AB.

Hökmark H, Lönnqvist M, Fälth B, 2010. THM-issues in repository rock. Thermal, mechanical, thermo-mechanical and hydro-mechanical evolution of the rock at the Forsmark and Laxemar sites. SKB TR-10-23, Svensk Kärnbränslehantering AB.

Isaksson H, Johansson L, 2020. Complementary lineament interpretation in the SDM-SAR drainage area at Forsmark. P-20-14, Svensk Kärnbränslehantering AB.

ITASCA, 2022. 3DEC Version 7.0: Distinct Element Modeling of Jointed and Blocky Material in 3D. Version: 7.0. ITASCA, 111 Third Avenue South, Suite 450, Minneapolis, MN 55401, USA. URL: https://www.itascacg.com/software/3dec [31 October 2022].

Jackson C P, Hoch A R, Todman S, 2000. Self-consistency of a heterogeneous continuum porous medium representation of a fractured medium. Water Resources Research. Volume 36, issue 1, p. 189–202.

Klimczak C, Schultz R A, Parashar R, Reeves D M, 2010. Cubic law with aperture-length correlation: implications for network scale fluid flow. Hydrogeology Journal. Volume 18, issue 4, p. 851–862. doi:10.1007/s10040-009-0572-6

Koistinen T, Stephens M B, Bogatchev V, Nordgulen O, Wennerström M, Korhonen J, 2001. Geological Map of the Fennoscandian Shield, Scale 1:2 000 000. Geological Surveys of Finland, Norway and Sweden and the North-West Department of Natural Resources of Russia. ISBN: 9516908128.

Komulainen J, Pekkanen J, Ripatti K, 2019. Forsmark site investigations. Difference flow logging in boreholes KFM14, KFM15, KFM16, KFM20, KFM21, KFM22 and KFM23. P-19-19, Svensk Kärnbränslehantering AB.

Krabbendam M, Palamakumbura R, Arnhardt C, Hall A, 2021. Rock fracturing by subglacial hydraulic jacking in basement rocks, eastern Sweden: the role of beam failure. Gff. Volume 143, issue 4, p. 390–405.

Krabbendam M, Dioguardi F, Arnhardt C, Roberson S, Hall A M, 2022a. Drag forces at the ice-sheet bed and resistance of hard-rock obstacles: the physics of glacial ripping. Journal of Glaciology. p. 1–17.

Krabbendam M, Hall A M, Palamakumbura R, Finlayson A, 2022b. Glaciotectonic disintegration of roches moutonnées during glacial ripping in east Sweden. Geografiska Annaler: Series A, Physical Geography. Volume 104, issue 1, p. 35–56.

LaForce T, Ebeida M, Jordan S, Miller T A, Stauffer P H, Park H, Leone R, Hammond G, 2022. Voronoi Meshing to Accurately Capture Geological Structure in Subsurface Simulations. Mathematical Geosciences. p. 1–33.

La Pointe P R, Olofsson I, Hermanson J, 2005. Statistical model of fractures and deformation zones for Forsmark. Preliminary site description Forsmark area – version 1.2. SKB R-05-26, Svensk Kärnbränslehantering AB.

Lei Q, Latham J P, Tsang C F, Xiang J, Lang P, 2015. A new approach to upscaling fracture network models while preserving geostatistical and geomechanical characteristics. Journal of Geophysical Research: Solid Earth. Volume 120, issue 7, p. 4784–4807.

Leijon B, 2005. Investigations of superficial fracturing and block displacements at drill site 5. Forsmark site investigation. SKB P-05-199, Svensk Kärnbränslehantering AB.

Libby S, Hartley L, Turnbull R, Cottrell M, 2019. Grown Discrete Fracture Networks: a new method for generating fractures according to their deformation history. American Rock Mechanics Association 19-1559, New York, June, 2019.

Libby S, Catley J, Hartley L, 2020. Shaft data heterogeneity analysis. Posiva Project Memorandum, Posiva Oy.

Libby S, Hartley L, Turnbull R, Cottrell M, Bym T, Josephson N, Munier R, Selroos J O, Mas Ivars D, 2024. Exploring the impact of fracture interaction on connectivity and flow channelling using grown fracture networks. Quarterly Journal of Engineering Geology and Hydrogeology. Volume 57, issue 1. doi:https://doi.org/10.1144/qjegh2023-010

Lidmar-Bergström K, 1994. Morphology of the bedrock surface. Geology. National Atlas of Sweden. p. 44–54.

Loh J, Stein M, 2004. Bootstrapping a spatial point process. J Statistica Sinica. p. 69–101.

Lundqvist J, 1994. The deglaciation. J Geology, National Atlas of Sweden, Fredén C . Almqvist Wiksell, Stockholm, Vol 208.

Lönnqvist M, Hökmark H, 2010. Assessment of potential for glacially induced hydraulic jacking at different depths. SKB R-09-35, Svensk Kärnbränslehantering AB.

Lönnqvist M, Hökmark H, 2013. Approach to estimating the maximum depth for glacially induced hydraulic jacking in fractured crystalline rock at Forsmark, Sweden. Journal of Geophysical Research: Earth Surface. Volume 118, issue 3, p. 1777–1791. doi:10.1002/jgrf.20106

Martel S J, 2011. Mechanics of curved surfaces, with application to surface-parallel cracks. Geophysical Research Letters. Volume 38, issue 20. doi.org/10.1029/2011GL049354

Martin C D, 2007. Quantifying in situ stress magnitudes and orientations for Forsmark. Forsmark stage 2.2. SKB R-07-26, Svensk Kärnbränslehantering AB.

Martin C D, Chandler N, 1993. Stress heterogeneity and geological structures. International Journal of Rock Mechanics and Mining Sciences & Geomechanics Abstracts. Volume 30, issue 1, p. 993–999. doi:https://doi.org/10.1016/0148-9062(93)90059-M

Mas Ivars D, Veiga Ríos M, Shiu W, Johansson F, Fredriksson A, 2014. Long term stability of rock caverns BMA and BLA of SFR, Forsmark. SKB R-13-53, Svensk Kärnbränslehantering AB.

Mattila J, Follin S, 2019. Does in situ state of stress affect fracture flow in crystalline settings? Journal of Geophysical Research: Solid Earth.

Mattila J, Viola G, 2014. New constraints on 1.7 Gyr of brittle tectonic evolution in southwestern Finland derived from a structural study at the site of a potential nuclear waste repository (Olkiluoto Island). J Journal of Structural Geology. Volume 67, p. 50–74.

Min K-B, Rutqvist J, Tsang C-F, Jing L, 2004. Stress-dependent permeability of fractured rock masses: a numerical study. International Journal of Rock Mechanics and Mining Sciences. Volume 41, issue 7, p. 1191–1210.

Moon S, Perron J, Martel S, Holbrook W, St. Clair J, 2017. A model of three-dimensional topographic stresses with implications for bedrock fractures, surface processes, and landscape evolution. Journal of Geophysical Research: Earth Surface. Volume 122, issue 4, p. 823–846.

Munier R, 2004. Statistical analysis of fracture data, adapted for modelling Discrete Fracture Networks-Version 2. SKB R-04-66, Svensk Kärnbränslehantering AB.

Munier R, Stenberg L, Stanfors R, Milnes A G, Hermanson J, Triumf C-A, 2003. Geological Site Descriptive Model. A strategy for the model development during site investigations. SKB R-03-07, Svensk Kärnbränslehantering AB.

Neretnieks I, 1979. Diffusion in the rock matrix – An important factor in radionuclide retardation? SKBF/KBS TR 79-19, Svensk Kärnbränslehantering AB.

Neretnieks I, 2006. Channeling with diffusion into stagnant water and into a matrix in series. Water resources research. Volume 42, issue 11.

Nishiyama S, Ohnishi Y, Ito H, Yano T, space, 2014. Mechanical and hydraulic behavior of a rock fracture under shear deformation. J Earth, planets. Volume 66, issue 1, p. 108.

Nordbäck N, Mattila J, 2018. Brittle Fault Systems of the ONKALO Underground Research Facility. WR 2018-20, Posiva Oy.

Oda M, 1985. Permeability tensor for discontinuous rock masses. Geotechnique. Volume 35, issue 4, p. 483–495.

Olofsson I, Simeonov A, Stephens M, Follin S, Nilsson A-C, Röshoff K, Lindberg U, Lanaro F, Fredriksson A, Persson L, 2007. Site descriptive modelling Forsmark, stage 2.2. A fracture domain concept as a basis for the statistical modelling of fractures and minor deformation zones, and interdisciplinary coordination. SKB R-07-15, Svensk Kärnbränslehantering AB.

Olson J E, 2003. Sublinear scaling of fracture aperture versus length: An exception or the rule? Journal of Geophysical Research: Solid Earth. Volume 108, issue B9. doi:10.1029/2001jb000419

Page L, Hermansson T, Söderlund P, Andersson J, Stephens M B, 2004. Bedrock mapping U-Pb, 40Ar/39Ar and (U-Th)/He geochronology. Forsmark site investigation. SKB P-04-126, Svensk Kärnbränslehantering AB.

Page L, Hermansson T, Söderlund P, Stephens M B, 2007. 40Ar/39Ar and (U-Th)/He geochronology: Phase 2. SKB P-06-211, Svensk Kärnbränslehantering AB.

Palmqvist K, 1990. Groundwater in crystalline bedrock. SKB TR 90-41, Svensk Kärnbränslehantering AB.

Pollard D D, Segall P, 1987. Theoretical displacements and stresses near fractures in rock: with applications to faults, joints, veins, dikes and solution surfaces. In Atkinson B K (ed). Fracture Mechanics of Rock. London: Academic Press Ltd.

POSIVA SKB, 2017. Safety functions, performance targets and technical design requirements for a KBS-3V repository. Conclusions and recommendations from a joint SKB and Posiva working group. Posiva SKB Report 01, Posiva Oy, Svensk Kärnbränslehantering AB.

Rhén I, Follin S, Hermanson J, 2003. Hydrological Site Descriptive Model – a strategy for its development during Site Investigations. SKB R-03-08, Svensk Kärnbränslehantering AB.

Rice J R, McMEEKING R M, Parks D M, Sorensen E P, 1979. Recent finite element studies in plasticity and fracture mechanics. Computer Methods in Applied Mechanics and Engineering. Volume 17, p. 411–442.

Rutqvist J, Wu Y-S, Tsang C-F, Bodvarsson G, 2002. A modeling approach for analysis of coupled multiphase fluid flow, heat transfer, and deformation in fractured porous rock. International Journal of Rock Mechanics and Mining Sciences. Volume 39, issue 4, p. 429–442.

Saintot A, Stephens M B, Viola G, Nordgulen Ø, 2011. Brittle tectonic evolution and paleostress field reconstruction in the southwestern part of the Fennoscandian Shield, Forsmark, Sweden. Tectonics. Volume 30, issue 4. doi.org/10.1029/2010TC002781

Sanderson D J, Nixon C W, 2015. The use of topology in fracture network characterization. Journal of Structural Geology. Volume 72, p. 55–66.

Sandström B, Tullborg E-L, Page L, 2008a. Fracture mineralogy and 40Ar/39Ar ages of adularia in fracture filling and K-feldspar in breccia. Data from drill cores KFM01C, KFM01D, KFM02B, KFM04A, KFM06A, KFM06B, KFM07A, KFM08A, KFM08B, KFM08C, KFM08D, KFM09A, KFM09B, KFM10A and KFM11A. Forsmark site investigation. SKB P-08-14, Svensk Kärnbränslehantering AB.

Sandström B, Tullborg E-L, Smellie J, MacKenzie A B, Suksi J, 2008b. Fracture mineralogy of the Forsmark site. SDM-Site Forsmark. SKB R-08-102, Svensk Kärnbränslehantering AB.

Sandström B, Tullborg E-L, Larson S-Å, Page L, 2009. Brittle tectonothermal evolution in the Forsmark area, central Fennoscandian Shield, recorded by paragenesis, orientation and $^{40}Ar/^{39}Ar$ geochronology of fracture minerals. Tectonophysics. Volume 478, issue 3-4, p. 158–174.

Scholz C H, Dawers N H, Yu J Z, Anders M H, 1993. Fault growth and fault scaling laws; preliminary results. Journal of Geophysical Research. Volume 98, issue B12, p. 21,951–21,961.

Schultz R A, 2003. A method to relate initial elastic stress to fault population strains. Geophysical Research Letters. Volume 30, issue 11.

Schultz R A, Okubo C H, Wilkins S J, 2006. Displacement-length scaling relations for faults on the terrestrial planets. Journal of Structural Geology. Volume 28, issue 12, p. 2182–2193.

Selroos J-O, Appleyard P, Bym T, Follin S, Hartley L, Joyce S, Munier R, 2015. The Stochastic-Deterministic Transition in Discrete Fracture Network Models and its Implementation in a Safety Assessment Application by Means of Conditional Simulation. Invited Talk, H53I-02, AGU Fall Meeting, San Fransisco, 14–18 December, 2015.

Selroos J-O, Mas Ivars D, Munier R, Hartley L, Libby S, Davy P, Darcel C, Trinchero P, 2022. Methodology for discrete fracture network modelling of the Forsmark site. Part 1 – concepts, data and interpretation methods. R-20-11, Svensk Kärnbränslehantering AB.

Sidborn M, Sandström B, Tullborg E-L, Salas J, Maia F, Delos A, Molinero J, Hallbeck L, Pedersen K, 2010. SR-Site: Oxygen ingress in the rock at Forsmark during a glacial cycle. SKB TR-10-57, Svensk Kärnbränslehantering AB.

Sih G C, 1973. Handbook of stress intensity factors. Institute of Fracture and Solid Mechanics, Lehigh University.

SKB, 2008. Site description of Forsmark at completion of the site investigation phase. SDM-Site Forsmark. SKB TR-08-05, Svensk Kärnbränslehantering AB.

SKB, 2010. Data report for the safety assessment SR-Site. SKB TR-10-52, Svensk Kärnbränslehantering AB.

SKB, 2011. Long-term safety for the final repository for spent nuclear fuel at Forsmark. Main report of the SR-Site project. SKB TR-11-01, Svensk Kärnbränslehantering AB.

SKB, 2013. Site description of the SFR area at Forsmark at completion of the site investigation phase. SDM-PSU Forsmark. SKB TR-11-04, Svensk Kärnbränslehantering AB.

SKB, 2015. Safety analysis for SFR Long-term safety. Main report for the safety assessment SR-PSU. Revised edition. SKB TR-14-01, Svensk Kärnbränslehantering AB.

SKB, 2018. Detailed site investigation programme for the construction and operation of the Repository for spent nuclear fuel. SKB R-17-16, Svensk Kärnbränslehantering AB.

Sneddon I N, Lowengrub M, 1969. Crack problems in the classical theory of elasticity. 1969, 221 P.

Stanfors R, 2006. Review of existing information from the Äspö HRL area, with focus on hydraulically important minor structures. SKB P-06-117, Svensk Kärnbränslehantering AB.

Stephens M B, 2009. Synthesis of the bedrock geology in the Bergslagen region, Fennoscandian Shield, south–central Sweden. Paper Ba 58, pp 259 pp, Sveriges geologiska undersökning (SGU).

Stephens M B, 2010. Bedrock geology – overview and excursion guide. Forsmark site investigation. SKB R-10-04, Svensk Kärnbränslehantering AB.

Stephens M B, Simeonov A, 2015. Description of deformation zone model version 2.3, Forsmark. SKB R-14-28, Svensk Kärnbränslehantering AB.

Stephens M B, Fox A, La Pointe P, Simeonov A, Isaksson H, Hermanson J, Öhman J, 2007. Geology Forsmark. Site descriptive modelling Forsmark stage 2.2. SKB R-07-45, Svensk Kärnbränslehantering AB.

Stephens M B, Bergman T, Isaksson H, Petersson J, 2008a. Bedrock geology Forsmark. Modelling stage 2.3. Description of the bedrock geological map at the ground surface. SKB R-08-128, Svensk Kärnbränslehantering AB.

Stephens M B, Simeonov A, Isaksson H, 2008b. Bedrock geology Forsmark. Modelling stage 2.3. Implications for and verification of the deterministic geological models based on complementary data. SKB R-08-64, Svensk Kärnbränslehantering AB.

Svensson U, Löfgren M, Trinchero P, Selroos J O, 2018. Modelling the diffusion-available pore space of an unaltered granitic rock matrix using a micro-DFN approach. Journal of Hydrology. Volume 559, issue 1, p. 182–191. doi: https://doi.org/10.1016/j.jhydrol.2018.02.041

Sævik P, Nixon C, 2017. Inclusion of topological measurements into analytic estimates of effective permeability in fractured media. Water Resources Research. Volume 53, issue 11, p. 9424–9443.

Söderbäck B, 2008. Geological evolution, palaeoclimate and historical development of the Forsmark and Laxemar-Simpevarp areas. Site descriptive modelling. SDM-Site. SKB R-08-19, Svensk Kärnbränslehantering AB.

Söderlund P, 2008. 40Ar/39Ar, AFT and (U-Th)/He thermochronologic implications for the low-temperature geological evolution in SE Sweden. [Doctoral Thesis (compilation), Lithosphere and Biosphere Science]. Department of Geology, Lund University**.**

Söderlund P, Hermansson T, Page L M, Stephens M B, 2009. Biotite and muscovite $^{40}Ar/^{39}Ar$ geochronological constraints on the post-Svecofennian tectonothermal evolution, Forsmark site, central Sweden. International Journal of Earth Sciences. Volume 98, p. 1835–1851.

Talbot C J, 2014. Comment on "Approach to estimating the maximum depth for glacially induced hydraulic jacking in fractured crystalline rock at Forsmark, Sweden" by M. Lönnqvist and H. Hökmark. Journal of Geophysical Research: Earth Surface. Volume 119, issue 4, p. 951–954.

Terzaghi R, 1965. Sources of error in joint surveys. Geotechnique. Volume 15, issue 3, p. 287–304.

Valli J, Hakala M, Mattila J, Winderholler R, 2023. Control of deterministically modelled structures on the stress variability at Forsmark. R-23-04, Svensk Kärnbränslehantering AB.

Van der Walt S, Schönberger J L, Nunez-Iglesias J, Boulogne F, Warner J D, Yager N, Gouillart E, Yu T, 2014. scikit-image: image processing in Python. PeerJ. Volume 2, p. e453.

Vermilye J M, Scholz C H, 1998. The process zone; a microstructural view of fault growth. Journal of Geophysical Research. Volume 103, issue B6, p. 12,223–12,237.

Wang X, 2005. Stereological interpretation of rock fracture traces on borehole walls and other cylindrical surfaces. PhD thesis Virginia Polytechnic Institute and State University.

Wickman F E, Åberg G, Levi B, 1983. Rb-Sr dating of alteration events in granitoids. Contributions to Mineralogy and Petrology. Volume 83, issue 3-4, p. 358–362.

Willis-Richards J, Watanabe K, Takahashi H, 1996. Progress toward a stochastic rock mechanics model of engineered geothermal systems. J Journal of Geophysical Research: Solid Earth. Volume 101, issue B8, p. 17481–17496.

Witherspoon P A, Wang J S Y, Iwai K, Gale J E, 1980. Validity of cubic law for fluid flow in a deformable rock fracture. Water Resources Research. Volume 16, issue 6, p. 1016–1024.

Zangerl C, Eberhardt E, Evans K, Löw S, 2008. Normal stiffness of fractures in granitic rock: a compilation of laboratory and in-situ experiments. International journal of rock mechanics and Mining Sciences. Volume 45, issue 8, p. 1500–1507.

Zou L, Jing L, Cvetkovic V, 2017. Modeling of flow and mixing in 3D rough-walled rock fracture intersections. Advances in Water Resources. Volume 107, p. 1–9. doi: https://doi.org/10.1016/j.advwatres.2017.06.003

Öhman J, Bockgård N, Follin S, 2012. Bedrock hydrogeology. Site investigation SFR. SKB R-11-03, Svensk Kärnbränslehantering AB.

Öhman J, Follin S, Odén M, 2013. Bedrock Hydrogeology – Groundwater flow modelling. Site investigation SFR. SKB R-11-10, Svensk Kärnbränslehantering AB.

Appendix

A1 Cluster Identification

The cluster identification method described here was used for two tasks: to quantify the number of sets in different parts of the fracture network (Section 4.2); and a trialled but eventually unused method to isolate fractures that might be associated with DZ midplanes (Appendix A2). The algorithm identifies clusters of points in orientation data, automating the process of picking out the 'hotspots' on a stereonet density plot.

There are three steps to the method:

1. Calculate the density distribution of the orientation data. This uses the exponential Kamb method with a sigma value of 3 and calculates density on a 100 by 100 grid.
2. Identify peaks in the grid of density data points using the peak_local_max function in the scikit-image image processing Python module (Van der Walt et al. 2014).
3. Filter clusters that are within 20 degrees of another, larger cluster, and filter clusters whose maximum density is < 90 % of the overall maximum density.

A2 Alternative methods for DZ-related intensity calculation

The preferred method for identify the intensity of DZ fractures is to calculate the average intensities inside and outside the DZ intervals and calculate the difference (see Subsection 5.3.3). However, three other alternative methods were tested.

The first alternative method is conceptually simplest and involves calculating the average intensity in the non-DZ internals above and below DZ intervals and then calculating the difference in intensity with the DZ interval. This method is successful in identifying the number of 'extra' fractures that are present in the SHI intervals, as shown in Figure A-1. However, it is not possible to reliably convert these fracture counts to an intensity as the counts are not specifically associated with an orientation, so the Terzaghi Wang (2005) and Chiles (Chilès et al. 2008) conversion techniques are not applicable. In addition, the method will be sensitive to the presence of peaks in fracture intensity adjacent to the SHI intervals (Figure A-1).

The second alternative method attempted to classify a subset of fractures in DZ intervals as being DZ associated by identifying fractures whose orientation was similar to that of the DZ midplane. However, this method was also not successful as the proportion of fractures sub-parallel to the ZFM midplane was not consistently higher inside the DZ interval than outside, as shown in Figure A-2.

The third alternative method uses the Interactive Set Identification System within FracMan (Dershowitz et al. 1998; Golder 2020) to isolate the cluster of fractures that is coplanar with the intersected DZ surfaces. The method has been used previously for objective set identification at Forsmark (Fox et al. 2007) and Olkiluoto (Fox et al. 2012). It finds the best fit between an input distribution of orientations and an arbitrary number of Fisher orientation distributions, and then divides the input distribution to those Fisher distributions accordingly. By selecting the cluster of fracture orientations closest to the orientation of a given DZ where it intersects the borehole, a subset of the data can be associated to that DZ. Two examples of identification of DZ-related fracture clusters for particular SHI interpreted DZ are shown in Figure A-3.

The intensity of this subset can then be calculated, first as a Terzaghi weighted P_{10} (with maximum weight of 7), and then converted to an average P_{32} for the DZ interval using the Chiles method (Chilès et al. 2008). Most intervals were split into three clusters, and only one of these associated with the DZ, matching the three main fracture sets. However, in some intervals with fewer fractures FracMan's set identification was configured to find one or two clusters. The number of clusters to split the data into was determined using the method described in Appendix A1. Collating these results over all DZ produces the distribution of intensities shown in Figure A-4. The mode for mean P_{32} across all DZ intervals is close to 9 m^2/m^3. The mode value for the distribution when $\alpha = \beta = 2.5$ is about 1.7 times this, so the maximum intensity is 15.3 m^2/m^3 at the midplane.

However, this method was also rejected due to its complexity and the inconsistency between the intensity of fractures it identified as non-DZ associated and the intensity of the background fracturing outside DZ intervals.

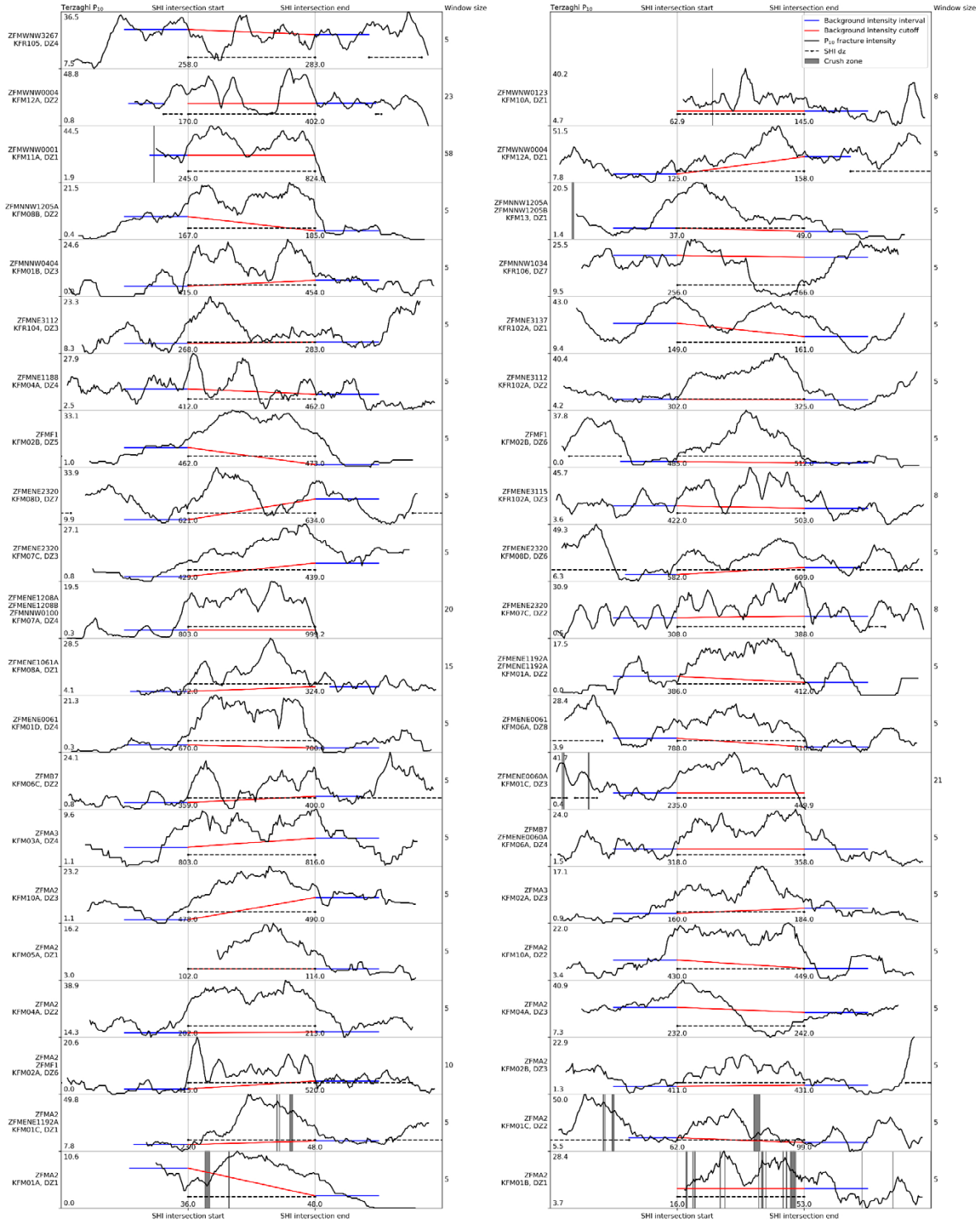

Figure A-1. *Graphs showing the P_{10} intensity distribution, calculated in subintervals ('windows') of the size given to the right of the graphs, across the SHI intervals (black lines) in comparison to the average intensity that might be expected inside the SHI interval without the influence of the DZ (red lines) according to the average intensity outside the SHI interval (blue lines). The DZ, borehole and interval each graph is valid for is shown on the left of each graph. The x axis of each graph represents depth down the borehole normalised so that the start and end of the SHI interval is aligned with the other graphs, to aid visual comparison of the different scales. The start and the end depth of each interval is labelled on the vertical lines adjacent to each graph. The y axis of each graph represents the P_{10} intensity, normalised to the maximum and minimum values shown at the left of each graph. The average intensity outside the SHI interval is measured in intervals up to half the SHI interval length but may be shorter if that interval contains the end of the logged borehole or another SHI interval. To avoid sensitivity to short intervals, those SHI intervals that were deemed to have an insufficient length of non-SHI fracture logging adjacent were not included in this analysis. This insufficient length was defined as the greater of 5 m, or 20 % of the length of the SHI interval.*

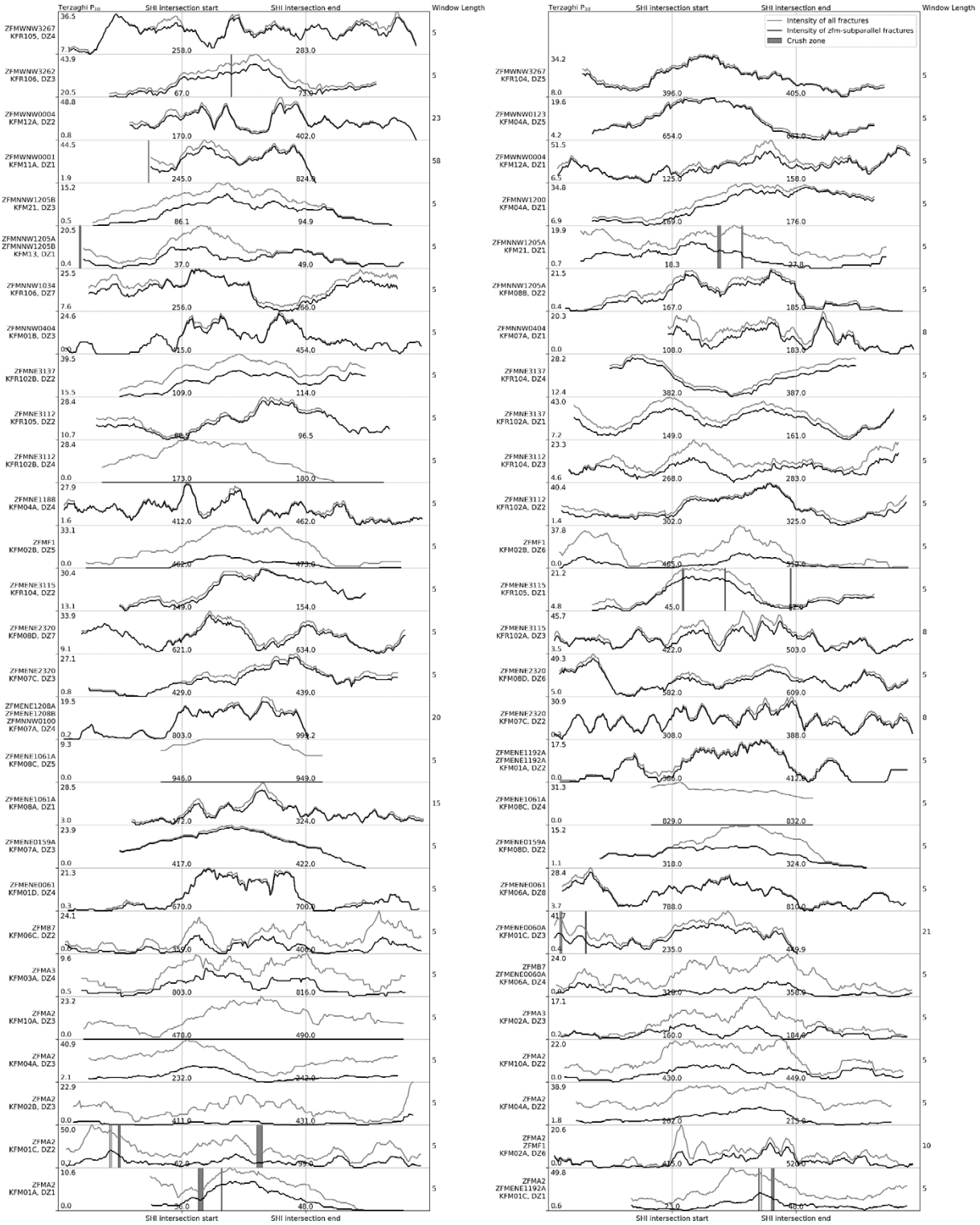

Figure A-2. *Graphs showing the P_{10} intensity distribution, calculated in subintervals ('windows') of the size given to the right of the graphs, across the SHI intervals (grey lines) in comparison to the intensity distribution of the subset of fractures within 60° dihedral angle of the DZ orientation (black lines). The DZ, borehole and interval each graph is valid for is shown on the left of each graph. The x axis of each graph represents depth down the borehole normalised so that the start and end of the SHI interval is aligned with the other graphs, to aid visual comparison of the different scales. The start and the end depth of each interval is labelled on the vertical lines adjacent to each graph. The y axis of each graph represents the P_{10} intensity, normalised to the minimum and maximum values shown at the left of each graph.*

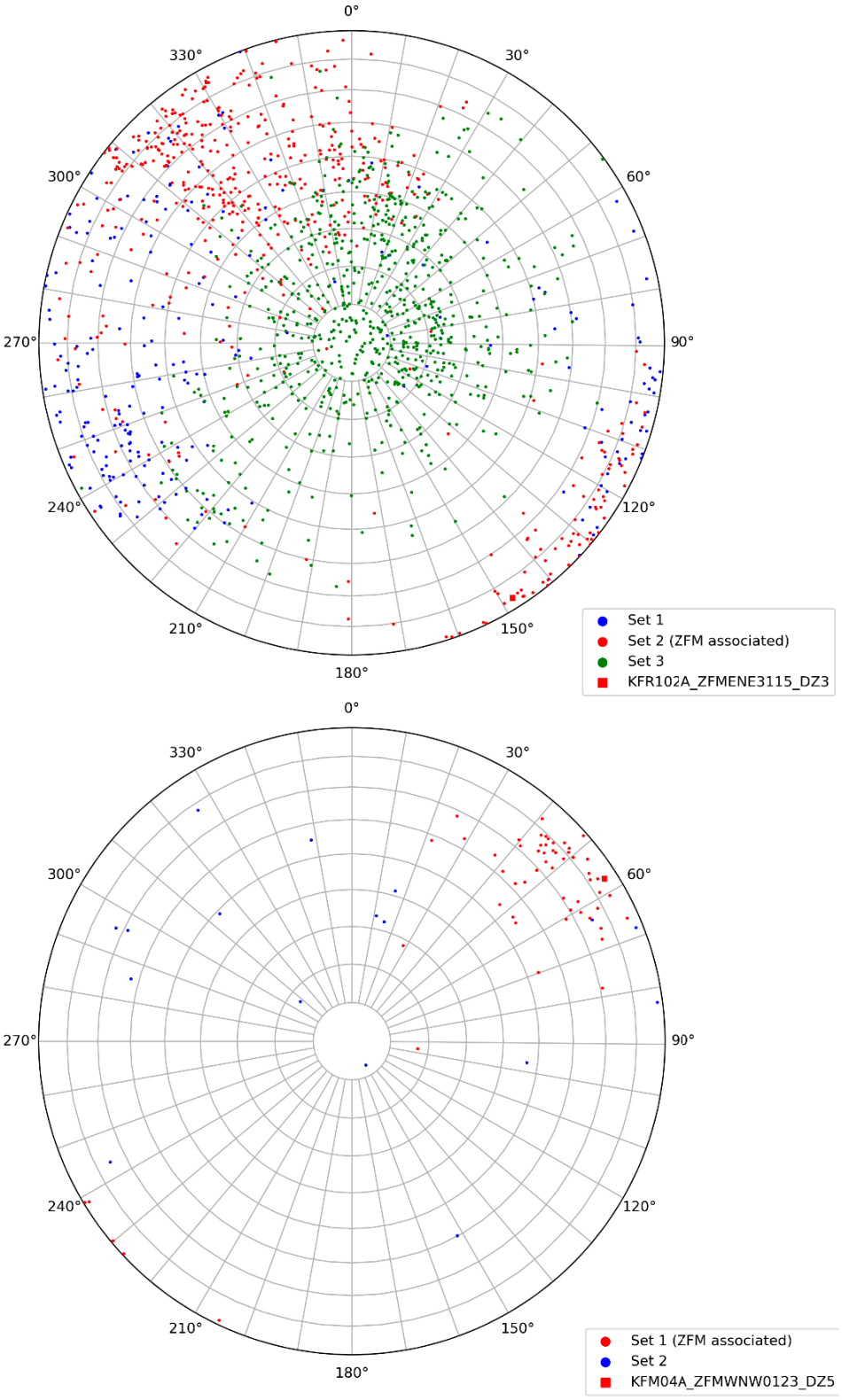

Figure A-3. *Stereonets showing SHI intervals: Top) KFR102A for the intersect with DZ3 (422–503 depth), Bottom) KFM04A for the intersect with DZ5 (654–661 m depth) indicating the results of FracMan's cluster analysis to identify DZ-related fractures versus background fractures. The red squares indicate the orientation of the midplanes of the DZs, and the red points indicate those fractures in the interval that are identified as DZ-related.*

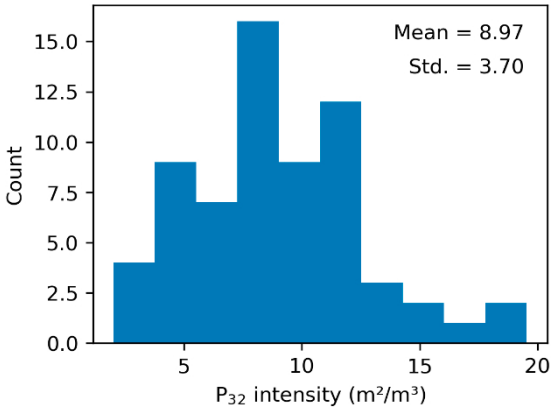

Figure A-4. *Histogram showing the distribution of average P_{32} of DZ-related fractures across each DZ SHI interval.*

A3 Voronoi Cells

One way to minimise numerical errors introduced by gridding is to simulate on Voronoi meshes (Abdelkader et al. 2020; LaForce et al. 2022). Voronoi meshes are extremely advantageous for meshing complex geometries for subsurface simulations as there is no constraint on cell topology, so any closed volume can be meshed to the desired degree of accuracy with sufficient grid refinement. By construction, in a Voronoi mesh the direction of the calculated flux between two adjacent cells is perpendicular to the element face connecting them. Thus, an important source of numerical error introduced by using flexed hexahedral or tetrahedral meshes is minimized. Voronoi meshes are particularly promising for simulators that use two-point flux approximations such as PFLOTRAN. In the context of fracture modelling, triangulated meshes represent the fracture planes with elements at the triangle vertices, as opposed to the triangle centres, to achieve up to six connections per element, as opposed to up to three. Thus, a better conceptualisation / visualisation of these properties may be achieved by considering the Voronoi cells of the triangular mesh (Figure A-5).

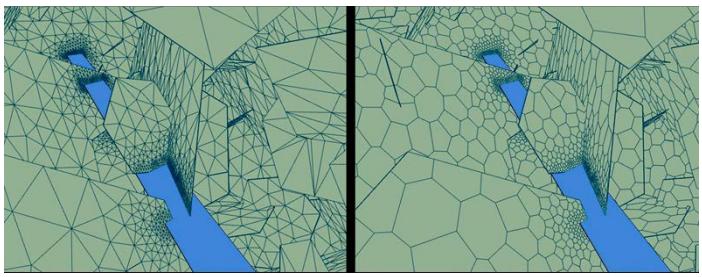

Figure A-5. *Images showing how a triangular fracture mesh around a tunnel (left) translates into Voronoi cells for the same mesh (right).*

Arkitektkopia AB, Bromma, 2024

SKB is responsible for managing spent nuclear fuel and radioactive waste produced by the Swedish nuclear power plants such that man and the environment are protected in the near and distant future.

skb.se